

# **Simulation of Resonant Tunnelling Diodes with the Non-Equilibrium Green's Function Formalism**

Pranav Acharya

SUBMITTED IN FULFILMENT OF THE REQUIREMENTS FOR THE  
DEGREE OF  
DOCTOR OF PHILOSOPHY

SCHOOL OF ENGINEERING  
COLLEGE OF SCIENCE AND ENGINEERING



**University  
ofGlasgow**

SEPTEMBER 2025

*To my parents and grandparents.*

# Abstract

This thesis describes the research carried out by the author in simulating resonant tunnelling diodes (RTDs), nanoelectronic devices which exhibit a region of negative differential resistance (NDR) due to quantum tunnelling, with device variation. This research was carried out with the nano-electronic simulation software (NESS), which is under development at the University of Glasgow. Chapter 1 describes the background and theory of RTDs, before following up with chapter 2 on the theory and methodology of using NESS with the non-equilibrium Green's function (NEGF) transport solver module within this thesis. In the following chapters 3, 4 and 5, respectively the effects of device dimension variation, random discrete dopants (RDDs) and interface roughness (IR) on RTD were investigated. Variation in current-voltage characteristics (IV) due to RDDs and IR were additionally shown to allow RTDs to encode information, and thus provides support for the potential of RTDs to compose physical unclonable functions (PUFs) which can uniquely identify items which they are placed on.

# Contents

<b>Abstract</b>	<b>iii</b>
<b>Acknowledgements</b>	<b>xxvi</b>
<b>Output</b>	<b>xxviii</b>
<b>Overview</b>	<b>xxix</b>
<b>Declaration</b>	<b>xxx</b>
<b>Abbreviations</b>	<b>xxxi</b>
<b>1 Literature Review</b>	<b>1</b>
1.1 Introduction . . . . .	1
1.2 RTD . . . . .	2
1.2.1 RTD History . . . . .	2
1.2.2 Theory of Operation . . . . .	4
1.2.3 RTD Applications . . . . .	9
1.3 Materials and Types of RTDs . . . . .	9
1.3.1 Materials . . . . .	9
1.3.2 Types of RTDs . . . . .	12
1.4 Stochastic Device Variation . . . . .	13
1.5 Physical Unclonable Functions . . . . .	15
1.5.1 PUF basics . . . . .	15
1.5.2 RTDs as PUFs . . . . .	19
1.6 Issues and Countermeasures . . . . .	21
1.7 RTDs for THz electronics . . . . .	25
1.7.1 THz gap . . . . .	26

1.7.2	RTD Oscillators . . . . .	27
1.7.3	THz Detectors . . . . .	33
1.7.4	Design of Device . . . . .	34
1.8	Conclusion . . . . .	37
<b>2</b>	<b>Theory and Methods</b>	<b>38</b>
2.1	Introduction . . . . .	38
2.2	Structure Generator . . . . .	41
2.2.1	Device Generation . . . . .	41
2.2.2	Random Discrete Dopants . . . . .	43
2.2.3	Interface Roughness . . . . .	46
2.3	Poisson solver . . . . .	55
2.4	Non-Equilibrium Green's Function (NEGF) Formalism . . . . .	57
2.4.1	Green's Functions . . . . .	57
2.4.2	Contacts . . . . .	61
2.4.3	Coupled Mode Space Approximation . . . . .	62
2.4.4	Electron-Phonon interactions . . . . .	64
2.5	Resonant Tunnelling Diode . . . . .	66
<b>3</b>	<b>Design of Experiment</b>	<b>72</b>
3.1	Introduction . . . . .	72
3.2	Methodology . . . . .	73
3.3	Results and Discussion . . . . .	74
3.3.1	Baseline Device . . . . .	75
3.3.2	Symmetric Barrier and QW Thickness Variation . . . . .	85
3.3.3	Asymmetric Barrier Thickness Variation . . . . .	91
3.4	Conclusion . . . . .	95
<b>4</b>	<b>Random Discrete Dopants</b>	<b>97</b>
4.1	Introduction . . . . .	97
4.2	Results and discussions . . . . .	98
4.2.1	'Smooth' RTD device—without RDDs . . . . .	98

4.2.2	Effect of RDDs on the device characteristics . . . . .	100
4.3	Conclusion . . . . .	110
<b>5</b>	<b>Interface Roughness</b>	<b>112</b>
5.1	Introduction . . . . .	112
5.2	Sensitivity of RTDs to IR . . . . .	113
5.2.1	IR with Different Interface Configurations . . . . .	113
5.2.2	RTDs with Full IR . . . . .	119
5.3	Interface Roughness in RTDs for PUFs . . . . .	123
5.3.1	Variation in Asperity and Correlation Length . . . . .	123
5.3.2	Min-entropy of RTDs with IR . . . . .	131
5.4	Impact of IR Correlation on RTD Variation . . . . .	132
5.4.1	Improved Isotropic Interface Roughness . . . . .	137
5.4.2	Improved Anisotropic Interface Roughness . . . . .	139
5.5	Conclusion . . . . .	143
<b>6</b>	<b>Conclusion</b>	<b>146</b>
6.1	Summary . . . . .	146
6.2	Further Work . . . . .	149
<b>Appendices</b>		<b>151</b>
A	Theory and Methods . . . . .	151
A1	Node-Centred Finite Volume Discretisation . . . . .	151
A2	Efficient solving of Poisson Potential . . . . .	154
A3	Contacts . . . . .	156
A4	Sancho-Rubio Iterative Method . . . . .	159
A5	Electron-Phonon interactions . . . . .	161
A6	Recursive Solving of Green's Functions . . . . .	164
A7	Matrix Inversion for Retard Greens Function Dyson Equation . . . . .	170
A8	Derivation of Iterative Equation for Left-Connected Retarded Green's Function . . . . .	171

# List of Tables

5.1	Mean $V_r$ and $I_r$ for the previous and ‘improved’ IR for different correlation lengths [10]. . . . .	137
5.2	Standard deviations of $V_r$ and $I_r$ for the previous and ‘improved’ IR for different correlation lengths [10]. . . . .	138

# List of Figures

- 1.1 Sketches of an idealised RTD band diagram under different bias and a corresponding IV characteristic in figure(a) and figure(b) respectively, with points of interest labelled. Point A at the origin has zero bias and current, point B is the resonant peak or local maxima with bias  $V_r$  and current peak  $I_r$ , and point C is the valley or local minima with bias  $V_v$  and current minima  $I_v$ . Figure(a) contains band diagram sketches through the centre of a double barrier quantum well RTD, with each subfigure under a different bias corresponding to the annotated points in figure(b). The conductance band minima (CBM)  $E_C$  for each subfigure within figure(a) (a black solid line) forms two potential barriers separating the emitter region on the left with an emitter Fermi level  $E_{F,E}$  (black dotted line), the QW in the middle with a ground quasibound energy of  $E_{QW}$  (red solid line), and a collector region to the right with a collector Fermi level  $E_{F,C}$  (black dotted line). Within figure(b), the resonant peak at point B and the valley at point C bound the NDR region. Figure(b) also does not account for the space-charge effect [44], which is shown in Fig. 1.3. . . . . 4



1.6 Combined figure [2] of schematic of a 3 RTD PUF array in figure(a) and an IV characteristic response in figure(b), from Figures 4 and 6 respectively of the paper [2]. Within figure(a) ‘ $V_{challenge}$ ’ is the input bias voltage, ‘ $I_{response}$ ’ is the output current, ‘SW’ refers to the bilateral/analogue switches [135], and ‘SWBp’ refers to the bypass switches which can be used to bypass certain RTDs if they fail [2]. A further explanation of the schematic array in figure(a) and the IV characteristic in figure(b) is given in the paper [2]. The figures [2] used in this combined figure are licensed under CC BY 4.0. . . . .	20
1.7 Scatterplot of powers and fundamental frequencies achieved by single RTD oscillators. The labels correspond to the following papers with the most recent ones listed first: a [4], b [69], c [70], d [43], e [71], f [72], g [73], h [170], i [171], j [172], k [34], l [173], and m [33]. Note that the marker ‘g’ overlaps on the ‘e’ marker because both have reported powers of $40\mu\text{W}$ [71, 73] and frequencies of 510GHz [73] and 507GHz [71] respectively. . . . .	27
1.8 Scatterplot of powers and frequencies achieved by arrays of RTDs, including oscillators making use of 2 RTDs. The labels correspond to the following papers with the most recent ones listed first: I [36], II [37], III [38], IV [39], V [40], VI [41], VII [42], VIII [43], and IX [174]. . . . .	28
1.9 Figure(a) is a schematic diagram of an amplitude-modulated(AM) continuous wave THz RTD radar and figure(b) is the error evaluated for different distances. This figure is from the following paper [3]. In figure(a) a sinusoidal modulation signal generated by the signal generator (SG) is superimposed on the bias voltage which causes the RTD signal to be amplitude-modulated, thus leading to an emitted AM-THz signal which hits a target object. The reflected signal is measured by a detector, in this case a Schottky barrier diode (SBD), which also demodulates the AM-THz wave to re-extract the sinusoidal signal. The time of flight (ToF) of the AM-THz signal is determined by the phase difference between a reference signal from the SG and the demodulated signal. Further discussion regarding this figure is given in [3]. This figure [3] is licensed under CC BY 4.0. . . . .	29

1.10 A schematic of a slot antenna [4] setup. The MIM (metal-insulator-metal) capacitor is formed by a separation of the upper and lower electrodes. The slot antenna is formed by a gap in the lower electrode and neighbouring dielectric and the highly n++ doped InGaAs layer. The ITO (indium-tin-oxide) shunt resistor suppresses parasitic oscillations at low frequencies. This figure [4] .is licensed under CC BY 4.0. . . . .	30
1.11 IV characteristic of an RTD detector [6]. Direct detection occurs when the RTD is biased in the PDR (Positive Differential Region) of current close to the resonant peak (labelled A and B) due to strong non-linearity in current. Coherent detection makes use of the NDR (Negative Differential Resistance), which is similarly annotated and labelled, wherein the RTD acts as an oscillator. This figure is sourced from a paper[6] first published and copyrighted by Engineers Australia© 2011, Engineers Australia. . . . .	33
1.12 Annotated IV characteristic of a simulated RTD [9]. The NDR (Negative Differential Resistance) between the resonant peak $I_r$ at $V_r$ and the valley $I_v$ at $V_v$ is highlighted blue. This figure [9] is licensed under CC BY 4.0. . . . .	35
2.1 Schematic of the modular structure of NESS, from [5]. Of these modules, this thesis makes use of the structure generator, the NEGF solver, and the Poisson solver. This figure [5] is licensed under CC BY 4.0. . . . .	39
2.2 An example of a heterostructure nanowire structure created by the structure generator of NESS [196], with materials for mesh cells visualised. This nanowire is composed of 1nm wide cubic cells, with dimensions of $8\text{nm} \times 3\text{nm} \times 3\text{nm}$ , and GaAs material composes the first 4nm along the X axis, and $\text{Al}_{0.3}\text{Ga}_{0.7}\text{As}$ composes other 4nm. . . . .	41
2.3 An example of an n-doped nanowire structure created by the structure generator of NESS [196], with dopant concentration $N_D\text{cm}^{-3}$ visualised. This nanowire is composed of 1nm wide cubic cells, with dimensions of $8\text{nm} \times 3\text{nm} \times 3\text{nm}$ , with a base dopant concentration of $1 \times 10^{15}\text{cm}^{-3}$ and a raised dopant concentration of $2 \times 10^{18}\text{cm}^{-3}$ for the nodes composing the first and last 2nm along the X axis. . . . .	42

2.4 This figure is a schematic of a $\text{Al}_{0.3}\text{Ga}_{0.7}\text{As}/\text{GaAs}$ RTD from [7]. The dimensions are $55\text{nm} \times 10\text{nm} \times 10\text{nm}$ , with $2 \times 10^{18}\text{cm}^{-3}$ n-doped source (0nm-19nm) and emitter (36nm-55nm) GaAs regions and a central $1 \times 10^{15}\text{cm}^{-3}$ n-doped heterostructure region. This central region is composed of 3nm GaAs spacers (19nm-22nm and 33nm-36nm) enclosing two 3nm $\text{Al}_{0.3}\text{Ga}_{0.7}\text{As}$ barriers (22nm-25nm and 30-33nm) and a 5nm GaAs QW (25nm-30nm) in the middle. This figure is licensed under CC BY 4.0, attached to an archived copy of [7] held by the University of Glasgow. The University of Glasgow has an agreement with IEEE allowing authors to self-archive manuscripts with an attached CC BY licence. © 2024, IEEE. . . . .	43
2.5 RTD with RDD (Random Discrete Dopant) positions shown as green spheres. The GaAs body and $\text{Al}_{0.3}\text{Ga}_{0.7}\text{As}$ barriers are both partially transparent volumes, which are blue and red respectively, to allow the visualisation of RDDs. . . . .	43
2.6 Frequency distribution of RDDs (Random Discrete Dopants) generated for 75 RTDs generated within this chapter, with a fitted Poisson Probability Mass Function curve. Details of the Poisson Probability Mass Function formulation and parameters ( $N=75$ , $\mu=4.348$ , and $\nabla k=2.261$ ) are noted within the inset. $N$ is the total number of RTDs and $k$ is a variable describing the number of RDDs, corresponding to the ‘x’ axis in the plot. . . . .	44
2.7 Figure(a) is created using AFM (Atomic Force Microscopy) image data of an $\text{Al}_{0.3}\text{Ga}_{0.7}\text{As}$ surface, which was graciously provided by the authors of [1]. Figure(b) is an autocorrelation function analysing the height data from figure(a) (along the x-axis), shown as a black solid line, with correlation length $L_C=22.6\text{nm}$ fitted. Here Gaussian and exponential functions are fitted as dashed blue and dotted red lines respectively. . . . .	46
2.8 GaAs/ $\text{Al}_{0.3}\text{Ga}_{0.7}\text{As}$ RTD with IR (Interface Roughness) along the $\text{Al}_{0.3}\text{Ga}_{0.7}\text{As}$ barriers [8], which has a correlation length of $2.5\text{nm}$ and an RMS (Root Mean Square) asperity of $0.3\text{nm}$ . The GaAs is a partially transparent blue volume to allow the visualisation of the IR on the red $\text{Al}_{0.3}\text{Ga}_{0.7}\text{As}$ barriers. This figure [8] is licensed under CC BY 4.0. . . . .	47

2.9	Average exponential autocorrelation function (black solid line) for 25 randomly generated RTDs, with IR (Interface Roughness) along all $\text{Al}_{0.3}\text{Ga}_{0.7}\text{As}/\text{GaAs}$ interfaces [8]. An exponential autocorrelation function fit (red dashed line), $e^{- x /L_C}$ , is plotted as well. This figure [8] is licensed under CC BY 4.0. . . . .	47
2.10	Visualisation of a device generated with an IR (Interface Roughness) of correlation length $L_C=2.5\text{nm}$ and an RMS (Root Mean Square) asperity of $0.3\text{nm}$ [10], one of 25 such RTD devices. The rough $\text{Al}_{0.3}\text{Ga}_{0.7}\text{As}$ barriers (shown in red) are embedded within a GaAs (transparent blue) nanowire body. This figure [10] is licensed under CC BY 4.0. . . . .	50
2.11	Visualisation of a device generated with ‘improved’ IR (Interface Roughness) of isotropic correlation lengths $L_C^Y=L_C^Z=2.5\text{nm}$ and an RMS (Root Mean Square) asperity of $0.3\text{nm}$ [10], one of 25 such RTD devices. The rough $\text{Al}_{0.3}\text{Ga}_{0.7}\text{As}$ barriers (shown in red) are embedded within a GaAs (transparent blue) nanowire body. This figure [10] is licensed under CC BY 4.0. . . . .	51
2.12	Visualisation of a device generated with ‘improved’ IR (Interface Roughness) of anisotropic correlation lengths $L_C^Y=2.5\text{nm}$ and $L_C^Z=5\text{nm}$ and an RMS (Root Mean Square) asperity of $0.3\text{nm}$ [10], one of 25 such RTD devices. The rough $\text{Al}_{0.3}\text{Ga}_{0.7}\text{As}$ barriers (shown in red) are embedded within a GaAs (transparent blue) nanowire body. This figure [10] is licensed under CC BY 4.0. . . . .	51
2.13	Average ACF (Autocorrelation Function) for $\text{GaAs}/\text{Al}_{0.3}\text{Ga}_{0.7}\text{As}$ interfaces of 25 RTD devices generated with an ‘improved’ IR of isotropic correlation lengths $L_C^Y=L_C^Z=2.5\text{nm}$ [10], plotted as solid blue and yellow lines for the Y and Z directions respectively. The exponential ACF [202] fits are given as dashed lines with the corresponding colours. This figure [10] is licensed under CC BY 4.0. . . . .	52
2.14	Average ACF (Autocorrelation Function) for $\text{GaAs}/\text{Al}_{0.3}\text{Ga}_{0.7}\text{As}$ interfaces of 25 RTD devices generated with an ‘improved’ IR of anisotropic correlation lengths $L_C^Y=2.5\text{nm}$ and $L_C^Z=5\text{nm}$ [10], plotted as solid blue and yellow lines for the Y and Z directions respectively. The exponential ACF [202] fits are given as dashed lines with the corresponding colours. This figure [10] is licensed under CC BY 4.0. . . . .	53

2.15 Average ACF (Autocorrelation Function) for GaAs/Al <sub>0.3</sub> Ga <sub>0.7</sub> As interfaces of 25 RTD devices generated with an ‘improved’ IR of anisotropic correlation lengths $L_C^Y=5\text{nm}$ and $L_C^Z=10\text{nm}$ and with a square cross-section of $20\text{nm}\times20\text{nm}$ [10], plotted as solid blue and yellow lines for the Y and Z directions respectively. The exponential ACF [202] fits are given as dashed lines with the corresponding colours. This figure [10] is licensed under CC BY 4.0 . . . . .	54
2.16 Diagram of node-centred control volume [205] (shown in grey) centred around a node ‘C’ at coordinate (i, j, k), with a fractional control sub-volume associated with vertex 1 of this control volume (shown in green). Neighbouring real-space nodes are denoted by red circles and labelled according to the directions of the compass and ‘F’ for ‘front’ and ‘B’ for ‘back’. . . . .	56
2.17 Layer representation of two-terminal device with N layers along the direction of current flow, and two semi-infinite contacts. . . . .	58
2.18 IV characteristic of a smooth RTD [10], such as the one visualised in Fig. 2.4, which is simulated in the ballistic regime. Key points of the IV characteristic are annotated, and the NDR (Negative Differential Resistance) region is shaded blue. This figure [10] is licensed under CC BY 4.0. . . . .	66
2.19 LDOS (Local Density of States) and CS (Current Spectra) for a smooth RTD, as shown in Fig. 2.4 along the x-axis, corresponding to the resonant current peak for the bias $V_r = 0.24\text{V}$ in Fig. 2.18. Figure(a) is the LDOS and in units of $\text{eV}^{-1}$ , wherein the red line along the y-axis is energy dependent transmission T(E), and figure(b) is the CS and in units of $\mu\text{AeV}^{-1}$ . For both subfigures, the black dashed line is the electrostatic potential energy, the white dashed line is the CBM (Conductance Band Minima), and the magenta dashed line is the energy corresponding to the 6th mode used for coupled mode simulations. . . . .	67
2.20 RTD current-voltage curve for NESS (blue line with plus markers) compared with the 1D RTD NEGF simulator [225] powered by NEMO5 and based on NEMO 1-D (red line with diagonal cross markers). The current-voltage curves match up until the current valley, whereafter the equal effective mass approximation has led to increased transmission between the source and QW for NESS. . . . .	69

3.1 A schematic illustration of the baseline GaAs-Al <sub>0.3</sub> Ga <sub>0.7</sub> As RTD device [8] with symmetric barrier widths $L_{B1}=L_{B2}=3\text{nm}$ and QW width $L_{QW}=5\text{nm}$ . The GaAs body is coloured blue and the Al <sub>0.3</sub> Ga <sub>0.7</sub> As barriers are red. The cross-section is $10\text{nm}\times10\text{nm}$ , with an overall length of $55\text{nm}$ for this baseline case. The $19\text{nm}$ thick source-drain regions are $2\times10^{18}\text{cm}^{-3}$ n-doped. The central $17\text{nm}$ region for the baseline case, including two $3\text{nm}$ spacers enclosing the barriers, is $1\times10^{15}\text{cm}^{-3}$ n-doped. This figure [8] is licensed under CC BY 4.0.	73
3.2 IV characteristic for the baseline RTD [8] shown in Fig. 3.1. The resonant peak, or local maximum in current $I_r$ at bias $V_r$ , and the valley, the local minima $I_v$ at $V_v$ , are two key points for this nonlinear IV characteristic. These bound the NDR, and define the figure of merit PVCR $I_r/I_v$ . Fig. 3.3(a), Fig. 3.3(b) and Fig. 3.4 are measured for the resonant peak in this figure. Similarly, Fig. 3.3(c) and Fig. 3.3(d) correspond to the valley. This IV characteristic includes electron-phonon scattering. This figure [8] is licensed under CC BY 4.0.	75
3.3 Figure(a) depicts the LDOS (Local Density of States), with colourbar units of $\text{eV}^{-1}$ , and energy dependent transmission T(E), a red vertical line, for the resonant peak at $0.22\text{V}$ shown in Fig. 3.2. Figure(b) is the CS (Current Spectra), with colourbar units of $\mu\text{AeV}^{-1}$ , for this resonant peak. Similarly, figure(c) and figure(d) respectively represent the LDOS and CS for the valley at $0.24\text{V}$ . The white dashed lines are the CBM (Conductance Band Minima), and the black dash-dot lines are the average potential energy. This figure is reproduced based on Figure 6 from [8], which is licensed under CC BY 4.0.	76
3.4 Line plot of electron charge density through the centre of the baseline RTD depicted in Fig. 3.1 for the resonant peak $0.22\text{V}$ seen in Fig. 3.2. Barrier interface positions are noted with slightly transparent vertical lines with corresponding markers. This figure is reproduced based on Figure 7 from [8], which is licensed under CC BY 4.0.	77

3.5 A comparison of IV characteristics for an RTD as depicted in Fig. 3.1, for the cases with phonons (black solid line with circle markers) and the ballistic case (orange dashed line with plus markers). The latter case in the ballistic regime is also plotted in Fig. 2.18, with corresponding LDOS and CS for the resonant peak shown in Fig. 3.7. The LDOS and CS for the resonant peak for the phonon case is shown in Fig. 3.6. This figure [8] is licensed under CC BY 4.0. . . . .	79
3.6 Figure(a) depicts the LDOS (with colourbar units of eV <sup>-1</sup> ) and energy dependent transmission (a red vertical line) for the resonant peak at 0.22V shown in Fig. 3.2, and figure(b) is the CS (with colourbar units of μAeV <sup>-1</sup> ) for the resonant peak. The white dashed lines are the CBM, and the black dash-dot lines are the average potential energy. . . . .	80
3.7 Figure(a) is the LDOS and transmission (red horizontal line plot), and Figure(b) is the CS, both of which correspond to the resonant peak bias of 0.24V for the ballistic regime in Fig. 3.5. The white dashed lines are the CBM, and the black dash-dot lines are the average potential energy. . . . .	82
3.8 Figure(a) is the LDOS and transmission (red horizontal line plot), and Figure(b) is the CS, both of which correspond to the perturbation in current at 0.28V for the IV characteristic with electron-phonon scattering in Fig. 3.5. The white dashed lines are the CBM, and the black dash-dot lines are the average potential energy. . . . .	84
3.9 Comparison of IV characteristics and electron charge density, through the centre of RTD cross-sections, for different symmetric barrier thicknesses $L_{B1}=L_{B2}$ with figure(a) and figure(b) respectively. Barriers of 2nm (orange dashed line with plus markers) and 4nm (blue dotted line with diagonal cross markers) are compared with the baseline case of 3nm (black solid line with dot markers). Within figure(b), barrier interface positions are noted with slightly transparent vertical lines with corresponding markers. This figure is reproduced based on Figure 9 from [8], which is licensed under CC BY 4.0. . . . .	86

3.10 Comparison of IV characteristics and electron charge density, through the centre of RTD cross-sections, for different QW widths $L_{QW}$ with figure(a) and figure(b) respectively. QW widths of 4nm (orange dashed line with plus markers) and 6nm (blue dotted line with diagonal cross markers) are compared with the baseline case of 5nm (black solid line with dot markers). Within figure(b), barrier interface positions are noted with slightly transparent vertical lines with corresponding markers. This figure is reproduced based on Figure 10 from [8], which is licensed under CC BY 4.0. . . . .	88
3.11 LDOS (with colourbar units of $eV^{-1}$ ) and CS (with colourbar units of $\mu AeV^{-1}$ ) for an RTD with a QW width $L_{QW}=4nm$ for the resonant peak at 0.31V, with figure(a) and figure(b) respectively. The LDOS plot (figure(a)) includes energy dependent transmission as a red line. The white dashed lines are the CBM, and the black dash-dot lines are the average potential energy. This figure is reproduced based on Figure 11 from [8], which is licensed under CC BY 4.0. . .	89
3.12 Comparison of IV characteristics and electron charge density, through the centre of RTD cross-sections, for different first barrier thicknesses $L_{B1}$ with figure(a) and figure(b) respectively. The second barrier thickness $L_{B2}$ is 3nm as in the baseline case. Barriers of $L_{B1}=2nm$ (orange dashed line with plus markers) and $L_{B1}=4nm$ (blue dotted line with diagonal cross markers) are compared with the baseline case of 3nm (black solid line with dot markers). Within figure(b), barrier interface positions are noted with slightly transparent vertical lines with corresponding markers. This figure is reproduced based on Figure 12 from [8], which is licensed under CC BY 4.0. . . . .	92

3.13 Comparison of IV characteristics and electron charge density, through the centre of RTD cross-sections, for different second barrier thicknesses $L_{B2}$ with figure(a) and figure(b) respectively. The first barrier thickness $L_{B1}$ is 3nm as in the baseline case. Barriers of $L_{B2}=2\text{nm}$ (orange dashed line with plus markers) and $L_{B2}=4\text{nm}$ (blue dotted line with diagonal cross markers) are compared with the baseline case of 3nm (black solid line with dot markers). Within figure(b), barrier interface positions are noted with slightly transparent vertical lines with corresponding markers. This figure is reproduced based on Figure 13 from [8], which is licensed under CC BY 4.0. . . . .	93
4.1 A schematic illustration of the GaAs-Al <sub>0.3</sub> Ga <sub>0.7</sub> As device under investigation, which has a square cross-section with dimensions of 10nm×10nm, and an overall length of 55nm. The device is divided into distinct sections shown by the black lines, namely the 19nm source and drain, two 3nm buffer regions, two 3nm Al <sub>0.3</sub> Ga <sub>0.7</sub> As barriers, and a 5nm QW. This figure is licensed under CC BY 4.0, attached to an archived copy of [7] held by the University of Glasgow. The University of Glasgow has an agreement with IEEE allowing authors to self-archive manuscripts with an attached CC BY licence. © 2024, IEEE. . . . .	98
4.2 IV characteristics of a smooth GaAs-Al <sub>0.3</sub> Ga <sub>0.7</sub> As nanowire RTD device with phonon scattering, comparing the base ‘smooth’ case shown in Fig. 4.1 (black line with plus markers) with a ‘double doping’ case (red line with dot markers) with twice the n-doping level of the base device. This figure is licensed under CC BY 4.0, attached to an archived copy of [7] held by the University of Glasgow. The University of Glasgow has an agreement with IEEE allowing authors to self-archive manuscripts with an attached CC BY licence. © 2024, IEEE. . . . .	99

4.3 The IV characteristics of devices No. 57, 65 and 39 are depicted, accompanied by an inset illustrating the distribution of RDDs represented by green dots. PVCRs for No. 57, No. 65, and No. 39 are 2.303, 2.077, and 1.784, respectively. The corresponding $I_r$ and $V_r$ are $0.2708\mu\text{A}$ at $0.175\text{V}$ , $0.2477\mu\text{A}$ at $0.15\text{V}$ and $0.3098\mu\text{A}$ at $0.1\text{V}$ . This figure is licensed under CC BY 4.0, attached to an archived copy of [7] held by the University of Glasgow. The University of Glasgow has an agreement with IEEE allowing authors to self-archive manuscripts with an attached CC BY licence. © 2024, IEEE. . . . .	100
4.4 The upper row shows the combined LDOS and T(E) of three RTD devices, specifically devices No. 57, 65 and 39. These calculations were performed at the bias voltages corresponding to the first resonant peak, which are $0.175\text{V}$ , $0.15\text{V}$ , and $0.1\text{V}$ , respectively. Consequently, the bottom row illustrates the energy-resolved CS of the aforementioned devices. This figure is licensed under CC BY 4.0, attached to an archived copy of [7] held by the University of Glasgow. The University of Glasgow has an agreement with IEEE allowing authors to self-archive manuscripts with an attached CC BY licence. © 2024, IEEE. . .	101
4.5 The central figure(a) is a scatter plot of resonant peak current $I_r$ against resonant peak voltage $V_r$ for the 65 devices that showed an NDR. The attached figure(b) and figure(c) respectively show the histograms of the current and voltage distribution with bin-widths of $0.05\text{V}$ and $0.05\mu\text{A}$ respectively. Normal distributions were fitted onto the histograms with a mean $\mu = 0.1554\text{V}$ and standard deviation $\sigma = 0.0549\text{V}$ for the peak voltage distribution in figure(b), and $\mu = 0.3053\mu\text{A}$ and $\sigma = 0.0971\mu\text{A}$ in figure(c). Figure(a) was also split into four quadrants with the mean of the normal distributions in figure(b) and figure(c), with annotations for the number of data points in the quadrant. This figure is licensed under CC BY 4.0, attached to an archived copy of [7] held by the University of Glasgow. The University of Glasgow has an agreement with IEEE allowing authors to self-archive manuscripts with an attached CC BY licence. © 2024, IEEE. . . . .	103

4.6 Quantile-Quantile plots for the resonant peak voltage $V_r$ and current $I_r$ in figures (a) and (b) respectively. Figure(a) plots the ordered peak bias values $V_r$ against corresponding quantiles from a normal distribution fit to it in Fig. 4.5(b), with mean $\mu = 0.1554\text{V}$ and standard deviation $\sigma = 0.0549\text{V}$ . Figure(b) similarly plots ordered peak current values $I_r$ against corresponding quantiles from a normal distribution fit to it in Fig. 4.5(c), with mean $\mu = 0.3053\mu\text{A}$ and standard deviation $\sigma = 0.0971\mu\text{A}$ . This figure is licensed under CC BY 4.0, attached to an archived copy of [7] held by the University of Glasgow. The University of Glasgow has an agreement with IEEE allowing authors to self-archive manuscripts with an attached CC BY licence. © 2024, IEEE. . . . .	104
4.7 IV characteristics of the 65 RTD devices which exhibited an NDR (grey dashed lines). Two IV characteristics with ‘smooth’ doping such as the base ‘smooth’ case (solid black line with plus markers) and ‘double doping’ case (solid red line with dot markers), which has double the n-doping of the base case, are plotted for reference. This figure is licensed under CC BY 4.0, attached to an archived copy of [7] held by the University of Glasgow. The University of Glasgow has an agreement with IEEE allowing authors to self-archive manuscripts with an attached CC BY licence. © 2024, IEEE. . . . .	105
4.8 The IV curve of Device No. 40 is shown, which has no NDR, along with an inset of Device No. 40 showing the distribution of RDDs as green dots. This figure is licensed under CC BY 4.0, attached to an archived copy of [7] held by the University of Glasgow. The University of Glasgow has an agreement with IEEE allowing authors to self-archive manuscripts with an attached CC BY licence. © 2024, IEEE. . . . .	106
4.9 The IV curve of Device No. 2 is shown, which has no NDR, along with an inset of Device No. 2 showing the distribution of RDDs as green dots. . . . .	107

5.1 Comparison of IV characteristics (figure(a)) and electron charge density (figure(b)), through the centre of RTD cross-sections, for the ‘smooth’ RTD (black solid line with dot markers) depicted in Fig. 5.7 and device 2 with IR along the inside of the QW (purple dashed line with star markers). Within figure(b), barrier interface positions are noted with slightly transparent vertical lines with dot markers. Figure(a) also depicts the average IV characteristic (red dotted line with diagonal cross markers), and the $\text{Al}_{0.3}\text{Ga}_{0.7}\text{As}$ barriers for device 2 with a rough second barrier as an inset. This figure is reproduced based on Figure 14 from [8], which is licensed under CC BY 4.0. . . . .	114
5.2 Comparison of IV characteristics (figure(a)) and electron charge density (figure(b)), through the centre of RTD cross-sections, for the ‘smooth’ RTD (black solid line with dot markers) depicted in Fig. 5.7 and device 1 with IR along the first $\text{Al}_{0.3}\text{Ga}_{0.7}\text{As}$ barrier (green dashed line with square markers). Within figure(b), barrier interface positions are noted with slightly transparent vertical lines with dot markers. Figure(a) also depicts the average IV characteristic (red dotted line with diagonal cross markers), and the $\text{Al}_{0.3}\text{Ga}_{0.7}\text{As}$ barriers for device 1 with a rough first barrier as an inset. This figure is reproduced based on Figure 15 from [8], which is licensed under CC BY 4.0. . . . .	116
5.3 Comparison of IV characteristics (figure(a)) and electron charge density (figure(b)), through the centre of RTD cross-sections, for the ‘smooth’ RTD (black solid line with dot markers) depicted in Fig. 5.7 and device 1 with IR along the second $\text{Al}_{0.3}\text{Ga}_{0.7}\text{As}$ barrier (pink dashed line with diamond markers). Within figure(b), barrier interface positions are noted with slightly transparent vertical lines with dot markers. Figure(a) also depicts the average IV characteristic (red dotted line with diagonal cross markers), and the $\text{Al}_{0.3}\text{Ga}_{0.7}\text{As}$ barriers for device 1 with a rough second barrier as an inset. This figure is reproduced based on Figure 16 from [8], which is licensed under CC BY 4.0. . . . .	118
5.4 A depiction of device 3 with IR along all $\text{Al}_{0.3}\text{Ga}_{0.7}\text{As}/\text{GaAs}$ interfaces. The rough $\text{Al}_{0.3}\text{Ga}_{0.7}\text{As}$ barriers are red, and are situated in the partially transparent blue GaAs body. . . . .	119

5.5 IV characteristics of 25 randomly generated RTDs (grey dashed lines) with IR along all $\text{Al}_{0.3}\text{Ga}_{0.7}\text{As}/\text{GaAs}$ interfaces [8], with an average (red dotted line with diagonal cross markers) and a ‘smooth’ RTD with no IR (black solid line with dot markers) plotted for comparison. This figure [8] is licensed under CC BY 4.0. . . . .	120
5.6 Comparison of IV characteristics (figure(a)) and electron charge density (figure(b)), through the centre of RTD cross-sections, for the ‘smooth’ RTD (black solid line with dot markers) depicted in Fig. 5.7 and device 3 with full IR along all $\text{Al}_{0.3}\text{Ga}_{0.7}\text{As}/\text{GaAs}$ interfaces (grey dashed line with diagonal cross markers) depicted in Fig. 5.4. Within figure(b), barrier interface positions are noted with slightly transparent vertical lines with dot markers. For comparison, the average IV characteristic (red dotted line with diagonal cross markers) is also plotted in figure(a). The inset for figure(a) are the $\text{Al}_{0.3}\text{Ga}_{0.7}\text{A}$ barriers of device 3. This figure is reproduced based on Figure 18 from [8], which is licensed under CC BY 4.0. . . . .	121
5.7 The GaAs- $\text{Al}_{0.3}\text{Ga}_{0.7}\text{As}$ RTD under investigation [9]. This is a 55nm long GaAs nanowire with a $10\text{nm} \times 10\text{nm}$ cross-section, interrupted by two $\text{Al}_{0.3}\text{Ga}_{0.7}\text{As}$ barriers. The device can be split into three regions, the 19nm source and drain which are $2 \times 10^{18}\text{cm}^{-3}$ n-doped, and the central 17nm device region which is $1 \times 10^{15}\text{cm}^{-3}$ n-doped. This central region has two 3nm buffer regions enclosing the 3nm $\text{Al}_{0.3}\text{Ga}_{0.7}\text{As}$ , which themselves enclose a 5nm QW. This particular device is ‘smooth’ because IR has not been implemented. This figure [9] is licensed under CC BY 4.0. . . . .	123
5.8 The annotated IV characteristic of the ‘smooth’ RTD [9] shown in Fig. 5.7, simulated in the ballistic regime. This figure [9] is licensed under CC BY 4.0. . .	124
5.9 $\text{Al}_{0.3}\text{Ga}_{0.7}\text{As}$ barriers for Device No. 1 with IR with an $L_C$ of 7.5nm and $\Delta_{RMS}$ of 0.3nm [9]. This figure [9] is licensed under CC BY 4.0. . . . .	125
5.10 IV characteristics for Device No. 1 (orange dashed line) [9], corresponding to the rough $\text{Al}_{0.3}\text{Ga}_{0.7}\text{As}$ barriers in Fig. 5.9, and a ‘smooth’ RTD IV characteristic (black solid line) as shown in Fig. 5.8. This figure [9] is licensed under CC BY 4.0. . . . .	125

5.11 Colour-map of the mean of PVCR of 25 RTDs with randomly generated IR, for different $L_C$ and $\Delta_{RMS}$ . This figure is reproduced based on Figure 7 from [9], which is licensed under CC BY 4.0. . . . .	126
5.12 Colour-map of standard deviation of fitted normal curves to the distribution of the resonant peak voltage $V_r$ , of 25 RTDs with randomly generated IR, for different $L_C$ and $\Delta_{RMS}$ . This figure is reproduced based on Figure 7 from [9], which is licensed under CC BY 4.0. . . . .	127
5.13 Colour-map of standard deviation of fitted normal curves to the distribution of the resonant peak current $I_r$ , of 25 RTDs with randomly generated IR, for different $L_C$ and $\Delta_{RMS}$ . This figure is reproduced based on Figure 7 from [9], which is licensed under CC BY 4.0. . . . .	128
5.14 IV characteristics for 150 randomly generated RTDs with exponential IR of $L_C=7.5\text{nm}$ and $\Delta_{RMS}=0.3\text{nm}$ as grey dashed lines [9]. The mean current-voltage characteristic is a solid red line with plus markers. This figure [9] is licensed under CC BY 4.0. . . . .	129
5.15 The resonant peak, or local maxima, of each current-voltage characteristic in Fig. 5.14 is shown in figure(a) and is split into 4 quadrants by the mean for the voltage ( $0.2717\text{ V}$ ) and current ( $0.1903\text{ }\mu\text{A}$ ) distributions as seen in figure(b) and figure(c) respectively. Figure(b) and figure(c) also show histograms and fitted normal distributions for occurrence of resonant peak values. This figure [9] is licensed under CC BY 4.0. . . . .	130
5.16 Visualisation of device 3 generated with an IR of correlation length $L_C=2.5\text{nm}$ [10], one of 25 such RTD devices. The rough $\text{Al}_{0.3}\text{Ga}_{0.7}\text{As}$ barriers (shown in red) are embedded within a GaAs (transparent blue) nanowire body. This figure [10] is licensed under CC BY 4.0. . . . .	132
5.17 Visualisation of device 15 generated with ‘improved’ IR of isotropic correlation lengths $L_C^Y=L_C^Z=2.5\text{nm}$ [10], one of 25 such RTD devices. The rough $\text{Al}_{0.3}\text{Ga}_{0.7}\text{As}$ barriers (shown in red) are embedded within a GaAs (transparent blue) nanowire body. This figure [10] is licensed under CC BY 4.0. . . . .	133

- 5.18 Visualisation of device 23 generated with ‘improved’ IR of anisotropic correlation lengths  $L_C^Y=2.5\text{nm}$  and  $L_C^Z=5\text{nm}$  [10], one of 25 such RTD devices. The rough  $\text{Al}_{0.3}\text{Ga}_{0.7}\text{As}$  barriers (shown in red) are embedded within a GaAs (transparent blue) nanowire body. This figure [10] is licensed under CC BY 4.0. . . . . 133
- 5.19 IV characteristic for the baseline RTD [10] shown in Fig. 5.7. The resonant peak, or local maxima in current  $I_r=0.2661\mu\text{A}$  at bias  $V_r=0.24\text{V}$ , and the valley, or local minima  $I_v=0.0793\mu\text{A}$  at  $V_v=0.25\text{V}$ , are two key points for this nonlinear IV characteristic. These bound the NDR, and define the figure of merit PVCR  $I_r/I_v$ . This figure [10] is licensed under CC BY 4.0. . . . . 134
- 5.20 A composite figure [10] visualising the IV characteristics of 25 RTDs generated with an IR of correlation length  $L_C=2.5\text{nm}$ . Figure(a) depicts all the IV characteristics (grey dashed lines), with an average (red dotted line with dot markers) and a ‘smooth’ RTD (solid black line with plus markers) for comparison. Figure(b) is a scatterplot of the resonant peak IV values taken from figure(a), and is bifurcated with dashed lines at the mean values of the resonant peak values,  $V_r=0.2736\text{V}$  and  $I_r=0.1918\mu\text{A}$ . Figure(c) and figure(d) are accompanying histograms and fitted normal distributions for the resonant peak voltage  $V_r$  and current  $I_r$  distributions respectively. This figure [10] is licensed under CC BY 4.0. . . . . 135
- 5.21 A composite figure [10] visualising the IV characteristics of 25 RTDs generated with an ‘improved’ isotropic IR of correlation lengths  $L_C^Y=L_C^Z=2.5\text{nm}$ . Figure(a) depicts all the IV characteristics (grey dashed lines), with an average (red dotted line with dot markers) and a ‘smooth’ RTD (solid black line with plus markers) for comparison. Figure(b) is a scatterplot of the resonant peak IV values taken from figure(a), and is bifurcated with dashed lines at the mean values of the resonant peak values,  $V_r=0.2680\text{V}$  and  $I_r=0.2270\mu\text{A}$ . Figure(c) and figure(d) are accompanying histograms and fitted normal distributions for the resonant peak voltage  $V_r$  and current  $I_r$  distributions respectively. This figure [10] is licensed under CC BY 4.0. . . . . 135

5.22	IV characteristics for device 3 (green dashed line with square markers) and the average (green dotted line) with IR of correlation length $L_C=2.5\text{nm}$ , compared against the ‘smooth’ device IV characteristic (black solid line with plus markers) [10]. The inset contains the rough $\text{Al}_{0.3}\text{Ga}_{0.7}\text{As}$ barriers for device 3, which is shown in Fig. 5.16. This figure [10] is licensed under CC BY 4.0. . . . .	136
5.23	IV characteristics for device 15 (cyan dashed line with diamond markers) and the average (cyan dotted line) with ‘improved’ IR of correlation lengths $L_C^Y=L_C^Z=2.5\text{nm}$ , compared against the ‘smooth’ device IV characteristic (black solid line with plus markers) [10]. The inset contains the rough $\text{Al}_{0.3}\text{Ga}_{0.7}\text{As}$ barriers for device 15, which is shown in Fig. 5.17. This figure [10] is licensed under CC BY 4.0. . . . .	137
5.24	Mean of current peak $I_r$ in microampere for different anisotropic correlation lengths $L_C$ [10]. This figure [10] is licensed under CC BY 4.0. . . . .	139
5.25	Standard deviation of current peak $I_r$ in nanoampere for different anisotropic correlation lengths $L_C$ [10]. This figure [10] is licensed under CC BY 4.0. . . . .	140
5.26	Mean of resonant voltage $V_r$ in Volts for different anisotropic correlation lengths $L_C$ [10]. This figure [10] is licensed under CC BY 4.0. . . . .	141
5.27	Standard deviation of resonant voltage $V_r$ in millivolts for different anisotropic correlation lengths $L_C$ [10]. This figure [10] is licensed under CC BY 4.0. . . . .	142
6	Diagram of node-centred control volume [205] (shown in grey) centred around a node ‘C’ at coordinate (i, j, k), with a fractional control sub-volume associated with vertex 1 of this control volume (shown in green). Neighbouring real-space nodes are denoted by red circles and labelled according to the directions of the compass and ‘F’ for ‘front’ and ‘B’ for ‘back’. . . . .	152
7	3D grid visualising red-black ordering [211], with nearest neighbour nodes for any given node being of the opposite colour. Permission has been granted by Springer Nature to include this figure [211] within this thesis. © 2018, Springer Nature. . . . .	156
8	Layer representation of two-terminal device with N layers along the direction of current flow, and two semi-infinite contacts. . . . .	171

# Acknowledgements

I would like to thank my family for supporting me through this PhD, my supervisor Professor Vihar Georgiev for guiding me, my seniors for providing help and advice, and for the University of Glasgow and EPSRC (Engineering and Physical Sciences Research Council) for providing the opportunity.

Needless to say, my family's support throughout these 4 years has helped me through difficulties such as starting my PhD during the pandemic. My supervisor's guidance has been invaluable in progressing through my PhD, and extends beyond the PhD itself as well. I am grateful to see Vihar assume the post of a Professor as he deserves during my PhD. My seniors have been of great help, and you'll see some of them appearing as co-authors in the papers forming the basis for most of these chapters. Of them, I would like to give special thanks to Dr Ankit Dixit, Dr Naveen Kumar, and Dr Ali Rezaei.

The University of Glasgow and EPSRC have my gratitude for providing the opportunity to carry out the PhD in the first place, by providing the environment and organisational support needed for such research.

I would also like to acknowledge everyone behind the numerous papers, textbooks, and theses I have referenced. This PhD was researched standing on your shoulders. The authors of [1] graciously provided the image data for Figure 4(d) in [1], which I used to create Fig. 2.7. I am grateful that Figures 1.6, 1.9, 1.10 and 2.1 from the respective pa-

pers [2], [3], [4] and [5] were made available under a Creative Commons BY 4.0 licence. I also acknowledge that [6] was first published and copyrighted by Engineers Australia. I also acknowledge that some figures have been reproduced from my first author papers [7–10], three of which are directly available under a Creative Commons BY 4.0 licence [8–10]. The fourth paper [7] has an attached Creative Commons BY 4.0 licence as well for an archived copy (made available through the attached web page address within the citation [7]). This is due to an agreement made between the University of Glasgow and IEEE for authors from the University of Glasgow to self-archive accepted manuscripts in an institutional or subject based repository with a self-attributed Creative Commons BY licence.

# Output

Over the course of researching my thesis I have achieved different outputs which are worth briefly mentioning.

Except for chapters 2 and 6, this thesis is composed based on first author papers by myself, which have either been accepted or are currently under review. Four of these papers [7–10] are currently published. One of these papers [9] corresponds to a presentation at the EuroSOI-ULIS 24 conference.

On top of this, two further NEGF simulation studies were co-authored [11, 12], including a SISPAD 2024 conference paper [11] using Machine Learning to accelerate NEGF simulations. As they are not directly related to this thesis, they will not be mentioned further.

Lastly, throughout my thesis I have improved the modular technology computer-aided design (TCAD) software NESS under development at the University of Glasgow, as noted in my papers [7–10]. Specifically, I have improved the structure generator module by allowing greater control over the occurrence of RDDs [7] and by extending the implementation surface roughness [13] to IR which is along heterostructure interfaces normal to the direction of current flow. I have also improved this IR to be correlated along two dimensions [10].

# Overview

Except for chapters 2 and 6, this thesis is composed based on first author papers by myself, which have either been accepted or are currently under review. Chapter 1 is a literature review on RTDs, intended as an introduction for those new to this device. Chapter 2 serves as an introduction to the theory involved in performing RTD research with the modular TCAD software NESS under development at the University of Glasgow, especially NEGF. Chapter 3 is a design of device study for RTD section thicknesses [8], covering both the symmetric variation of both barriers and the QW and asymmetric variation of both barriers. Chapter 4 is a study on the effects of RDDs on RTD device behaviour [7], and how the resulting variation in IV characteristics allows RTDs to encode information, and thus potentially be used to construct PUFs. Chapter 5 is a comprehensive study on the impact of IR on RTD device behaviour [8–10], investigating the impact of RTDs on different parts of the RTD [8] and for IR of different correlation lengths and roughness asperity [9, 10]. IR was also found to cause variation which similarly positions RTDs as a potential PUF building block. Finally, chapter 6 concludes the research achieved in this thesis.

# Declaration

I declare that, except where explicit reference is made to the contribution of others, that this dissertation is the result of my own work and has not been submitted for any other degree at the University of Glasgow or any other institution

---

**Pranav Acharya**

# Abbreviations

- ACF — Autocorrelation Function
- AFM — Atomic Force Microscopy
- AM — Amplitude-Modulated
- CBM — Conductance Band Minima
- CS — Current Spectra
- DBQW — Double Barrier Quantum Well
- ETSI — European Telecommunications Standards Institute
- IC — Integrated Circuit
- IR — Interface Roughness
- IV — Current-Voltage
- LDOS — Local Density of States
- NDR — Negative Differential Resistance
- NEGF — Non-Equilibrium Green's Function
- NESS — Nano-Electronic Simulation Software
- PVCR — Peak-to-Valley Current Ratio
- PUF — Physical Unclonable Function
- QW — Quantum Well
- RDD — Random Discrete Dopant
- RITD — Resonant Interband Tunnelling Diode
- RMS — Root Mean Square
- RTD — Resonant Tunnelling Diode

- SCBA — Self-Consistent Born Approximation
- SBD — Schottky Barrier Diode
- SG — Signal Generator
- SOR — Successive Over Relaxation
- TCAD — Technology Computer-Aided Design
- ToF — Time of Flight

# Chapter 1

## Literature Review

### 1.1 Introduction

Resonant tunnelling diodes (RTDs) are diodes which allow electrons (and holes) with certain resonant energies to pass through due to quantum tunnelling, leading to their prized characteristic of a region of negative differential resistance (NDR)  $R = \frac{dI}{dV} < 0$ . This means that an RTD is an active device which can compensate for energy losses in a paired resonator, such as an LRC circuit, allowing for RTD oscillators to be built [14].

Moreover, because quantum tunnelling allows RTDs to achieve Terahertz (THz) frequency oscillations at room temperature [15], these RTD oscillators can function as THz electronics [16] which can fill the THz gap in sources [17, 18]. This THz potential means that RTDs have drawn interest for applications such as high-speed telecommunications [19] and sensing [20]. RTDs are also sensitive to stochastic variation, which can be intentionally leveraged to encode information in parameter variation. This has prompted research [2, 7, 21, 22] into using RTDs to construct physical unclonable functions (PUFs) [23, 24] on integrated circuits (ICs) in order to uniquely identify them for combating semiconductor counterfeiting and for cryptographic purposes.

The basics of RTDs are covered in section 1.2, including a brief history, and different types of materials and RTD structures are noted in section 1.3. The different types of stochastic variation RTDs experience are introduced in section 1.4, followed by an exploration of RTDs for PUFs in section 1.5. Issues faced by RTDs and countermeasures for them are listed in section 1.6. Research on RTD oscillators as THz electronics is reviewed in section 1.7, including design of device considerations, before concluding this review article in section 1.8.

## 1.2 RTD

This section is composed of a brief history of RTDs in subsection 1.2.1, followed by the theory of their operation in subsection 1.2.2, before ending with mentions of applications in subsection 1.2.3.

### 1.2.1 RTD History

RTDs with two or more barriers were demonstrated theoretically with simulations in 1973 [25], and RTDs were realised experimentally shortly afterwards in 1974 [26]. Though even before this, the behaviour of resonant tunnelling was theoretically predicted [27].

Roughly a decade after this initial demonstration of RTDs [26], RTDs with an NDR at room temperature were developed [28, 29]. The capacity of RTDs for THz technology [15] prompted early research interest [30], leading to a rapid early increase in frequencies of RTD oscillators [30–32] leading to oscillations above 700GHz observed in 1991 [32].

Later progress slowed down somewhat, with THz frequencies achieved at room temperature with higher harmonics in 2005 [33]. After this, THz fundamental frequencies at room temperature were attained in 2010 [34], and nearly 2 THz fundamental frequencies were realised in 2017 [35]. Since then, there has been a surge of research for arrays of multiple RTDs [36–43] which can achieve higher powers as THz sources.

### 1.2.2 Theory of Operation

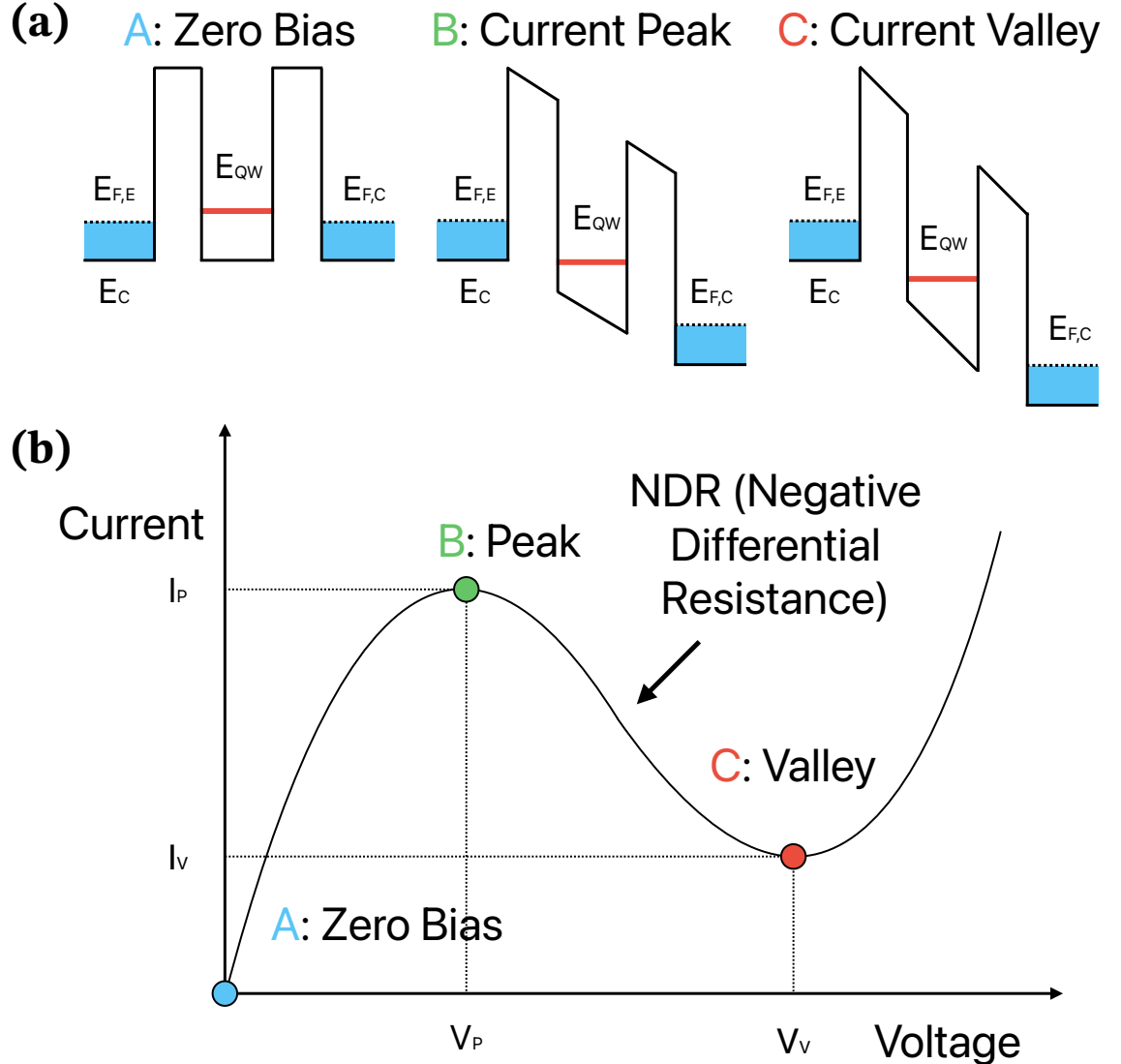


**Figure 1.1:** Sketches of an idealised RTD band diagram under different bias and a corresponding IV characteristic in figure(a) and figure(b) respectively, with points of interest labelled. Point A at the origin has zero bias and current, point B is the resonant peak or local maxima with bias  $V_r$  and current peak  $I_r$ , and point C is the valley or local minima with bias  $V_v$  and current minima  $I_v$ . Figure(a) contains band diagram sketches through the centre of a double barrier quantum well RTD, with each subfigure under a different bias corresponding to the annotated points in figure(b). The conductance band minima (CBM)  $E_C$  for each subfigure within figure(a) (a black solid line) forms two potential barriers separating the emitter region on the left with an emitter Fermi level  $E_{F,E}$  (black dotted line), the QW in the middle with a ground quasibound energy of  $E_{QW}$  (red solid line), and a collector region to the right with a collector Fermi level  $E_{F,C}$  (black dotted line). Within figure(b), the resonant peak at point B and the valley at point C bound the NDR region. Figure(b) also does not account for the space-charge effect [44], which is shown in Fig. 1.3.

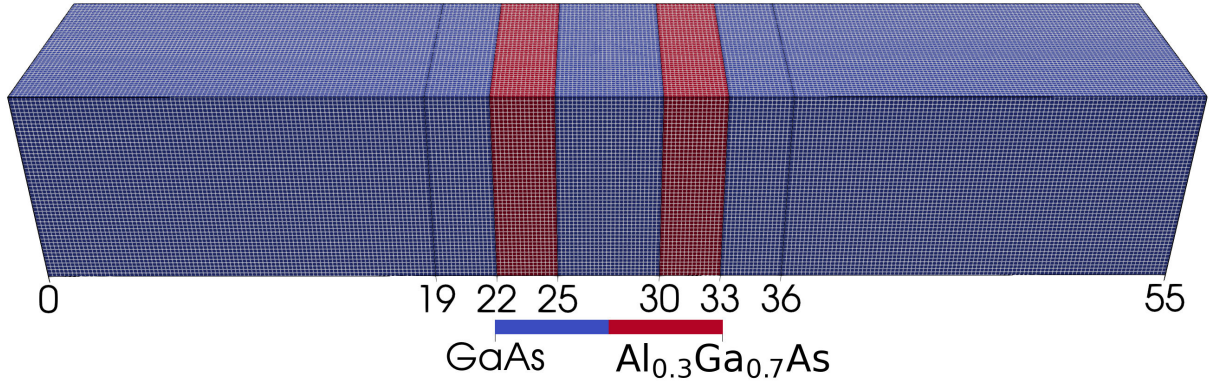


**Figure 1.2:** This figure is a schematic of a Al<sub>0.3</sub>Ga<sub>0.7</sub>As/GaAs RTD from [7], with key positions along the horizontal ‘x’ axis (and direction of current flow) labelled with nanometre values from 0nm to 55nm. The dimensions are 55nm×10nm×10nm, with  $2 \times 10^{18}\text{cm}^{-3}$  n-doped source (0nm-19nm) and emitter (36nm-55nm) GaAs regions and a central  $1 \times 10^{15}\text{cm}^{-3}$  n-doped heterostructure region. This central region is composed of 3nm GaAs spacers (19nm-22nm and 33nm-36nm) enclosing two 3nm Al<sub>0.3</sub>Ga<sub>0.7</sub>As barriers (22nm-25nm and 30-33nm) and a 5nm GaAs QW (25nm-30nm) in the middle. This figure is licensed under CC BY 4.0, attached to an archived copy of [7] held by the University of Glasgow. The University of Glasgow has an agreement with IEEE allowing authors to self-archive manuscripts with an attached CC BY licence. © 2024, IEEE.

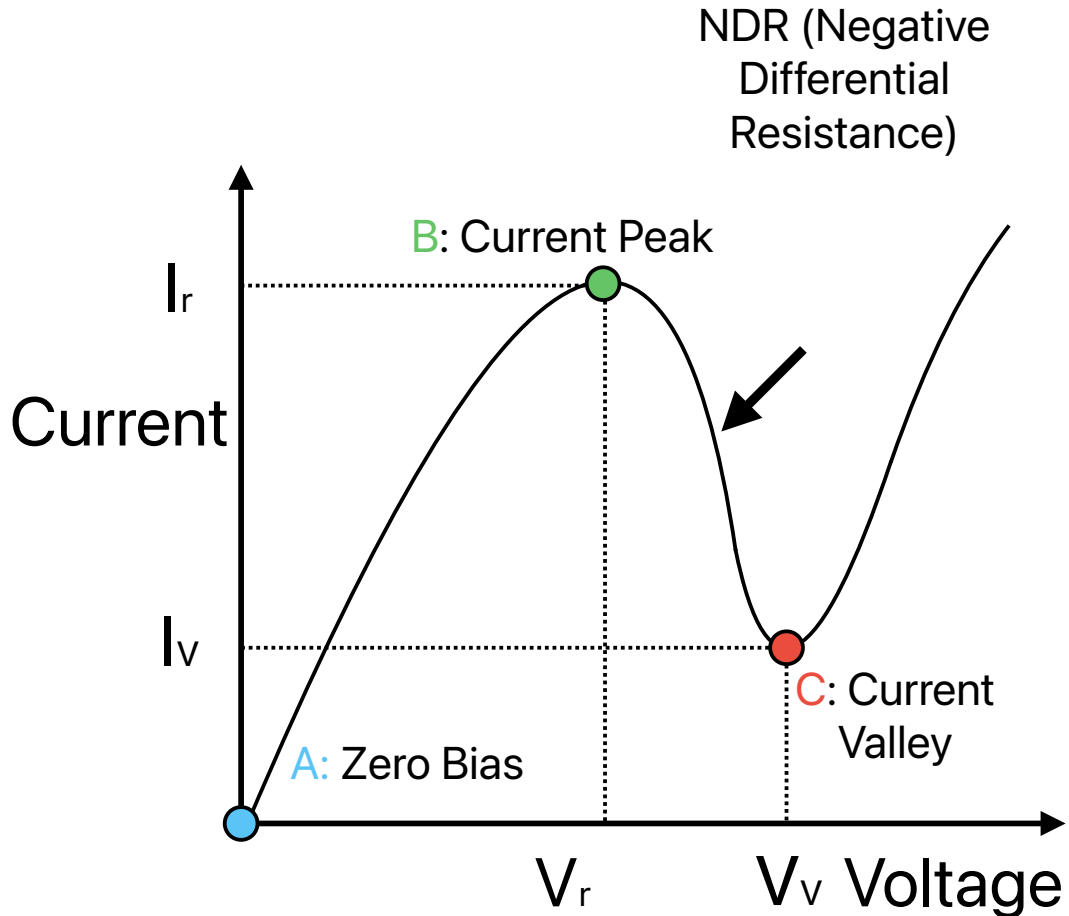


**Figure 1.3:** A modification of the RTD IV characteristic sketch shown in Fig. 1.1(b), with the inclusion of the space-charge effect [44] which perturbs regions of higher current to greater bias, due to the greater charge present within the QW at greater current, thereby leading to an 'N' shaped IV characteristic.

The defining features of RTDs are their nonlinear IV characteristic and their extremely fast operation reaching THz speeds [35] at room temperature. The heterostructure of RTDs is formed by layers of material with different band structures, resulting in mismatches in band structure which act as potential barriers as seen in Fig. 1.1(a). A local maxima in current as seen in Figure 1.1(b) occurs because for low bias current is dominated by quantum tunnelling through the barriers formed by the band structure of the heterostructure, for which the transparency is voltage dependent as explained below.

In the case of  $\text{Al}_{0.3}\text{Ga}_{0.7}\text{As}/\text{GaAs}$  RTDs like Fig. 1.2 the nanowire body of GaAs has a greater electron affinity than  $\text{Al}_{0.3}\text{Ga}_{0.7}\text{As}$  [45], leading to a CBM lower than the  $\text{Al}_{0.3}\text{Ga}_{0.7}\text{As}$  layers. Hence, the CBM in the  $\text{Al}_{0.3}\text{Ga}_{0.7}\text{As}$  acts as the barriers of a quantum well (QW), which consequently have quantised quasi-bound electron energy levels. When the energy of incoming electron from the emitter region matches with the aforementioned quasi-bound energy levels in the QW, transmission probability maximises, and otherwise is suppressed. This alignment of the emitter region and the QW is controlled by bias voltage, introducing the voltage dependence of transmission and thus current, leading to the resonant peak and NDR.

Fig. 1.1(a) demonstrates how the CBM deforms under bias, corresponding to different points of Fig. 1.1(b). As drain-source bias voltage is increased from zero bias at point ‘A’ in Fig. 1.1(b), the drain side of the CBM is perturbed to lower energies, also perturbing the QW and quasi-bound states to lower energy. When the resonant peak bias  $V_r$  is reached at point ‘B’, the emitter Fermi level aligns with the ground QW energy level, allowing maximal tunnelling current. As bias increases further, these energy levels mis-align and the ground QW energy drops below the emitter-side CBM, suppressing elastic tunnelling. The device hence reaches a local minimum or resonant valley at point ‘C’ with valley voltage  $V_v$ . The region of decreasing current bound by the peak ‘B’ and valley ‘C’ has a differential resistance  $R = \frac{dV}{dI}$  that is effectively negative, and is thus referred to as the NDR (negative differential resistance) region. For higher bias than this local minima ‘C’, thermionic emission of bias starts to dominate which leads to ohmic current which increases with bias. Another effect which comes into play is the space-charge effect [44], or Coulomb repulsion due to charge in the QW, which results in the ‘N’ shaped IV characteristic shown in Fig. 1.3(b). When current through the QW is greater, electron charge within the QW at that moment is also greater which results in greater Coulomb repulsion potential from said charge. This repulsion potential needs to be overcome with greater drain-source bias, consequently points of higher current are skewed to greater bias, result-

ing in the ‘N’ shape of Fig. 1.3. Additionally, the quasibound QW energies in electronvolts, with respect to the emitter-side Fermi level, are roughly half the corresponding resonant peak voltage values[26, 29], because bias voltage perturbs the drain to lower energies while only roughly half this reduction in energy is observed in the QW.

The nonlinear curved shape of RTD IV characteristics can also be explained with the conservation of transverse momenta[46, 47] during tunnelling. The longitudinal component of electron momenta  $k_x$  for incoming electrons is important for RTDs [29], because the transverse component of momenta is conserved during elastic tunnelling [46] into the QW, limiting states allowing tunnelling. The electron energy in the emitter region is given by the following equation 1.1 where the transverse component of momenta is defined by

$$k_{\perp} = \sqrt{k_y^2 + k_z^2}$$

$$E_E = E_C + \frac{\hbar^2 k_x^2}{2m_x} + \frac{\hbar^2 k_{\perp}^2}{2m_{\perp}} \quad (1.1)$$

Similarly, we can split the QW energies into the quantised longitudinal component  $E_{x,n}$  and the transverse momenta component [47], which for the ground state where  $n = 0$  is given by the following equation 1.2

$$E_{QW} = E_{x,0} + \frac{\hbar^2 k_{\perp}^2}{2m_{\perp}} \quad (1.2)$$

Since emitter electrons energies are bounded by the emitter Fermi level  $E_{F,E}$  and the CBM, this constrains longitudinal momenta to  $k'_x = \sqrt{\frac{2m_x}{\hbar^2}(E_{x,0} - E_C)} \leq k_{F,E}$  for electrons which tunnel elastically into the QW into the quasibound ground state. Transmission due to resonant tunnelling for electrons is maximal when the states of incoming electrons align with those in the QW with an energy of  $E_{QW}$  as seen in Fig. 1.1(a). Bias controls the alignment of the QW energy  $E_{QW}$  and the emitter region. Assuming the conservation of transverse momenta, this means that a maxima is reached at  $k'_x=0$ , in other words when  $E_{x,0}$  overlaps with the emitter-side  $E_C$ , leading to maximum resonant tunnelling current at the resonant tunnelling current peak. As bias increases further  $E_{x,0}$  drops below  $E_C$  and emitter electrons can no longer tunnel into the QW while conserving transverse momenta, leading to a sharp drop in current.

### 1.2.3 RTD Applications

RTDs have garnered interest for a variety of use cases. As room temperature THz devices, RTDs are well positioned for various applications [16] such as telecommunications and high speed data transmission [19], and for sensing applications [20]. Within the purview of sensing, an advantage for medical and security applications is that THz radiation is non-ionising [16] and transparent [48, 49] to a wide range of materials, and RTDs are highly sensitive detectors [6, 50]. Sensing applications also include radar [51], high resolution imaging [20] and spectroscopy [52]. As explored later in section 1.5 RTDs also have potential [2, 7, 21, 22] as PUFs [23, 24] to uniquely identify ICs [53] in order to combat the issue of semiconductor chip counterfeiting [54, 55]. RTDs have also recently attracted interest for neuromorphic computing [56, 57].

## 1.3 Materials and Types of RTDs

This section notes the different materials and configurations used for RTDs respectively in subsections 1.3.1 and 1.3.2.

### 1.3.1 Materials

RTD research began with AlGaAs/GaAs [25, 26, 28] RTDs, including their demonstration as a simulation study [25], the first experimentally realised RTDs [26] and room temperature RTDs [28]. AlAs/GaAs were also used in early research [29, 31], with sub-TH RTD oscillators reaching 420GHz [31]. These GaAs based RTDs were appealing [58] because of the lattice matching [59] of GaAs with AlAs or AlGaAs which meant that there was less strain between materials.

Unfortunately a limiting factor of such RTDs [58] is their low barrier height formed from the CBM offset between GaAs and AlAs or AlGaAs, which allows thermionic emission over the barrier and thus a valley current which limits peak-to-valley current ratio (PVCR), which is especially the case for AlGaAs/GaAs RTDs. PVCR is considered a figure of merit for RTDS in literature that measures the distinctiveness of the NDR in RTD IV characteristics. Due to the limited CBM offset, PVCR values in literature for  $\text{Al}_{0.3}\text{Ga}_{0.7}\text{As}/\text{GaAs}$  RTDs [60–62] vary roughly around 1.5 to 3.5, with an early experimental paper [60], achieving a PVCR of 1.8. For the latter paper, a simulation comparison assumed a CBM offset of 0.23eV. Further details on such RTDs can be found in the following review paper [58].

The use of indium is a solution to the low barrier heights [63] experienced with the above GaAs based RTDs, albeit necessitating thin barriers due to strain [59, 64], with the achievement of fundamental THz oscillations at room temperature [34] with InGaAs/AlAs. An advantage of using indium is that different mole fractions of indium in  $\text{In}_x\text{Ga}_{x-1}\text{As}$  can be used, allowing modification of the CBM band structure such as creating a lower energy InGaAs QW with a greater indium mole fraction [65] or a InAs QW subwell [66] and graded InGaAs emitter regions [34, 67], which as discussed in section 1.6 all improve the performance of RTDs for THz applications. Subwells [66] refer to a layer within a QW with a lower offset, as is achieved with InAs [66] within an InGaAs QW, which achieves the effect of reducing QW ground energy level for the whole QW [68]. Graded emitters are emitters where the bandstructure is graded with intermediate offsets rather than having one offset with the barrier, and can be achieved through grading the mole fraction of the material [34, 67]. Graded emitters are also called step emitters [67]. InGaAs is currently very dominant in THz RTD research [37, 43, 65, 66, 69–73].

Group III nitride GaN/AlN RTDs [74–77] have gained interest due to their high voltage operations and their high current density [76], which along with their thermal stability is promising for high power oscillators [74]. High contact resistance [78], a large lattice mismatch and polarisation charges are among the issues [74] faced by such RTDs. Efforts are being made to improve their PVCR, with values over 2 recently achieved [77], and frequencies achieved remain somewhat limited, with a 17GHz GaN/AlN RTD oscillator demonstrated recently [75]. A review article delving further into such RTDs is [74].

InAs/AlSb RTDs [32, 79, 80] have achieved the then record-breaking sub-THz frequencies of 712GHz in 1991 [32], though currently they are not as dominant in recent THz RTD research [79]. A key disadvantage of such RTDs is poor growth quality due to lattice mismatch with commonly used substrates [80] like GaAs and GaSb. Such antimonide-based RTDs can also be constructed to function based on interband tunnelling between the valence and conduction bands through staggering the type II heterostructure offsets, such as by including a GaSb QW [80], in which case they are referred to as resonant interband tunnelling Diodes (RITDs) [81, 82] which is explained further below and shown in Fig. 1.4(c).

Si/SiGe RTDs [83–87] are another material type which has been researched. The appeal of such RTDs is CMOS integration [88], but they are disadvantaged by limited barrier heights [89]. Such RTDs have been researched with both hole [83] and electron tunnelling [84], and can also construct RITDs [85] and triple barrier RTDs [86].

Recently, graphene based RTDs have also begun to be researched [90–92], with an NDR shown even in single barrier structures [91, 92] as well as the triple barrier case [93], although it is debatable whether such single barrier structures can be considered ‘true’ RTDs.

### 1.3.2 Types of RTDs

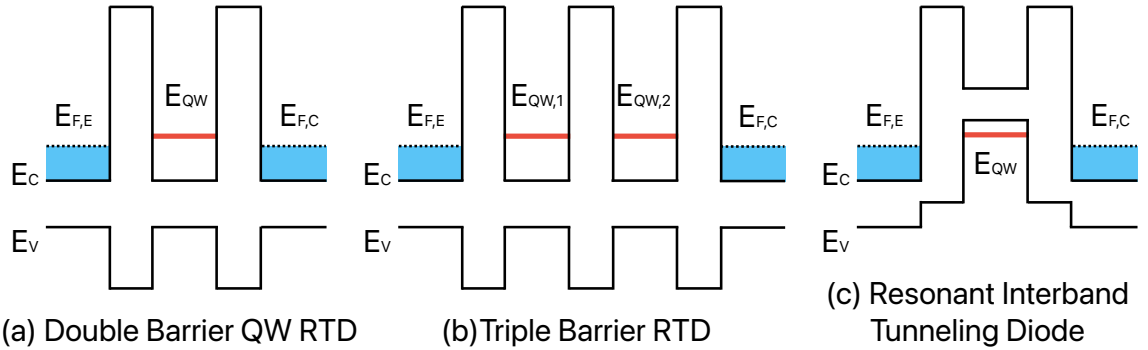


**Figure 1.4:** Band diagram sketches for (a) double barrier RTDs with a single QW, (b) triple barrier RTDs which have two QWs, and (c) double barrier interband RTDs which depend on tunnelling between the valence and conductance bands.

The three main types of RTDs are presented in Fig. 1.4. The most extensively researched type of RTDs are Double Barrier QW RTD, sometimes referred to as a DBQW RTD in literature, which function with intraband tunnelling within the conductance band through a single QW confined by two potential barriers. Unless otherwise specified, when RTDs are mentioned in literature it refers to these DBQW RTDs, and similarly this is the type of RTD explained in section 1.2.

Two variations on this basic structure are triple barrier RTDs, which are known for their sensitivity [94], and interband RTDs, or RITDs [81], where tunnelling occurs between the valence and conductance bands. Triple barrier RTDs [87, 94–96], with a band diagram sketch depicted in Fig. 1.4(b), hold potential as sensitive nonlinear THz detectors [94] with tunnelling based on alignment between two QW energy levels. Zero bias operation with direct detection is possible with triple barrier RTDs, aiding their sensitivity [94].

RITDs [81, 82, 85] depend on interband tunnelling between the valence and conduction bands, as shown in Fig. 1.4(c) where electrons tunnel into the hole states in the QW. Very high PVCRs have been achieved with RITDs [82, 97], even going up to 144 [97]. Currently though, as far as I am aware, sub-THz or THz RITD devices have not yet been realised.

## 1.4 Stochastic Device Variation

As nanoelectronic devices which function based on quantum phenomena [98], like QW energy level quantisation and tunnelling, RTDs are sensitive to stochastic nanometre-scale device variations. This includes both the barriers [99–101] and the QW [100, 102, 103]. Such device variation can alter device behaviour and degrade key metrics [7, 104, 105] such as PVCR and resonant peak current. Thankfully, this has not stopped the development of RTDs for THz applications.

On the other hand, stochastic variation also imbues RTDs with the potential to construct [7, 21, 22] PUFs [23, 24]. PUFs can uniquely identify devices they are placed on against a manufacturer database, and in the case of integrated circuits [53] deal with the semiconductor chip counterfeiting issue [54, 55]. Details of RTDs as PUFs are further expanded upon in section 1.5.

Interface roughness (IR) [68, 104, 105] along the heterostructure interfaces lining the barriers and QW in RTDs affects barrier thickness, which has an exponential influence on tunnelling probability and thus current [99–101], and QW width, which similarly has a strong influence on the ground quasibound energy level [106] and thus resonant peak voltage [100]. The latter is due to the QW formed by RTDs, which can be interpreted as a finite square QW [106] where the energy levels are inversely correlated to the square of the QW width. Roughness has become a major issue in semiconductor devices generally

as they have scaled down to nanometre dimensions [107, 108], and with RTDs especially due to its impact on the highly sensitive device structure [100]. IR appears in RTDs composed of different materials [109–112] and RTDs created by different manufacturing processes [113, 114]. The main degradation in device performance due to IR is an increased valley current [104, 115, 116], which along with a reduction in peak current [104, 115] degrades PVCR. Thankfully, with modern RTDs such variations are limited to monolayers [117], which while still having an impact on device performance [99], still allows the use of RTDs for THz applications.

Semiconductor doping is another factor which RTDs are sensitive to [100] and stochastic local concentrations in doping are called random discrete dopants (RDDs) [7, 118–126], and alternatively termed Random Dopant Fluctuations [119, 122]. RDDs are of concern to modern nanoelectronic devices in general as they have scaled down [7, 118–126]. RDD research for RTDs[7, 118] indicates the variation caused by taking into account RDDs for device simulations, and with resonant peak IV values varying to follow normal distributions [7]. Similarly, a normal distribution of voltage [121–124] and current [124] is observed with other devices with RDDs in literature such as MOSFETs. RDDs are also a concern for InGaAs devices [119, 120], indicating that RDDs could be of concern for manufacturing reproducible THz InGaAs based RTDs.

For RTDs, especially those used in THz applications, uniformity of material composition is important [99, 127]. Thankfully such issues are not a major concern for THz RTDs, with a high degree of control over Indium molar fraction in InGaAs RTDs [99, 127] and in any case such factors have a lower influence on resonant peak IV values in comparison to thickness or dopant variation [100].

To summarise, stochastic device variations impact RTDs and cause variations in device performance, but are still under enough control to allow the manufacture of RTDs for THz applications. And such variations conversely allow RTDs to construct PUFs to uniquely identify items they are placed on as explored in the following section 1.5.

## 1.5 Physical Unclonable Functions

PUFs [23, 128–130] are, as the name implies, physical devices which act as functions with random outputs for given inputs and which are practically unfeasible to clone. Recent studies have demonstrated the potential for RTDs with stochastic variation to create PUFs [2, 7, 21, 22]. RTDs can also be integrated onto ICs [22]. This positions RTDs to combat the major issue of semiconductor chip counterfeiting, which costs billions annually [53, 54] and causes security issues for infrastructure [55], including military systems [131]. This section briefly introduces the basics of PUFs in subsection 1.5.1, and discusses the current state of literature regarding the use of RTDs for PUFs in the following subsection 1.5.2.

### 1.5.1 PUF basics

PUFs encode information in the format of Challenge-Response-Pairs (CRPs), where for a given challenge or read request/input a random output is given as the response. Multiple of these CRPs for a given PUF form a random ‘fingerprint’ which uniquely identifies that PUF. This means that devices with PUFs can be checked against a manufacturer database [23], to make sure that the device in question is authentic and not counterfeited.

The most important aspect of PUFs is their uncloneability [132], which RTDs excel at due to the stochastic variation they can experience, as discussed in section 1.4, which can consequently alter device behaviour. The sensitivity of RTD to atomic scale variations in the RTD, such as the QW [100] and barriers [99–101] or with RDDs [7], means that cloning RTD PUFs would require atomic level manufacturing which makes counterfeiting in this manner unfeasible [21]. This sensitivity is due to RTDs functioning based on quantum confinement, which effectively magnifies the effect of this structural variation [132]. Randomness is also an important aspect of PUFs, avoiding patterns in information encoded in the PUF which could otherwise give attackers a statistical advantage in predicting responses [132].

Uniformity and uniqueness are two other aspects of PUFs which concerns CRPs within and between individual PUFs respectively. First addressing uniformity, if bits of information are assigned to the CRPs within a PUF they can be quantified with the Hamming Weight percentage [128, 129] as shown below in equation 1.3. Here,  $r_{n,m}$  is the value of  $n$  out of  $p$  bits of information encoded within PUF  $m$  out of  $q$  PUFs.

$$w_H = 100\% \times \frac{1}{p \times q} \sum_{m=1}^q \sum_{n=1}^p r_{n,m} \quad (1.3)$$

An ideal uniform distribution results in a Hamming weight of 50% according to equation 1.3. If the CRPs were to each encode exactly one bit of information, in this case would mean that on average a CRP within a PUF has a 50% chance of encoding a ‘1’ bit state, with this as an average for multiple PUFs. Hence, an attacker would not be able to gain a statistical advantage by knowing that one state is more likely than the other.

Uniqueness on the other hand refers to the difference between PUFs, or the inter-chip Hamming Distance [128, 129] which should also in an ideal case lead to 50% in equations 1.4 and 1.5.

$$H_D^{inter} = 100\% \times \frac{2}{p \times q(q-1)} \sum_{i=1}^{q-1} \sum_{j=i+1}^q H_D(R_i, R_j) \quad (1.4)$$

$$H_D^{inter} = 100\% \times \frac{2}{p \times q(q-1)} \sum_{i=1}^{q-1} \sum_{j=i+1}^q \sum_n^p |r_{n,i} - r_{n,j}| \quad (1.5)$$

$R_i$  and  $R_j$  refers to the bit-strings, composed of  $p$  bits, respectively within the PUFs  $i$  and  $j$  out of  $q$  PUFs. The Hamming Distance  $H_D$  between  $R_i$  and  $R_j$  is the number of bits which are different between them, leading to equation 1.5. Another way of looking at uniqueness is that a given CRP located within a PUF should not be biased to a particular value, so if exactly one bit were to be encoded in each CRP then the chance of encoding a ‘1’ bit state within the CRP  $n$  would be 50% when averaged over multiple PUFs.

Reliability, or repeatable measurements, is another aspect which means that repeated measurement under different conditions achieve the same results. A way of quantifying the bit error rate is the intra-chip Hamming Distance  $H_D^{intra}$  [128, 129] as shown below in equation 1.6, which can be subtracted from 100% to get the reliability.

$$H_D^{intra} = 100\% \times \frac{1}{p \times q \times s} \sum_{m=1}^q \sum_{t=1}^s H_D(R_m, R'_{m,t}) \quad (1.6)$$

Within equation 1.6 the bit string of length  $p$  measured for a PUF under normal conditions is  $R_m$ , and is compared against measurements of the same PUFs under  $s$  different conditions which each result in a bit string  $R'_{m,t}$ . The Hamming Distance comparisons can then be averaged among PUFs to get a measurement of bit error rate, or reliability with  $100\% - H_D^{intra}$ . In the context of reliability, RTDs are reliable even with temperature variation [22] because near room temperature RTDs do not experience much dependence on temperature [133].

To summarise, a good PUF is one which is unclonable and random, with a high uniformity within a PUF and a high uniqueness between PUFs, which can also be read reliably. This means that in an ideal case the respective values are a Hamming weight of 50%, an inter-chip Hamming Distance of 50%, and an intra-chip Hamming Distance of 0%.

PUFs can be further separated into weak and strong PUFs [134], which depends on how well their quantity of CRPs scales with device size. Generally speaking weak PUFs do not scale as well, with linear or low-order polynomial scaling, while strong PUFs can scale exponentially or with high-order polynomial scaling. The key difference this introduces is that weak PUFs can have all their CRPs measured to create a virtual model of the device, without actually cloning the device, whereas this is not feasible for strong PUFs. This consequently means that for weak PUFs authentication needs to be carried out through in situ measurement next to the device, rather than by remotely requesting responses to challenges. Conversely, for strong PUFs with large enough CRP sets there is even the potential to only use each CRP set once, which is helpful for secure communications while protecting against third parties [132].

A review article discussing different types of RTDs is [134] which attempts to classify the different types of PUFs, including RTDs, and is useful for further reading on the topic of PUFs as a whole.

### 1.5.2 RTDs as PUFs

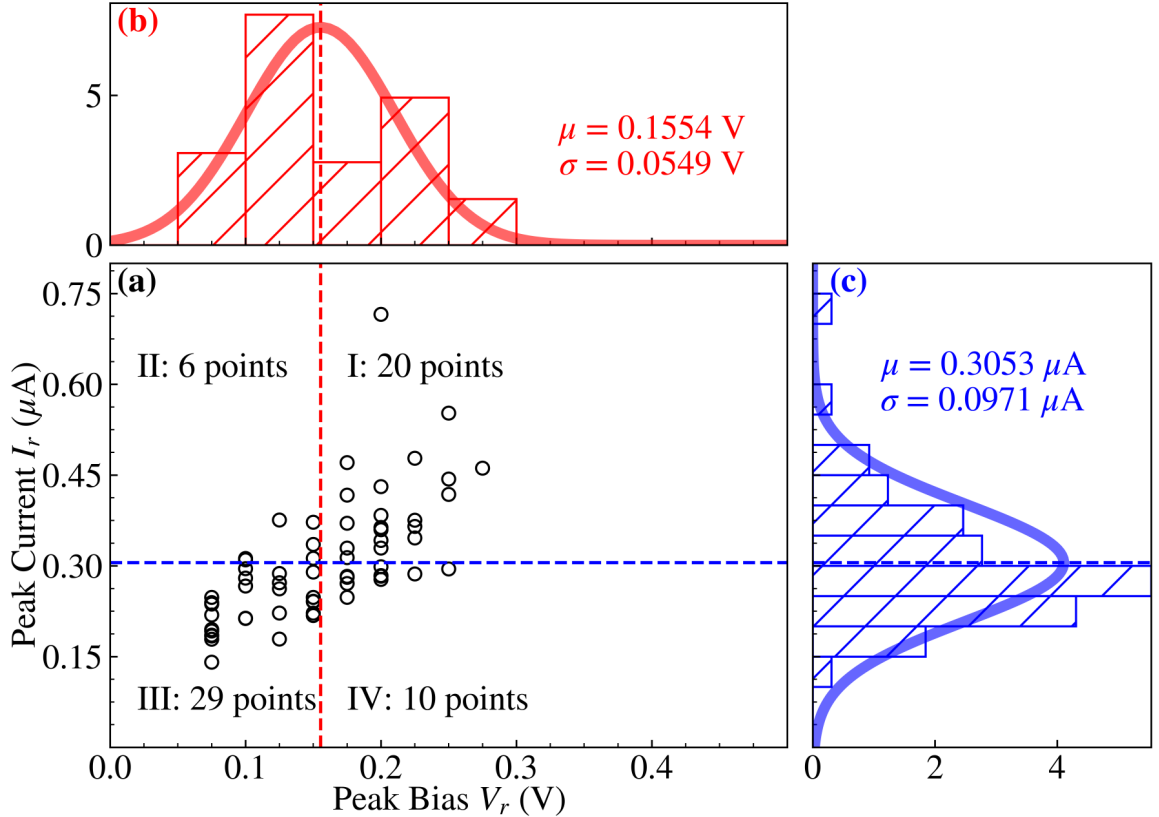


**Figure 1.5:** A scatterplot (figure a) of resonant peak IV values and attached histograms for the  $V_r$  (figure b) and  $I_r$  (figure c) for RTDs simulated with RDDs [7] in chapter 4. This figure is licensed under CC BY 4.0, attached to an archived copy of [7] held by the University of Glasgow. The University of Glasgow has an agreement with IEEE allowing authors to self-archive manuscripts with an attached CC BY licence. © 2024, IEEE.

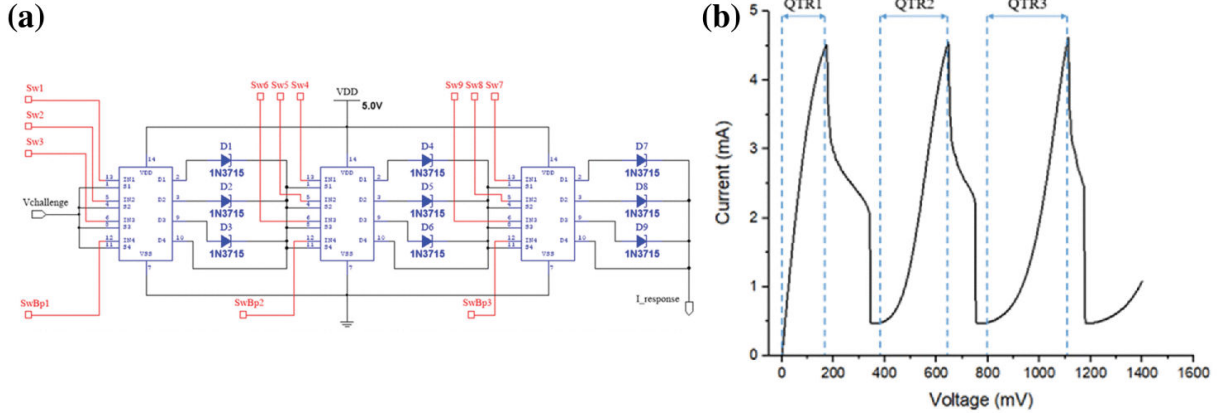


**Figure 1.6:** Combined figure [2] of schematic of a 3 RTD PUF array in figure(a) and an IV characteristic response in figure(b), from Figures 4 and 6 respectively of the paper [2]. Within figure(a) ‘ $V_{challenge}$ ’ is the input bias voltage, ‘ $I_{response}$ ’ is the output current, ‘SW’ refers to the bilateral/analogue switches [135], and ‘SWBp’ refers to the bypass switches which can be used to bypass certain RTDs if they fail [2]. A further explanation of the schematic array in figure(a) and the IV characteristic in figure(b) is given in the paper [2]. The figures [2] used in this combined figure are licensed under CC BY 4.0.

While RTDs are weak PUFs, they have nonetheless attracted a research focus due to their robustness to repeated measurements leading to a strong bit error rate, and their dependence on atomic scale variation which makes reproducing them for counterfeiting purposes unfeasible.

There is also the potential for RTDs to create strong PUFs [2, 132] by combining multiple RTDs in series to achieve a complicated IV characteristic with greater scaling of CRPs. This is seen in Figure 1.6 from a recent proof of concept study[2] on encoding of information in the PDR of RTDs which form an array.

RTDs also have the potential to be integrated onto CMOS chips [22], positioning them for combatting chip counterfeiting [53, 54].

Since RTDs have potential for use in wireless and 6G technology [19], this opens up the possibility of use in security schemes involved in such. Even on a small scale with 128 bits, the popular Advanced Encryption Standard can be used to encode wireless devices [136], which is more than feasible with one RTD PUF paper [22] mentioning the ability to construct 50000 devices on one 8 inch wafer.

RTDs are classified under the category of quantum PUFs [134], and make use of quantum confinement to magnify the effects of atomic variation. Information can be encoded in the resulting variation in the resonant peak IV values [7, 22].

Even more than one bit can be encoded into an RTD, by using  $V_r$  and  $I_r$  variation simultaneously [7, 9], as quantified by min-entropy [137]. Min-entropy [137]  $H_{min} = -\log_2(P_{max})$ , where  $P_{max}$  is the probability of the most likely outcome, is the most conservative measure of information stored in probabilistic systems. Such a probabilistic system can be obtained by splitting the distribution of resonant peaks values into 4 quadrants and then measuring probabilities for each quadrant such as seen in Fig. 1.5.

RTDs have also been demonstrated for the related concept of random number generation [138]. Currently, the use of RTDs as weak PUFs is promising yet research is limited, with no applications utilising RTD PUFs for security demonstrated yet.

## 1.6 Issues and Countermeasures

Thermionic emission over barriers is a major point of concern for RTDs, and a limiting factor for the range of bias over which RTDs can perform with their nonlinear IV characteristic and also the PVCR [139]. Thermionic emission is the emission of high energy electrons over the CBM barriers [47]. For great enough bias, thermionic bias dominates

resonant tunnelling current, destroying the NDR which would correspond to higher QW quasibound energy levels. For RTDs with limited barrier heights like with a GaAs body and AlGaAs and AlAs barriers, this is of particular concern. The most obvious countermeasure to thermionic emission is using heterostructure barriers with a greater offset, which has motivated the incorporation of Indium to form InGaAs/As RTDs as noted in subsection 1.3.1. The greater barrier height offered by such InGaAs RTDs suppresses the contribution to valley current from room temperature thermionic emission, thereby increasing PVCR [63].

Strain in RTDs is a consequence of different lattice constants for the materials composing RTDs [59]. Strain imposes a critical thickness[59, 64], beyond which the formation of dislocations is energetically favourable [59], which partially motivates the extremely narrow central device dimensions observed in THz InGaAs based RTDs [43, 69–72]. Strain compensation [95, 102] is a technique where tensile and compressive strains of layers can compensate for each other, thereby surpassing the critical thickness limit [140]. Strain can also be used intentionally such as for InP substrate InGaAs/AlAs RTDs [140], where the AlAs barriers are under tensile strain [102] with lattice constant smaller than the InP substrate and consequently their CBM increases, which leads to greater barriers. The compressively strained InGaAs QW also leads to a lower energy CBM, and consequently a reduced quasibound ground QW level and therefore a reduced resonant peak bias [65]. Strain can also be used to reduce contact resistance, by avoiding lattice matching with the substrate for the parts of the RTD in contact with electrodes [65, 72]. Further details of strain in RTDs can be found in the following PhD thesis [140].

Resistance is a limiting factor for RTD device performance including power and frequency [141] as noted in subsection 1.7.4, and is composed of multiple parts including contact, spreading and bulk resistances. Contact resistance is the resistance between the RTD semiconductor and the metal contacts. Heavy doping of the layers in contact with the metal electrodes are used to reduce Ohmic contact resistance [65, 72]. As noted above, indium rich strained layers [65, 72] are also used to reduce contact resistance. Increasing

mesa area is another method that leads to a reduction in contact resistance [141], though this also increases current and thus causes self heating effects and additional parasitic resistance [141]. A mesa is the cross-section of the semiconductor nanoelectronic device, such as an RTD.

The spreading resistance associated with current spreading from the mesa to the under-layer connecting the RTD to the contact [141–144] is another contribution to RTD resistance, which is due to the skin effect which becomes greater as frequency increases [141–143]. The spreading resistance can be minimised through reducing the dimensions of this highly doped layer connecting the RTD to the contact to submicron sizes [67, 141, 142, 144], and even more so by removing it [72]. Bulk resistance of the RTD mesa itself [145] is also another component of RTD which needs to be taken into account [67, 141], and can be reduced with smaller device lengths and through doping [146].

As noted in section 1.4, IR [104, 115, 116] increases valley current and thus degrades the PVCR of RTDs. Moreover, IR variation is stochastic, which is problematic for the reproducibility of RTDs. To combat the influence of IR, there is a focus on achieving a high degree of uniformity [99, 117].

Thermal effects are important to take into account for RTDs and have motivated innovations, such as graded emitters [34, 67] and subwells [66], which are seen in RTDs that have achieved THz frequencies. Self heating [147, 148] occurs due to resistive losses, which can become more of an issue with higher current densities and resonant peak voltage  $V_r$ . Thermally activated current contributes to and increases valley current  $I_v$ , and consequently reduces the PVCR and the theoretical maximum power of an RTD [127], which is  $P_{max} = \frac{3}{16}(V_v - V_r)(I_r - I_v)$ . Though for valley current, thermal current is less of a concern than structural imperfections brought about by IR [127]. While temperature variation has been found to cause variations in output power [133] due to resistive losses in a THz RTD oscillator [72], this was minimal around room temperature [133]. Thermal break-

down is a major concern for high frequency RTDs, which is exacerbated by the trend of using thin barriers to achieve high current densities [149]. Thermal breakdown is a breakdown of nanoelectronic devices due to resistive heating, which can occur at high currents. RTDs with large mesa areas are also prone to thermal breakdown [40]. Hence, considerations in managing thermal effects are to not have too great of a current density [149] and mesa size [40, 141]. Thermal degradation is a related issue resulting in alterations in the IV characteristic [150]. Under accelerated ageing simulated with thermal annealing [150], the degradation of Ohmic contacts and the alteration of the IV characteristic has been observed. Metal contacts are a point of concern for such thermal degradation which motivates the use of contact materials which are thermally stable at high temperature [151], such as TiW [152], though currently stacked Ti/Pd/Au contacts [40, 153] are more widely used in RTD literature. Minimising the resonant peak bias  $V_r$  is a key way to minimise self heating, through reducing the energy difference at zero bias between the ground quasibound energy level  $E_{QW}$  and the emitter Fermi level  $E_{F,E}$ , depicted in Figure 1.1(a), such as through graded emitters [34] and subwells [66]. Graded emitters [34, 67] with a raised CBM due to a lower Indium mole fraction, and which vary the indium concentration in layers, raise the emitter Fermi level  $E_{F,E}$ . Indium rich QWs [65, 100] and InAs subwells [66, 100] both achieve the purpose of lowering the QW quasibound ground energy level with respect to the emitter region. Rapid thermal annealing has also been found to be a potential means to reduce the bias peak voltage  $V_r$  [154]. Heatsinking is also recommended [127] as a way to manage temperature, such as through embedding a highly doped InP layer in the InP substrate to dissipate heat away [151].

While doping is a crucial part of RTD design which increases charge mobility [146], it also leads to RDDs [7, 118–126] as discussed in section 1.4. As also mentioned previously, doping helps reduce contact [65, 72] and bulk resistance [146], and the source and drain regions are often highly doped [3] to achieve high current densities. High n-doping in the emitter region [63] increases the current density. Doped collector layers are also important for reaching high frequencies of operation [155]. Less doped spacer layers are needed to surround the central RTD structure including the barriers and the QW, in order to protect

this active region from this diffusion of dopants during wafer growth [63, 156], due to the large influence which RDDs can have on the IV characteristics there [7]. Even just having RDDs in the source and drain regions can potentially have a stochastic effect on IV characteristics [7, 118]. Depending on the doping process used, lattice mismatch can also be influenced to either increase or decrease as doping concentration increases [157].

Phonons [158, 159], which are lattice vibrations, need to be taken into account for modelling RTDs [47, 160–162] due to their influence on RTD mechanisms, such as being absorbed or emitted by incoming electrons to assist with resonant tunnelling [47]. The PVCR is reduced due to phonon scattering [160], and a replica phonon peak can appear in the valley regions due to phonon assisted inelastic scattering [163]. A further discussion of phonons in RTDs can be found in the following textbook chapters [158, 159].

Beyond the direct bandgap  $\Gamma$  valley which forms the CBM, intervalley scattering [159, 164] involving the indirect bandgap L [65, 165] and X [159, 166] valleys also contributes to RTD operation. Indeed, one of the motivations for graded emitters was to suppress transitions to the indirect L valley [34, 167], which are believed to possibly contribute to the transition time in the collector region of the RTD.

## 1.7 RTDs for THz electronics

This section reviews research on RTDs as THz devices, starting with the introduction of the ‘THz gap’ [20], before reviewing RTDs oscillators and the powers and frequencies achieved by them. Following this, a brief overview of RTDs as THz detectors is made, before finishing with design of device considerations for RTD oscillators.

### 1.7.1 THz gap

The ETSI (European Telecommunications Standards Institute) defines the frequency band of 100GHz to 10THz as ‘THz’ [168], which corresponds to wavelengths ranging from 3 millimetres to 0.03 millimetres due to the relation  $\lambda = \frac{c}{f}$ , hence another name for THz radiation is millimetre waves. The THz band of electromagnetic radiation has been receiving attention [16], which can be explained by the wide range of applications enabled by THz electronics, which range from sensing [20, 48, 169] to high-speed telecommunications [19]. Historically there has been a lack of mass-producible options for the generation and detection of THz waves, which has been referred to as the ‘THz gap’. In order to fill this gap, multiple competing technologies are under development [16], including RTDs. As seen in the following subsections 1.7.2 and 1.7.3, over the past two decades research has been pushing RTDs to fill the THz gap, and has made it a strong contender [16]. Further recommended reading on other THz devices under development is the following chapter [16].

### 1.7.2 RTD Oscillators

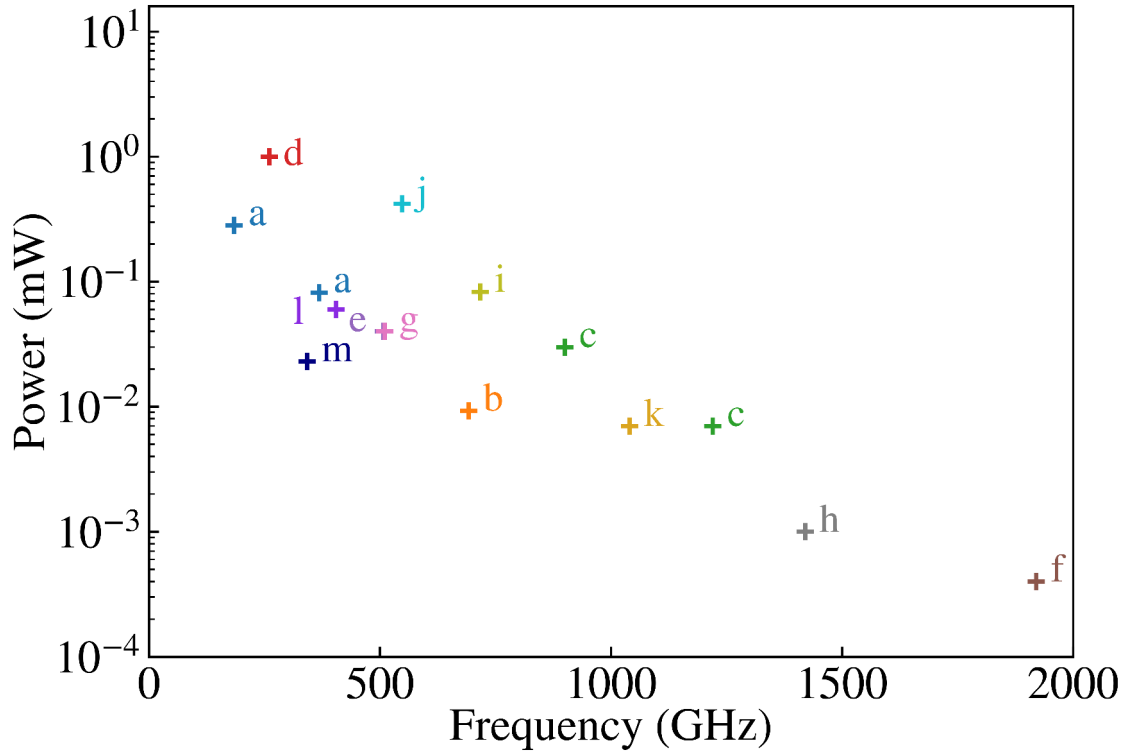


**Figure 1.7:** Scatterplot of powers and fundamental frequencies achieved by single RTD oscillators. The labels correspond to the following papers with the most recent ones listed first: a [4], b [69], c [70], d [43], e [71], f [72], g [73], h [170], i [171], j [172], k [34], l [173], and m [33]. Note that the marker 'g' overlaps on the 'e' marker because both have reported powers of  $40\mu\text{W}$  [71, 73] and frequencies of 510GHz [73] and 507GHz [71] respectively.

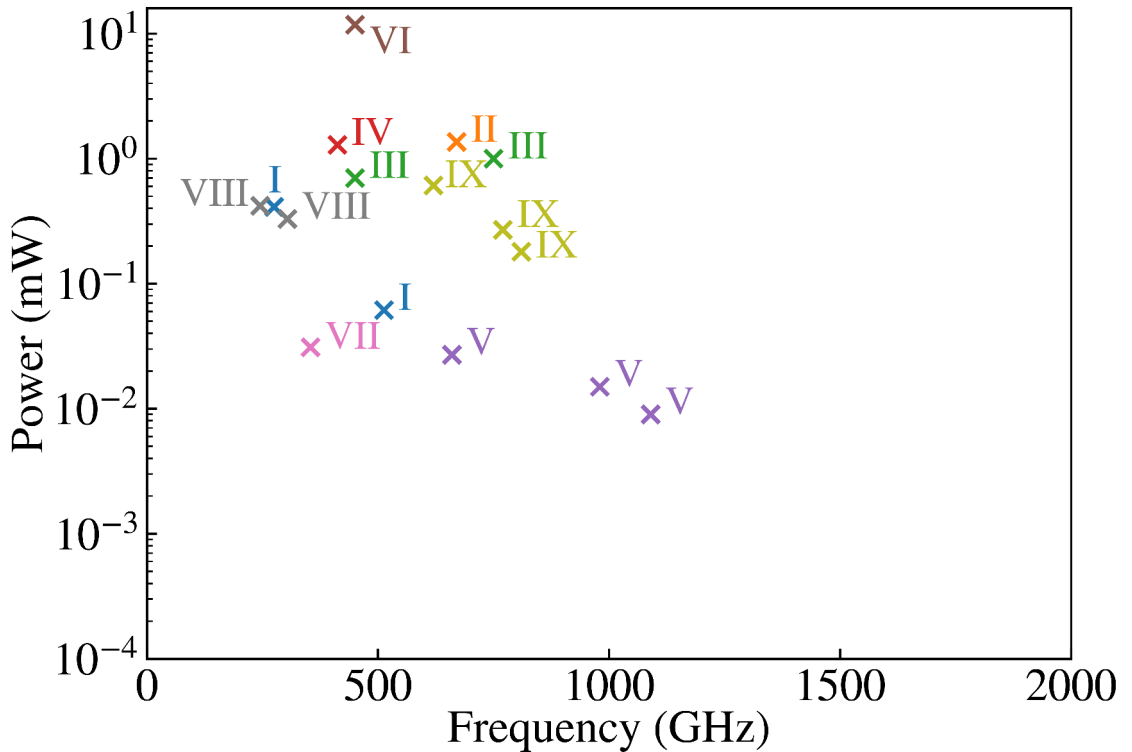


**Figure 1.8:** Scatterplot of powers and frequencies achieved by arrays of RTDs, including oscillators making use of 2 RTDs. The labels correspond to the following papers with the most recent ones listed first: I [36], II [37], III [38], IV [39], V [40], VI [41], VII [42], VIII [43], and IX [174].

RTDs when coupled with lossy resonators, like an LC circuit, can compensate for these losses when biased into the NDR, leading to an oscillator with energy moving back and forth between these components. With room temperature quantum tunnelling, the fundamental operation frequency of RTD oscillators reach into THz frequencies [35, 72], opening up the potential for RTDs as THz devices [16]. RTD oscillators act as DC to Resonant Frequency (RF) converters, and if the resonator includes an antenna as the load then this power can be radiated out through the antenna [175]. Powers and frequencies achieved for single RTD oscillators, with fundamental frequencies, and RTD arrays are depicted in Fig. 1.7 and Fig. 1.8 respectively.

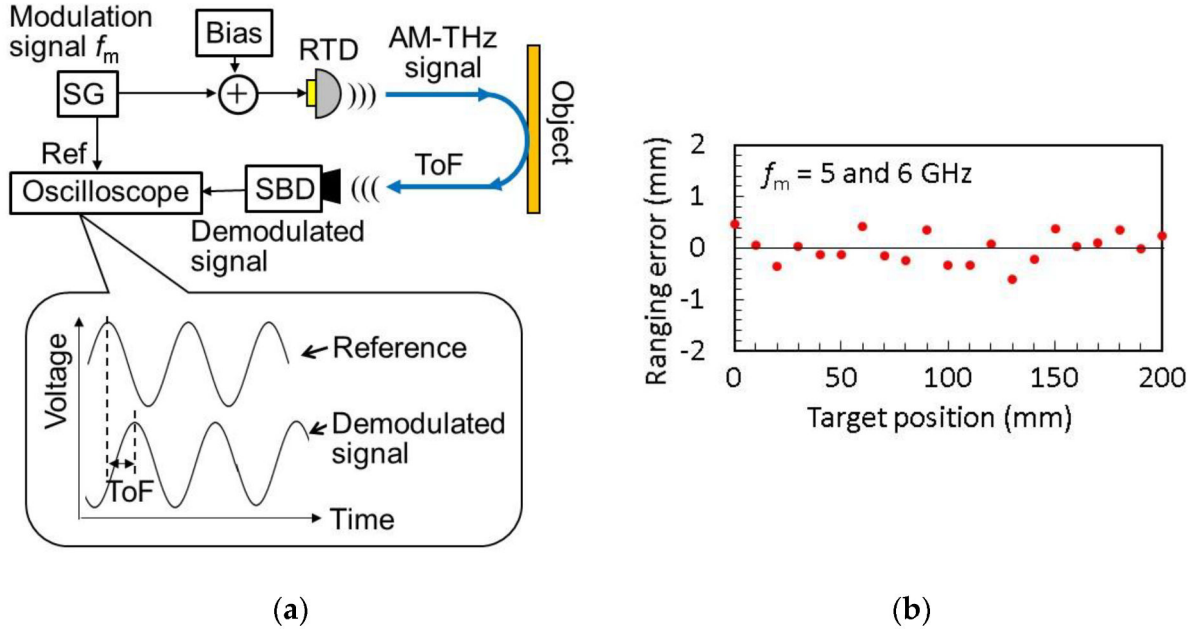


**Figure 1.9:** Figure(a) is a schematic diagram of an amplitude-modulated(AM) continuous wave THz RTD radar and figure(b) is the error evaluated for different distances. This figure is from the following paper [3]. In figure(a) a sinusoidal modulation signal generated by the signal generator (SG) is superimposed on the bias voltage which causes the RTD signal to be amplitude-modulated, thus leading to an emitted AM-THz signal which hits a target object. The reflected signal is measured by a detector, in this case a Schottky barrier diode (SBD), which also demodulates the AM-THz wave to re-extract the sinusoidal signal. The time of flight (ToF) of the AM-THz signal is determined by the phase difference between a reference signal from the SG and the demodulated signal. Further discussion regarding this figure is given in [3]. This figure [3] is licensed under CC BY 4.0.

One way of using THz RTD emitters is for THz radar [3], as shown in Fig. 1.9 which is from [3].

There are different types of oscillators developed, with slot antennas [4, 36, 38, 145, 170–172, 176] being the dominant modality which has achieved nearly 2THz fundamental frequencies [35, 72]. The output of the slot antenna is then often directed with a hemispherical Si lens [33, 35, 72].

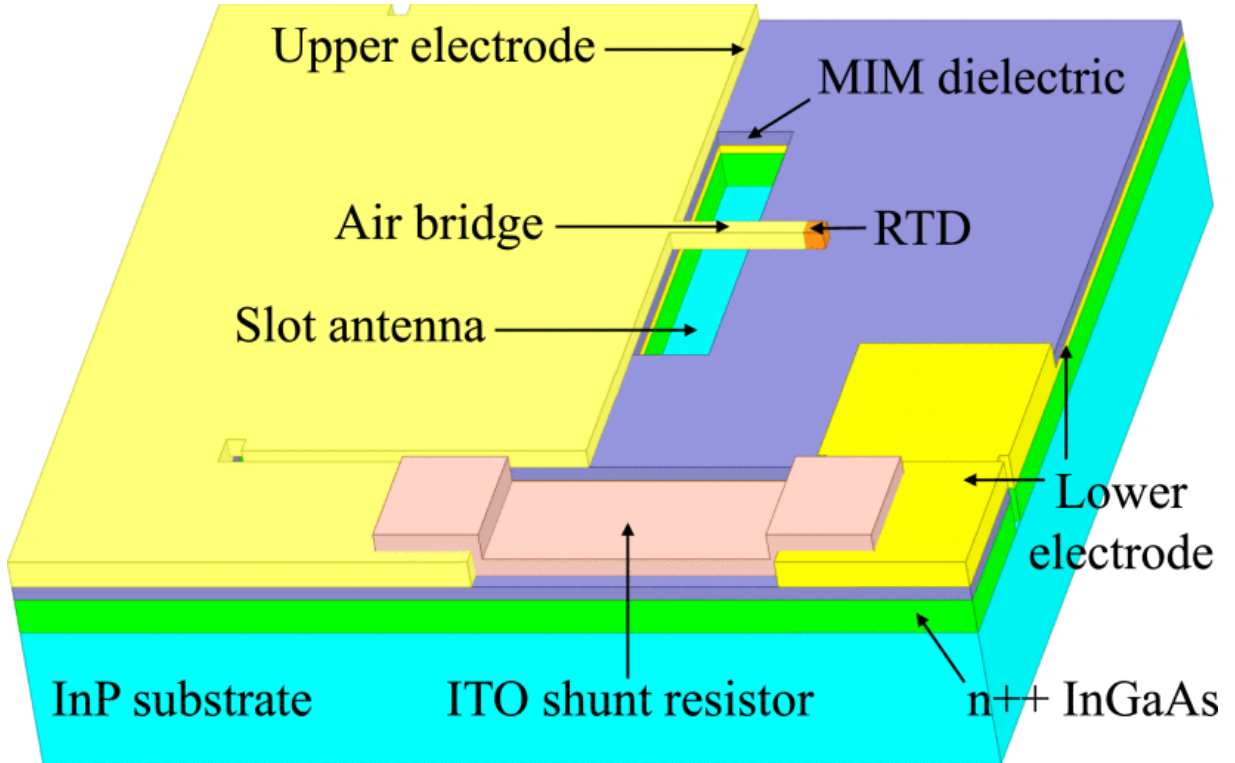


**Figure 1.10:** A schematic of a slot antenna [4] setup. The MIM (metal-insulator-metal) capacitor is formed by a separation of the upper and lower electrodes. The slot antenna is formed by a gap in the lower electrode and neighbouring dielectric and the highly n++ doped InGaAs layer. The ITO (indium-tin-oxide) shunt resistor suppresses parasitic oscillations at low frequencies. This figure [4] is licensed under CC BY 4.0.

A schematic of a slot antenna RTD setup is seen in Fig. 1.10, where the top and bottom electrodes form a MIM (metal-insulator-metal) capacitor and a slot gap in the lower electrode and neighbouring layers forms the slot antenna. The MIM acts as a short circuit, which allows current flow [177], at the operating frequencies of the RTD oscillator and an open circuit, which stops current flow [177], with a DC voltage. The ITO (indium-tin-oxide) stabilising shunt resistor is there to suppress parasitic oscillations at low frequencies [4, 141]. Recommended reading for further explanations of slot antenna RTD oscillators includes [4, 176].

Split ring oscillators [70] are a recent development on top of slot antenna oscillators [149]. For this, MIMs are first removed from the slot antenna [178], along with stabilising resistors being placed on either side of the slot. To combat the limited oscillation frequency due to the Ohmic loss of these stabilisation resistors, the split ring resonator is used [70, 179, 180], which concentrates the electric field at the split gap and thus reduces loss [70]. The benefit of split ring oscillators is the simplification of manufacturing through the removal of MIMs [149]. A reduced variation in resonators due to this simplification in manufacturing [180] also provides potential for building large arrays with these resonators [149].

Slot-ring oscillators [39, 42, 181, 182] are a recent development of dual RTD planar arrays using one or two slot-ring antennas [39] which promise high directivity and power [39] along with THz frequencies [181, 182] of operation. High powers over 1mW with frequencies greater than 600GHz have also been very recently achieved with a dual RTD slot-ring array integrated with a cavity resonator [37].

Patch antennas are another RTD oscillator configuration which have made use of two RTD arrays [40, 183] to achieve THz operations with fundamental frequencies [40]. With a greater array of 72 RTDs and 36 patch antennas [41] powers over 10mW and a high directivity, potentially not requiring a Si lens to focus, has been achieved. An integration of patch antennas with a slot resonator RTD oscillator can also replace the use of a Si lens [73].

Terminated stubs of coplanar waveguides or microstrip lines can also be used to construct RTD oscillators [43], resulting in relatively high powers ranging up to 1mW above 200GHz in the case of microstrip lines, with output waves guided by coplanar waveguides. Coplanar waveguides can also be integrated into other oscillators, such as a patch antenna RTD oscillator [69].

Similar to patch antennas, Yagi-Uda [184] and Vivaldi [66] antennas have both been used to direct radiation in place of Si lens for slot antenna RTD oscillators which have achieved THz frequencies. Radial line slot antennas [71] have achieved a similar focussing feat with a circularly polarised output. Advantages of such a circular polarisation, as opposed to the more common linear polarisation [3], are that wireless communications can continue even if receivers and transmitters rotate [149] and a robustness [3, 185] to external reflections [186] since the polarisation of reflected waves rotates in the reverse direction [185].

Varactor diodes can be used to vary the frequency of operation of RTD oscillators [187], making it useful for applications such as spectroscopy [52]. Varactor diodes can also be used to suppress linewidths of RTD oscillators (measured as Full-Width-at-Half-Minimum) to less than 1 Hz [188, 189] from values of the order of 1 [188] to 10 [189] MHz. A further explanation of varactor diodes in RTD oscillators is given in the following review article [3].

### 1.7.3 THz Detectors

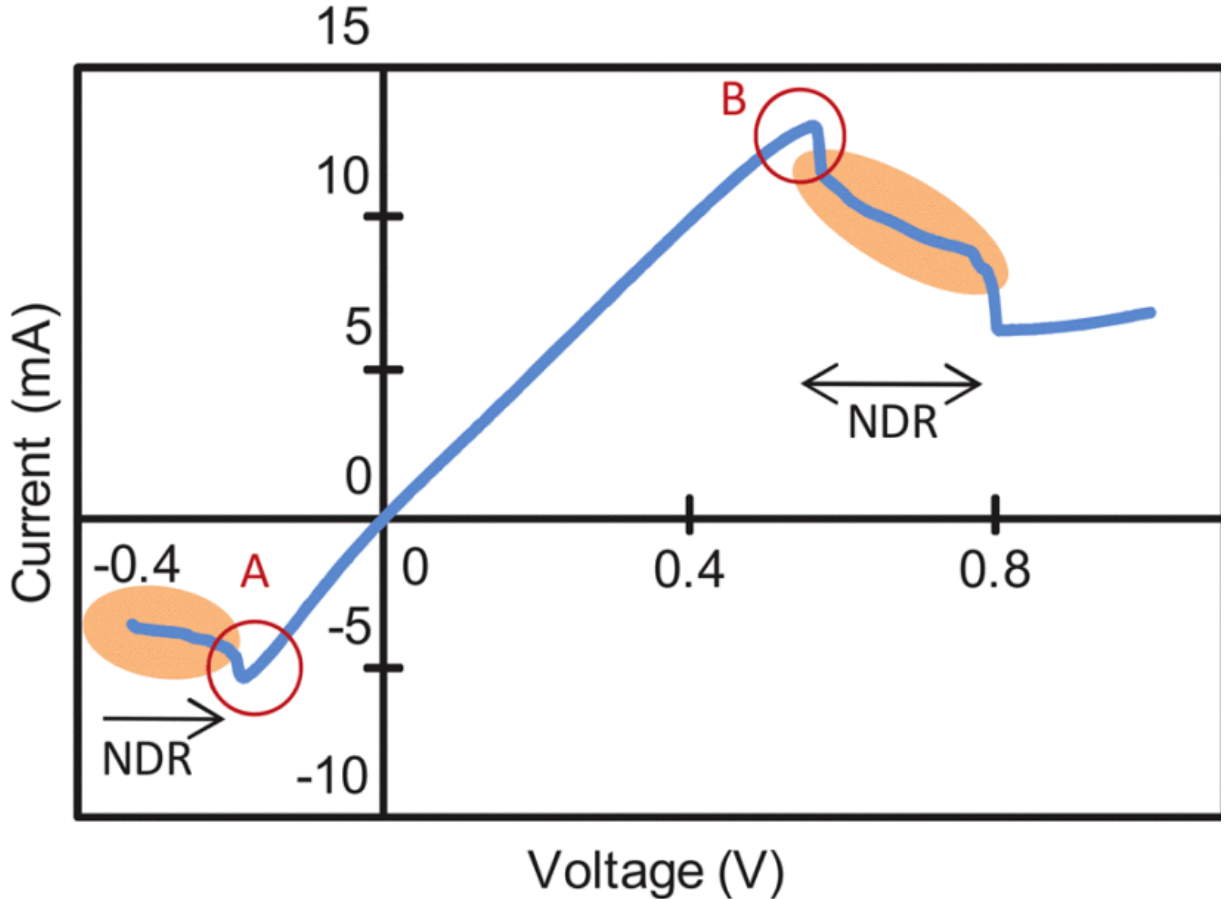


**Figure 1.11:** IV characteristic of an RTD detector [6]. Direct detection occurs when the RTD is biased in the PDR (Positive Differential Region) of current close to the resonant peak (labelled A and B) due to strong non-linearity in current. Coherent detection makes use of the NDR (Negative Differential Resistance), which is similarly annotated and labelled, wherein the RTD acts as an oscillator. This figure is sourced from a paper[6] first published and copyrighted by Engineers Australia© 2011, Engineers Australia.

Aside from being THz sources, RTDs also function well as THz frequency detectors. This dual-capability as transmitter and receiver in the THz regime positions RTDs for high speed wireless communication [19] and for imaging [20]. Detection modes for RTDs can be split into two modes [19, 20], direct detection [6, 94] and indirect/coherent detection [50], with the regimes noted in Fig. 1.11. Direct detection with RTDs occurs when the bias is in the PDR (Positive Differential Region) of current, with bias lesser than the resonant peak  $V_r$ , and depends on the non-linearity in current and is hence the greatest near the resonant peak  $V_r$  [6]. RTD detectors have been found to be more sensitive than Schottky barrier

diodes (SBD) at room temperature at 300GHz [6], though with a lower dynamic range in detectable frequencies due to being positioned close to the  $V_r$  in these cases, where a high enough amplitude can perturb the RTD state into the NDR [19]. Triple barrier RTDs [94, 96], where current depends on alignment between the energy levels in the two QW, have also been manufactured as direct detectors with a highly non-linear IV characteristic at zero bias. This zero bias operation of triple barrier RTDs has the advantages of reducing noise, thus increasing sensitivity, and of reducing the need for circuitry to bias the RTD, thereby making it more compact and power-efficient [94].

Coherent detection [50, 190] is a relatively recent development for RTDs [19, 20]. Coherent detection has been shown to be much more sensitive than direct detection in a comparison at 300GHz [50] and promises the measurement of data beyond just amplitude, including phase, frequency, and polarisation. A further explanation of coherent detection is given in the following papers [50, 190].

#### 1.7.4 Design of Device

RTD oscillators can be designed to achieve higher powers and frequencies of operation as THz devices. This subsection will briefly touch on such design considerations beyond what was covered in sections 1.4 and 1.6 which focus on the issues faced by the RTD device itself.

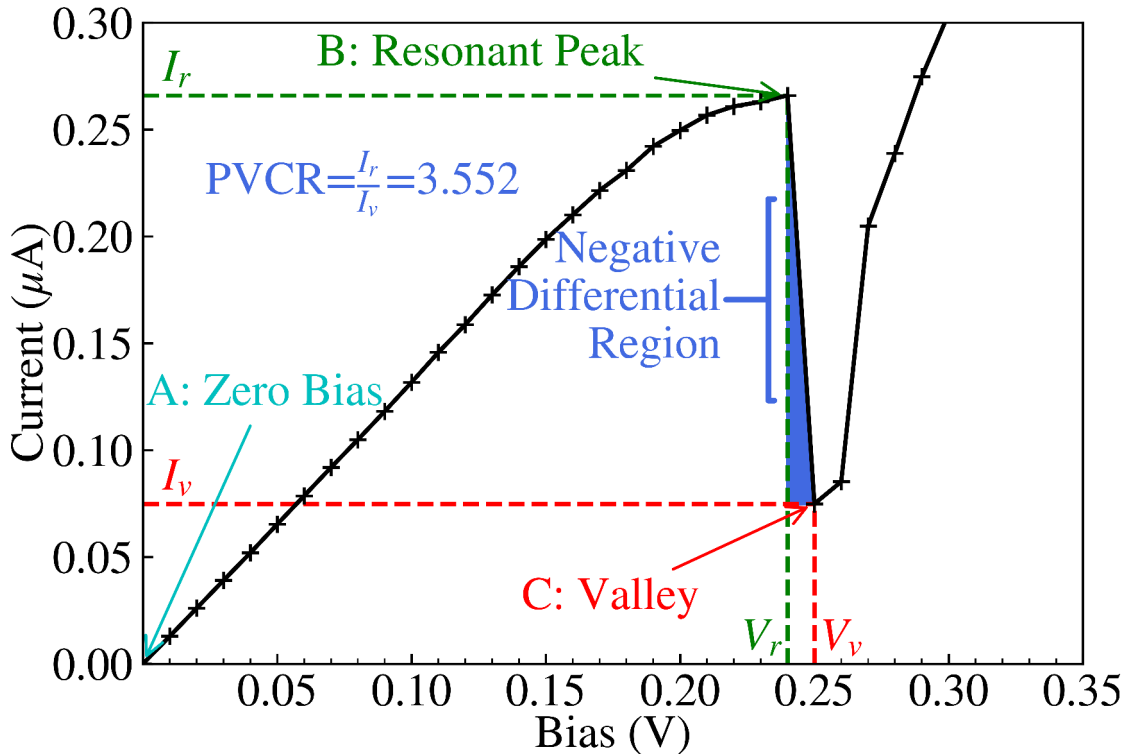


**Figure 1.12:** Annotated IV characteristic of a simulated RTD [9]. The NDR (Negative Differential Resistance) between the resonant peak  $I_r$  at  $V_r$  and the valley  $I_v$  at  $V_v$  is highlighted blue. This figure [9] is licensed under CC BY 4.0.

RTD oscillators work due to RTDs themselves possessing a negative differential conductance which can compensate for the load of antenna, leading to the oscillating behaviour, but this is frequency dependent [14] and limited by internal and external conditions which impose a frequency limit [191]. Internal to the RTD is the time it takes for charge to travel through the device, which has encouraged the manufacture of thin RTD dimensions [43, 69–72], and external issues are device parasitics such as contact resistance, for which measures to minimise are noted in section 1.6. Maximum theoretical power, without taking into account impedance matching [175, 192] and parasitics, can be estimated as [127]  $P_{max} = \frac{3}{16}(V_v - V_r)(I_r - I_v)$ , hence increasing current and PVCR are key ways to increase power.

Reducing the conductance loss which needs to be compensated [72] is a method to achieve higher frequencies, such as by thickening antenna electrodes [149]. Conductance loss can also be reduced by integrating cavity resonators onto RTD oscillators [37] to achieve very high frequencies [193, 194]. This increased area, and thus current, brought about by cavity resonators along with reduced current loss has also helped to achieve a power exceeding 1mW above 600GHz [37].

Reducing thicknesses for device sections such as the barrier and the QW reduces the transit times [67] for electrons, and thus increases the frequency of operation. Such a reduction in thicknesses also increases the current density [141], and thus the output power of RTDs, albeit at the cost of heating and possible thermal breakdown as noted in section 1.6. This increase in frequency and power has motivated the use of very thin  $\sim$ 1nm barriers, such as with the first room temperature THz RTD [34], and thin QWs [67, 72]. Optimising the spacer regions [63, 65, 67, 156, 170, 187] is also a way to reduce transit times associated with them. Though, protection against unwanted dopants [7] entering this active device region during manufacture limits how thin spacers can be [63, 156].

Using higher harmonics [33, 181, 191] is another method to achieve higher frequencies than the fundamental frequency, albeit at the cost of reduced output power.

Current can be increased through measures such as increased mesa size [195], though as noted in section 1.6 this needs to be balanced with self-heating effects such as thermal breakdown in these large mesa areas [40]. Decreasing valley current can be done through better more uniform smooth RTDs with less IR [127], which is another way of increasing PVCR and thus power. Impedance matching [175, 192] between the RTD and antenna is an important factor in maximising RTD output power [174]. Directivity of RTD output is also important, which is a reason for the use of Si lens [33, 35, 72] or other additional antennas integrated on an RTD oscillator as noted in subsection 1.7.2.

As mentioned in subsection 1.7.2, arrays of RTDs are a method to increase output power, with it being a focus of a lot of recent research [36–43], with resulting powers and frequencies displayed in Fig. 1.8.

## 1.8 Conclusion

This chapter serves as an introductory guide to RTDs, their theory of operation, variations and other issues and corresponding countermeasures for them, and RTDs as THz devices and PUFs. RTD research has developed to the point where applications as THz devices and PUFs are within reach. A direction for future RTD research is to focus on realising RTDs for such applications.

# Chapter 2

## Theory and Methods

### 2.1 Introduction

This chapter serves as an introduction to the theory involved in performing RTD research with the modular technology computer-aided design (TCAD) nano-electronic simulation software (NESS) under development at the University of Glasgow.

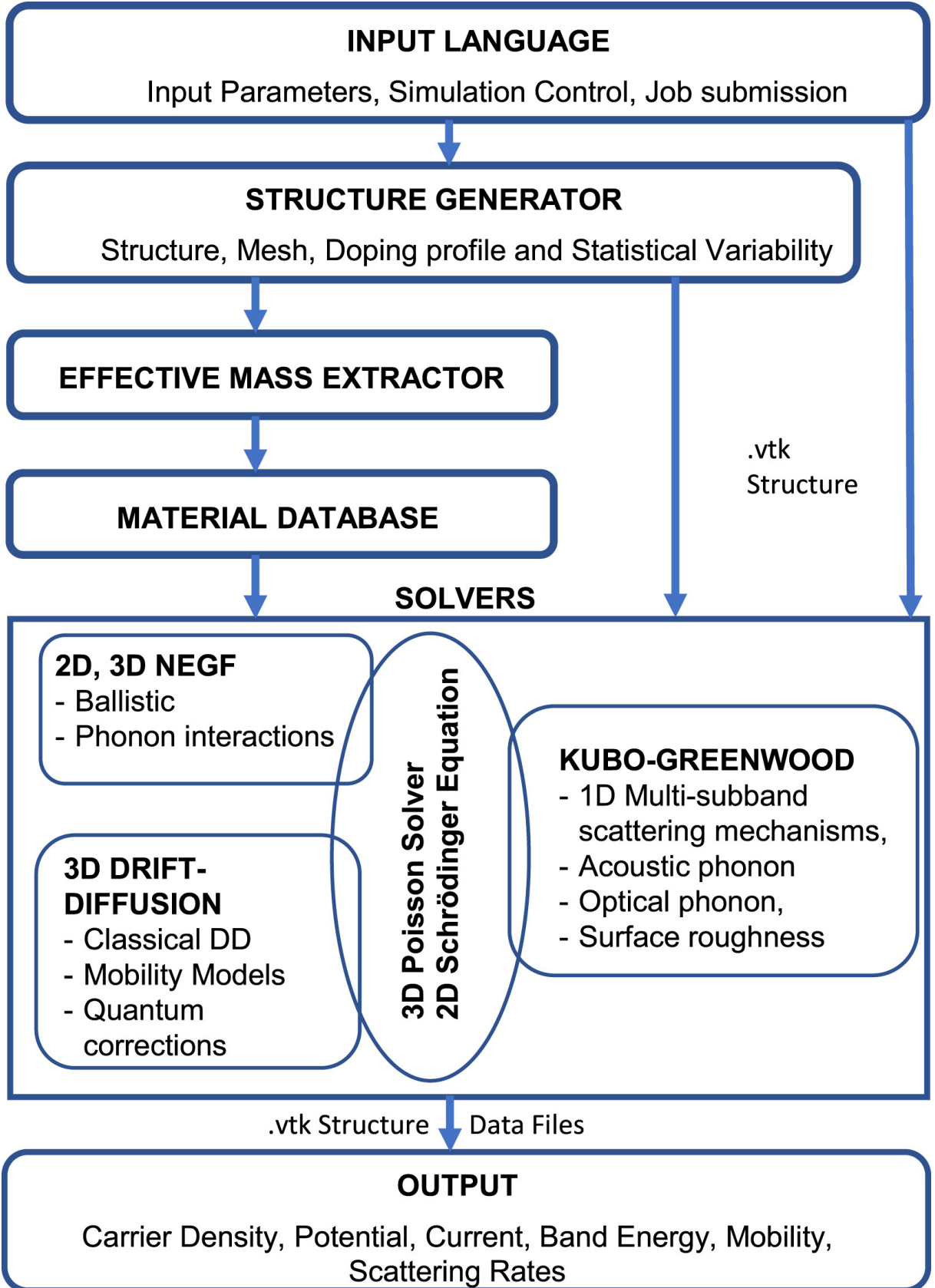


**Figure 2.1:** Schematic of the modular structure of NESS, from [5]. Of these modules, this thesis makes use of the structure generator, the NEGF solver, and the Poisson solver. This figure [5] is licensed under CC BY 4.0.

To simulate RTDs, a Structure Generator module is necessary to first generate the device, which is explored in the following section 2.2. This device generation includes variation such as RDDs and IR in subsections 2.2.2 and 2.2.3 respectively. Within the aforementioned subsections additions to NESS over the source of this thesis are noted; the ability to choose RDD generation probability on top of a separate smooth doping, and the addition and development of IR. These additions to NESS are then made use of later in chapters 4 and 5, which study RDDs and IR respectively. As nanoelectronic devices, electrostatic potential needs to be taken into account during simulations. For this, NESS has a Poisson Solver module which can solve the Poisson equation to get the electrostatic potential profile, which is briefly explained in section 2.3, depending on the charge. This charge as well as current can be obtained from the non-equilibrium Green's function (NEGF) solver module, which is covered in section 2.4 and itself depends on the potential profile. Before this thesis began, NESS could already self-consistently solve the Poisson and NEGF solver modules to capture the quantum behaviour that define RTDs such as energy-dependent quantum tunnelling, and sections 2.3 and 2.4 describe their capabilities. This self-consistent loop is then repeated for each bias voltage specified. A schematic describing the modular structure of NESS is shown in Fig. 2.1. Finishing off this chapter, a smooth ‘baseline’ RTD is shown in section 2.5.

## 2.2 Structure Generator

### 2.2.1 Device Generation

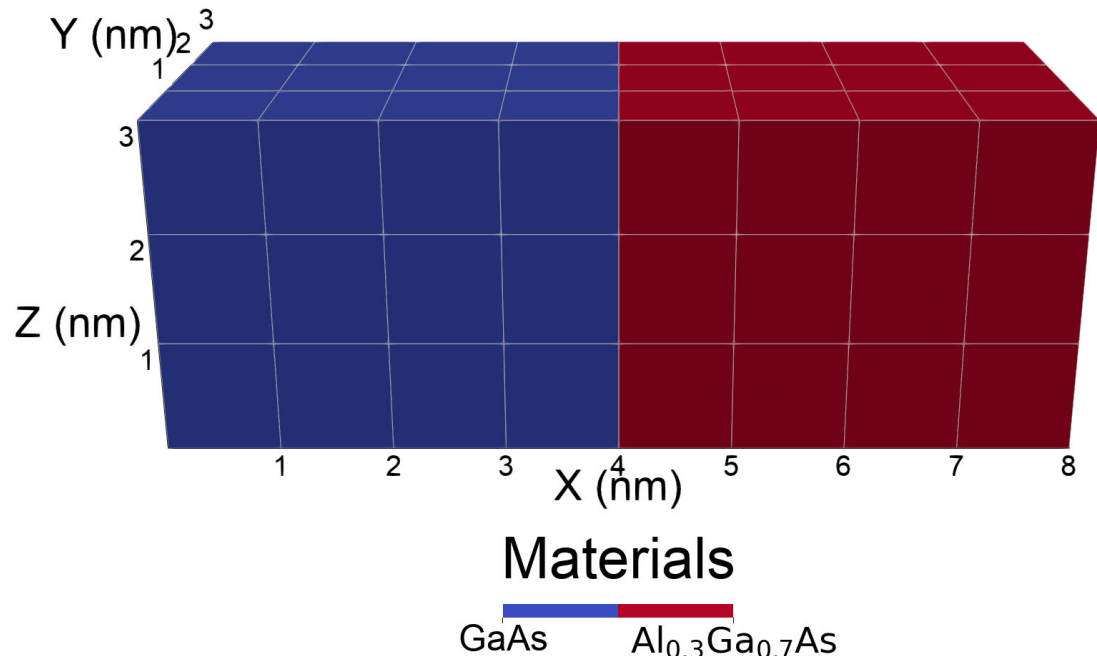


**Figure 2.2:** An example of a heterostructure nanowire structure created by the structure generator of NESS [196], with materials for mesh cells visualised. This nanowire is composed of 1nm wide cubic cells, with dimensions of  $8\text{nm} \times 3\text{nm} \times 3\text{nm}$ , and GaAs material composes the first 4nm along the X axis, and  $\text{Al}_{0.3}\text{Ga}_{0.7}\text{As}$  composes other 4nm.

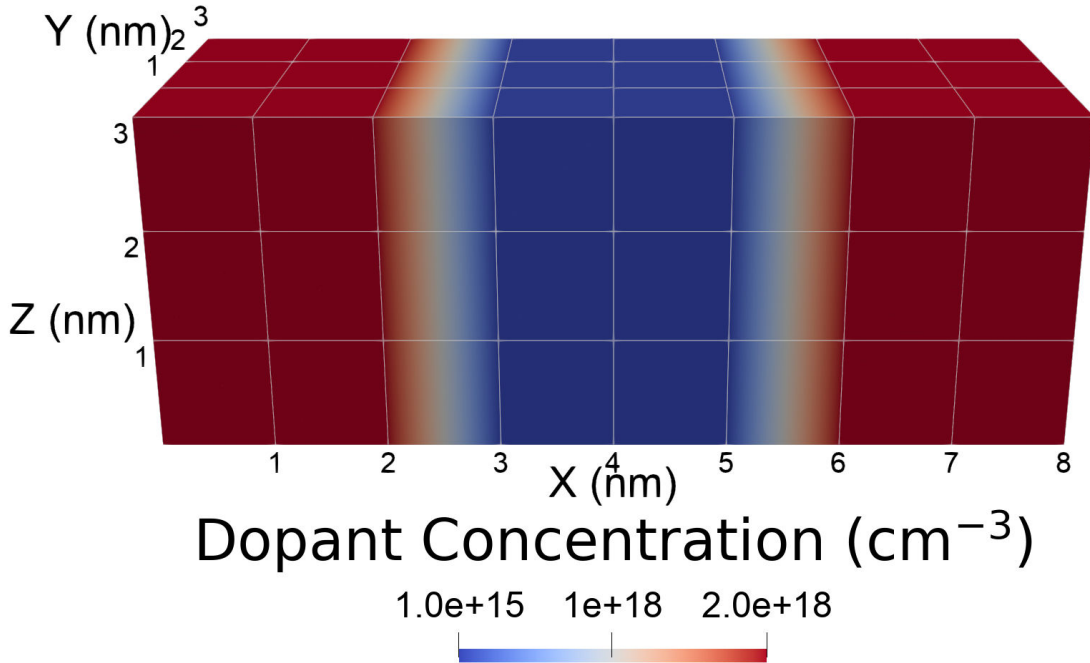


**Figure 2.3:** An example of an n-doped nanowire structure created by the structure generator of NESS [196], with dopant concentration  $N_D \text{cm}^{-3}$  visualised. This nanowire is composed of 1nm wide cubic cells, with dimensions of  $8\text{nm} \times 3\text{nm} \times 3\text{nm}$ , with a base dopant concentration of  $1 \times 10^{15}\text{cm}^{-3}$  and a raised dopant concentration of  $2 \times 10^{18}\text{cm}^{-3}$  for the nodes composing the first and last 2nm along the X axis.

The structure generator in NESS generates devices with a 3D cuboid mesh, with a chosen doping for the nodes and chosen materials filling the cuboid mesh cells. A key advantage of the structure generator in NESS is the inclusion of device variation [196], of which I have made use of RDDs and IR as noted in subsections 2.2.2 and 2.2.3 respectively.

An example of an n-doped heterostructure device generated by the structure generator is shown in Fig. 2.2 and Fig. 2.3, which respectively visualise the material type in cells and the dopant concentrations assigned to nodes bounding the cells.

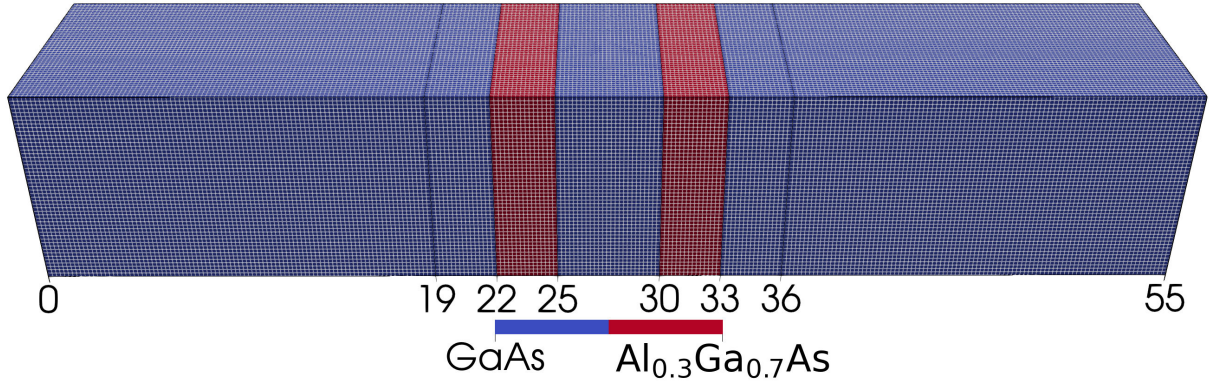


**Figure 2.4:** This figure is a schematic of a Al<sub>0.3</sub>Ga<sub>0.7</sub>As/GaAs RTD from [7]. The dimensions are 55nm×10nm×10nm, with  $2\times 10^{18}\text{cm}^{-3}$  n-doped source (0nm-19nm) and emitter (36nm-55nm) GaAs regions and a central  $1\times 10^{15}\text{cm}^{-3}$  n-doped heterostructure region. This central region is composed of 3nm GaAs spacers (19nm-22nm and 33nm-36nm) enclosing two 3nm Al<sub>0.3</sub>Ga<sub>0.7</sub>As barriers (22nm-25nm and 30-33nm) and a 5nm GaAs QW (25nm-30nm) in the middle. This figure is licensed under CC BY 4.0, attached to an archived copy of [7] held by the University of Glasgow. The University of Glasgow has an agreement with IEEE allowing authors to self-archive manuscripts with an attached CC BY licence. © 2024, IEEE.

A visualisation akin to Fig. 2.2, except for RTDs is Fig. 2.4

### 2.2.2 Random Discrete Dopants

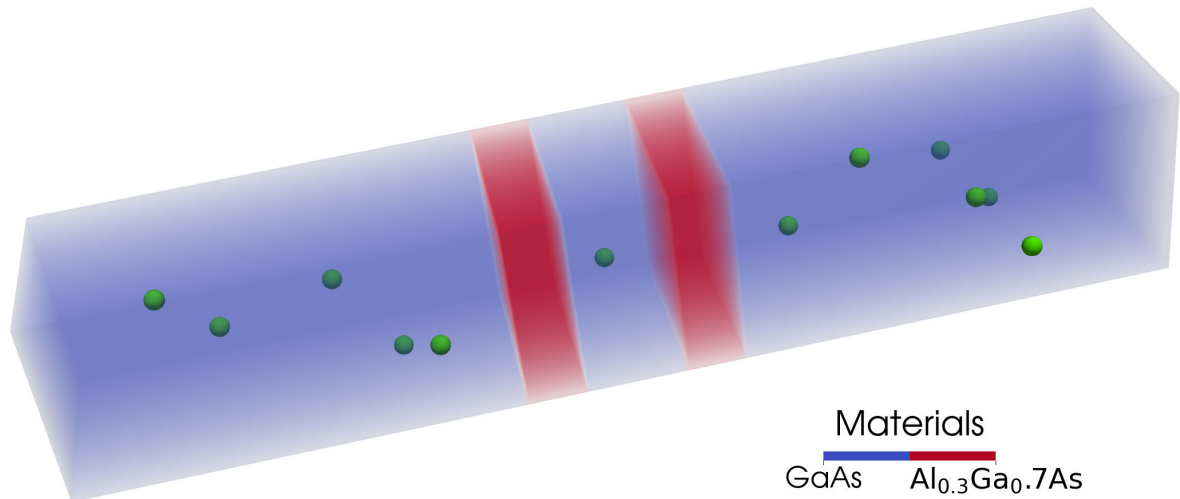


**Figure 2.5:** RTD with RDD (Random Discrete Dopant) positions shown as green spheres. The GaAs body and Al<sub>0.3</sub>Ga<sub>0.7</sub>As barriers are both partially transparent volumes, which are blue and red respectively, to allow the visualisation of RDDs.

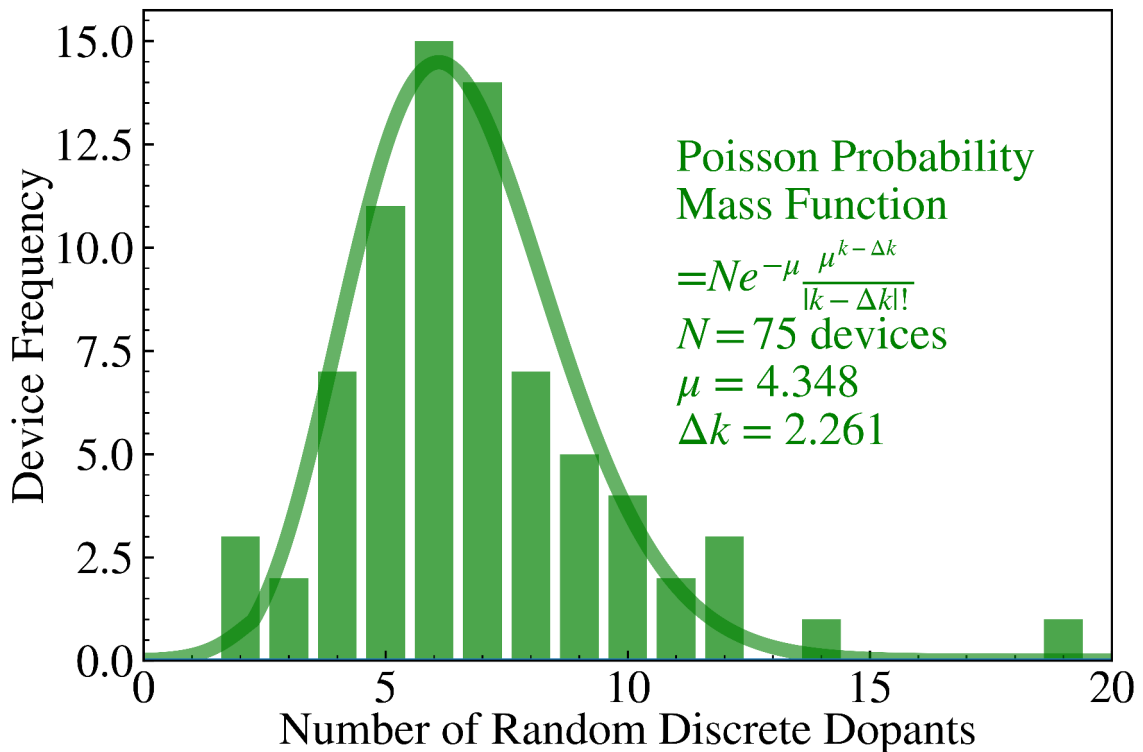


**Figure 2.6:** Frequency distribution of RDDs (Random Discrete Dopants) generated for 75 RTDs generated within this chapter, with a fitted Poisson Probability Mass Function curve. Details of the Poisson Probability Mass Function formulation and parameters ( $N=75$ ,  $\mu=4.348$ , and  $\Delta k=2.261$ ) are noted within the inset.  $N$  is the total number of RTDs and  $k$  is a variable describing the number of RDDs, corresponding to the 'x' axis in the plot.

RDDs (Random Discrete Dopants) are a feature of NESS used to take into account statistical variability [7, 118, 197], which can be defined during device creation by the structure generator, where discrete points of doping implanted within the mesh cell volumes represent ionised dopant atoms in nanometre-scale devices instead of using a smooth doping distribution. As devices have shrunk to the nanometre scale, taking into account the discrete variation of semiconductor doping is increasingly important [198].

The possible positions of RDDs in NESS by default follow a face-centred-cubic lattice structure as seen with diamond and silicon, modelled as if an RDD had substituted a lattice position, with the lattice parameter of 0.543nm chosen by default. Unfortunately, I only noticed this after completing chapter 4, but thankfully it will lead to a similar

RDD distribution as with the case of using a lattice parameter of 0.565nm [45] due to the probability of RDDs appearing within a given device volume being independent of this lattice parameter and instead depending on the doping concentration. At each possible RDD position, there is a probability of an RDD appearing, and a randomly generated number is compared with this probability. If the randomly generated number is less than this RDD probability, than an RDD is added to that point. By default, the probability of RDDs appearing in a region chosen to have RDDs is linearly proportional to the defined doping level multiplied by the volume corresponding to that RDD point. I modified the structure generator RDD probability to also be able to be manually chosen, by allowing the choice of an effective doping level for RDDs which feeds into the probability of RDD occurrence. This modification also means that RDD doping can be applied on top of a base ‘smooth’ doping, and has been used to explore the impact of RDDs in the published paper [7], and chapter 4 which is based on it.

The frequency distribution of RDDs generated for a given RTD device follows a Poisson Mass Function as shown in Fig. 2.6 which corresponds to the RTDs with RDDs in chapter 4.

For the case of n-type doping, as seen in the simulated RTD in Fig. 2.5, the RDDs are donor dopants and the surrounding mesh nodes have greater n-type doping, which is taken into account when the Poisson solver calculates the electrostatic potential. This doping is of the same type as the doping chosen in a region of the device, which for the RTD is p-doping with RDD donor dopants.

Whichever mesh cell is within RDD leads to a raised dopant value for the surrounding 8 mesh node vertices dependent on how close they are to the RDD. The doping added for a node at  $\mathbf{r}_N = x_N\hat{x} + y_N\hat{y} + z_N\hat{z}$  with a dopant at  $\mathbf{r}_D = x_D\hat{x} + y_D\hat{y} + z_D\hat{z}$  is proportional to  $(1 - \frac{|x_N-x_D|}{\Delta x})(1 - \frac{|y_N-y_D|}{\Delta y})(1 - \frac{|z_N-z_D|}{\Delta z})$ , where mesh spacing is given by  $\Delta x$ ,  $\Delta y$ , and  $\Delta z$ . Furthermore, the doping value added by the RDD to a given node is inversely proportional to the volume which corresponds to the node. Research on the impact of RDDs on RTD performance is explored in chapter 4.

### 2.2.3 Interface Roughness

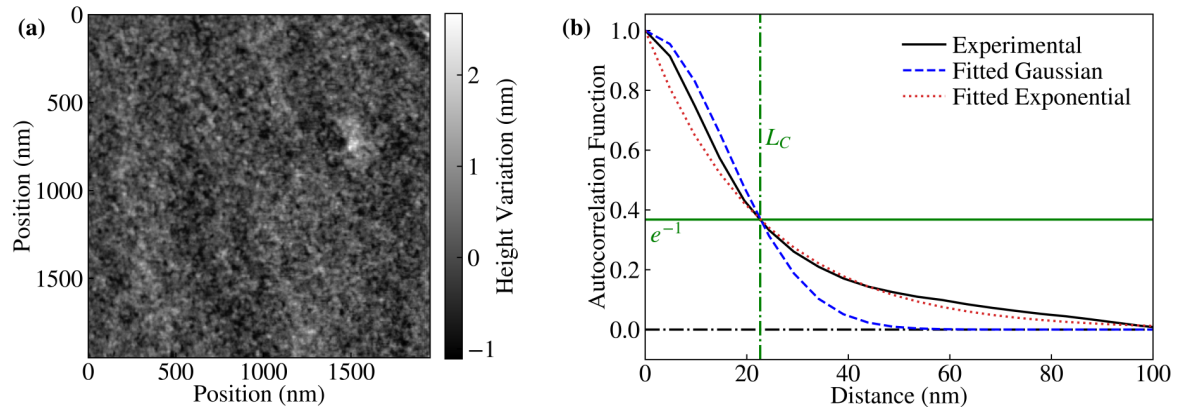


**Figure 2.7:** Figure(a) is created using AFM (Atomic Force Microscopy) image data of an  $\text{Al}_{0.3}\text{Ga}_{0.7}\text{As}$  surface, which was graciously provided by the authors of [1]. Figure(b) is an autocorrelation function analysing the height data from figure(a) (along the x-axis), shown as a black solid line, with correlation length  $L_C=22.6\text{nm}$  fitted. Here Gaussian and exponential functions are fitted as dashed blue and dotted red lines respectively.

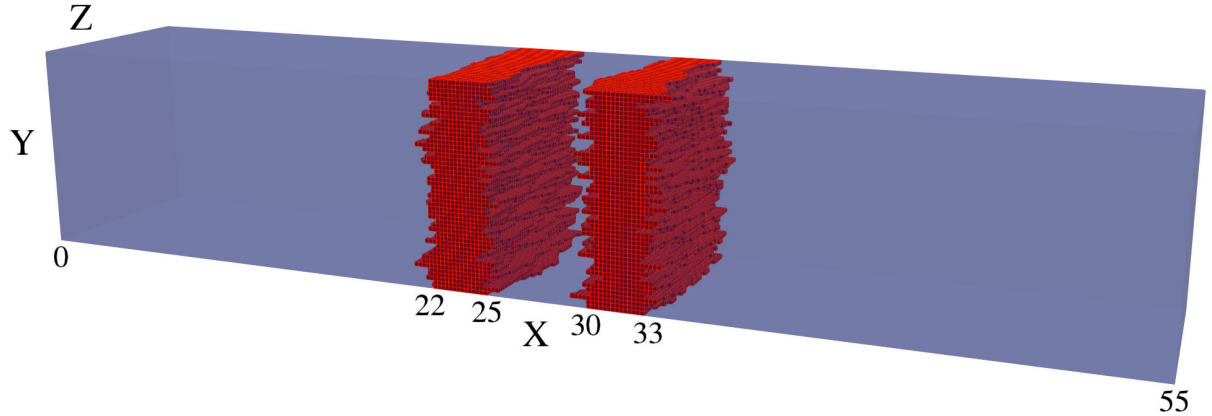


**Figure 2.8:** GaAs/Al<sub>0.3</sub>Ga<sub>0.7</sub>As RTD with IR (Interface Roughness) along the Al<sub>0.3</sub>Ga<sub>0.7</sub>As barriers [8], which has a correlation length of 2.5nm and an RMS (Root Mean Square) asperity of 0.3nm. The GaAs is a partially transparent blue volume to allow the visualisation of the IR on the red Al<sub>0.3</sub>Ga<sub>0.7</sub>As barriers. This figure [8] is licensed under CC BY 4.0.

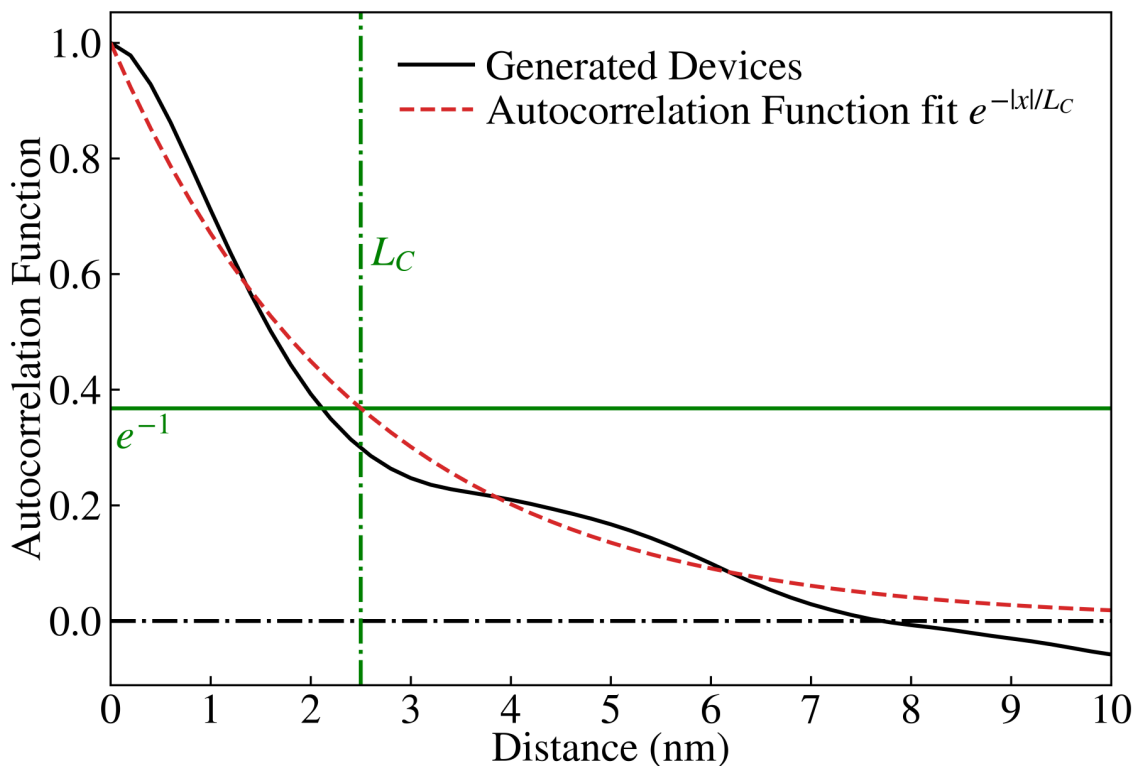


**Figure 2.9:** Average exponential autocorrelation function (black solid line) for 25 randomly generated RTDs, with IR (Interface Roughness) along all Al<sub>0.3</sub>Ga<sub>0.7</sub>As/GaAs interfaces [8]. An exponential autocorrelation function fit (red dashed line),  $e^{-|x|/L_C}$ , is plotted as well. This figure [8] is licensed under CC BY 4.0.

IR [199, 200] appears in heterostructure interfaces between two materials when manufacturing quantum devices like RTDs, hence it is important to include it in RTD simulations [104, 105]. RTDs are sensitive to such variations in device structure [105], such as QW thickness [103] and the two tunnelling barriers [101] which enclose the QW. Respectively, tunnelling probability through a barrier and the energy levels of a QW depend on these thicknesses. Multiple factors influence IR, including manufacturing process conditions [113, 114], and the mole fraction of Al for  $\text{Al}_x\text{Ga}_{1-x}\text{As}/\text{GaAs}$  [201]. IR also appears in RTDs composed of different materials [109–112], where similarly the manufacture process controls IR formation.

Previously only surface roughness was implemented in NESS [13], and IR is an extension of this. The IR functionality generates roughness along flat heterostructure interfaces normal to current flow, with a correlation length  $L_C$  and root-mean-square (RMS) asperity variation  $\Delta_{RMS}$  from this interface. To justify the implementation of IR for the  $\text{Al}_{0.3}\text{Ga}_{0.7}\text{As}/\text{GaAs}$  interface, I have analysed an AFM (atomic force microscopy) image of  $\text{Al}_{0.3}\text{Ga}_{0.7}\text{As}$  in Fig. 2.7. I was graciously provided the raw RGB colour AFM image corresponding to Figure 4(d) in [1]. This was converted into greyscale with the ITU-R 601-2 luma transform (which converts RGB colour values as  $L = R \times \frac{299}{1000} + G \times \frac{587}{1000} + B \times \frac{114}{1000}$ ) and sampled a central 400-by-400 pixel section, resulting in Fig. 2.7(a). For the image 205 pixel-lengths correspond to  $\sim 1\mu\text{m}$ , so the dimensions of Fig. 2.7(a) are roughly  $1.95\mu\text{m}$  by  $1.95\mu\text{m}$ . To extract height data  $z$  for each pixel, I rescaled the 8 greyscale shading distribution to have the provided RMS standard deviation of  $0.401\text{nm}$  for this image and centred this distribution on the mean of ‘0’. I then sampled the greyscale image in a line across the ‘x’ axis for each ‘y’ value, to calculate its autocorrelation function (ACF) for that ‘y’ value in the following equation 2.1.

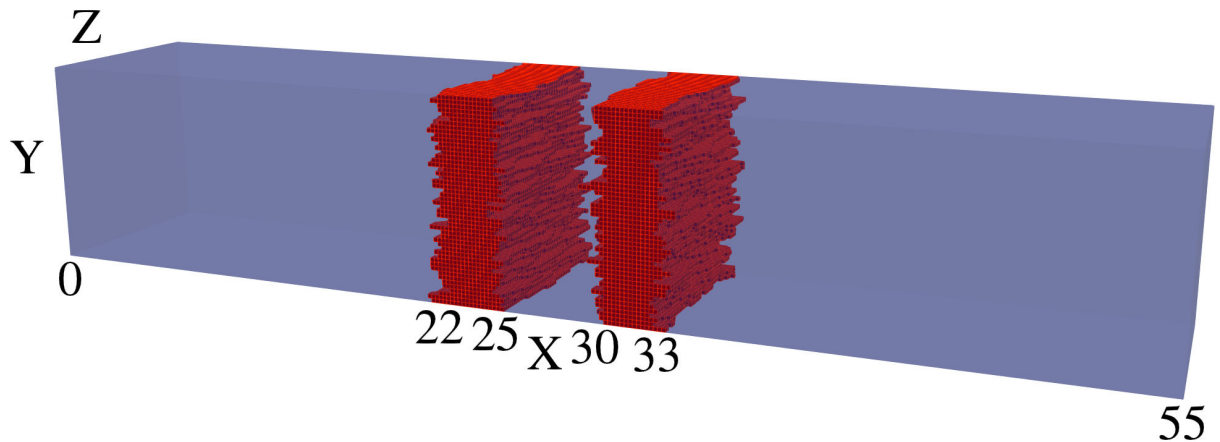
$$R(r = md) = \frac{\sigma^2}{N - m} \sum_{i=md}^{N-m} z_i \times z_{i+m} \quad (2.1)$$

In equation 2.1  $d$  is the pixel density of  $\sim 4.88\text{nm}$ ,  $N$  is the length of the line array (400 pixels), and  $r$  is the displacement between two points (separated by  $m$  pixels). The mean ACF for different ‘y’ values was then plotted in Fig. 2.7(b) as a black line. From Fig. 2.7(b), I fitted a vertical line for the correlation length  $L_C=22.6\text{nm}$  where the ACF drops to  $e^{-1}$ . Based around this correlation length I also fitted two commonly used ACF for simulating IR [202], the Gaussian correlation function  $e^{-(\frac{x}{L_C})^2}$  and the exponential correlation function  $e^{-|\frac{x}{L_C}|}$ , as blue and red dashed lines respectively. The exponential ACF in Fig. 2.7(b) visually appears to be a better fit, so this has been used for IR simulations going forward in this thesis. For  $\text{Al}_{0.3}\text{Ga}_{0.7}\text{As}/\text{GaAs}$  experimental [199] and simulation [200] papers RMS roughness height  $\Delta_{RMS}$  is roughly  $\sim 0.24\text{-}0.3\text{nm}$ , corresponding to the monolayer thickness [200]  $\sim 0.28\text{nm}$  of  $\text{Al}_{0.3}\text{Ga}_{0.7}\text{As}$  and GaAs, which itself is half the lattice constants of both [45]. With the isometric lattice spacing of  $0.2\text{nm}$  used in my RTD simulations, it seems appropriate to choose an RMS  $0.3\text{nm}$  because it is exactly 1.5 times this lattice spacing. This also fits in with the exploration of evenly spaced RMS asperity parameters (of  $0.1\text{nm}$ ,  $0.2\text{nm}$ ,  $0.3\text{nm}$ ,  $0.4\text{nm}$ ,  $0.5\text{nm}$ , and  $0.6\text{nm}$ ) in section 5.3, differing from each other by increments equal to half the lattice spacing of  $0.2\text{nm}$ . Hence, the default value of  $\Delta_{RMS}$  used going forward in chapter 4 is  $0.3\text{nm}$ .

Roughness, as originally implemented in NESS was parallel to the direction of current transport, the ‘x’ direction [13]. I extended this to work along flat heterostructure planes normal to the current direction, as seen in Fig. 2.8 where I defined IR with a correlation length of  $2.5\text{nm}$  and RMS of  $0.3\text{nm}$  at the interface between the  $\text{Al}_{0.3}\text{Ga}_{0.7}\text{As}$  barriers and the GaAs body.

To summarise briefly, the positions along this interface plane correspond to indexes of a correlated 1D list, where the value of the elements are the displacement of the preceding material from the chosen mean of the heterostructure interface plane at ‘x’. For example, if at a given point on the y-z interface at  $x=19\text{nm}$ , between a preceding GaAs region and the first  $\text{Al}_{0.3}\text{Ga}_{0.7}\text{As}$  barrier, the value is  $\Delta x=-0.3\text{nm}$  then the GaAs would end at  $x=18.8\text{nm}$  and  $\text{Al}_{0.3}\text{Ga}_{0.7}\text{As}$  would be shifted back by  $0.2\text{nm}$ . The mode of operation here

is that whichever cell volume  $x+\Delta x$  appears in for a given  $yz$  position is the position of the preceding material, which in this example is GaAs. An example for the average ACF for 25 RTDs (with all 4 planes of IR included) is given in Fig. 2.9, with a fitted exponential ACF as a red dashed line. NESS [13] generates this aforementioned correlated list by convolving [203, 204] a list of randomly generated numbers with either a Gaussian or exponential kernel, resulting in the corresponding Autocorrelation Function (ACF) with a specified correlation length  $L_C$ . Specifically, weights of  $e^{-\frac{|i|}{2L_C*c}}$  with a spacing correction factor  $c = \frac{1}{5\Delta s}$  (which is 1 for a spacing  $\Delta s$  of 0.2nm), are then normalised where used in the case of the exponential kernel. ACF plots for generated devices as demonstrated by Fig. 2.8 and other ACF plots in this subsection and chapter 5, confirm that this approach generates random exponential roughness described with the expected correlation length and RMS asperity.



55

**Figure 2.10:** Visualisation of a device generated with an IR (Interface Roughness) of correlation length  $L_C=2.5\text{nm}$  and an RMS (Root Mean Square) asperity of  $0.3\text{nm}$  [10], one of 25 such RTD devices. The rough  $\text{Al}_{0.3}\text{Ga}_{0.7}\text{As}$  barriers (shown in red) are embedded within a GaAs (transparent blue) nanowire body. This figure [10] is licensed under CC BY 4.0.

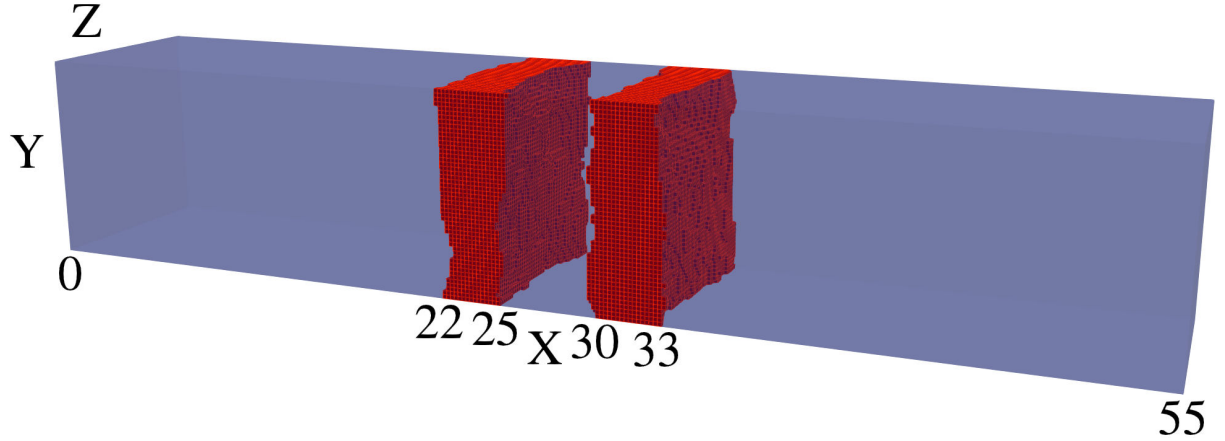


**Figure 2.11:** Visualisation of a device generated with ‘improved’ IR (Interface Roughness) of isotropic correlation lengths  $L_C^Y=L_C^Z=2.5\text{nm}$  and an RMS (Root Mean Square) asperity of  $0.3\text{nm}$  [10], one of 25 such RTD devices. The rough  $\text{Al}_{0.3}\text{Ga}_{0.7}\text{As}$  barriers (shown in red) are embedded within a GaAs (transparent blue) nanowire body. This figure [10] is licensed under CC BY 4.0.

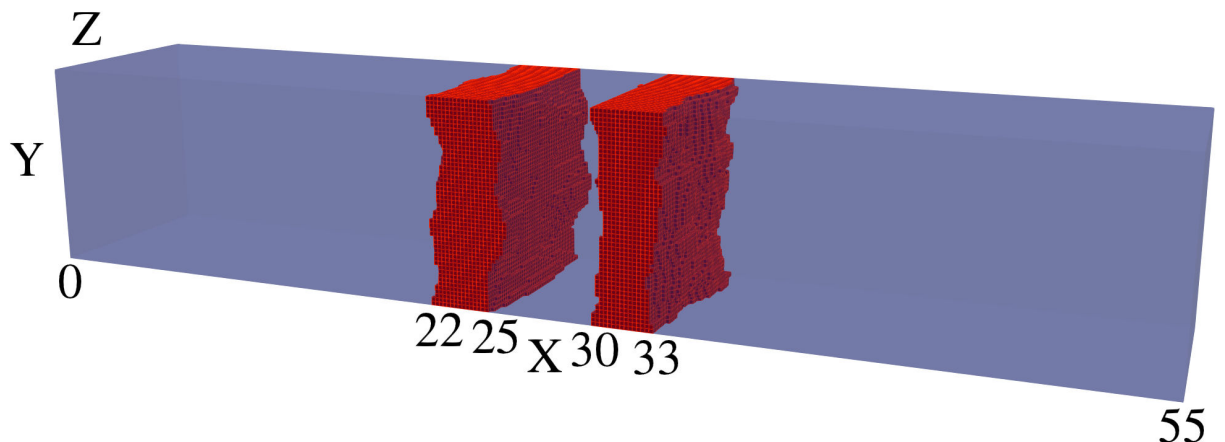


**Figure 2.12:** Visualisation of a device generated with ‘improved’ IR (Interface Roughness) of anisotropic correlation lengths  $L_C^Y=2.5\text{nm}$  and  $L_C^Z=5\text{nm}$  and an RMS (Root Mean Square) asperity of  $0.3\text{nm}$  [10], one of 25 such RTD devices. The rough  $\text{Al}_{0.3}\text{Ga}_{0.7}\text{As}$  barriers (shown in red) are embedded within a GaAs (transparent blue) nanowire body. This figure [10] is licensed under CC BY 4.0.

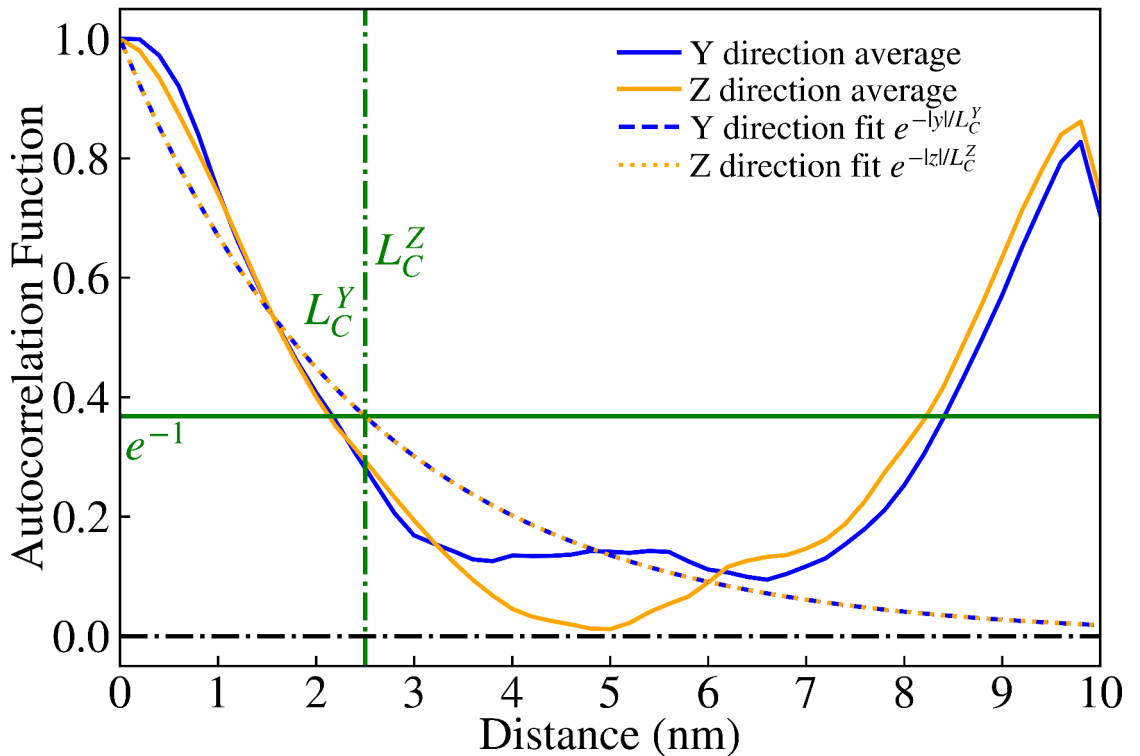


**Figure 2.13:** Average ACF (Autocorrelation Function) for GaAs/Al<sub>0.3</sub>Ga<sub>0.7</sub>As interfaces of 25 RTD devices generated with an ‘improved’ IR of isotropic correlation lengths  $L_C^Y=L_C^Z=2.5\text{nm}$  [10], plotted as solid blue and yellow lines for the Y and Z directions respectively. The exponential ACF [202] fits are given as dashed lines with the corresponding colours. This figure [10] is licensed under CC BY 4.0.

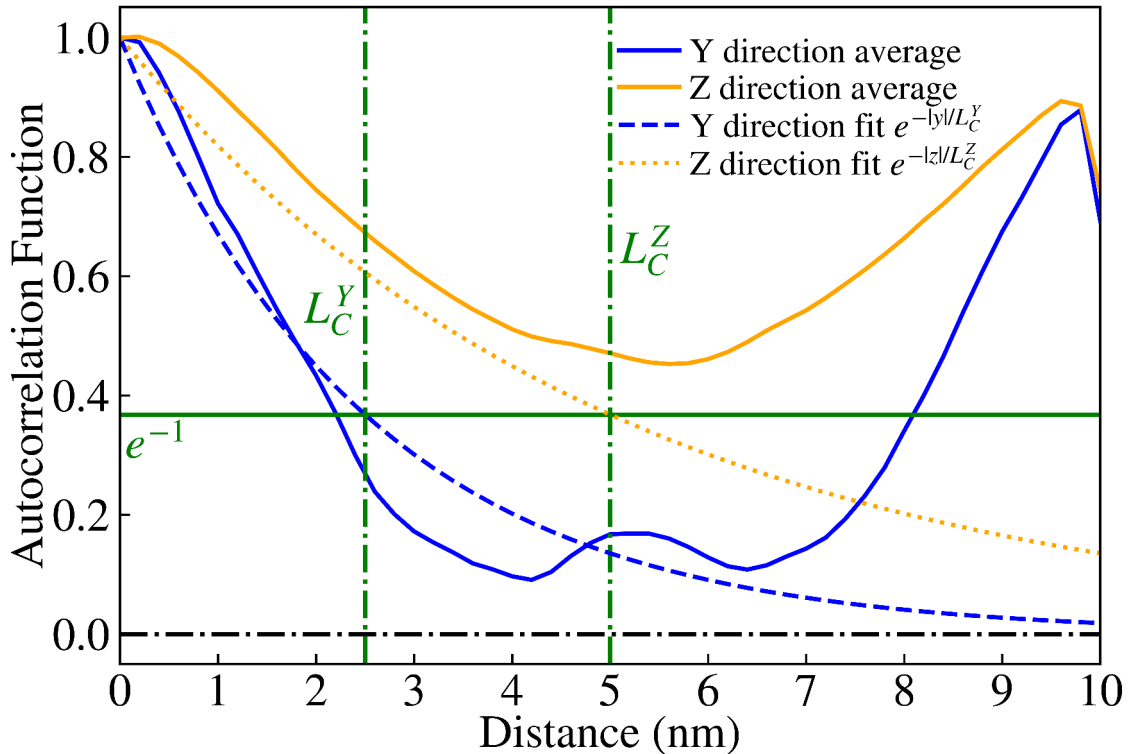


**Figure 2.14:** Average ACF (Autocorrelation Function) for GaAs/Al<sub>0.3</sub>Ga<sub>0.7</sub>As interfaces of 25 RTD devices generated with an ‘improved’ IR of anisotropic correlation lengths  $L_C^Y=2.5\text{ nm}$  and  $L_C^Z=5\text{ nm}$  [10], plotted as solid blue and yellow lines for the Y and Z directions respectively. The exponential ACF [202] fits are given as dashed lines with the corresponding colours. This figure [10] is licensed under CC BY 4.0.

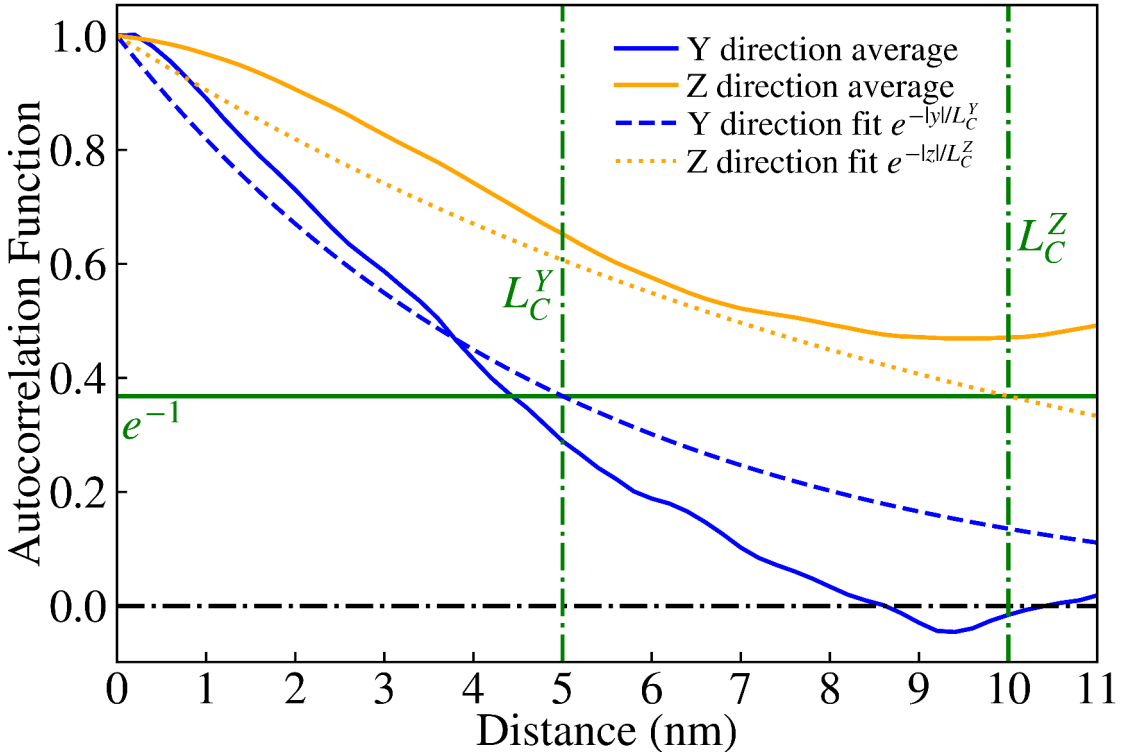


**Figure 2.15:** Average ACF (Autocorrelation Function) for GaAs/Al<sub>0.3</sub>Ga<sub>0.7</sub>As interfaces of 25 RTD devices generated with an ‘improved’ IR of anisotropic correlation lengths  $L_C^Y=5\text{nm}$  and  $L_C^Z=10\text{nm}$  and with a square cross-section of  $20\text{nm}\times20\text{nm}$  [10], plotted as solid blue and yellow lines for the Y and Z directions respectively. The exponential ACF [202] fits are given as dashed lines with the corresponding colours. This figure [10] is licensed under CC BY 4.0.

Another addition made during this PhD was to add a second correlation length. After some exploration, it was found that simply correlating in both directions after effectively transposing the equivalent matrix was an effective solution which fit the ACF for devices in Fig. 2.11 and Fig. 2.12 and corresponding ACF plots Fig. 2.13 and Fig. 2.14. As mentioned above in the previous implementation of roughness [9, 13], correlation was generated using a 1D randomly generated list, which was applied along one direction (the Y axis in this case) before incrementing along the other direction (the Z axis) and repeating the process. This resulted in devices like those shown in Fig. 2.10, with a correlation length of  $L_C=2.5\text{nm}$ . I have expanded on this approach by including another correlation parameter, allowing for correlation along both axes with their own correlation lengths  $L_C^Y$  and  $L_C^Z$ . The isotropic case of correlation lengths  $L_C^Y=L_C^Z=2.5\text{nm}$  creates devices such as Fig. 2.11,

and the anisotropic case of  $L_C^Y=2.5\text{nm}$  and  $L_C^Z=5\text{nm}$  creates devices such as Fig. 2.12. This correlation along both directions was achieved by taking the output from the correlated 1D list (with a kernel with a given  $L_C^Z$  already applied), effectively transposing so that the physical axes corresponding to each element ‘switches’, then applying correlation again (with a kernel for a given  $L_C^Y$ ). The unusual artefact of increased ACF in comparison to the ACF fit (dashed lines) past a correlation length of 5nm in Fig. 2.13 and Fig. 2.14 is due to the lack of data points for such a high correlation length. Indeed, when the width of the square cross-section of the RTD was increased to 20nm, which is twice that of 10nm, the ACF was observed to follow the fit for up to 10nm, as illustrated in Fig. 2.15. As explored in section 5.4, including two correlation lengths increases variation due to IR, which highlights both the strong influence of IR on RTD IV characteristics and the subsequent importance of including IR in simulations of heterostructure nanoelectronic devices like RTDs.

## 2.3 Poisson solver

NESS self-consistently uses a NEGF and Poisson solver [196]. After charge carrier concentration is calculated in NEGF, the Poisson equation can be solved to acquire the potential  $V$  as follows

$$\nabla \cdot (\epsilon \nabla V) = -q(p(\mathbf{r}) - n(\mathbf{r}) + N_D(\mathbf{r}) - N_A(\mathbf{r})) \quad (2.2)$$

Wherein  $N_D(\mathbf{r})$  and  $N_A(\mathbf{r})$  are respectively the donor and acceptor concentrations for location  $(\mathbf{r})$ , and  $q$  is the electron charge magnitude. This Poisson potential is then used in the NEGF charge and transport calculations, which then feed back into the Poisson solver. This loop occurs until the chosen convergence criteria are met, which in the case of this thesis is the error in absolute potential between iterations.

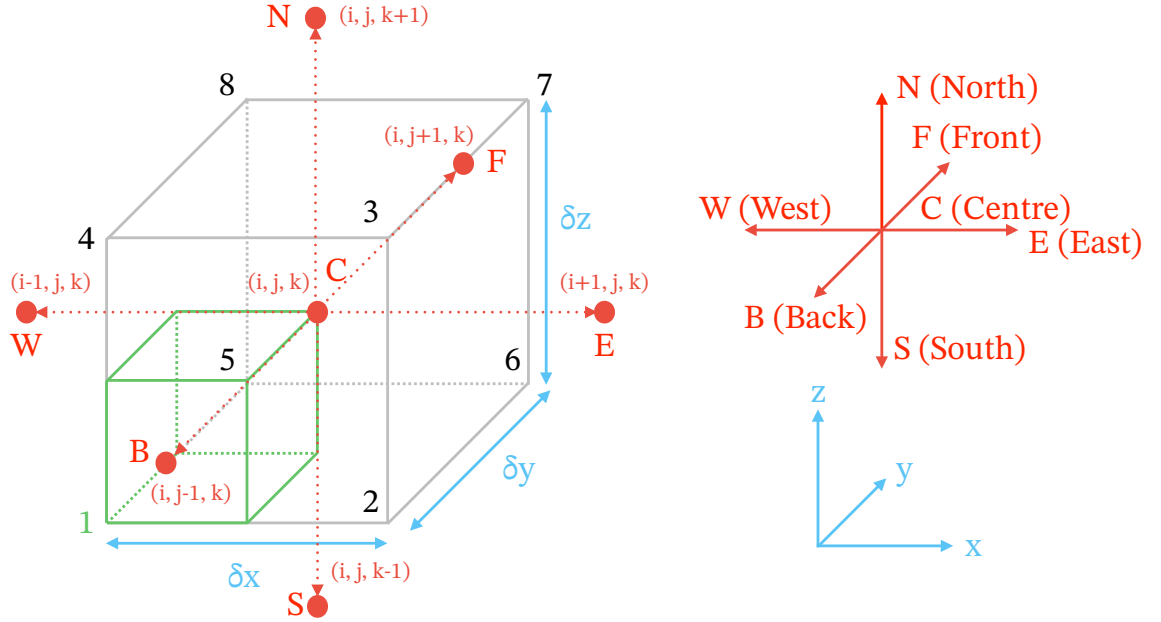


**Figure 2.16:** Diagram of node-centred control volume [205] (shown in grey) centred around a node ‘C’ at coordinate  $(i, j, k)$ , with a fractional control sub-volume associated with vertex 1 of this control volume (shown in green). Neighbouring real-space nodes are denoted by red circles and labelled according to the directions of the compass and ‘F’ for ‘front’ and ‘B’ for ‘back’.

The Poisson solver in NESS uses finite volume discretisation [196], specifically a node-centred control volume scheme [205], where each control-volume is centred on a node instead of coinciding with the mesh cells. Further details are noted in the appendix A1.

NESS makes use of the Newton-Raphson method [206] to iteratively solve a vector of electrostatic potential  $V$ , which is sped up using [207] the successive-over-relaxation (SOR) method [208, 209] with the Chebyshev acceleration method [210] used to determine the relaxation factor, and the red-black method of parallelisation [211]. Further details are given within the appendix A2.

## 2.4 Non-Equilibrium Green's Function (NEGF) Formalism

This section describes the NEGF formalism which is used within NESS [196] for the NEGF solver module.

As this NEGF module was not modified or a research focus of this thesis itself, derivations related to the NEGF formalism are listed within appendix A rather than being listed here. This is excluded for brevity's sake, but still kept within the appendix A to provide further reading for future readers, which is itself based on the following sources [196, 212–221].

### 2.4.1 Green's Functions

The NEGF formalism describes transport in nano-electronic devices through the language of Quantum-Field Theory, where particles are created and destroyed, and the eponymous Green's function is a correlation function which describes the evolution of particles. For instance, the Green's function  $G(\mathbf{r}, \mathbf{k}, t; \mathbf{r}', \mathbf{k}', t')$  is the probability amplitude that a particle created at position  $\mathbf{r}'$  with momentum  $\mathbf{k}'$  at time  $t'$ , will propagate to position  $\mathbf{r}$  with momenta  $\mathbf{k}$  at time  $t$  where it is annihilated. The lesser Green's function  $G^<$  describes electron correlation, and the greater Green's function  $G^>$  describes hole correlation. Corresponding lesser/greater self-energies  $\Sigma^{\leq}$  take into account the electron/hole interactions. This is why lesser/greater self-energies  $\Sigma^{\leq}$  are used to calculate electron/hole charge density [212], as well as the corresponding current.

Two other Green's functions which can also describe a nano-electronic device with contacts, and can be used to calculate  $G^{\leq}$ , are the retarded Green's function  $G^R$  and its self-adjoint, the advanced Green's function  $G^A = [G^R]^\dagger$ .  $G^R$  and  $G^A$  have corresponding self-energies  $\Sigma^R$  and  $\Sigma^A$ , which both have components for electron interactions with contacts and electron-phonon scattering.

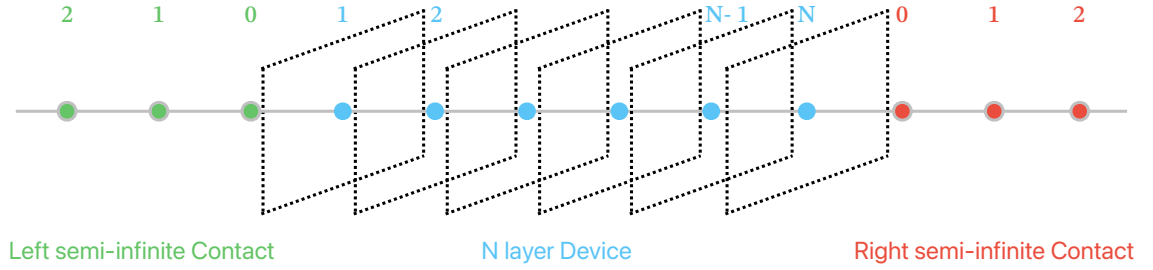


**Figure 2.17:** Layer representation of two-terminal device with  $N$  layers along the direction of current flow, and two semi-infinite contacts.

The NEGF solver in NESS treats devices as a layered structure, as seen in Figure 2.17. With this layered structure the one particle effective mass hamiltonian  $h$  can be represented with a block tridiagonal representation when discretised in NESS [196] as seen below in equation 2.3.

$$h(r) = \begin{pmatrix} h_{1,1} & h_{1,2} & 0 & \cdots & \cdots & \cdots & 0 \\ h_{2,1} & h_{2,2} & h_{2,3} & 0 & \cdots & \cdots & \vdots \\ 0 & h_{3,2} & h_{3,3} & h_{3,4} & 0 & \cdots & \vdots \\ \vdots & 0 & h_{4,3} & \ddots & \ddots & \ddots & \vdots \\ \vdots & \vdots & 0 & \ddots & \ddots & \ddots & \vdots \\ \vdots & \vdots & \vdots & \vdots & \ddots & \ddots & h_{N-1,N} \\ 0 & \cdots & \cdots & \cdots & 0 & h_{N,N-1} & h_{N,N} \end{pmatrix} \quad (2.3)$$

Note, each ‘block’  $h_{i,i}$  and  $h_{i,i+1}$  is a matrix of size  $N_y N_z \times N_y N_z$  representing respectively the transverse layer  $i$ , out of  $N_x$  layers, or coupling between layers  $i$  and  $i + 1$ . This is a common approximation for such layered structures [212], where off-diagonal elements in the matrix being zero represents vanishing coupling beyond nearest neighbour layers.

Using this single particle hamiltonian  $h$  and self-energy  $\Sigma^R$ ,  $G^R$  and  $G^A$  can be calculated as seen below.

$$G^R(E) = [(E + i\eta) \cdot \mathbb{I} - h - \Sigma^R(E)]^{-1} \quad (2.4)$$

$$G^A(E) = [G^R(E)]^\dagger \quad (2.5)$$

$$G^{\lessgtr}(E) = G^R(E) \cdot \Sigma^{\lessgtr}(E) \cdot G^A(E) \quad (2.6)$$

Here,  $E$  is the energy of the particle and  $\Sigma^R$  ( $\Sigma^{\lessgtr}$ ) is the leads’ retarded (lesser/greater) self-energy.  $\eta$  is an infinitesimal positive real number and  $\mathbb{I}$  is the identity matrix.

Self energy  $\Sigma$  can be split as  $\Sigma = \Sigma_C + \Sigma_S$ , into contact self energy  $\Sigma_C$  and scattering self energy  $\Sigma_S$ . The contact or lead self energies  $\Sigma_C$  take into account interactions with the contacts [196], which is further expanded in subsection 2.4.2. The scattering self energies  $\Sigma_S$  similarly take into account the scattering of particles, including the electron-phonon scattering which is briefly covered in subsection 2.4.4.

Similar to equation 2.3,  $G_{l+1,l}^<$  are the matrix elements between the basis states on layers  $l$  and  $l + 1$ , and only tridiagonal elements have to be calculated [196, 213, 214] under the assumption of tridiagonal hamiltonians and only local scattering in real space. This allows the use of an efficient recursive algorithm [218] to solve only tridiagonal elements within NESS, as explained in appendix A6.

The retarded Green's function  $G^R$  contains information about the allowed electronic states and hence can be used to calculate the spectral function  $A$ , the diagonal elements of which are the local density of states (LDOS)  $\rho$ , and the trace of which is the density of states  $N$ , as seen in the relations below [212].

$$A(\mathbf{r}, \mathbf{r}'; E) = i[G^R(\mathbf{r}, \mathbf{r}'; E) - G^A(\mathbf{r}, \mathbf{r}'; E)] \quad (2.7)$$

$$\rho(\mathbf{r}; E) = \frac{1}{2\pi} A(\mathbf{r}, \mathbf{r}; E) = -\frac{1}{\pi} \Im \{G^R(\mathbf{r}, \mathbf{r}; E)\} \quad (2.8)$$

$$N(E) = \text{Tr}[A(E)] \quad (2.9)$$

$$N(E) = \int d\mathbf{r} A(\mathbf{r}, \mathbf{r}; E) \quad (2.10)$$

The lesser/greater Green's functions which are calculated from the retarded (and advanced) Green's function and self-energies as shown in equation 2.6 contain information about particle statistics, and can consequently be used to calculate charge and current density as shown below in equations 2.11 and 2.12.

$$n(\mathbf{r}) = \frac{-i}{2\pi} \int dE (G^<(\mathbf{r}, \mathbf{r}; E)) \quad (2.11)$$

$$J_{l \rightarrow l+1}(E) = \frac{-2e}{\hbar} \int \frac{dE}{2\pi} \times 2\Re(\text{Tr}[h_{l,l+1} G_{l+1,l}^<(E)]) \quad (2.12)$$

Equation 2.11 can be explained as the correlation of electrons with themselves in real space,  $-i\hbar G^<(\mathbf{r}, t; \mathbf{r}, t)$ , which is integrated over energy in steady state conditions, as described in [212]. Equation 2.12 assumes the layered structure as seen in Figure 2.17. So equation 2.12 calculates current density  $J_{l \rightarrow l+1}(E)$  between layers  $l$  and  $l + 1$  can be calculated.

## 2.4.2 Contacts

NEGF can be used to split two terminal nanoelectronic devices into an active region of  $N$  layers composed of the device itself and two semi-infinite contacts [212] as seen in Fig. 2.17 which only affect layers ‘1’ and ‘ $N$ ’ of the device. As described in appendix A3, this allows us to derive a relation for the surface Green’s functions  $g_C^R$  for a contact  $C$ . For RTDs there are two contacts, as seen in Fig. 2.17; the left and right contacts. The surface Green’s functions [212] for a given contact are the elements of the Green’s function corresponding to the neighbouring contact layer 0 in Fig. 2.17 for that given contact.

The Sancho-Rubio iterative method [215], noted in appendix A4, can then be used to efficiently solve the surface Green’s functions, effectively by repeatedly halving the semi-infinite contact layers through  $i$  iterations until effectively  $2^i$  layers are included in layer 0 connected to the device itself.

This retarded contact self-energy  $\Sigma_C^R$  for a given contact can then be used to calculate the corresponding rate operator  $\Gamma_C$  with equation 2.13 [196, 216]. The lesser and greater contact self-energy for a contact  $C$  can then be calculated using the corresponding rate operator  $\Gamma_C$  and Fermi level  $\mu_C$ , in equations 2.14 and 2.15 respectively [216].

$$\Gamma_C(E) = i[\Sigma_C^R(E) - \Sigma_C^A(E)] \quad (2.13)$$

$$\Sigma_C^< = i\Gamma_C(E)f(E - \mu_C) \quad (2.14)$$

$$\Sigma_C^> = -i\Gamma_C(E)(1 - f(E - \mu_C)) \quad (2.15)$$

### 2.4.3 Coupled Mode Space Approximation

Another approximation NEGF can take, which NESS makes use of [196], is carrying out simulations in coupled mode space rather than real space, which will be explained in this subsection. A real space hamiltonian is composed of the transverse component  $h_T$  which describes the layers in Fig. 2.17, and the longitudinal component  $h_L$  which describes the coupling between them, as depicted below in equation 2.16.

$$h(x) = \underbrace{\left[ -\frac{\hbar^2}{2m_{y,z}^*} \Delta_{y,z} + V(r) \right]}_{h_T} - \underbrace{\frac{\hbar^2}{2m_{y,z}^*} \frac{\partial^2}{\partial x^2}}_{h_L} \quad (2.16)$$

In such a case, the transverse directions have either a closed or periodic boundary condition [212], which in the case of NESS is closed due a limited cross-section with finite width along both transverse dimensions.

Each slice is a 2D cross-section confined in both  $y$  and  $z$  dimensions represented by  $h_T$ , and its two-dimensional Schrödinger equation which can be solved to determine the eigenvalues and eigenmodes  $\phi_m(y, z; l)$  for each layer  $l$  corresponding to  $h_{l,l}$  in real-space. These eigenmodes  $\phi_m(y, z; l)$  form an orthogonal basis set of eigenvectors  $\phi_m(l) = [\phi_m(y_1, z_1; l) \cdots \phi_m(y_{N_y}, z_{N_z}; l)]$  for mode  $m$  and layer  $l$ . The eigenvectors  $\phi_m(l)$  hold the following properties [217]

$$h_{l,l}\phi_m(l) = E_m\phi_m(l) \quad (2.17)$$

$$\int dy dz \phi_n(y, z; l) \phi_m^*(y, z; l) = \delta_{n,m} \quad (2.18)$$

$$\sum_m \phi_n(y_1, z_1; l) \phi_m^*(y_2, z_2; l) = \delta(y_1 - y_2) \delta(z_1 - z_2) \quad (2.19)$$

For nanostructures with strong confinement along transverse directions, only a few modes  $N_m$  are needed to describe it [217] because only these lower energy eigenmodes are occupied, meaning that the computational cost can be greatly reduced.

These eigenvectors  $\phi_m(l)$  can be used to construct a block diagonal transform matrix  $U$  of size  $N_x N_y N_z \times N_x N_m$  as noted in [217], which converts the Hamiltonian and Green's functions into the Coupled Mode Space representation,

$$U = \begin{pmatrix} U_{1,1} & 0 & \cdots & \cdots & 0 \\ 0 & U_{2,2} & \cdots & \cdots & 0 \\ \vdots & \vdots & \ddots & \cdots & 0 \\ 0 & \cdots & \cdots & \cdots & U_{N_x,N_x} \end{pmatrix} \quad (2.20)$$

where the block diagonal components are  $U_{l,l} = [\phi_1(l) \cdots \phi_{N_m}(l)]$  of size  $N_y N_z \times N_m$ . So the relation  $H_m = U^\dagger H U$  is used to compress the dimensions from  $N_x N_y N_z \times N_x N_y N_z$  to  $N_x N_m \times N_x N_m$ , reducing the tridiagonal elements by a factor of roughly  $(\frac{N_y N_z}{N_m})^2$ . This lets us convert the non-zero tridiagonal elements in the real-space Hamiltonian  $h$  in equation 2.3 into the coupled mode space hamiltonian  $\tilde{h}$  with the following relations [196, 217].

$$\tilde{h}_{l,l} = U_{l,l}^\dagger h_{l,l} U_{l,l} \quad (2.21)$$

$$\tilde{h}_{l,l+1} = U_{l,l}^\dagger h_{l,l+1} U_{l+1,l+1} \quad (2.22)$$

For the elements of Green's functions, including retarded/advanced  $G^{R/A}$  and lesser/greater  $G^{\leq}$  Green's functions, the same relation holds. This means that for the Green's function matrix elements corresponding to modes  $n$  and  $m$  respectively on layers  $l$  and  $l' = l \pm 1$  can be calculated as seen below in equation 2.23 [196]

$$\tilde{G}(l, n; l', m; E) = \sum_{y,z} \sum_{y',z'} \phi_n^*(y, z, l) G(l, y, z; l', y', z'; E) \phi_m(y', z', l') \quad (2.23)$$

Then, these slices are coupled along the transport direction and the carrier transport is calculated using a 1D NEGF solver [196], implemented using the recursive Green's function algorithm [218], which is described in appendix A6.

As seen in this subsection the advantage of coupled mode space is that by describing the confined transverse states in terms of eigenstates rather than physical locations, the computational cost can be reduced while still taking into the device physics [212, 219]. The coupled mode space approximation can also reproduce behaviour caused by device variations like roughness and RDDs [196, 219].

#### 2.4.4 Electron-Phonon interactions

Electron-phonon interactions can be included in scattering self-energies, and solved self-consistently with the Green's functions using the self-consistent Born approximation (SCBA) in NESS [196]. NESS has currently implemented acoustic and optical electron-phonons interactions [196], with their self-energies assumed [196, 212, 213, 220] to be local in time and space. This makes such self-energies block diagonal [212, 220], allowing the use of the efficient recursive method [218] mentioned in appendix A6. A further explanation of this assumption is given in subsection 7.3 of the following textbook [212].

Though currently, optical phonons in polar materials like GaAs, which is a type III-V semiconductor alloy, have not been implemented in NESS yet, because of which I will not simulate optical phonon interactions within NESS for my thesis. Of these optical phonons in polar materials, longitudinal optical phonons lead to a secondary current peak in the RTD IV characteristics [158, 159, 163]. Thankfully for the purposes of studying the impact of variation in this thesis, the main value of interest is the resonant current peak while longitudinal optical phonon phonons create secondary phonon peaks for biases greater than this.

The implementation of electron-phonon scattering self-energies in NESS is described within appendix A5, which is based on the explanation within a paper describing NESS [196]. To summarise, acoustic and optical coupling constants [196, 213, 221, 222] are used to calculate lesser/greater electron-phonon scattering self energies, which can also be calculated in coupled mode space, and can be converted into retarded self energy with the relation in equation 2.24 below.

$$\Sigma^R = \frac{1}{2}[\Sigma^<(\mathbf{r}; E) - \Sigma^>(\mathbf{r}; E)] \quad (2.24)$$

$$\Sigma^R = \Sigma_C^R + \Sigma_S^R \quad (2.25)$$

$$\Sigma^{\leqslant} = \Sigma_C^{\leqslant} + \Sigma_S^{\leqslant} \quad (2.26)$$

As also noted in subsection 2.4.1,  $\Sigma = \Sigma_C + \Sigma_S$  which can be specified for  $\Sigma^R$  and  $\Sigma^{\leqslant}$  in equations 2.25 and 2.26 respectively.

Within NESS [214], the SCBA [213, 214] implements a self-consistent solving of the Green's functions in equations 2.4, 2.5, and 2.6 and the self-energies in equations 2.24, 2.25, and 2.26. The self-consistency here refers to how they influence one another [212].

## 2.5 Resonant Tunnelling Diode

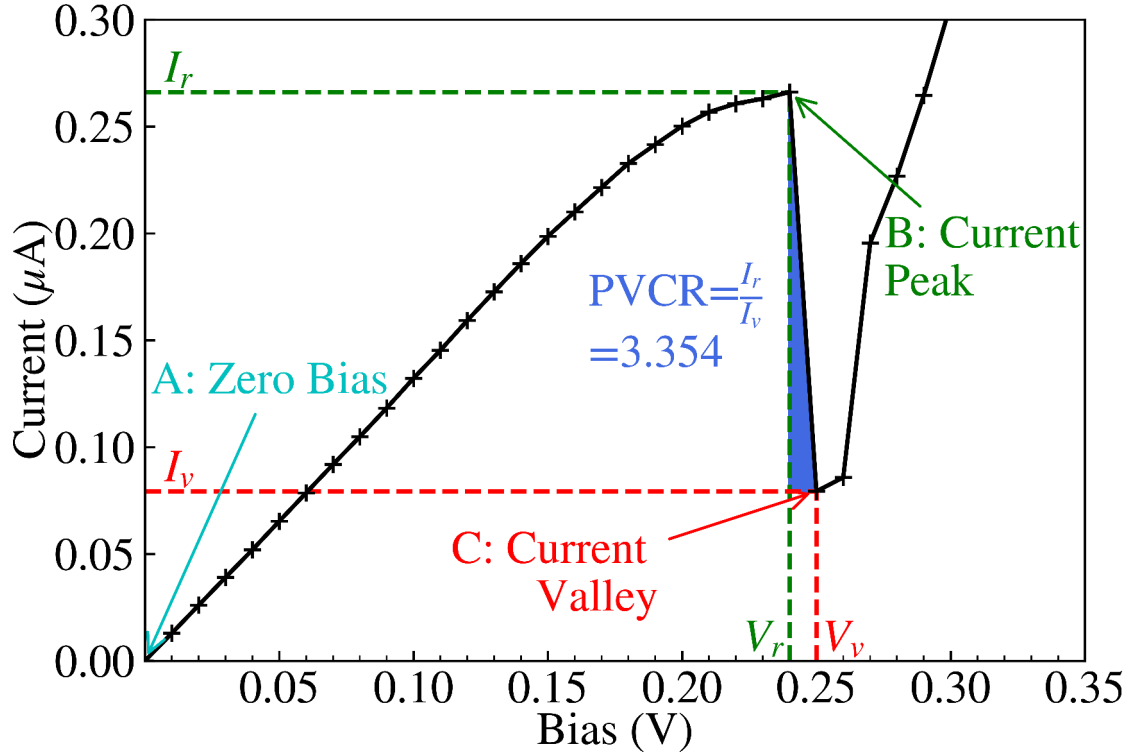


**Figure 2.18:** IV characteristic of a smooth RTD [10], such as the one visualised in Fig. 2.4, which is simulated in the ballistic regime. Key points of the IV characteristic are annotated, and the NDR (Negative Differential Resistance) region is shaded blue. This figure [10] is licensed under CC BY 4.0.

## RTD with 6th Mode Visualised

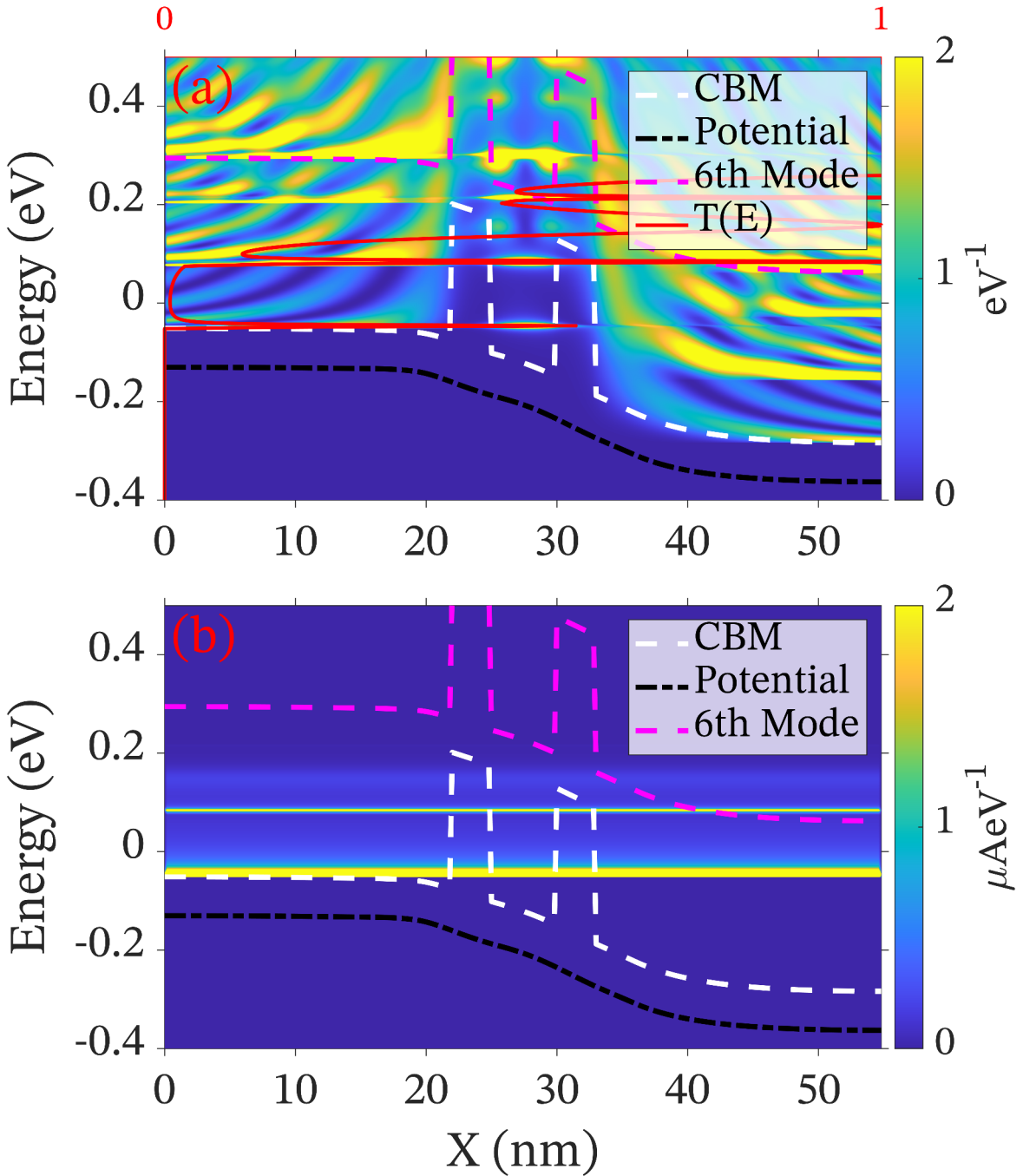


**Figure 2.19:** LDOS (Local Density of States) and CS (Current Spectra) for a smooth RTD, as shown in Fig. 2.4 along the x-axis, corresponding to the resonant current peak for the bias  $V_r = 0.24\text{V}$  in Fig. 2.18. Figure(a) is the LDOS and in units of  $\text{eV}^{-1}$ , wherein the red line along the y-axis is energy dependent transmission  $T(E)$ , and figure(b) is the CS and in units of  $\mu\text{AeV}^{-1}$ . For both subfigures, the black dashed line is the electrostatic potential energy, the white dashed line is the CBM (Conductance Band Minima), and the magenta dashed line is the energy corresponding to the 6th mode used for coupled mode simulations.

For this thesis, 6 modes in coupled mode space have been used. This can be visualised by plotting a magenta dashed line for the energy corresponding to the sixth mode in Fig. 2.19, which are the LDOS and CS for the resonant peak for the baseline RTD without device variation shown in Fig. 2.4. For reference, the first mode corresponds with the CBM.

For this thesis, the energy mesh has energy steps of 1meV. For two terminal devices like RTDs, NESS defines the energy range with regards to the Fermi levels at the source and drain contacts,  $E_{F,S}$  and  $E_{F,D}$  respectively. For this thesis, the minimum energy is chosen as 0.3eV, so  $E_{\min} = E_{F,D} - 0.3\text{eV}$ , and the maximum energy is chosen as 0.5eV, so  $E_{\max} = E_{F,S} + 0.5\text{eV}$ . Within this thesis, including LDOS and CS (Current Spectra) plots, ‘zero’ energy is a reference set as the Fermi level of the source contact  $E_{F,S}$ .

As apparent in Fig. 2.4, the drain-source bias is applied over the central 17nm of the RTD including the 3nm spacers, 3nm barriers, and 5nm QW. If the thickness of these sections within central device region changes, then the length over which the bias is applied scales with the dimensions of these sections, as seen in chapter 3.

Device material parameters are taken from [45], and electron-phonon scattering parameters for  $\text{Al}_{0.3}\text{Ga}_{0.7}\text{As}$  were obtained through linear interpolation [223] from AlAs and GaAs parameters from [224] as  $X_{\text{Al}_{0.3}\text{Ga}_{0.7}\text{As}} = 0.3X_{\text{AlAs}} + 0.7X_{\text{GaAs}}$ .

An issue with RTD simulations with NESS was that the expected non-differential conductance didn’t appear for simulations when using bulk values for  $\text{Al}_{0.3}\text{Ga}_{0.7}\text{As}$  and GaAs. I investigated why this happened by varying parameters and checking the NESS code. The issue turned out to be that NESS currently does not exhibit quantum tunnelling across a heterojunction when the density of states on either side is unequal. NESS uses an effective mass approximation, and the bulk effective masses [45] for  $\text{Al}_{0.3}\text{Ga}_{0.7}\text{As}$  and GaAs are different, which has lead to this situation. A current workaround for this is using the same electron effective masses for both materials in the RTD, which is the mean of the

$\Gamma$  effective masses for both materials (the  $\Gamma$  valley is the lowest valley of the conductance band for GaAs and  $\text{Al}_{0.3}\text{Ga}_{0.7}\text{As}$  [45]). I believe this approximation is valid because as a nanometre-scale device the effective masses used are not the same as bulk devices. This approximation was supported by a comparison with the NEMO 1D RTD NEGF simulator [225] as shown in Fig. 2.20.

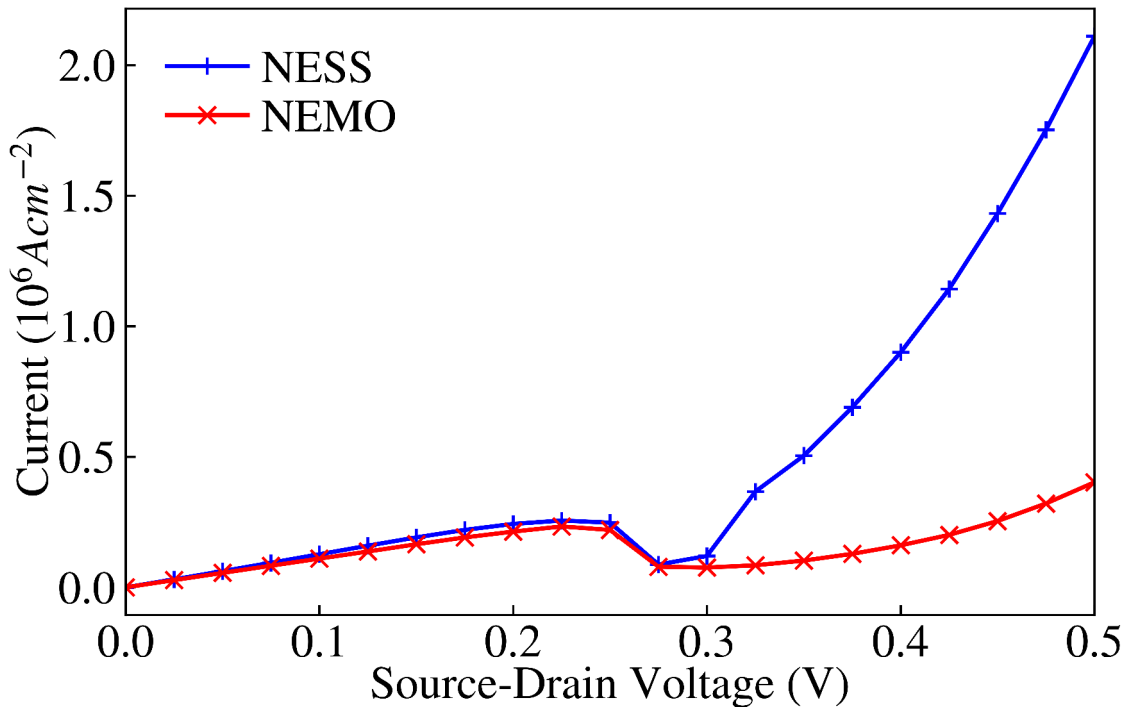


**Figure 2.20:** RTD current-voltage curve for NESS (blue line with plus markers) compared with the 1D RTD NEGF simulator [225] powered by NEMO5 and based on NEMO 1-D (red line with diagonal cross markers). The current-voltage curves match up until the current valley, whereafter the equal effective mass approximation has led to increased transmission between the source and QW for NESS.

The simulation showcase [225] in particular was powered by NEMO5 [226], which is also licenced commercially as ‘Victory Atomistic’ [227] by Silvaco, and used a tight-binding Hamiltonian and single band physics as described in the following paper [228], unlike the atomistic NESS. The PVCR for both curves in Fig. 2.20 are similar, with 2.92 for the NEMO simulation and 3.07 for NESS. Though, it does seem that the NESS simulation leads to higher current after the NDR, which is likely due to the approximation taken.

This approximation likely meant that the conductance band density of states between the source and QW was higher than expected, causing greater current after the NDR. Fortunately for RTD applications the key region is the NDR, and not the second region of increasing current, which was simulated with the expected behaviour by NESS. This validates that NESS reproduces the quantum tunnelling based phenomena of resonant tunnelling and provides grounding for further simulations. This does however mean current values after the resonant valley cannot be studied. The NEGF models in NESS are furthermore verified with the atomistic tool OMEN [229]. I equated the simulation parameters as far as possible for the given comparison. For the NEMO simulation I chose the option to use the Hartree approximation, which is solved self consistently with NEGF to capture the quantum character of charge, like confinement of charge in the QW, according to their manual [225]. To compare with NESS with NEGF-Poisson self-consistent loops, naturally a method which treats charge as being quantum rather than semi-classical is more accurate and appropriate. I set up the same length and doping for regions as noted above and used  $\text{Al}_{0.3}\text{Ga}_{0.7}\text{As}$  barriers. I also equated Poisson error for the simulation at 1meV, used an energy discretisation of 1meV, and an energy range of 0.3eV below the source Fermi level to 0.5eV above the Fermi level. For the NESS simulation, I used the same conduction band-edge offset between GaAs and  $\text{Al}_{0.3}\text{Ga}_{0.7}\text{As}$  of 0.2779eV which the NEMO had set as constant. I also set the NESS effective electron masses as the mean of the NEMO effective electron masses for GaAs and  $\text{Al}_{0.3}\text{Ga}_{0.7}\text{As}$ ,  $m_e^* = \frac{0.067+0.0919}{2} = 0.07945m_0$  compared to the free electron mass  $m_0$ . Further details of the NEMO simulation are given in their supporting documents [225], including a user manual and a video demonstration.

For simulations explained within this thesis, energy mesh is discretised by steps of 1meV, and the 3D spatial mesh used is isotropic in all directions and the spacing is 0.2nm. The temperature of the device simulations is 300K.

A specific limitation faced in carrying out device simulations was that the simulations were run on a shared computing cluster. To manage this shared computing cluster, administrators would sometimes kill long-running jobs when loads got too high, and issued complaints when there were too many of such jobs. To avoid such scenarios, convergence loop limits were necessary. This unfortunately lead to some devices not converging within the convergence loop limits, but was necessary for shared usage of finite computing resources.

Within this thesis, NEGF-Poisson convergence is chosen to be checked with an absolute difference in potential between the latest and current NEGF-Poisson iterations. To exit the loop, this absolute difference needs to be less than or equal to the error criterion chosen, while the number of loops so far has not overstepped the maximum number of iterations specified. For this thesis, the error criterion was chosen to be 1meV, though differing maximum numbers of convergence loops were chosen depending on the availability of computing resources at the time.

Within the Poisson solver, iterations are carried out until the difference between iterations in potential is less than the chosen Poisson error, with a default maximum of 100000 Poisson iterations. For this thesis, the convergence criteria was chosen as  $1 \times 10^{-5}$ eV.

The following chapters 3, 4, and 5 use the methods and theory expanded within this section and chapter to investigate RTDs with device variation.

# Chapter 3

## Design of Experiment

### 3.1 Introduction

This chapter is based on material from my first author paper [8], and is a variation study of double barrier RTDs which investigates thickness variation of the barriers and the QW. Regarding device dimension variation, while there has been previous research [61, 230–232], this study is a more comprehensive study of barrier and QW thickness variation. This includes both the symmetric variation, of both barriers and the QW, and asymmetric variation of both barriers [230].

A brief methodology section 3.2 is followed by the results section 3.3. Firstly within the results section 3.3, the baseline device is demonstrated in subsection 3.3.1, along with an explanation of the impact of including acoustic electron-phonon scattering in subsubsection 3.3.1.2. Symmetric and asymmetric device variation for the thicknesses of barriers and QW is explored in subsection 3.3.2 and subsection 3.3.3 respectively. Concluding this chapter, the observed behaviour is summarised in the conclusion section 3.4. These observations are referred to later in section 5.2 within chapter 5 to describe the influence of IR along different GaAs/Al<sub>0.3</sub>Ga<sub>0.7</sub>As interfaces in terms of such device variation.

## 3.2 Methodology

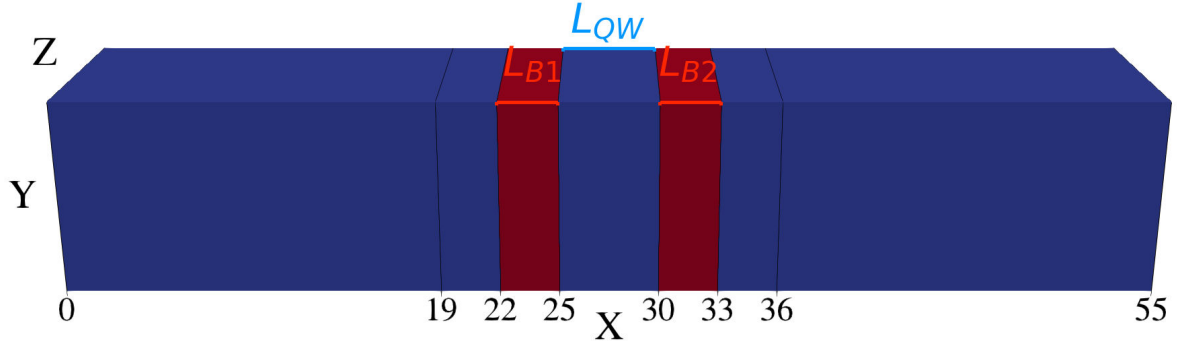


**Figure 3.1:** A schematic illustration of the baseline GaAs-Al<sub>0.3</sub>Ga<sub>0.7</sub>As RTD device [8] with symmetric barrier widths  $L_{B1}=L_{B2}=3\text{nm}$  and QW width  $L_{QW}=5\text{nm}$ . The GaAs body is coloured blue and the Al<sub>0.3</sub>Ga<sub>0.7</sub>As barriers are red. The cross-section is  $10\text{nm}\times10\text{nm}$ , with an overall length of 55nm for this baseline case. The 19nm thick source-drain regions are  $2\times10^{18}\text{cm}^{-3}$  n-doped. The central 17nm region for the baseline case, including two 3nm spacers enclosing the barriers, is  $1\times10^{15}\text{cm}^{-3}$  n-doped. This figure [8] is licensed under CC BY 4.0.

The baseline RTD as shown in Fig. 3.1 follows the simulation parameters noted in section 2.5, with other details noted here. Acoustic electron-phonon scattering is included, with the effects explored in subsubsection 3.3.1.2. A maximum of 25 NEGF-Poisson convergence loops are allowed in the case with electron-phonon interactions, due to the long times such tasks took with the acoustic plot in Fig 3.5 taking 22917.6 minutes or  $\sim 15.9$  days of computational time on 8 cores from an AMD EPYC 7401 24-Core Processor node.

In subsection 3.3.2 and subsection 3.3.3 barrier or QW thicknesses are varied by increments of 1nm, but otherwise the same simulation parameters hold.

### 3.3 Results and Discussion

In this section, I first investigate the baseline RTD with 3nm symmetric barriers and a 5nm QW in subsection 3.3.1, and investigate the effects of acoustic electron-phonon scattering in subsubsection 3.3.1.2. In subsection 3.3.2 I symmetrically vary barrier thicknesses  $L_{B1}=L_{B2}$  to 2nm and 4nm and vary QW width  $L_{QW}$  to 4nm and 6nm. For subsection 3.3.3 I asymmetrically vary each barrier to 2nm and 4nm whilst keeping the other barrier at 3nm. Of the ‘smooth’ devices studied I also found that the baseline RTD had the maximal PVCR. The PVCR is the ratio of current between the resonant peak and valley  $I_r/I_v$ , and is a key figure of merit for RTDs.

### 3.3.1 Baseline Device

#### 3.3.1.1 Baseline Device Behaviour

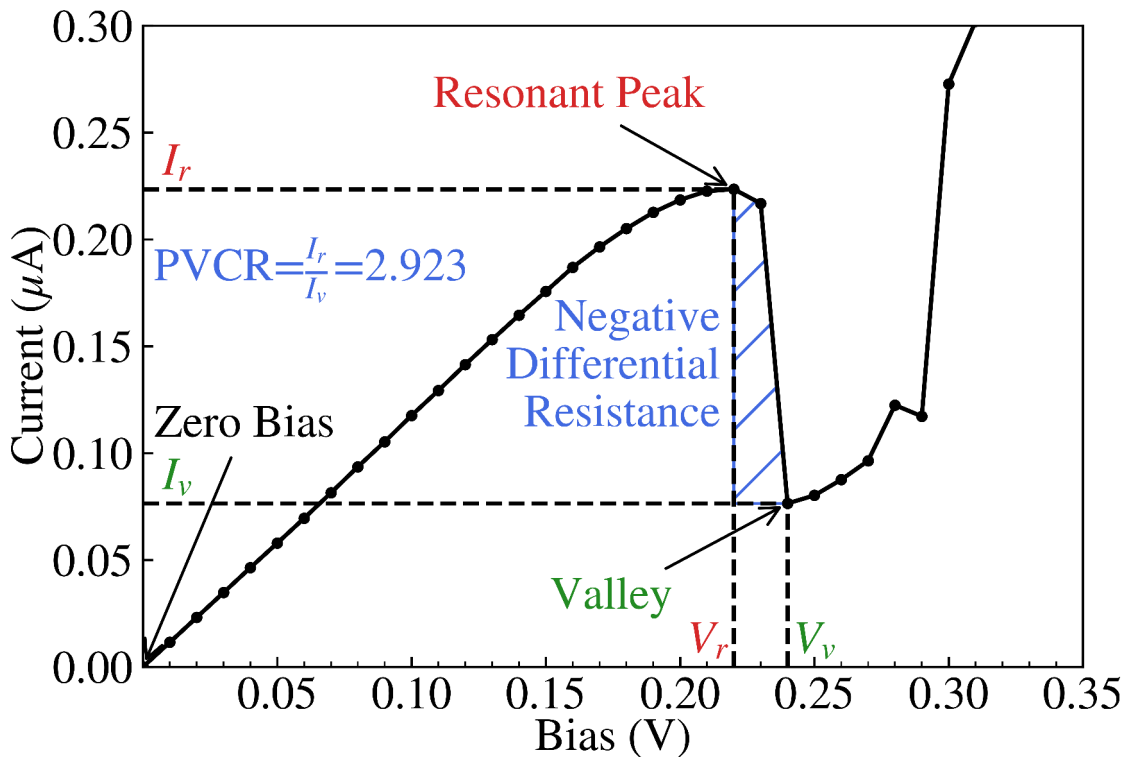


**Figure 3.2:** IV characteristic for the baseline RTD [8] shown in Fig. 3.1. The resonant peak, or local maximum in current  $I_r$  at bias  $V_r$ , and the valley, the local minima  $I_v$  at  $V_v$ , are two key points for this nonlinear IV characteristic. These bound the NDR, and define the figure of merit PVCR  $I_r/I_v$ . Fig. 3.3(a), Fig. 3.3(b) and Fig. 3.4 are measured for the resonant peak in this figure. Similarly, Fig. 3.3(c) and Fig. 3.3(d) correspond to the valley. This IV characteristic includes electron-phonon scattering. This figure [8] is licensed under CC BY 4.0.

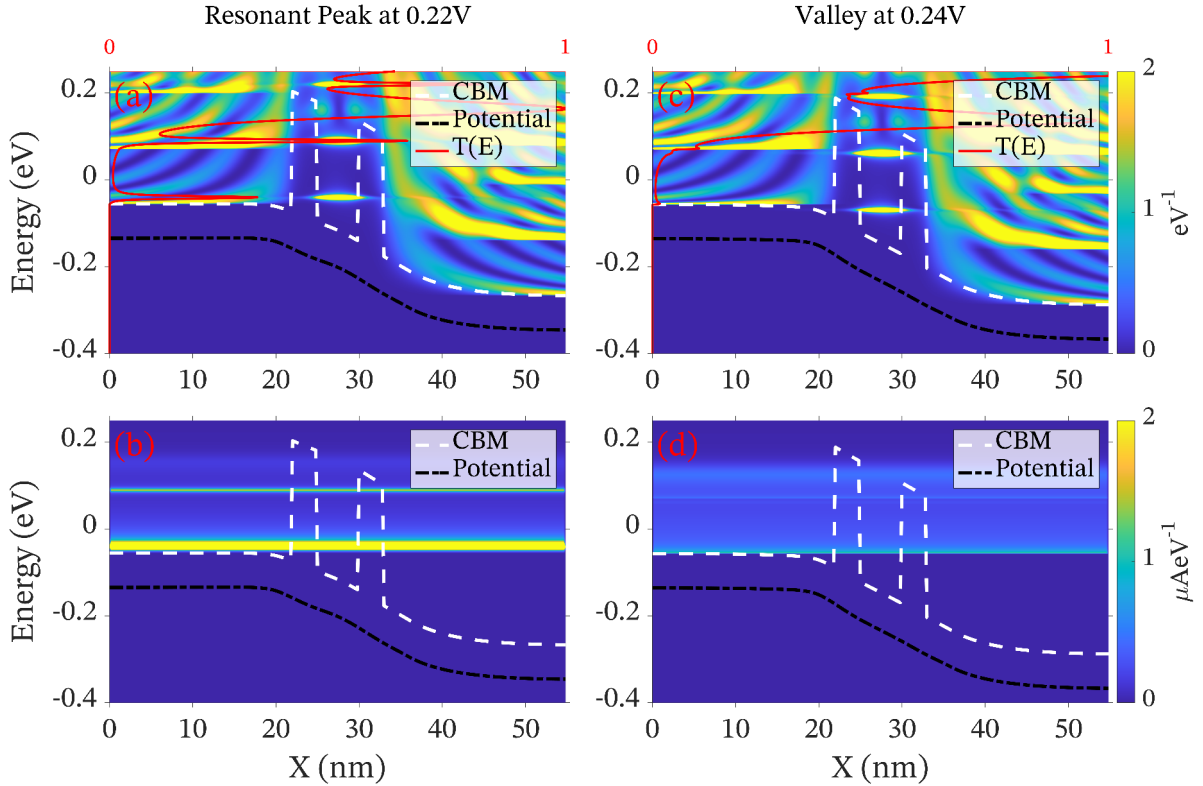


**Figure 3.3:** Figure(a) depicts the LDOS (Local Density of States), with colourbar units of  $\text{eV}^{-1}$ , and energy dependent transmission  $T(E)$ , a red vertical line, for the resonant peak at 0.22V shown in Fig. 3.2. Figure(b) is the CS (Current Spectra), with colourbar units of  $\mu\text{AeV}^{-1}$ , for this resonant peak. Similarly, figure(c) and figure(d) respectively represent the LDOS and CS for the valley at 0.24V. The white dashed lines are the CBM (Conductance Band Minima), and the black dash-dot lines are the average potential energy. This figure is reproduced based on Figure 6 from [8], which is licensed under CC BY 4.0.

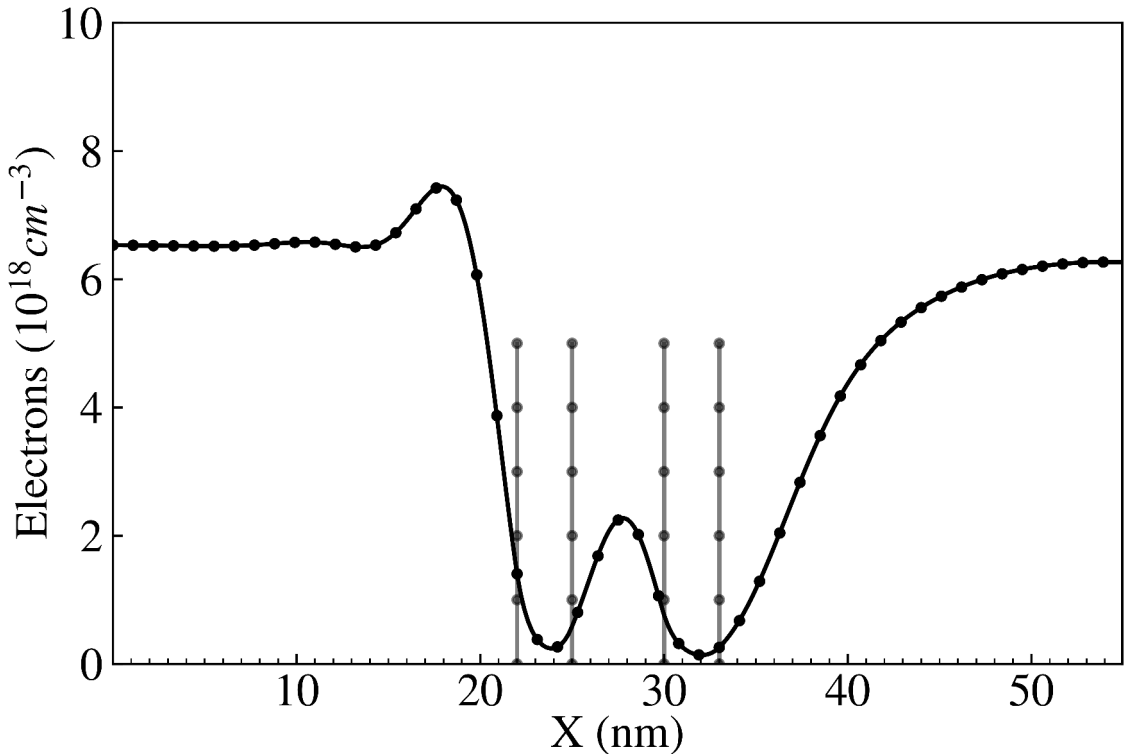


**Figure 3.4:** Line plot of electron charge density through the centre of the baseline RTD depicted in Fig. 3.1 for the resonant peak 0.22V seen in Fig. 3.2. Barrier interface positions are noted with slightly transparent vertical lines with corresponding markers. This figure is reproduced based on Figure 7 from [8], which is licensed under CC BY 4.0.

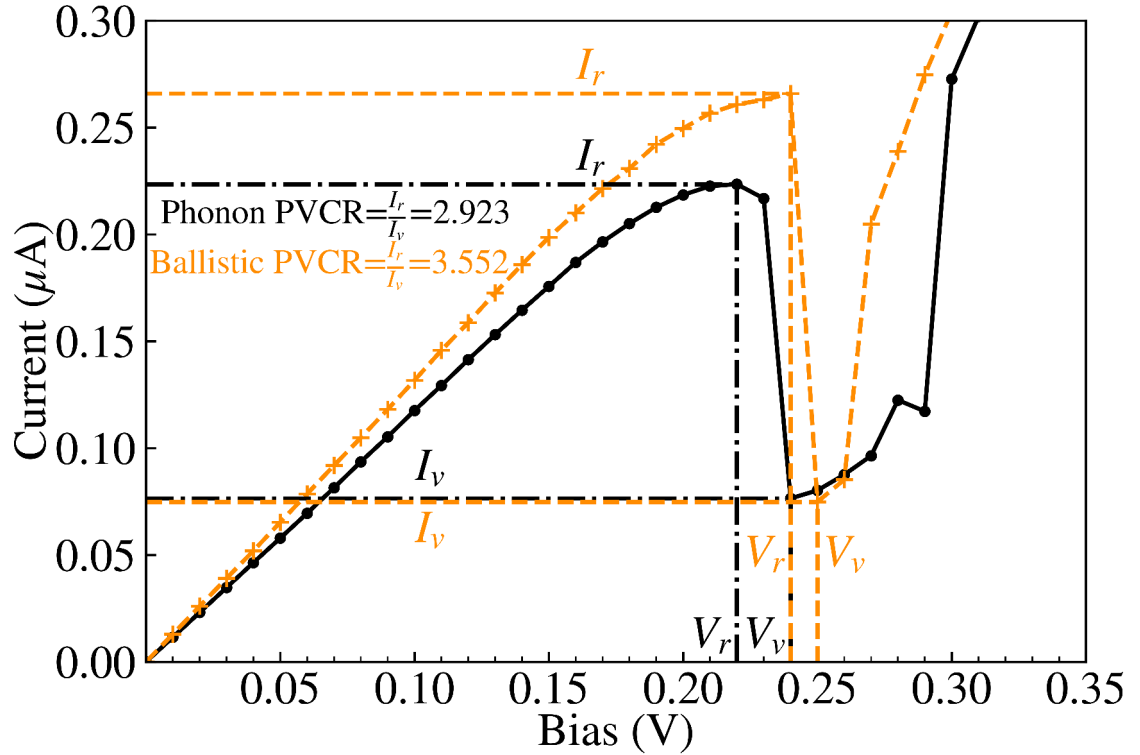
The baseline 55nm long RTD shown in Fig. 3.1 results in the IV characteristic Fig. 3.2, and the corresponding LDOS (Local Density of States) and CS (Current Spectra) graphs for the resonant peak at 0.22V and valley at 0.24V depicted in Fig. 3.3. The  $\text{Al}_{0.3}\text{Ga}_{0.7}\text{As}$  barriers raise the CBM (Conductance Band Minima) with respect to the GaAs body, which is depicted as white dashed lines in Fig. 3.3, and bounds a GaAs QW.

The nonlinear IV characteristic of RTDs, with a NDR (Negative Differential Resistance) of conductance between the resonant peak and valley in Fig. 3.2, is due to current for such biases in RTDs being dominated by resonant tunnelling, which reaches a local maximum at the resonant peak bias  $V_r$ . Resonant tunnelling in RTDs is the quantum tunnelling of electrons from the emitter region into the QW and back out again, and hence largely

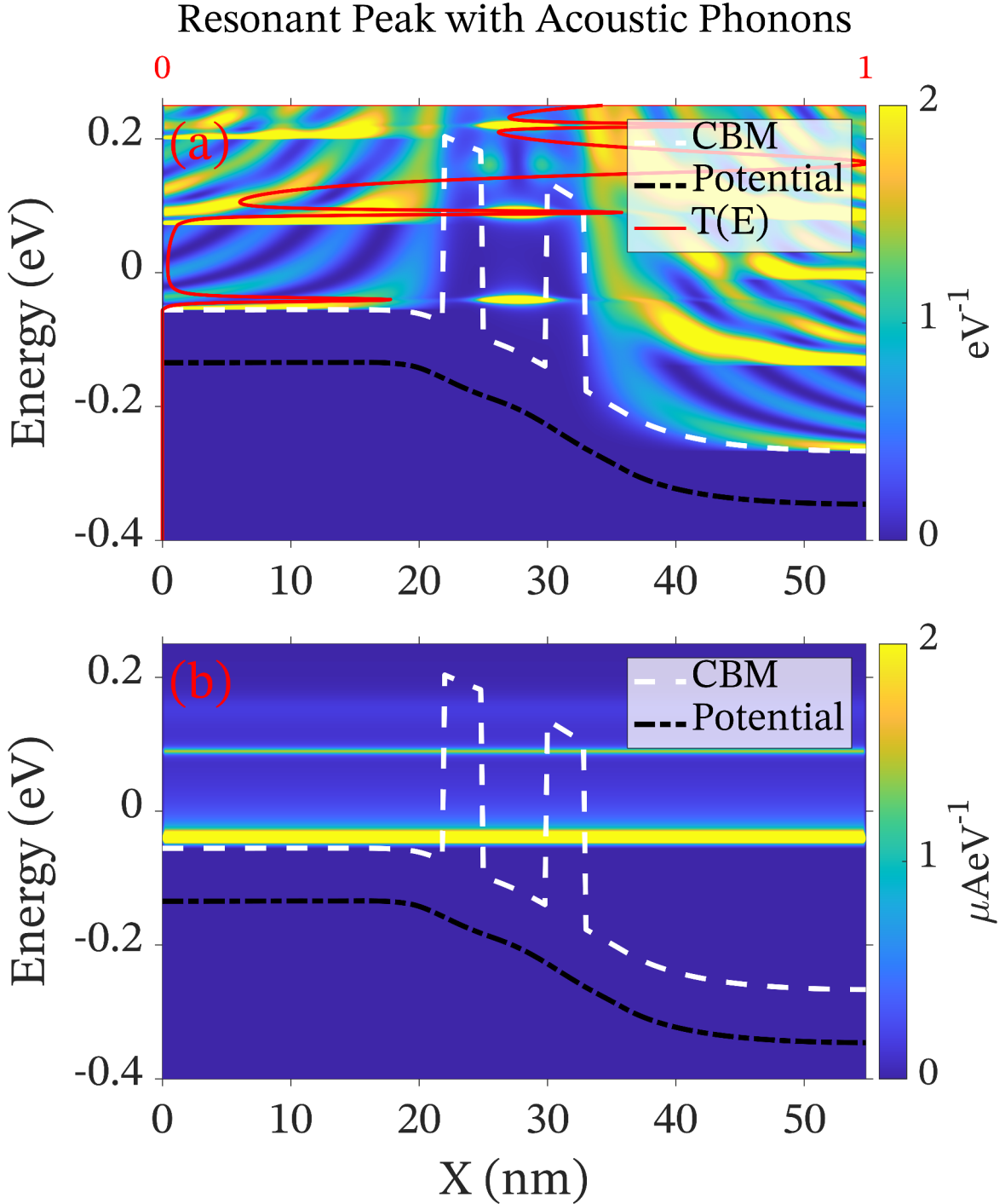
depends on the alignment of LDOS between the emitter and QW. The conservation of transverse momenta during tunnelling works to exclude states that are not aligned in reciprocal space. The LDOS for the resonant peak at  $V_r=0.22V$ , Fig. 3.3(a), has the ground QW eigenvalue aligned with the emitter Fermi level, which leads the energy dependent transmission function  $T(E)$  (red line) to reach a local maximum for this energy. The resulting CS for the resonant peak in Fig. 3.3(b) depicts a strong band of current through the ground QW and a smaller current channel through the first excited QW eigenvalue. With the increase of bias to the valley at  $V_v=0.24V$ , the ground QW LDOS in Fig. 3.3(c) is perturbed below the CBM on the source and thus the emitter-side LDOS, suppressing transmission and the CS bands shown in Fig. 3.3(d). The PVCR in this case is 2.923. For bias greater than the valley, thermionic emission of electrons over the barrier begins to dominate.

Fig. 3.4 is a lineplot of electron charge density through the centre of the RTD, for the resonant peak  $V_r=0.22V$  corresponding to Fig. 3.2. Fig. 3.4 has local maxima where charge accumulates in the emitter region, where a triangular QW forms as seen in Fig. 3.3, and the QW. Charge in the QW results in the space-charge effect [14], which is responsible for the ‘N’ shape of the IV characteristics in Fig. 3.2. This is because when current is greater, any charge within the QW at a given moment is greater, resulting in greater Coulomb repulsion caused by this QW charge. The repulsion causes a positive perturbation in the potential profile of the RTD which needs to be overcome with greater bias. Consequently, points of higher current in Fig. 3.2 are skewed to greater bias. The space-charge effect is also important in explaining the effects of varying barrier widths on the IV characteristics in subsection 3.3.2 and subsection 3.3.3, due to how they control the accumulation of charge in the QW.

### 3.3.1.2 Comparison with Ballistic Regime

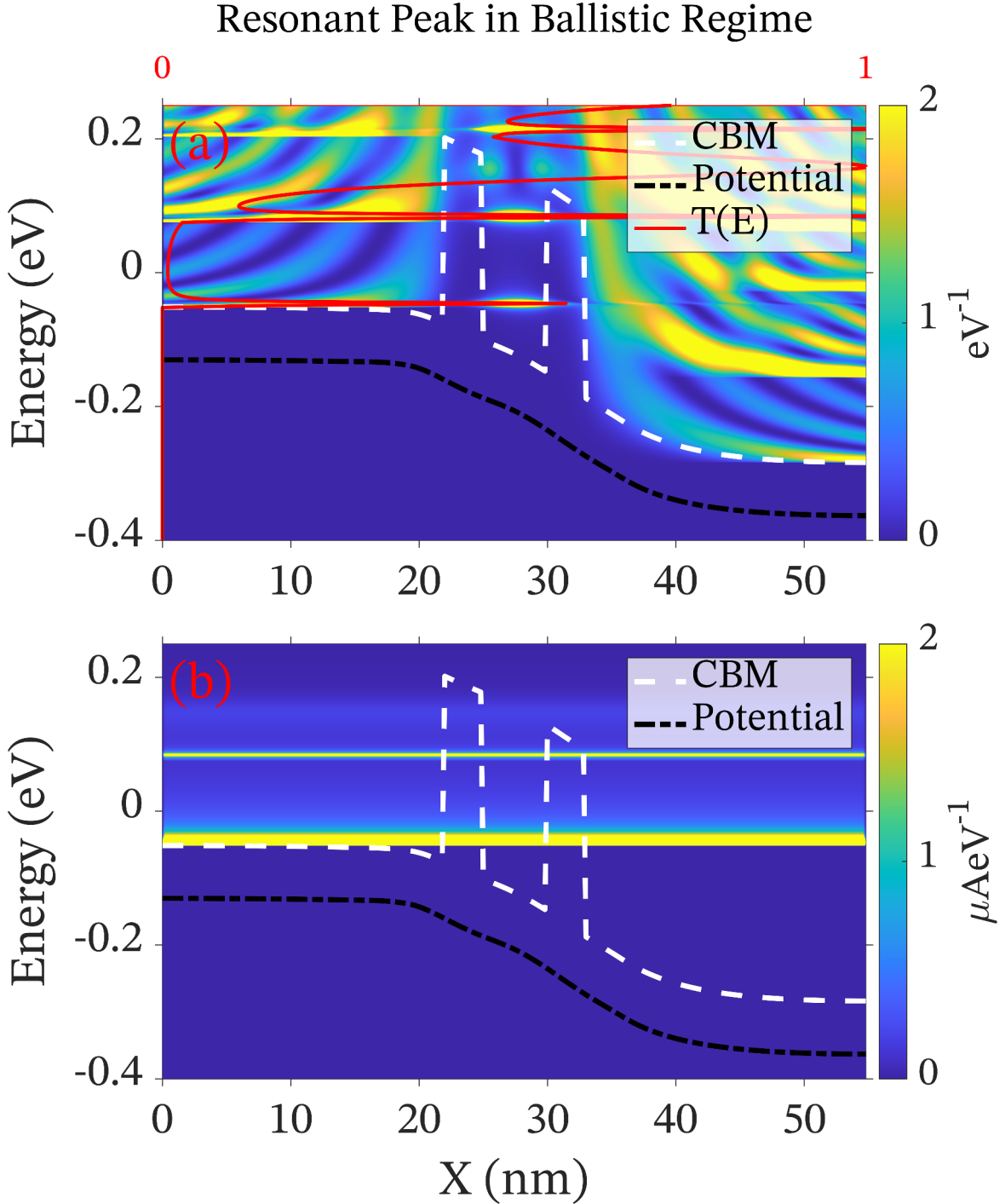


**Figure 3.5:** A comparison of IV characteristics for an RTD as depicted in Fig. 3.1, for the cases with phonons (black solid line with circle markers) and the ballistic case (orange dashed line with plus markers). The latter case in the ballistic regime is also plotted in Fig. 2.18, with corresponding LDOS and CS for the resonant peak shown in Fig. 3.7. The LDOS and CS for the resonant peak for the phonon case is shown in Fig. 3.6. This figure [8] is licensed under CC BY 4.0.



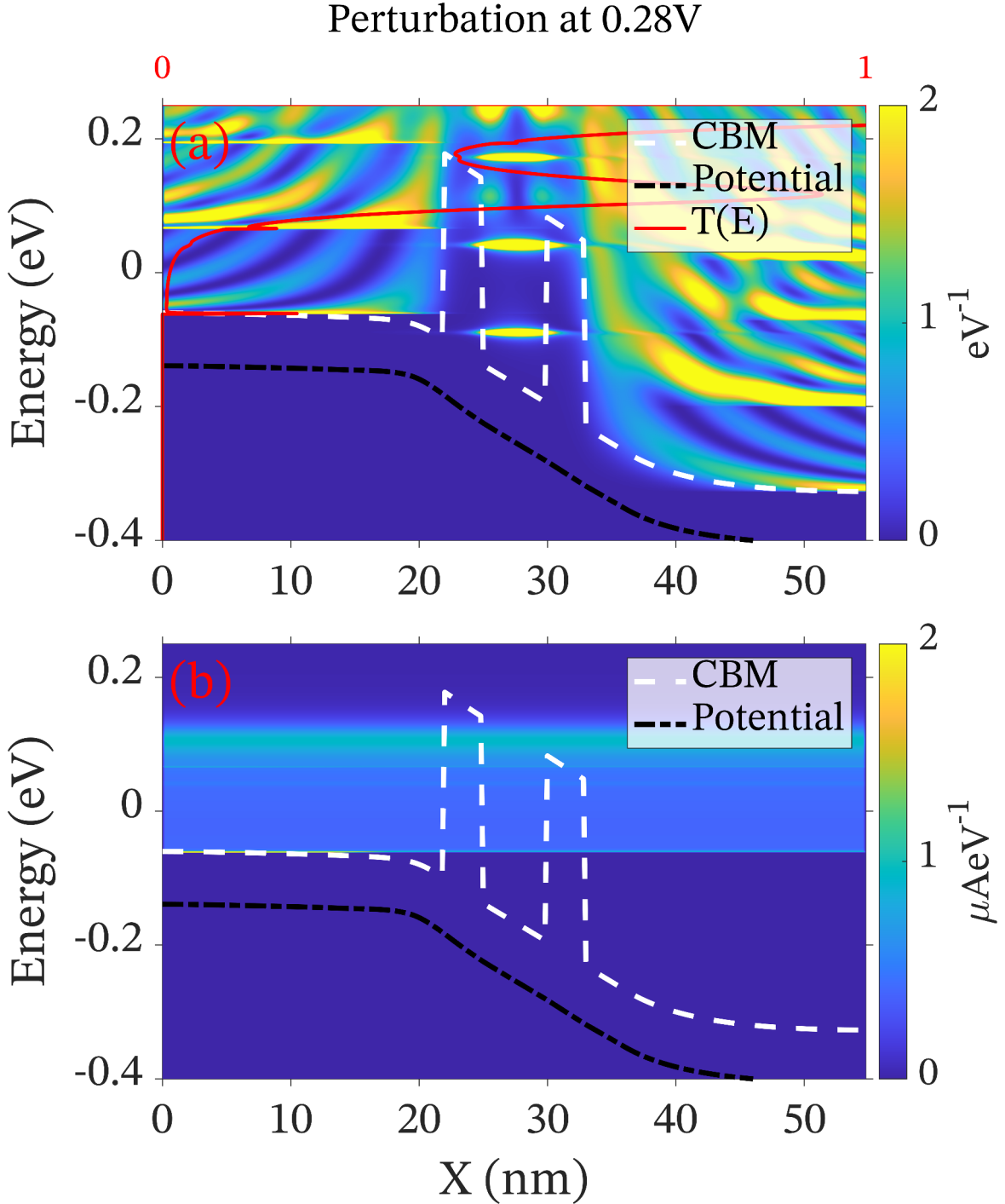
**Figure 3.6:** Figure(a) depicts the LDOS (with colourbar units of  $\text{eV}^{-1}$ ) and energy dependent transmission (a red vertical line) for the resonant peak at 0.22V shown in Fig. 3.2, and figure(b) is the CS (with colourbar units of  $\mu\text{AeV}^{-1}$ ) for the resonant peak. The white dashed lines are the CBM, and the black dash-dot lines are the average potential energy.

Fig. 3.5 shows the effect of including electron-phonon scattering as a black solid line, specifically with acoustic phonons [224] taken into account, in comparison to the ballistic regime as an orange dashed line. There is a reduction in current and the perturbation of the resonant peak bias  $V_r$  to lower bias, caused by the inclusion of acoustic electron-phonon scattering as shown in Fig. 3.5. Additionally, the PVCR drops from 3.552 to 2.923. This change in the IV characteristic supports the use of acoustic electron-phonon scattering in this study, consequently, the results in subsection 3.3.2 and subsection 3.3.3 take this into account. As discussed in subsection 2.4.4 in chapter 2, optical phonons have not been included because currently NESS cannot simulate optical phonons in polar materials such as GaAs. The main effect of optical phonons on RTDs is the creation of a replica secondary current peak [158, 159, 163]. Thankfully, the main focus of this chapter is the resonant peak rather than such high bias behaviour.



**Figure 3.7:** Figure(a) is the LDOS and transmission (red horizontal line plot), and Figure(b) is the CS, both of which correspond to the resonant peak bias of 0.24V for the ballistic regime in Fig. 3.5. The white dashed lines are the CBM, and the black dash-dot lines are the average potential energy.

The impact of acoustic phonons can also be observed somewhat with the LDOS and CS plots for the resonant IV peaks for the ballistic case at 0.22V in Fig. 3.7, and the phonon regime at 0.24V in Fig. 3.6. Specifically, a suppression in the energy-dependent transmission, the solid red line, and a slight blurring of the lower CS bands is observed. This observed reduction in current transport likely lead to the reduced current peak from  $0.2235\mu\text{A}$  to  $0.2660\mu\text{A}$  with the inclusion of electron-phonon scattering, and a consequential reduction of the PVCR (Peak-to-Valley Current Ratio) of the IV characteristics from 3.552 to 2.923.



**Figure 3.8:** Figure(a) is the LDOS and transmission (red horizontal line plot), and Figure(b) is the CS, both of which correspond to the perturbation in current at 0.28V for the IV characteristic with electron-phonon scattering in Fig. 3.5. The white dashed lines are the CBM, and the black dash-dot lines are the average potential energy.

Specifically in Fig. 3.5 a perturbation is observed for 0.28V with phonon scattering, with LDOS and CS for this voltage visualised in Fig. 3.8. The small peak in transmission in Fig. 3.8(a) and the slight CS band in Fig. 3.8(b) show that there is some current flow through the barrier which is likely due to acoustic phonons scattering assisting tunnelling from the emitter-side Fermi level to the ground QW energy.

The baseline 55nm long RTD shown in Fig. 3.1 results in the IV characteristic Fig. 3.2, and the corresponding LDOS and CS graphs for the resonant peak at 0.22V and valley at 0.24V depicted in Fig. 3.3. The  $\text{Al}_{0.3}\text{Ga}_{0.7}\text{As}$  barriers raise the CBM with respect to the GaAs body, which is depicted as white dashed lines in Fig. 3.3, and bounds a GaAs QW.

### 3.3.2 Symmetric Barrier and QW Thickness Variation

In this subsection I investigate symmetric barrier variation, of 2nm and 4nm in Fig. 3.9, and variation of QW widths, of 4nm and 6nm in Fig. 3.10. This was compared to the baseline case of two 3nm  $\text{Al}_{0.3}\text{Ga}_{0.7}\text{As}$  barriers and a 5nm QW shown in the previous subsection 3.3.1.

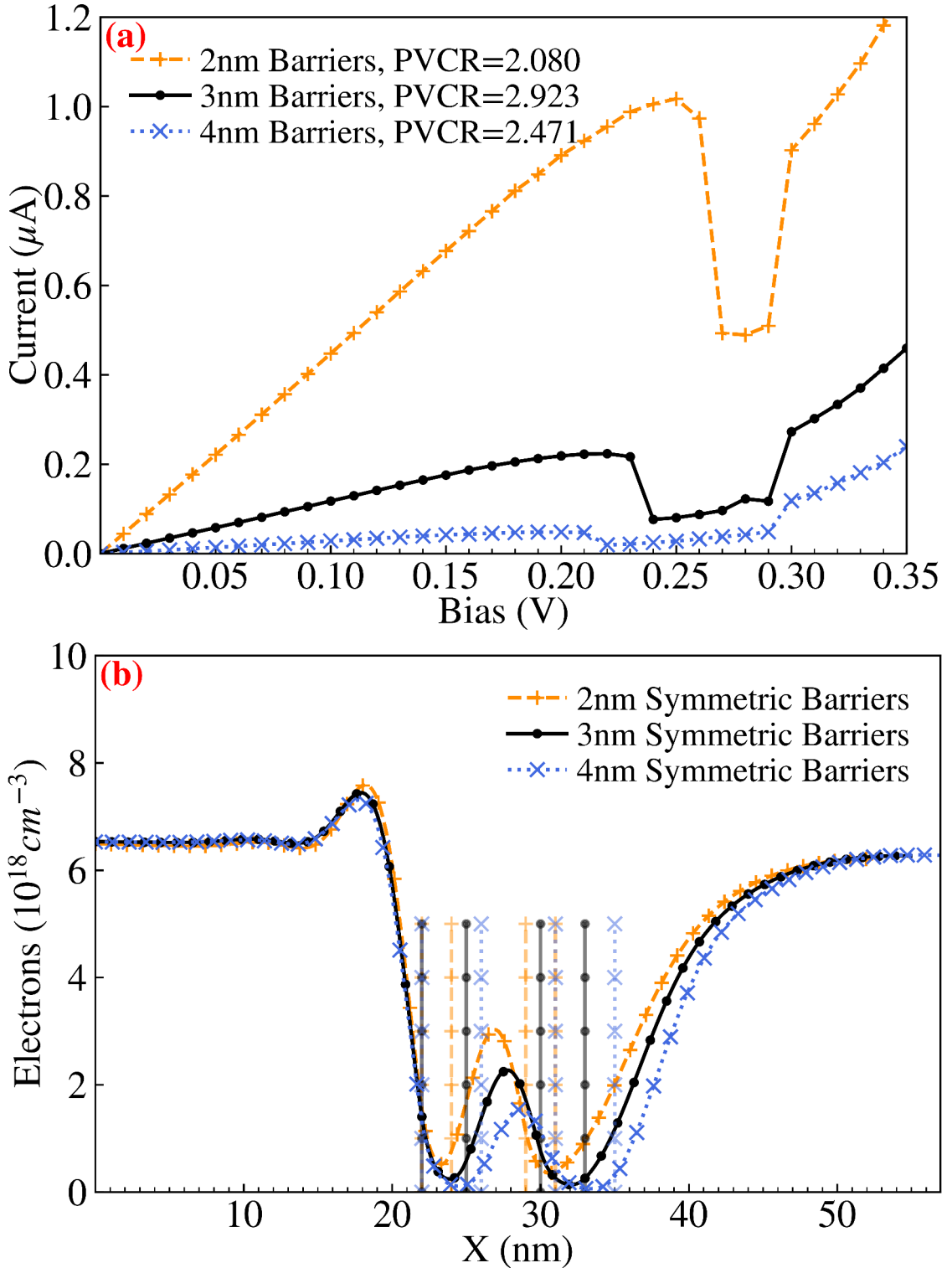


**Figure 3.9:** Comparison of IV characteristics and electron charge density, through the centre of RTD cross-sections, for different symmetric barrier thicknesses  $L_{B1}=L_{B2}$  with figure(a) and figure(b) respectively. Barriers of 2nm (orange dashed line with plus markers) and 4nm (blue dotted line with diagonal cross markers) are compared with the baseline case of 3nm (black solid line with dot markers). Within figure(b), barrier interface positions are noted with slightly transparent vertical lines with corresponding markers. This figure is reproduced based on Figure 9 from [8], which is licensed under CC BY 4.0.

Symmetric barrier widths  $L_{B1}=L_{B2}$  in Fig. 3.9 are shown to inversely impact current and the resonant peak bias  $V_r$ , including the resonant peak. Narrower 2nm barriers lead to greater current flow in Fig. 3.9(a) due to the higher transmission through narrower barriers. This greater current flow leads to a greater charge density within the QW as shown in Fig. 3.9(b). This greater charge density means there's a greater space-charge effect [14], in other words, there is a greater Coulomb repulsion to be overcome by bias, increasing the resonant bias peak  $V_r$  from 0.22V to 0.25V. Increasing barrier thicknesses to 4nm (blue dotted line with diagonal cross markers in Fig. 3.9) causes the opposite effects of reducing current and QW charge density, thus perturbing the resonant peak to the reduced  $V_r=0.2V$ .

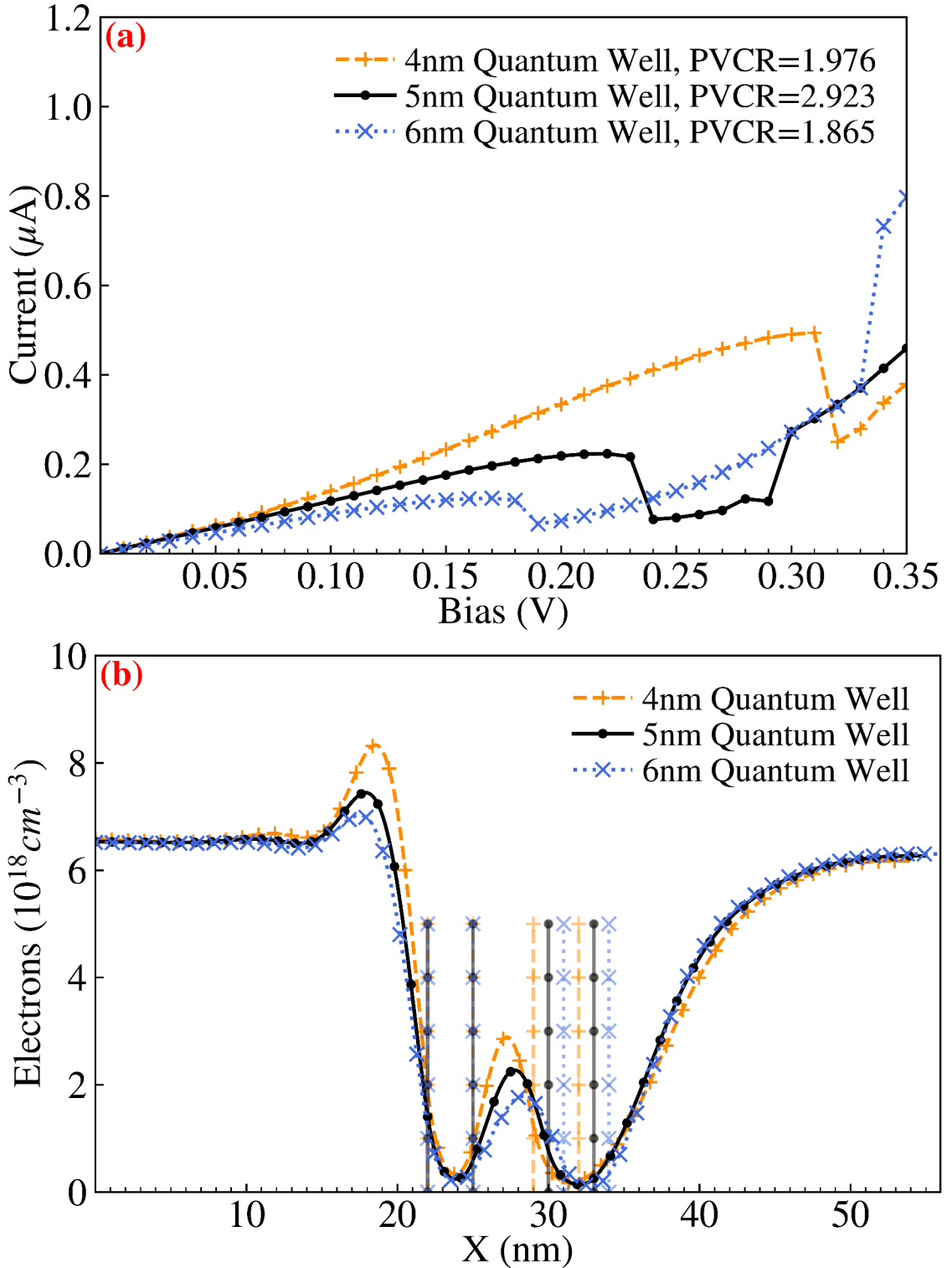


**Figure 3.10:** Comparison of IV characteristics and electron charge density, through the centre of RTD cross-sections, for different QW widths  $L_{\text{QW}}$  with figure(a) and figure(b) respectively. QW widths of 4nm (orange dashed line with plus markers) and 6nm (blue dotted line with diagonal cross markers) are compared with the baseline case of 5nm (black solid line with dot markers). Within figure(b), barrier interface positions are noted with slightly transparent vertical lines with corresponding markers. This figure is reproduced based on Figure 10 from [8], which is licensed under CC BY 4.0.

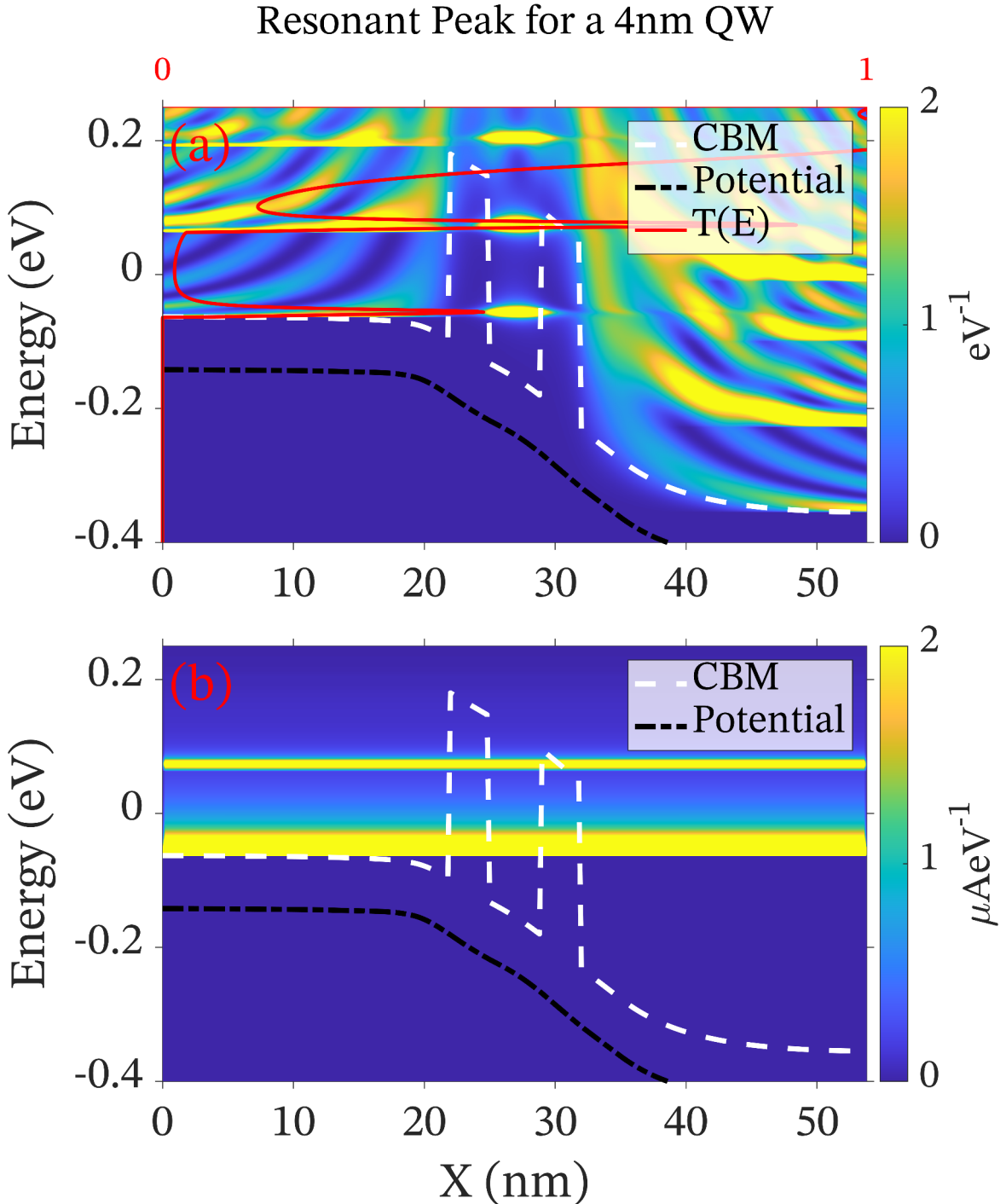


**Figure 3.11:** LDOS (with colourbar units of  $\text{eV}^{-1}$ ) and CS (with colourbar units of  $\mu\text{AeV}^{-1}$ ) for an RTD with a QW width  $L_{QW}=4\text{ nm}$  for the resonant peak at 0.31V, with figure(a) and figure(b) respectively. The LDOS plot (figure(a)) includes energy dependent transmission as a red line. The white dashed lines are the CBM, and the black dash-dot lines are the average potential energy. This figure is reproduced based on Figure 11 from [8], which is licensed under CC BY 4.0.

Variation of QW width  $L_{QW}$  inversely affects the resonant peak bias  $V_r$ . A thinner QW increases the ground QW eigenvalue energy [233]. This greater ground QW eigenvalue requires a greater bias  $V_r=0.31V$  to align the QW ground state and the emitter Fermi level to reach the resonant peak as shown in Fig. 3.11. This causes a perturbation of the resonant peak bias  $V_r$  to greater values. For a wider QW of 6nm, the resonant peak bias  $V_r$  is reduced to  $V_r=0.17V$ .

In Fig. 3.10(b), I observed changes in the QW charge density similar to that seen with symmetric barrier variation in Fig. 3.9(b). For both 4nm QW and 2nm barriers, where these regions are narrower than the baseline, there is an increase in QW charge density. For the narrow 4nm QW, the resonant peak current is greater because the resonant peak bias  $V_r$  itself is greater due to the greater ground eigenvalue energy. This greater current flowing through the QW results in a greater charge density within the QW at a given moment, resulting in a greater bias.

Unlike for the QW region, variations in the emitter region charge density are not the same for QW and symmetric barrier variations. For the narrower  $L_{QW}=4\text{nm}$  emitter charge density increases, while variation of such a magnitude has not been observed for symmetric barrier variation. The greater charge density in the emitter region for the 4nm QW, unlike the  $L_{B1}=L_{B2}=2\text{nm}$  barrier case in Fig. 3.9, is due to the higher energy ground QW eigenvalue for a narrower QW. With such a greater ground QW eigenvalue, a correspondingly greater bias  $V_r$  is needed to reach the resonant peak, and unlike the space-charge effect, it does not perturb the band-structure to greater energies with the Coulomb repulsion potential. This likely means that the triangular QW that forms in the emitter region becomes ‘deeper’, leading to greater charge density accumulating in the emitter region for the resonant peak. Whilst a narrower QW leads to similar effects as narrower symmetric barriers for the IV characteristic and QW charge density, this is not

the case for emitter region charge density. The differences observed in the emitter charge density effects demonstrate that the mechanisms for their impact are different, with  $L_{QW}$  controlling ground QW energy eigenvalue and  $L_{B1}=L_{B2}$  modulating the space-charge effect.

### 3.3.3 Asymmetric Barrier Thickness Variation

For this subsection, I investigate the asymmetric variation of RTD barrier thickness and compare it against the baseline RTD studied in subsection 3.3.1. I first investigate varying the first barrier width  $L_{B1}$  to 2nm and 4nm in Fig. 3.12 whilst keeping the second barrier width  $L_{B2}$  constant at 3nm. Following this I similarly vary the second barrier width  $L_{B2}$  whilst keeping  $L_{B1}$  constant in Fig. 3.13. The perturbation of the resonant peak bias  $V_r$  with respect to the baseline IV characteristic in Fig. 3.2 appears to be due to changes in charge accumulation in the QW which in turn modulates the space-charge effect, as was seen with the symmetric barrier variation in Fig. 3.9. This was in turn caused by differences in the transparency between the two barriers.

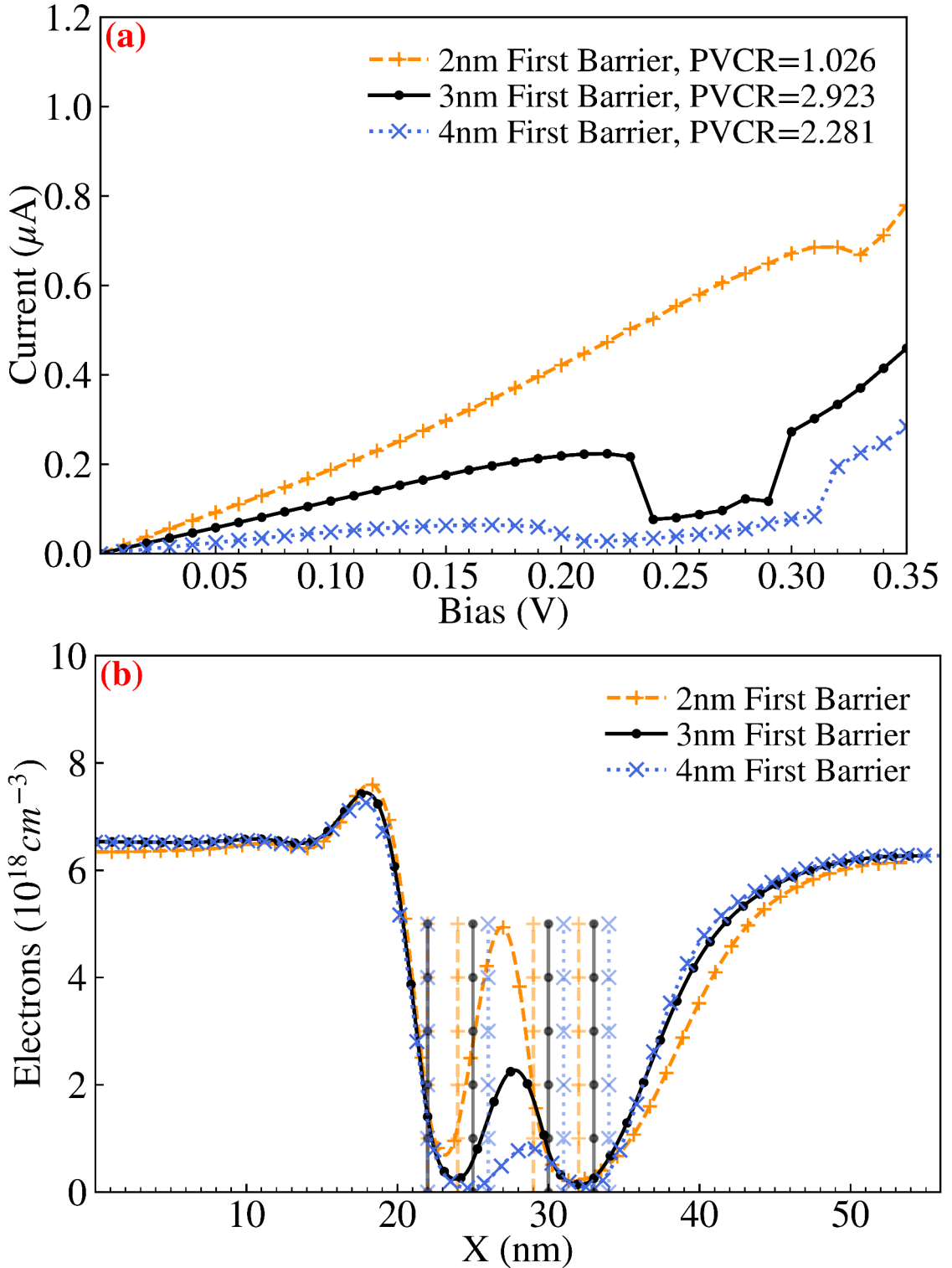


**Figure 3.12:** Comparison of IV characteristics and electron charge density, through the centre of RTD cross-sections, for different first barrier thicknesses  $L_{B1}$  with figure(a) and figure(b) respectively. The second barrier thickness  $L_{B2}$  is 3nm as in the baseline case. Barriers of  $L_{B1}=2\text{nm}$  (orange dashed line with plus markers) and  $L_{B1}=4\text{nm}$  (blue dotted line with diagonal cross markers) are compared with the baseline case of 3nm (black solid line with dot markers). Within figure(b), barrier interface positions are noted with slightly transparent vertical lines with corresponding markers. This figure is reproduced based on Figure 12 from [8], which is licensed under CC BY 4.0.

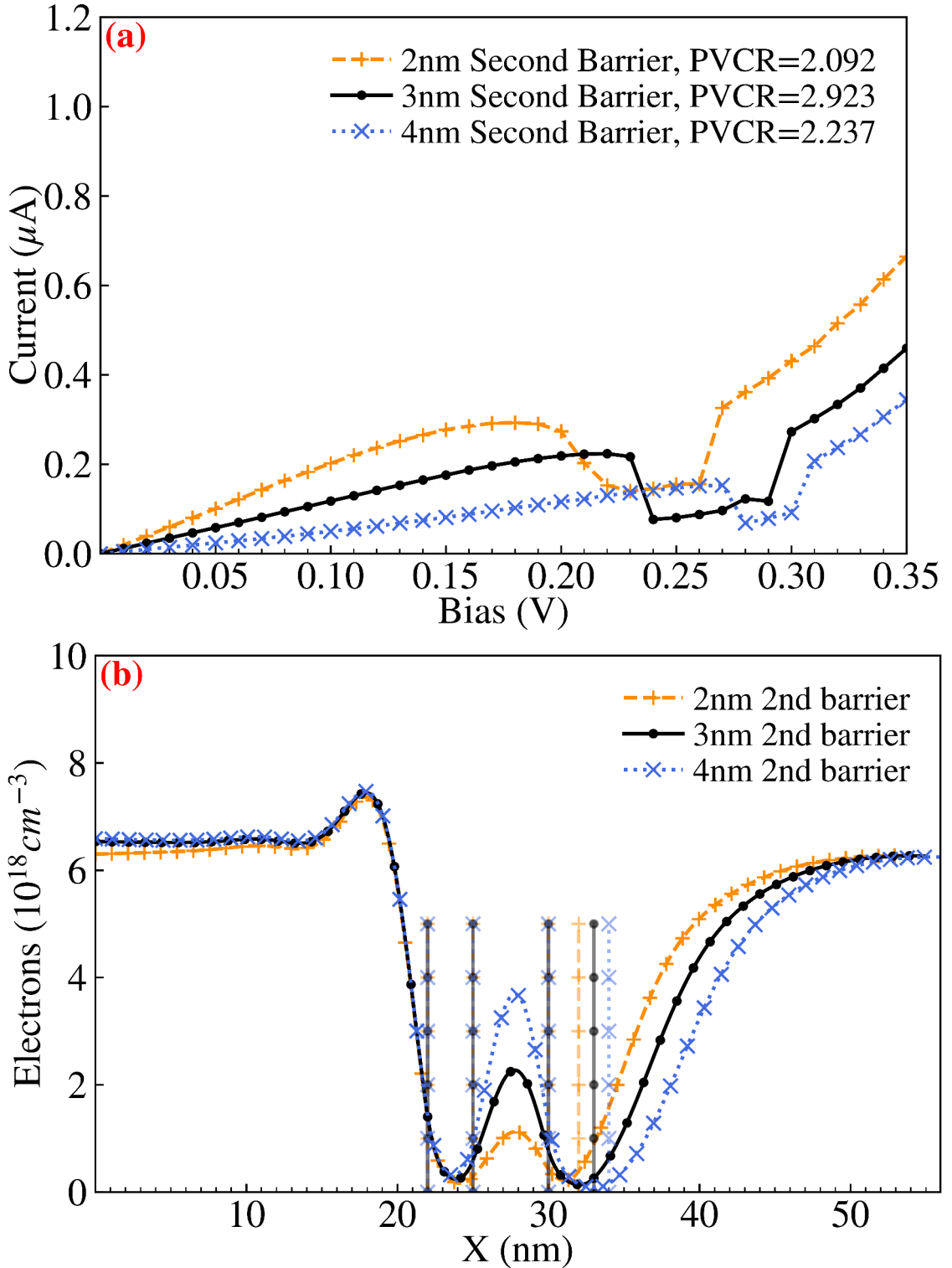


**Figure 3.13:** Comparison of IV characteristics and electron charge density, through the centre of RTD cross-sections, for different second barrier thicknesses  $L_{B2}$  with figure(a) and figure(b) respectively. The first barrier thickness  $L_{B1}$  is 3nm as in the baseline case. Barriers of  $L_{B2}=2\text{nm}$  (orange dashed line with plus markers) and  $L_{B2}=4\text{nm}$  (blue dotted line with diagonal cross markers) are compared with the baseline case of 3nm (black solid line with dot markers). Within figure(b), barrier interface positions are noted with slightly transparent vertical lines with corresponding markers. This figure is reproduced based on Figure 13 from [8], which is licensed under CC BY 4.0.

A thinner first barrier with  $L_{B1}=2\text{nm}$  in Fig. 3.12 has higher transmission than the second barrier  $L_{B2}=3\text{nm}$ , hence it is comparatively easier for electrons to tunnel into the QW than to tunnel out, thereby increasing QW charge density. This comparatively increased QW charge density in Fig. 3.12(b) results in a greater space-charge effect, perturbing the resonant peak bias  $V_r$  to  $V_r=0.32\text{V}$  from the baseline of  $V_r=0.22\text{V}$ . I also observe a near disappearance of the NDR for the  $L_{B1}=2\text{nm}$  case, due to the domination of thermionic emission with such a high bias, leading to a PVCR of 1.026. A thicker first barrier with  $L_{B1}=4\text{nm}$  leads to a weaker space-charge effect due to a lower QW charge density, leading to the resonant peak bias  $V_r$  comparatively reducing to  $V_r=0.17\text{V}$ .

A similar but inverse effect occurs for second barrier variation, where a thicker second barrier  $L_{B2}=4\text{nm}$ , whilst keeping  $L_{B1}=3\text{nm}$ , results in greater QW charge accumulation behind the second barrier, and thus a perturbation of the resonant peak bias  $V_r$  to greater bias with  $V_r=0.27\text{V}$ . With a thinner second barrier  $L_{B2}=2\text{nm}$ , the resonant peak bias  $V_r$  relatively perturbs to lower bias with  $V_r=0.18\text{V}$ .

The perturbations in the resonant peak current  $I_r$  from the baseline of  $0.224\mu\text{A}$  brought about by first barrier variation are greater than for the second barrier variation. For first barrier variation, peak current reduces to  $I_r=0.064\mu\text{A}$  for  $L_{B1}=4\text{nm}$ , and increases to  $I_r=0.686\mu\text{A}$  for  $L_{B1}=2\text{nm}$ . Whilst for second barrier variation, peak current only reduces to  $I_r=0.153\mu\text{A}$  for  $L_{B2}=4\text{nm}$ , and only increases to  $I_r=0.293\mu\text{A}$  for  $L_{B2}=2\text{nm}$ . For both cases, narrower barriers lead to greater current like with symmetric barrier variation.

As discussed above, variations in  $L_{B1}$  and  $L_{B2}$  lead to similar but opposite effects on the resonant peak bias  $V_r$  and the charge density for such a bias. For both barriers, barrier width inversely correlates with resonant peak current  $I_r$ . Changes in  $L_{B1}$  have a greater impact than  $L_{B2}$  as seen by the greater perturbation of resonant peak IV values, and for  $L_{B1}=2\text{nm}$  the NDR almost disappears. The perturbation in  $V_r$  from the baseline of  $0.22\text{V}$

is lower for changes in symmetric barrier widths, with only an increase to  $V_r=0.25V$  for 2nm barriers and a decrease to  $V_r=0.2V$  for 4nm barriers. This weaker variation in  $V_r$  suggests that different barriers cancel out their space-charge effects to an extent, with changes in the first barrier width winning out.

### 3.4 Conclusion

In this work, I have done a NEGF study of the RTD barrier/quantum-well thickness perturbations and captured the pronounced effects on the device characteristics. Variation of barrier thickness from a baseline of 3nm modulates the accumulation of charge in the QW. The resonant peak bias  $V_r$  is controlled by the intensity of the space-charge effect due to this QW charge.

Narrower 2nm symmetric barriers have increased current flow, and thus more charge in the QW at a given moment, which perturbs the resonant peak bias  $V_r$  to greater bias. Narrower 2nm first barriers, with an unchanged 3nm second barrier, lead to greater charge accumulation and thus a perturbation of the resonant peak bias  $V_r$  to greater bias, and also causes the near elimination of the PVCR. A thicker 4nm second barrier, with a 3nm first barrier, similarly leads to greater charge accumulation and consequential perturbation to greater bias. In all such cases, narrower barriers leads to greater current, with the first barrier having a greater effect in this respect. QW width inversely affects the ground QW eigenvalue, so narrowing the QW width from 5nm to 4nm perturbs the resonant peak bias  $V_r$  to greater bias.

In summarising the results, three main observations can be made:

1. A narrower 4nm QW and thinner 2nm symmetric barriers, compared to a baseline RTD with a 5nm QW and 3nm symmetric barriers, both resulted in a perturbation of resonant peak bias  $V_r$  to greater values of 0.31V and 0.25V respectively from a baseline of 0.22V.
2. Asymmetric variation of the barriers controlled the perturbation of the resonant peak bias  $V_r$ , with a thinner 2nm first barrier resulting in a perturbation to a greater bias of  $V_r=0.32V$ , and a thinner 2nm second barrier resulting in the inverse effect of reduced bias of  $V_r=0.18V$ .
3. Both barrier thicknesses inversely impacted the current, with the first barrier having a greater impact. Specifically, a thicker 4nm first barrier reduced resonant peak current  $I_r$  from  $0.224\mu\text{A}$  to  $0.064\mu\text{A}$ , while a thicker 4nm second barrier only reduced  $I_r$  to  $0.153\mu\text{A}$ .

These observations are later used to describe the influence of IR along different GaAs/ $\text{Al}_{0.3}\text{Ga}_{0.7}\text{As}$  interfaces in terms of such device variation in section 5.2 within chapter 5.

The conclusions drawn here can be used to assist design of RTDs. For example, if optimising for a lower resonant peak voltage, a thinner first barrier or thicker second barrier or wider QW can be considered.

# Chapter 4

## Random Discrete Dopants

### 4.1 Introduction

ICs (Integrated Circuits) described within section 1.5, RTDs (Resonant Tunnelling Diodes) have the potential to construct [7, 21, 22] PUFs (Physical Unclonable Functions) [23, 24] due to stochastic device variation. These PUFs can then be used to uniquely identify integrated chips [53] in order to combat the issue of semiconductor chip counterfeiting [54, 55]. This has motivated me to study the impact of RDDs (Random Discrete Dopants) on the current-voltage (IV) characteristics of RTDs, and investigate the potential of RTDs with RDDs as PUF components. This has led me to publish a paper [7] on this, the material of which is used to write this chapter.

The simulation methodology is described in section 2.5, and like in chapter 3 there is a maximum of 25 NEGF-Poisson convergence loops. RDDs within this chapter are applied on top of smooth doping, as is described in subsection 2.2.2, allowing an exploration of the impact of RDDs on top of a base ‘smooth’ doping. Moreover, such a choice allowed this study to build on top of a previous study [118] by investigating the impact of RDDs within the QW.

In Section 4.2.1, I have described the RTD device operations of so called ‘smooth’ devices (with no sources of variability). In Section 4.2.2 I have used NESS to introduce RDDs as a source of variability, and investigated their impact on the current-voltage (IV) characteristics of devices. Also in the same section 4.2.2 I have discussed how this randomness can be used to encode information in RTDs for use as a PUF building block [22] through analysing the min-entropy. Finally, I conclude by summarising the key findings in Section 4.3.

## 4.2 Results and discussions

### 4.2.1 ‘Smooth’ RTD device—without RDDs

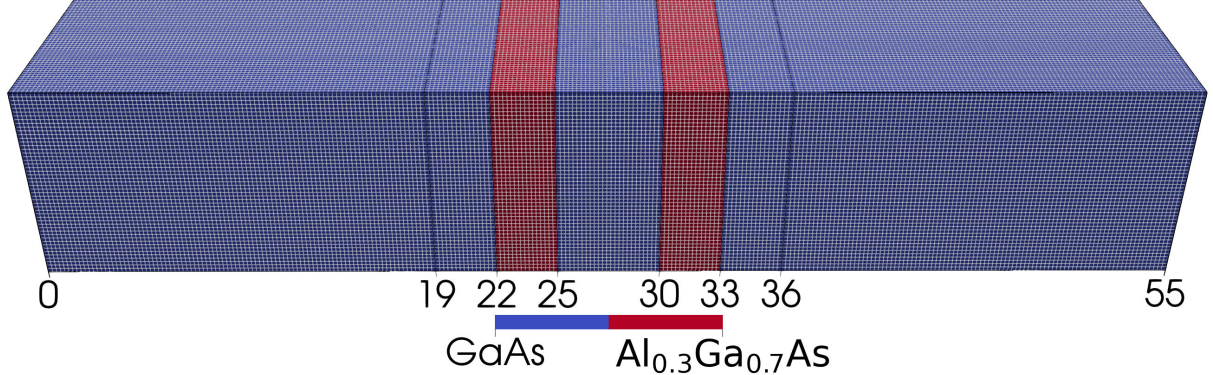


**Figure 4.1:** A schematic illustration of the GaAs-Al<sub>0.3</sub>Ga<sub>0.7</sub>As device under investigation, which has a square cross-section with dimensions of 10nm×10nm, and an overall length of 55nm. The device is divided into distinct sections shown by the black lines, namely the 19nm source and drain, two 3nm buffer regions, two 3nm Al<sub>0.3</sub>Ga<sub>0.7</sub>As barriers, and a 5nm QW. This figure is licensed under CC BY 4.0, attached to an archived copy of [7] held by the University of Glasgow. The University of Glasgow has an agreement with IEEE allowing authors to self-archive manuscripts with an attached CC BY licence. © 2024, IEEE.

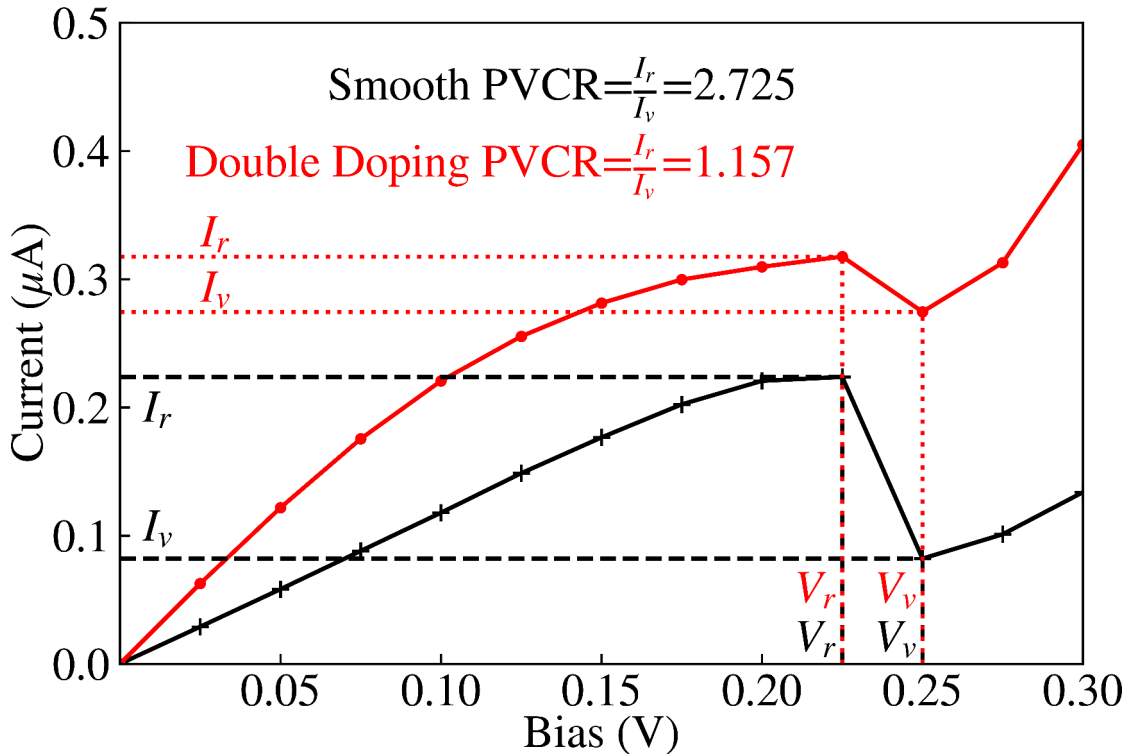


**Figure 4.2:** IV characteristics of a smooth GaAs-Al<sub>0.3</sub>Ga<sub>0.7</sub>As nanowire RTD device with phonon scattering, comparing the base ‘smooth’ case shown in Fig. 4.1 (black line with plus markers) with a ‘double doping’ case (red line with dot markers) with twice the n-doping level of the base device. This figure is licensed under CC BY 4.0, attached to an archived copy of [7] held by the University of Glasgow. The University of Glasgow has an agreement with IEEE allowing authors to self-archive manuscripts with an attached CC BY licence. © 2024, IEEE.

It should be emphasised that the baseline ‘smooth’ RTD has a smooth  $2 \times 10^{18}\text{cm}^{-3}$  n-doped source and drain regions which are both 19nm long, as described in section 2.5 in chapter 2. As noted in subsection 2.2.2, the addition of RDDs increases n-type doping of the mesh nodes. To provide another comparison device with similarly such increased doping, I have also simulated a ‘double doping’ device where I have uniformly doubled the doping levels across the base ‘smooth’ device described by Fig. 4.1. As shown in Fig. 4.2 this results in an increased current, with an  $I_r$  of  $0.3177\mu\text{A}$ , and a decreased PVCR of 1.157 compared to the base ‘smooth’ device due to an increased valley current.

### 4.2.2 Effect of RDDs on the device characteristics

In order to evaluate the impact of statistical variability of the device characteristics in this subsection, I have simulated 75 RTDs with unique RDD configurations, which vary the number and position of RDDs. RDD doping is applied across three regions, from 3nm to 19nm in the source, the central 3nm of the QW, and 36nm to 52nm in the drain. I have avoided the generation of RDDs close to the contact (where the boundary conditions are applied) due to convergence issues. Hence, the dopants are applied only in the GaAs III-V material 3nm far away for the contact region. Considering all 75 RTDs I have obtained a mean number of RDDs of 6.87. I have presented three devices with very different IV curve profiles and different positions and numbers of RDDs in Fig. 4.3.

In this subsection, as a first step, I demonstrate how RDDs cause variations in RTD IV characteristics. This is followed by a visualization of resonant peak IV values from an ensemble of RDD doped devices, before finishing with an assessment of the capacity of these IV values to encode information for the use of RTDs as PUF building blocks.

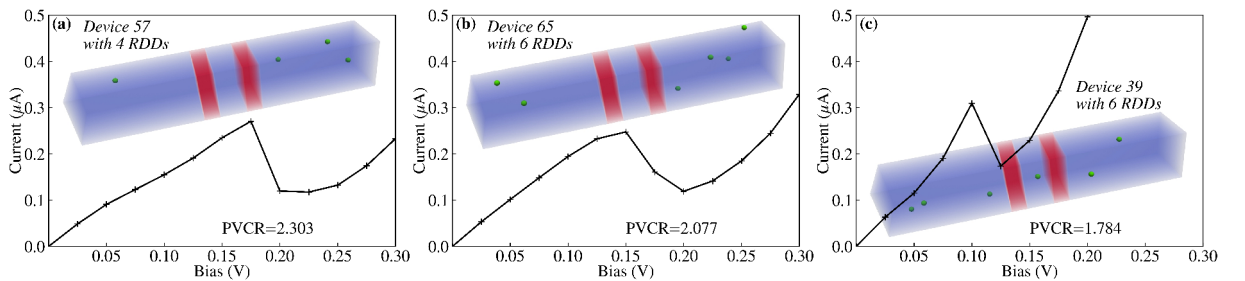


**Figure 4.3:** The IV characteristics of devices No. 57, 65 and 39 are depicted, accompanied by an inset illustrating the distribution of RDDs represented by green dots. PVCRs for No. 57, No. 65, and No. 39 are 2.303, 2.077, and 1.784, respectively. The corresponding  $I_r$  and  $V_r$  are  $0.2708\mu\text{A}$  at  $0.175\text{V}$ ,  $0.2477\mu\text{A}$  at  $0.15\text{V}$  and  $0.3098\mu\text{A}$  at  $0.1\text{V}$ . This figure is licensed under CC BY 4.0, attached to an archived copy of [7] held by the University of Glasgow. The University of Glasgow has an agreement with IEEE allowing authors to self-archive manuscripts with an attached CC BY licence. © 2024, IEEE.

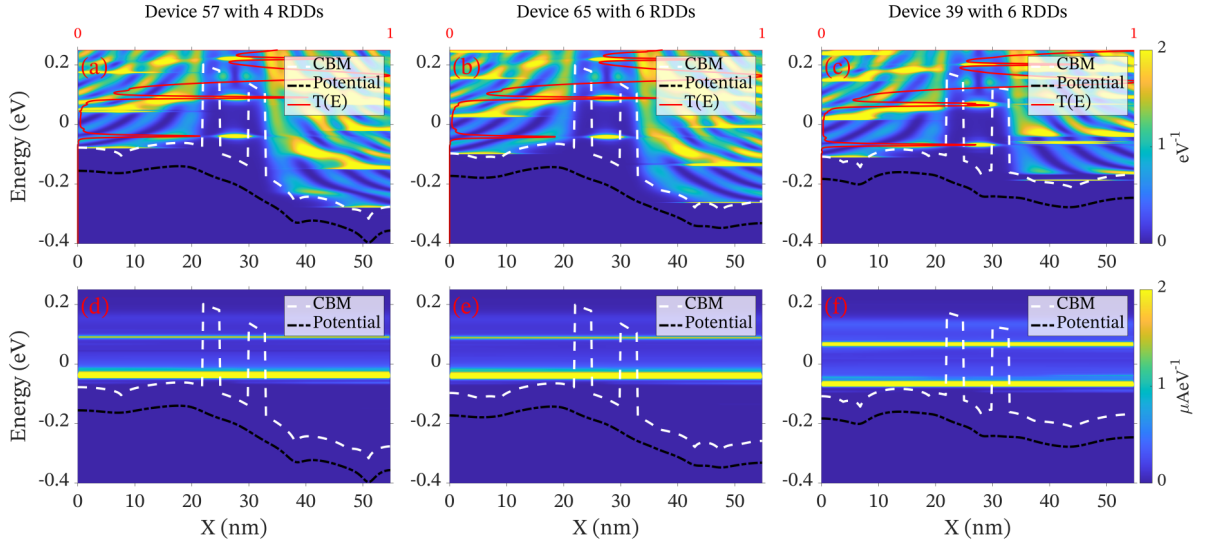


**Figure 4.4:** The upper row shows the combined LDOS and  $T(E)$  of three RTD devices, specifically devices No. 57, 65 and 39. These calculations were performed at the bias voltages corresponding to the first resonant peak, which are 0.175V, 0.15V, and 0.1V, respectively. Consequently, the bottom row illustrates the energy-resolved CS of the aforementioned devices. This figure is licensed under CC BY 4.0, attached to an archived copy of [7] held by the University of Glasgow. The University of Glasgow has an agreement with IEEE allowing authors to self-archive manuscripts with an attached CC BY licence. © 2024, IEEE.

The impact of RDDs is shown in Fig. 4.3, and Fig. 4.4 with devices No. 57, 65, and 39, with 4, 6 and 6 RDDs respectively. Fig. 4.3 shows the IV characteristics, with inset devices where the green dots are the distribution of RDDs. Generalising the impact of RDDs in the drain and QW regions, there is a shift of the resonant peak voltage and the NDR to a more negligible value because of the shifting of the ground QW state to lower energies relative to the source Fermi level. Device No. 57 has 3 RDDs in the drain region (compared to 1 in the source). In this case the NDR is observed to be between 0.175V and 0.200V. This can be explained with perturbation of the potential and hence the conduction band profile in the source and drain region (please see the dips in the white dashed lines in Fig. 4.4(a)). Furthermore, a lower bias of 0.175V needs to be applied to achieve a resonant peak compared to 0.225V with no RDDs.

Device No. 39 has an RDD in the QW which visibly perturbs the band structure and density of states in the QW down with respect to the  $\text{Al}_{0.3}\text{Ga}_{0.7}\text{As}$  barriers, resulting in a much lower resonant peak voltage  $V_r$  of 0.1V, showing the greater impact of RDDs in the QW compared to ones in the source region.

All three devices shown in Fig. 4.3 have RDDs in the source region which increases the conductivity. I believe this behaviour is due to RDDs increasing the overall n-doping in the source region, and thus the charge carrier concentration and conductance. As a result, the resonant current peak  $I_r$  for all three is comparable to the double doping resonant peak current  $I_r=0.3177\mu\text{A}$ , and greater than the  $I_r$  of  $0.2238\mu\text{A}$  for a smooth device with phonon scattering.

The results show that there is a direct relation between the distribution of the RDDs and the resulting  $I_r$  and  $V_r$  which can indeed be used as a fingerprint for unique identification. Furthermore, in Fig. 4.4 the changes due to the number and the position of the RDDs are visible in terms of the average potential (black dashed lines), and the band structure (white dashed lines). I also observed that energy-dependent transmission  $T(E)$ , plotted as a red solid line, spikes at different energy levels, and the current conduction through the channels has different weights for each case. I would like to emphasise that the results discussed above are a 2D representation of 3D quantum mechanical simulations. Hence, although some perturbation in the potential or the LDOS might not seem notable, this is due to the 2D representation. Indeed, the change of the potential from device to device due to the position and the number of RDDs is pronounced.

The notable differences in terms of the potential, band alignment conditions, and transmission spectra all reflect the variations in the IV characteristics of these devices—displaying how the quantum nature of the resonance condition can be noticeably altered with the variability of RDDs in these III-V nanowire RTD structures.

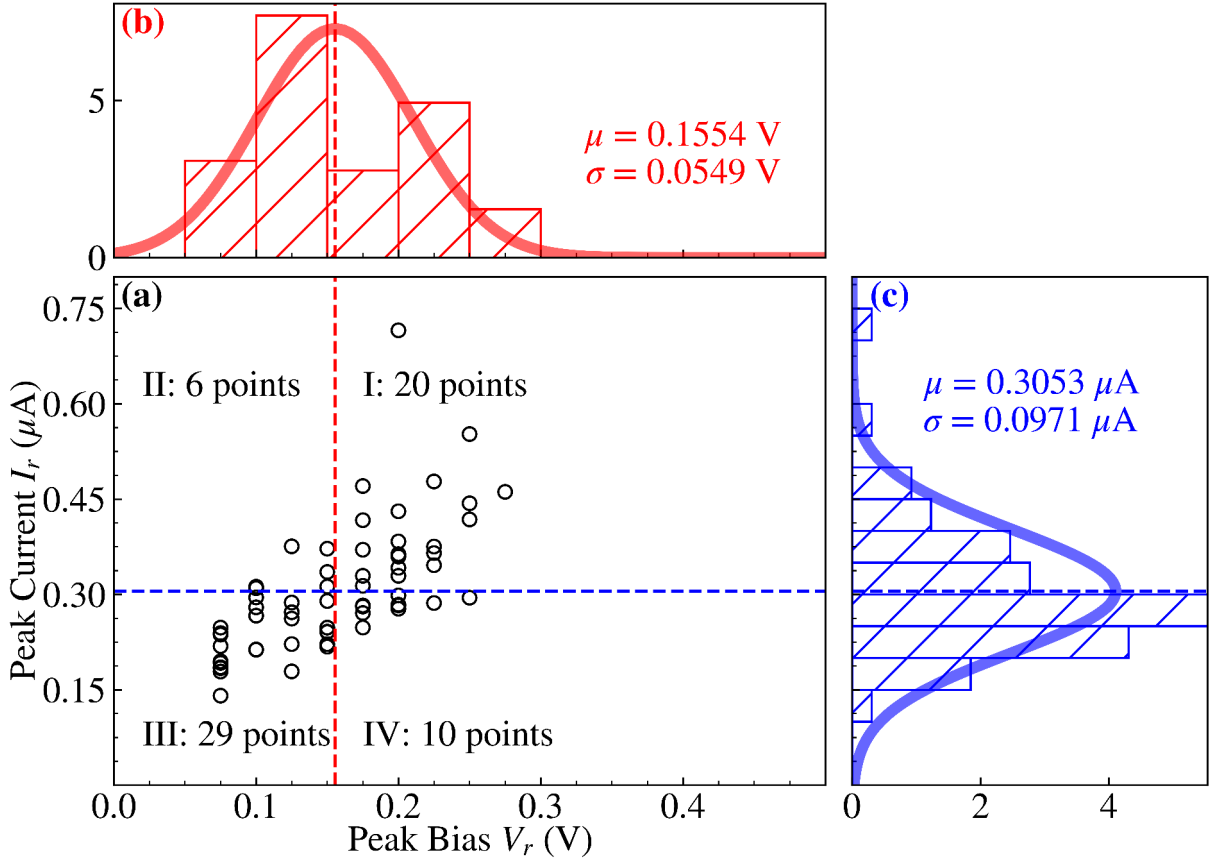


**Figure 4.5:** The central figure(a) is a scatter plot of resonant peak current  $I_r$  against resonant peak voltage  $V_r$  for the 65 devices that showed an NDR. The attached figure(b) and figure(c) respectively show the histograms of the current and voltage distribution with bin-widths of 0.05V and 0.05 $\mu\text{A}$  respectively. Normal distributions were fitted onto the histograms with a mean  $\mu = 0.1554\text{V}$  and standard deviation  $\sigma = 0.0549\text{V}$  for the peak voltage distribution in figure(b), and  $\mu = 0.3053\mu\text{A}$  and  $\sigma = 0.0971\mu\text{A}$  in figure(c). Figure(a) was also split into four quadrants with the mean of the normal distributions in figure(b) and figure(c), with annotations for the number of data points in the quadrant. This figure is licensed under CC BY 4.0, attached to an archived copy of [7] held by the University of Glasgow. The University of Glasgow has an agreement with IEEE allowing authors to self-archive manuscripts with an attached CC BY licence. © 2024, IEEE.

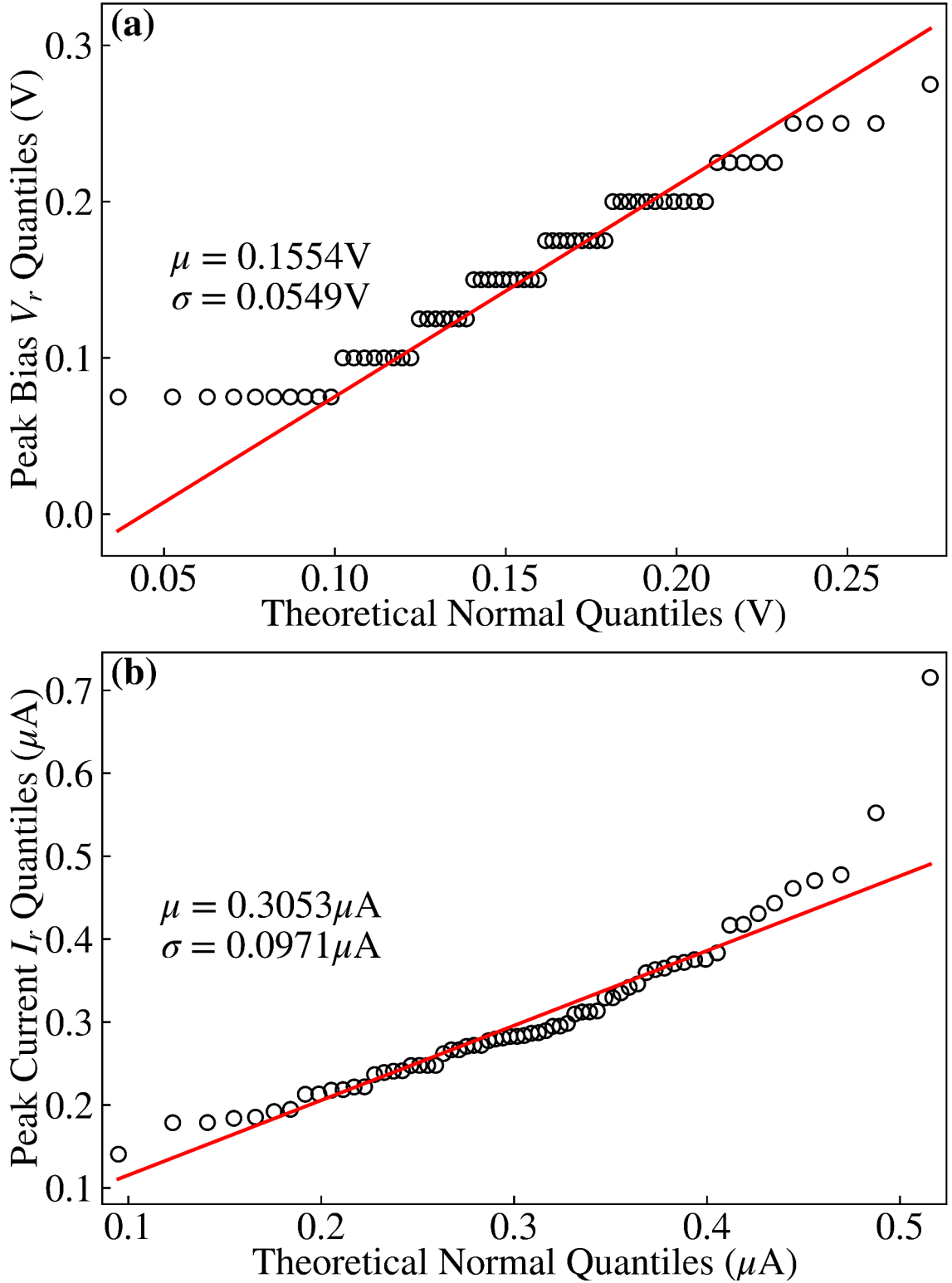


**Figure 4.6:** Quantile-Quantile plots for the resonant peak voltage  $V_r$  and current  $I_r$  in figures (a) and (b) respectively. Figure(a) plots the ordered peak bias values  $V_r$  against corresponding quantiles from a normal distribution fit to it in Fig. 4.5(b), with mean  $\mu = 0.1554\text{V}$  and standard deviation  $\sigma = 0.0549\text{V}$ . Figure(b) similarly plots ordered peak current values  $I_r$  against corresponding quantiles from a normal distribution fit to it in Fig. 4.5(c), with mean  $\mu = 0.3053\mu\text{A}$  and standard deviation  $\sigma = 0.0971\mu\text{A}$ . This figure is licensed under CC BY 4.0, attached to an archived copy of [7] held by the University of Glasgow. The University of Glasgow has an agreement with IEEE allowing authors to self-archive manuscripts with an attached CC BY licence. © 2024, IEEE.

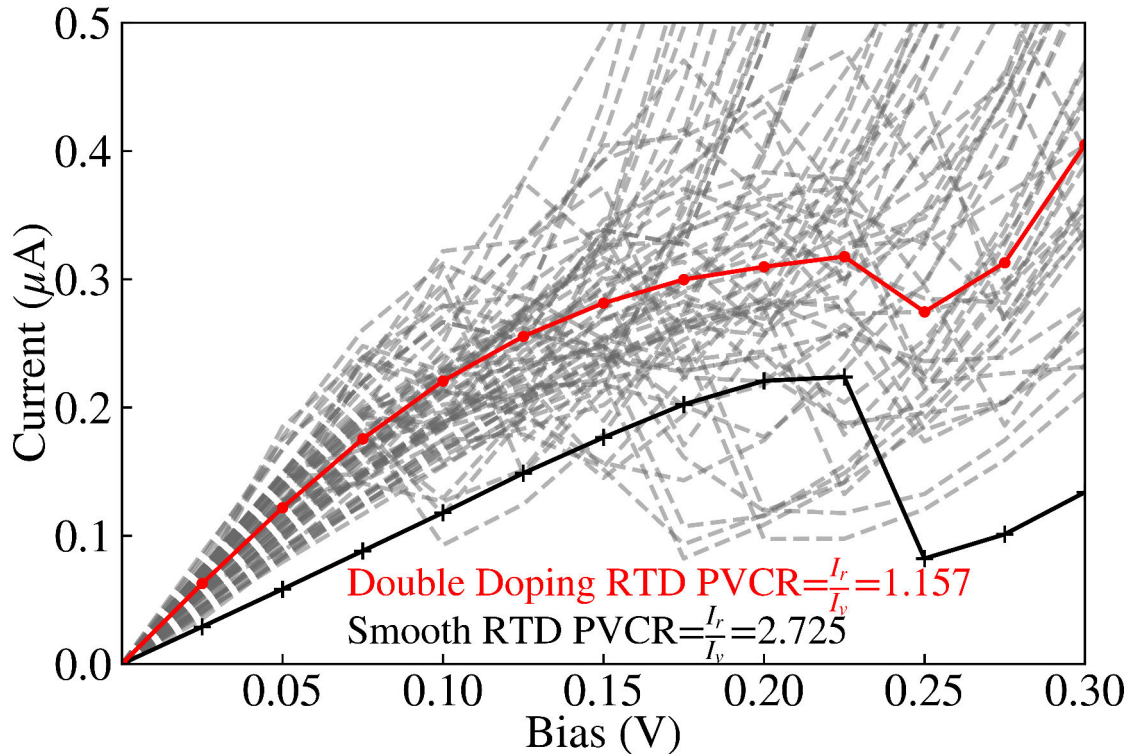


**Figure 4.7:** IV characteristics of the 65 RTD devices which exhibited an NDR (grey dashed lines). Two IV characteristics with ‘smooth’ doping such as the base ‘smooth’ case (solid black line with plus markers) and ‘double doping’ case (solid red line with dot markers), which has double the n-doping of the base case, are plotted for reference. This figure is licensed under CC BY 4.0, attached to an archived copy of [7] held by the University of Glasgow. The University of Glasgow has an agreement with IEEE allowing authors to self-archive manuscripts with an attached CC BY licence. © 2024, IEEE.

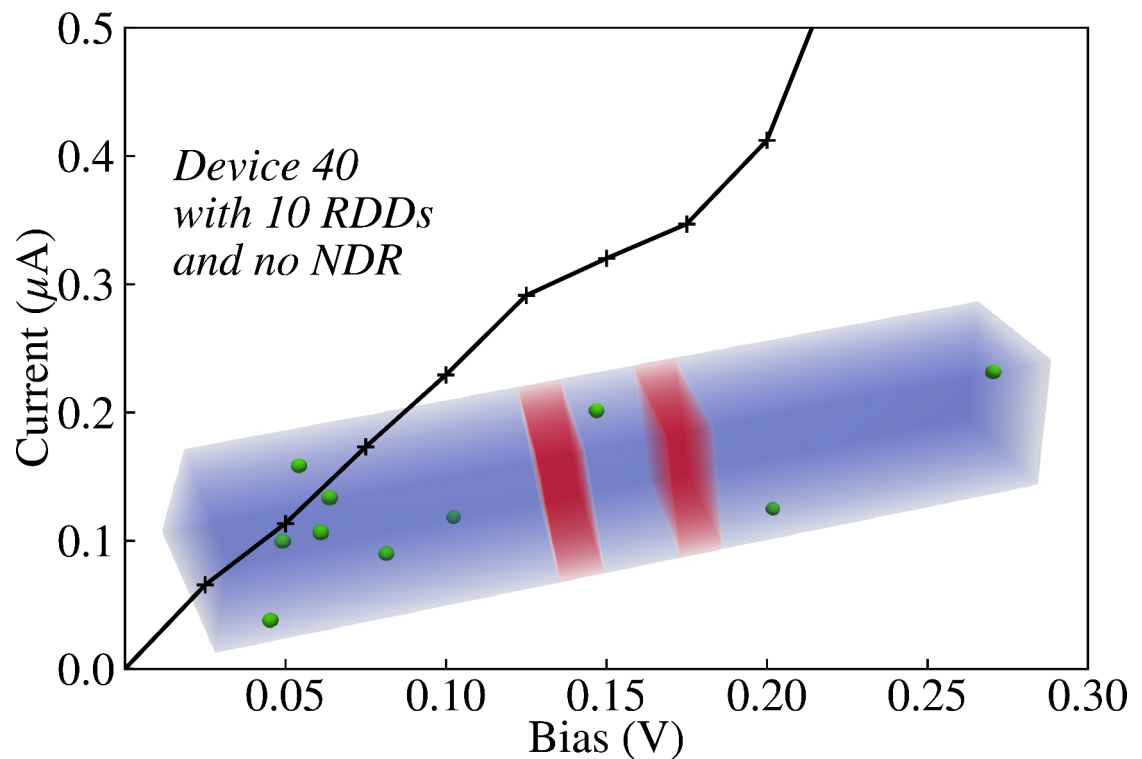


**Figure 4.8:** The IV curve of Device No. 40 is shown, which has no NDR, along with an inset of Device No. 40 showing the distribution of RDDs as green dots. This figure is licensed under CC BY 4.0, attached to an archived copy of [7] held by the University of Glasgow. The University of Glasgow has an agreement with IEEE allowing authors to self-archive manuscripts with an attached CC BY licence. © 2024, IEEE.

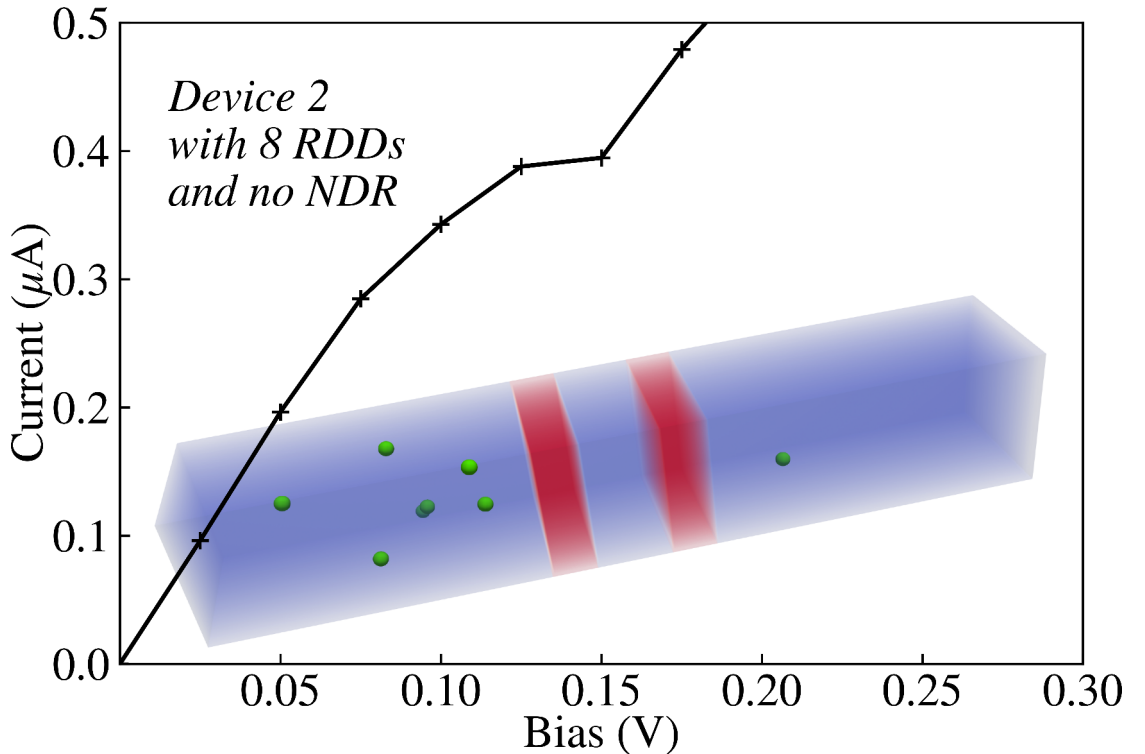


**Figure 4.9:** The IV curve of Device No. 2 is shown, which has no NDR, along with an inset of Device No. 2 showing the distribution of RDDs as green dots.

In this chapter, I have simulated 75 RTDs in total. Of 75 RTDs with RDDs, 65 showed an NDR region in their IV characteristics, which are shown in Fig. 4.7, with a local resonant peak voltage  $V_r$  and corresponding  $I_r$  at the start of the NDR. The remaining 10 devices did not exhibit NDRs, and for this reason, I have decided to exclude them from further analysis of the  $V_r$  and  $I_r$  distributions in Fig. 4.5 and Fig. 4.6. These devices without an NDR were identified through the lack of a local maxima in current identified by a script going through the IV characteristics. One such device with no NDR is device No. 40 in Fig. 4.8, in contrast to device No. 39 in Fig. 4.3(c) which also has 1 RDD in the QW yet still has an NDR. Additionally, another device with no NDR is device No. 2 in Fig. 4.9, which has no RDDs in the QW. Though device No. 2 was the only one of the 10 devices without an NDR to not feature an RDD in the QW. For reference, 25 RTDs featured an RDD within the QW, and for 9 of these devices there was no NDR. This shows that including RDDs within the QW holds a great risk of removing the NDR of RTDs.

The resonant values for the 65 RTDs with an NDR are demonstrated as a scatter plot in Fig. 4.5(a), with attached histograms and fitted normal distributions in Fig. 4.5(b) and Fig. 4.5(c). The mean  $V_r=0.1554\text{V}$  is lower than the  $V_r=0.225\text{V}$  for the smooth and double doping devices with IV characteristics depicted in Fig. 4.2, due to the presence of RDDs in the QW and drain on average shifting the QW ground resonant state to lower energy as noted previously. Due to the increase in doping brought about by RDDs, mean  $I_r=0.3053\mu\text{A}$  is comparable to the  $I_r$  of  $0.3177\mu\text{A}$  for the ‘double doping’ case and greater than the  $I_r=0.2238\mu\text{A}$  for smooth device with phonon scattering. This mean  $I_r$  is marginally less than that for the double doping case, likely due to RDDs not being generated within 3nm of the source and drain contact region. This influence of increased doping also reflects in how the double doping IV characteristic (red solid line with dot markers) shown in Fig. 4.7 appears to be more similar to the IV characteristics of devices with RDDs (grey dashed lines) than the base smooth case (black solid line with plus markers). The mean PVCR of the 65 devices with NDR is 1.414, and by including devices without NDR as a PVCR of 0 this average PVCR decreases to 1.225, which is comparable to the PVCR of 1.157 for the double doping case.

To further investigate whether these distributions fit a normal distribution, Quantile-Quantile plots for these measured values against the normal distributions were taken in Fig. 4.6. Quantiles are points that divide a distribution into equal portions, and the Quantile-Quantile plots in Fig. 4.6 compare the quantiles of the measured distribution against the expected quantiles for the fitted normal distributions, with a line fit through the quantiles. The measured quantiles, in this case, are the 65 devices with PVCR, ordered by increasing value along the y-axis, with an x value corresponding to the similarly ordered 65 normal distribution quantiles. Of note is that the measured  $V_r$  values are discrete here with ‘steps’ forming at simulated bias values in Fig. 4.6(a), whereas experimental measured  $V_r$  would be continuous and result in a smoother curve akin to that in Fig. 4.6(b).  $V_r$  is light-tailed, with an ‘s’ shape due to the sharp cut-off measured at  $0.075\text{V}$  and a less steep one at  $0.275\text{V}$ .  $I_r$  is right skewed, with a tail for higher current spreading out in comparison to the fitted normal distribution. Other than that, both  $V_r$  and  $I_r$  Quantile-

Quantile plots follow the normal distribution for the central part of the distribution, so it seems appropriate to split both distributions with the mean of the fitted normal distributions, leading to the quadrants shown in Fig. 4.5(a). This division means that I can determine whether a data point is before or after the mean in a given distribution to encode information. The standard deviation of the fitted  $V_r$  normal distribution  $\sigma = 0.0549V$  is greater than the voltage mesh spacing of 0.025V, allowing me to fit the voltage normal distribution.

In order to check the randomness of the data ( $V_r$  and  $I_r$ ) for information encoding purposes, I performed three different non-parametric statistical tests to compare these two datasets. These are the Wilcoxon Signed-Rank test [234], Kolmogorov–Smirnov test [235] and Mann–Whitney test [236]. For all 3 tests, I rejected the null hypothesis for a significance level of 0.001, which implies that the two datasets are not from the same population and are significantly different. The Pearson correlation coefficient [237] between  $V_r$  and  $I_r$  was 0.663 indicating a strong correlation, and as seen in Fig. 4.5(a) it is clear that there is a positive correlation between  $V_r$  and  $I_r$ , with quadrants I and III having the majority of data points.

With these non-equivalent yet correlated datasets, it is appropriate to encode information in both distributions simultaneously using the probability of getting a result within a given quadrant, for which the min-entropy can be calculated. The min-entropy is the most conservative measure of information [22] and is  $H_{min} = -\log_2(p_{max})$  where  $p_{max}$  is the probability of the most likely result, which in this case is 29 for quadrant III. If I only look at the 65 results with NDRs,  $H_{min} = -\log_2(\frac{29}{65}) = 1.164$ . If I include the 10 results without NDR, and thereby the fifth possibility of measuring an RTD with no NDR,  $H_{min} = -\log_2(\frac{29}{75}) = 1.371$ . This result appears robust, even under a finer voltage spacing and with the devices at  $V_r=0.15V$  which are close to the voltage mean of  $\mu=0.1554$ . If when simulated with a finer voltage spacing a few devices measured as having  $V_r=0.15$  were to move from below the mean to above it, that would lead to a reduction in the number of points in quadrant III and the  $p_{max}$ , and therefore min-entropy  $H_{min}$  would

increase. This means that if 100 RTDs were produced and combined into a PUF, one could reasonably expect to encode a fingerprint composed of  $\sim 137$  bits of information. This is enough to generate a 128-bit secret key for the popular Advanced Encryption Standard to authenticate wireless devices[136]. While this is an idealized result, that does not consider possible issues such as mismeasuring resonant current and voltage as being in the wrong quadrant, it nonetheless presents a promising case for the use of RTDs with RDDs to generate PUFs.

### 4.3 Conclusion

I have investigated an ensemble of 75 NEGF simulations of RTDs with RDDs, enabled with the nano-electronic device simulator NESS, 65 of which exhibited NDR behaviour. I have shown that the positions and the number of RDDs strongly perturb the electronic and transport properties of RTDs. This is clearly projected in the resulting resonant peak current and voltage for each RTD. These resonant peak current and voltage distributions were proven through non-parametric tests to not be equivalent distributions and yet were strongly correlated, with a Pearson coefficient of 0.663. When taking into account both distributions and devices without an NDR a min-entropy of 1.371 was achieved. The unique, random, and difficult to predict nature of RTDs with RDDs along with their information encoding capacity makes them promising candidates for PUF applications. Furthermore, the results demonstrate that NESS can indeed be used to predict and tailor RTD behaviour as the main building block in PUF circuits.

In summary, the following key three points were concluded within this chapter

1. RDDs strongly perturb the IV characteristics of RTDs, as well as the LDOS and CS for the resonant peak

2. The variation of resonant peak current  $I_r$  and resonant peak voltage  $V_r$  values due to RDDs form strongly correlated normal-like distributions which are not equivalent, with a Pearson coefficient of 0.663
3. When taking into account both  $I_r$  and  $V_r$  distributions and devices without an NDR, a min-entropy of 1.371 can be assigned to a given RTD with RDDs. This shows promise for composing a PUF out of multiple such RTDs with RDDs.

For future research and design of RTD based PUFs, RDDs provide the potential to act as PUF components, though they also hold the potential to destroy the NDR, especially when within the QW. Hence, for the design of PUFs with RDDs, I would suggest either to avoid doping the QW region where there is a risk of destroying the NDR and/or take into account RTDs without an NDR to also encode information.

# Chapter 5

## Interface Roughness

### 5.1 Introduction

Due to the importance of IR in RTDs, I have studied and submitted multiple papers on the topic. This chapter is composed of content from three such first author papers of mine [8–10]. Sections 5.2, 5.3 and 5.4 each correspond to the papers [8], [9], and [10] respectively.

Section 5.2 investigates the influence of IR at different  $\text{GaAs}/\text{Al}_{0.3}\text{Ga}_{0.7}\text{As}$  interfaces, comparing to the variation in barrier and QW thicknesses in chapter 3. Section 5.3 investigates how varying the correlation length and RMS (Root-Mean Square) asperity of IR on RTDs influences them within subsection 5.3.1, and how RTDs with IR can be used as PUFs (Physical able Functions) in subsection 5.3.2. Section 5.4 builds upon the preceding section by improving the implementation of IR to allow two correlation lengths, which is compared to the previous implementation and found to increase variation in IV (Current-Voltage) characteristics further, further emphasising the importance of taking into account IR in RTDs. Additionally, anisotropic IR for different correlation lengths is briefly investigated. Finally, section 5.5 concludes the chapter and draws key points.

## 5.2 Sensitivity of RTDs to IR

This section investigates the influence of IR at different GaAs/Al<sub>0.3</sub>Ga<sub>0.7</sub>As interfaces, comparing to the variation in barrier and QW thicknesses in chapter 3. Similarly, the parameters as noted in chapter 3 are used, including acoustic electron-phonon scattering.

### 5.2.1 IR with Different Interface Configurations

In this subsection, I investigate the selective inclusion of IR along different interfaces. The configurations are roughness along the QW (at x=25nm and x=30nm), the ‘first’ barrier (at x=22nm and x=25nm), and the ‘second’ barrier (at x=30nm and x=33nm). The IR follows the exponential autocorrelation model of roughness [202], and has an RMS roughness asperity  $\Delta_{RMS}=0.3\text{nm}$  and correlation length  $L_C$  [199, 200]. For each such configuration, I randomly generated and simulated 25 devices, resulting in an average IV characteristic (red dotted line with diagonal cross markers) and a comparison with the ‘smooth’ case (black solid line with dot markers) in Fig. 5.1, Fig. 5.2 and Fig. 5.3. In the aforementioned figures, I also investigate individual devices for their IV characteristic and charge density at the resonant peak, and in the insets there are visualizations of Al<sub>0.3</sub>Ga<sub>0.7</sub>As barriers for those particular devices. All devices chosen had an IV characteristic which was representative of the average of their IR configuration.

Acoustic electron-phonon scattering is included for simulations within this section, with the effects explored in subsubsection 3.3.1.2. A maximum of 25 NEGF-Poisson convergence loops were allowed for this section.

The IV characteristic for the ‘smooth’ baseline device is as shown in Fig. 3.2 in chapter 3.

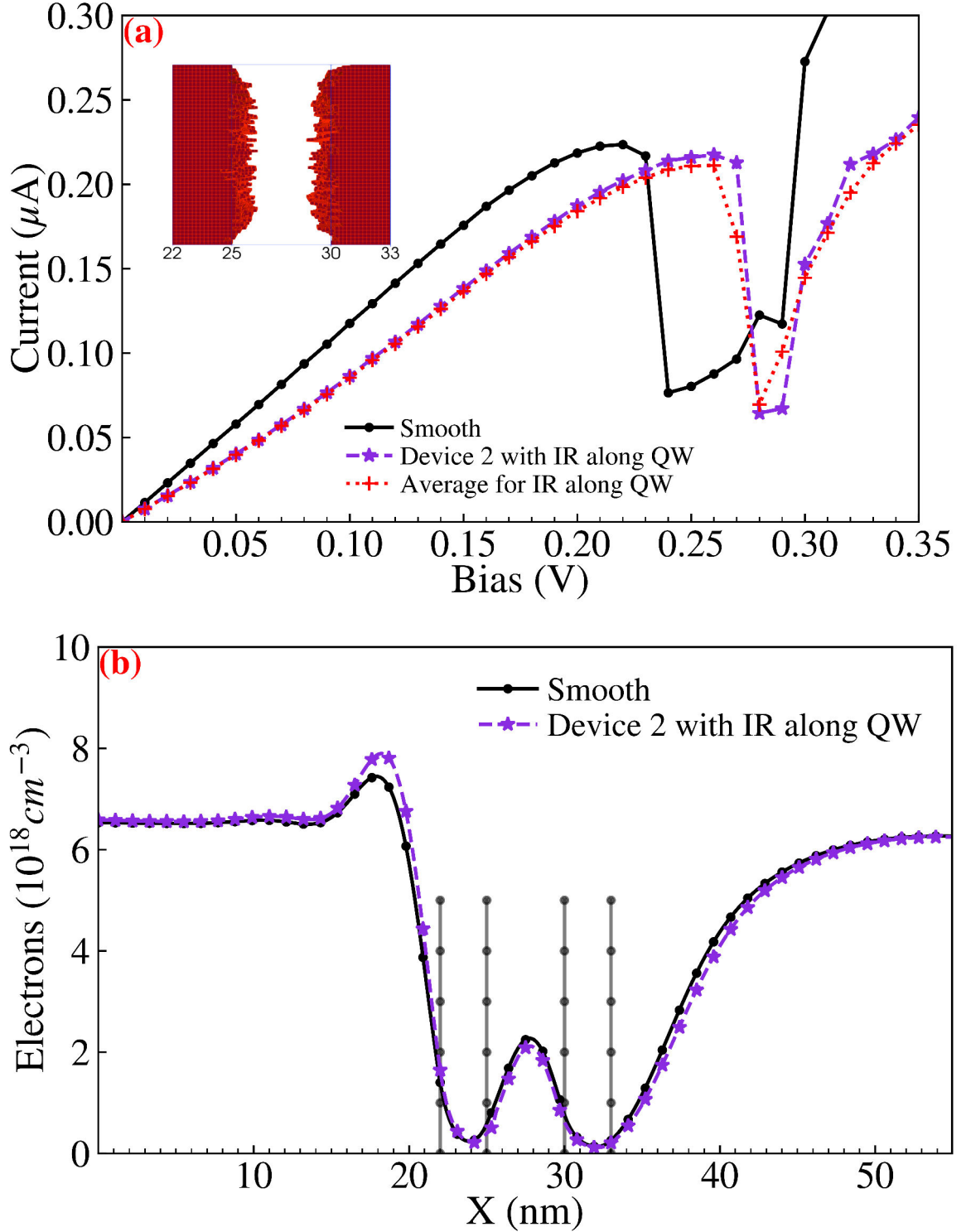


**Figure 5.1:** Comparison of IV characteristics (figure(a)) and electron charge density (figure(b)), through the centre of RTD cross-sections, for the ‘smooth’ RTD (black solid line with dot markers) depicted in Fig. 5.7 and device 2 with IR along the inside of the QW (purple dashed line with star markers). Within figure(b), barrier interface positions are noted with slightly transparent vertical lines with dot markers. Figure(a) also depicts the average IV characteristic (red dotted line with diagonal cross markers), and the  $\text{Al}_{0.3}\text{Ga}_{0.7}\text{As}$  barriers for device 2 with a rough second barrier as an inset. This figure is reproduced based on Figure 14 from [8], which is licensed under CC BY 4.0.

For roughness along the QW, I observed behaviour similar to narrowing the QW width in Fig. 3.10, with a perturbation of the resonant peak bias  $V_r$  to greater bias and an increase in emitter region charge density compared to the baseline ‘smooth’ case. Unlike the ‘smooth’  $L_{QW}=4\text{nm}$  case however, I see a slight reduction in current with the addition of IR along the QW, including a drop of  $I_r$  from  $0.224\mu\text{A}$  to  $0.217\mu\text{A}$ . I also observe a consequential slight reduction in QW charge density as seen in Fig. 5.1(b). This lack of increased QW charge density also means that the space-charge effect due to QW charge did not contribute to the perturbation of the resonant peak bias  $V_r$  to higher bias, with  $V_r$  increasing from  $0.22\text{V}$  to  $0.26\text{V}$ . Instead, as noted for the  $L_{QW}=4\text{nm}$  case, the narrower QW led to a greater ground state eigenvalue [233], which necessitated a greater bias  $V_r$  to align with the source Fermi level and thus reach the resonant peak. The average resonant peak IV values of 25 devices with IR along the QW shows a similar perturbation from  $I_r=0.224\mu\text{A}$  and  $V_r=0.22\text{V}$ , with a decrease to  $I_r=0.212\mu\text{A}$  and an increase to  $V_r=0.256\text{V}$ .

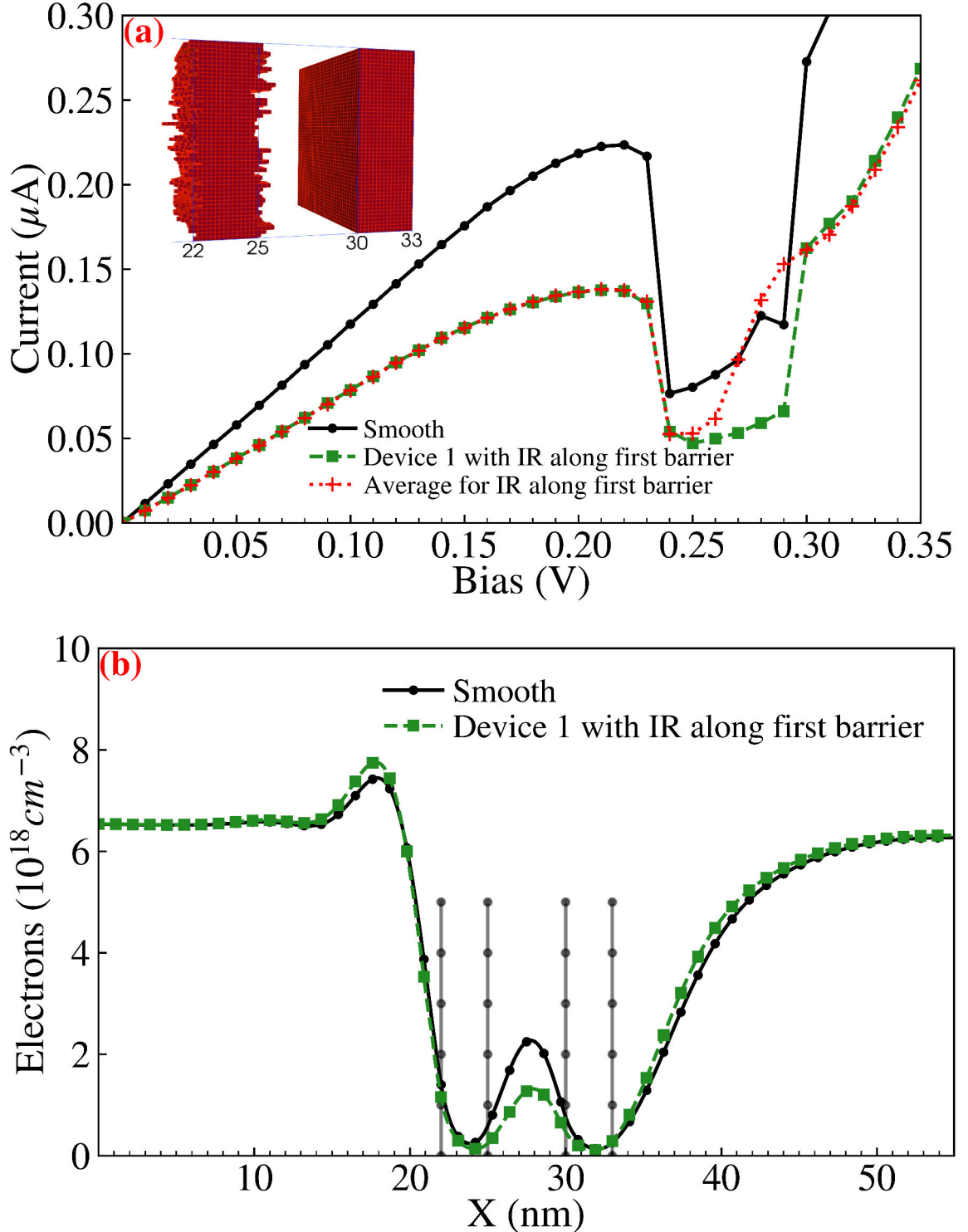


**Figure 5.2:** Comparison of IV characteristics (figure(a)) and electron charge density (figure(b)), through the centre of RTD cross-sections, for the 'smooth' RTD (black solid line with dot markers) depicted in Fig. 5.7 and device 1 with IR along the first Al<sub>0.3</sub>Ga<sub>0.7</sub>As barrier (green dashed line with square markers). Within figure(b), barrier interface positions are noted with slightly transparent vertical lines with dot markers. Figure(a) also depicts the average IV characteristic (red dotted line with diagonal cross markers), and the Al<sub>0.3</sub>Ga<sub>0.7</sub>As barriers for device 1 with a rough first barrier as an inset. This figure is reproduced based on Figure 15 from [8], which is licensed under CC BY 4.0.

A rough first barrier in Fig. 5.2 exhibits an IV characteristic akin to thickening the barrier as seen in Fig. 3.12 for  $L_{B1}=4\text{nm}$ , with a reduction in current, with  $I_r$  reducing from  $0.224\mu\text{A}$  to  $0.138\mu\text{A}$ , and a lower charge QW charge density as seen in Fig. 5.2(b). There is also a slight perturbation of the resonant peak bias  $V_r$  to lower bias measured, with  $V_r$  reducing from  $0.22\text{V}$  to  $0.21\text{V}$ . Though unlike for  $L_{B1}=4\text{nm}$ , I observe a slight increase in the emitter region charge density, perhaps due to IR scattering keeping some charge confined there. The average resonant peak IV values of 25 devices with IR along the first barrier shows a similar perturbation from  $I_r=0.224\mu\text{A}$  and  $V_r=0.22\text{V}$ , with a decrease to  $I_r=0.138\mu\text{A}$  and a slight decrease to  $V_r=0.212\text{V}$ .

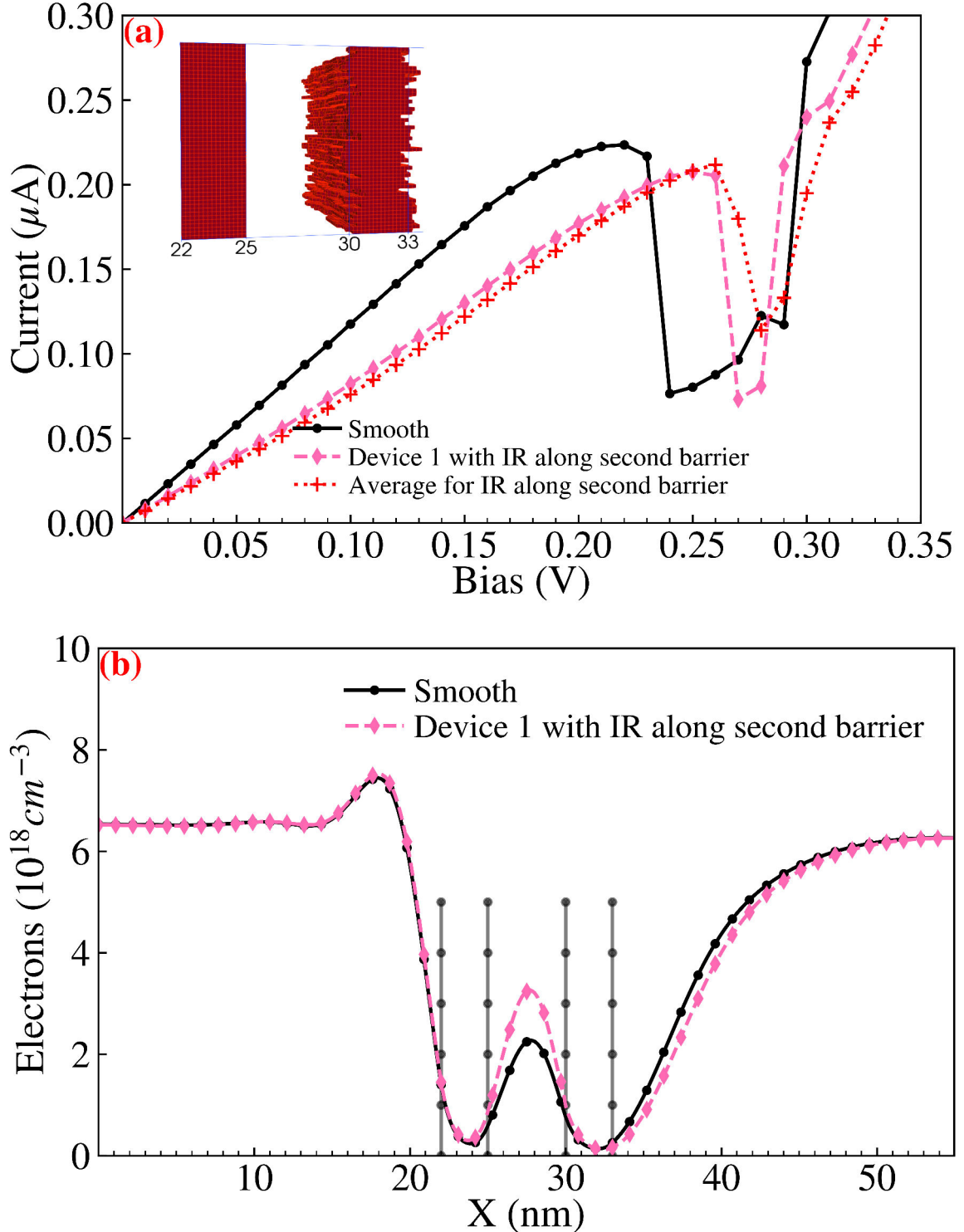


**Figure 5.3:** Comparison of IV characteristics (figure(a)) and electron charge density (figure(b)), through the centre of RTD cross-sections, for the ‘smooth’ RTD (black solid line with dot markers) depicted in Fig. 5.7 and device 1 with IR along the second  $\text{Al}_{0.3}\text{Ga}_{0.7}\text{As}$  barrier (pink dashed line with diamond markers). Within figure(b), barrier interface positions are noted with slightly transparent vertical lines with dot markers. Figure(a) also depicts the average IV characteristic (red dotted line with diagonal cross markers), and the  $\text{Al}_{0.3}\text{Ga}_{0.7}\text{As}$  barriers for device 1 with a rough second barrier as an inset. This figure is reproduced based on Figure 16 from [8], which is licensed under CC BY 4.0.

With Fig. 5.3(a), the IV characteristic of the rough second barrier acts as if the barrier was thicker than the ‘smooth’ baseline RTD, similar to what is seen in Fig. 3.13(a) with  $L_{B2}=4\text{nm}$ . There is a perturbation of the resonant peak bias  $V_r$  to greater bias, with  $V_r$  increasing from 0.22V to 0.25V, and a slight reduction in current, with  $I_r$  decreasing from  $0.224\mu\text{A}$  to  $0.208\mu\text{A}$ . I also observe greater QW charge density in Fig. 5.3(b), as with  $L_{B2}=4\text{nm}$ , due to charge accumulating behind the second barrier. The average resonant peak IV values of 25 devices with IR along the second barrier shows a similar perturbation from  $I_r=0.224\mu\text{A}$  and  $V_r=0.22\text{V}$ , with a slight reduction to  $I_r=0.214\mu\text{A}$  and an increase to  $V_r=0.266\text{V}$ .

To summarise this subsection, IR along barriers leads to effective thickening of barriers, except for slightly increased emitter region charge density with rough first barriers. Similarly, IR along the QW leads to an effective narrowing of the QW, aside from a slightly reduced current and charge density.

### 5.2.2 RTDs with Full IR

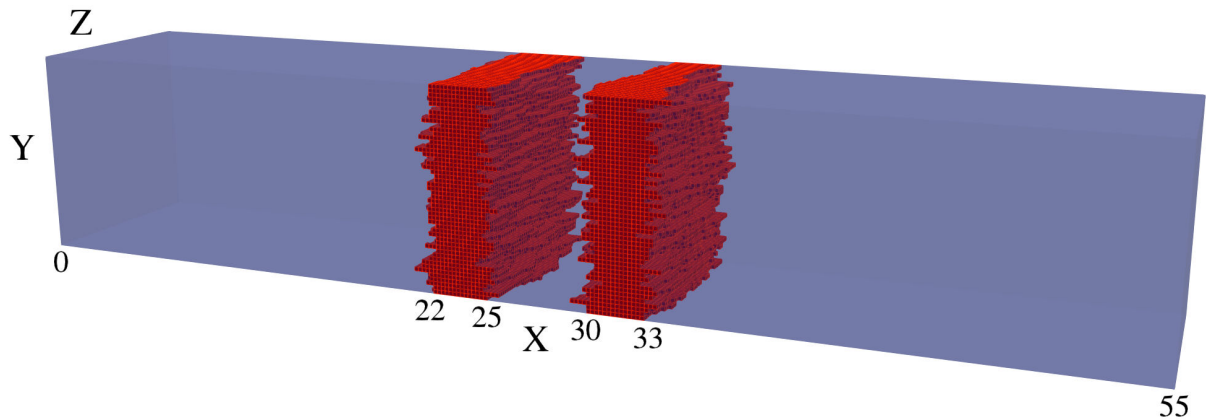


**Figure 5.4:** A depiction of device 3 with IR along all  $\text{Al}_{0.3}\text{Ga}_{0.7}\text{As}/\text{GaAs}$  interfaces. The rough  $\text{Al}_{0.3}\text{Ga}_{0.7}\text{As}$  barriers are red, and are situated in the partially transparent blue GaAs body.

In this subsection I depict the case with IR along all four  $\text{Al}_{0.3}\text{Ga}_{0.7}\text{As}/\text{GaAs}$  interfaces, plotting the IV characteristics for the 25 randomly generated devices (grey dashed lines) in Fig. 5.5 along with an average (red dotted line with diagonal cross markers) and a comparison to the ‘smooth’ device (black solid line with dot markers) in Fig. 3.2. In particular, I investigate device 3 with full roughness, as depicted in Fig. 5.4.

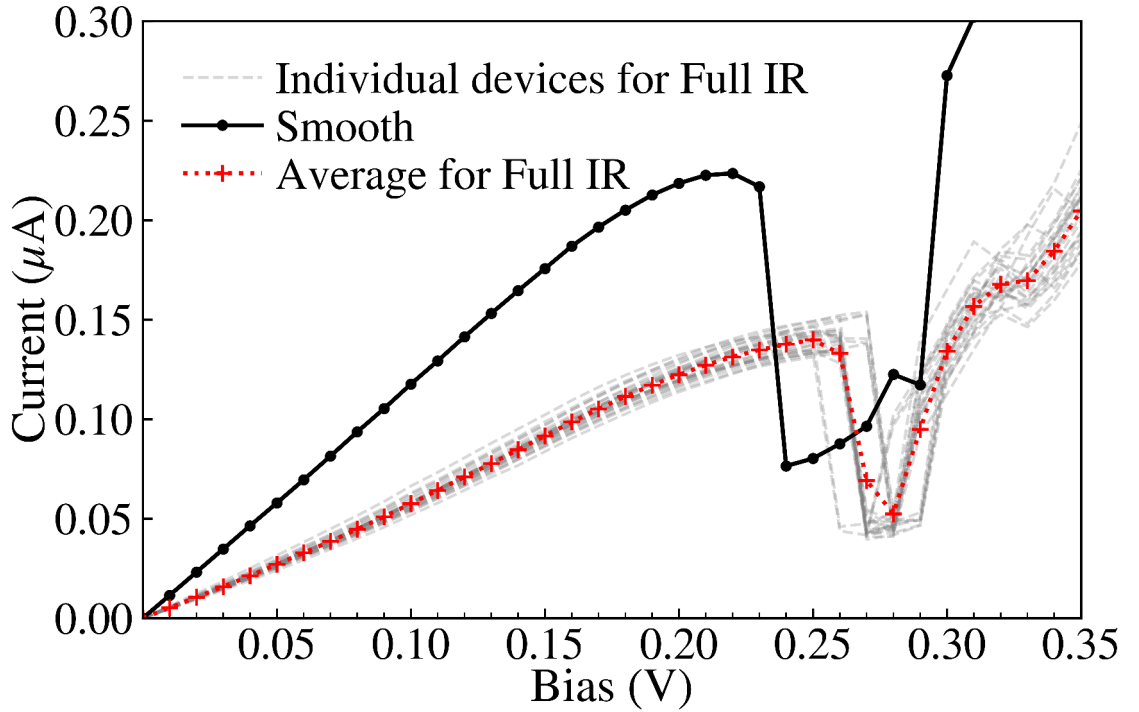


**Figure 5.5:** IV characteristics of 25 randomly generated RTDs (grey dashed lines) with IR along all  $\text{Al}_{0.3}\text{Ga}_{0.7}\text{As}/\text{GaAs}$  interfaces [8], with an average (red dotted line with diagonal cross markers) and a ‘smooth’ RTD with no IR (black solid line with dot markers) plotted for comparison. This figure [8] is licensed under CC BY 4.0.

As shown in Fig. 5.5, IR leads to a noticeable decrease in current and a perturbation of the resonant peak bias  $V_r$  to greater bias for all devices in comparison to the ‘smooth’ case. This strong impact by IR with an RMS roughness asperity of 0.3nm, close to only one monolayer, showcases the importance of taking IR in RTD simulations. To further explore the behaviour of IR I have investigated device 3 with full IR, which is depicted in Fig. 5.4 with red coloured rough  $\text{Al}_{0.3}\text{Ga}_{0.7}\text{As}$  barriers.

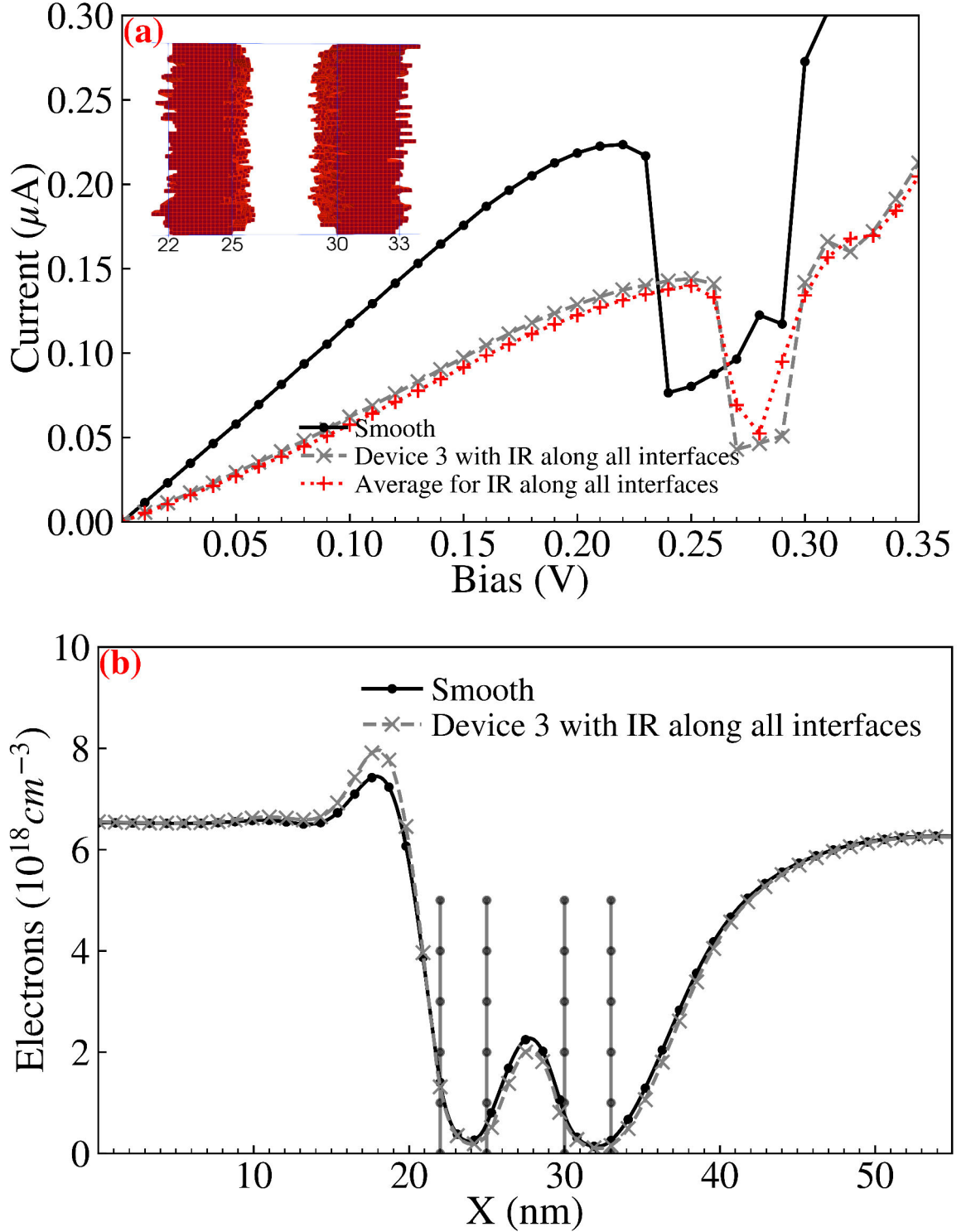


**Figure 5.6:** Comparison of IV characteristics (figure(a)) and electron charge density (figure(b)), through the centre of RTD cross-sections, for the ‘smooth’ RTD (black solid line with dot markers) depicted in Fig. 5.7 and device 3 with full IR along all Al<sub>0.3</sub>Ga<sub>0.7</sub>As/GaAs interfaces (grey dashed line with diagonal cross markers) depicted in Fig. 5.4. Within figure(b), barrier interface positions are noted with slightly transparent vertical lines with dot markers. For comparison, the average IV characteristic (red dotted line with diagonal cross markers) is also plotted in figure(a). The inset for figure(a) are the Al<sub>0.3</sub>Ga<sub>0.7</sub>A barriers of device 3. This figure is reproduced based on Figure 18 from [8], which is licensed under CC BY 4.0.

Device 3 with full IR is representative of the ensemble of randomly generated devices, as shown by the similarity of its IV characteristic (grey dashed line with diagonal cross markers) with the average (red dotted line with diagonal cross markers) in Fig. 5.6(a). Compared to the ‘smooth’ case, current has reduced from  $I_r=0.224\mu\text{A}$  to  $0.144\mu\text{A}$  and the resonant peak bias  $V_r$  has perturbed to greater bias with  $V_r$  increasing from 0.22V to 0.25V. The average resonant peak IV values of 25 devices with full IR shows a similar perturbation from  $I_r=0.224\mu\text{A}$  and  $V_r=0.22\text{V}$ , with a decrease to  $I_r=0.142\mu\text{A}$  and an increase to  $V_r=0.258\text{V}$ . There is also a slight reduction in QW charge density and an increase in emitter charge density plotted for the resonant peak, compared to the smooth case, in Fig. 5.6(b).

The contributions from IR along different parts of the RTD to device 3 with full roughness in Fig. 5.6 can be considered by comparing with the preceding subsection 5.2.1. The reduction in current and QW charge density seems to be due to effectively thicker barriers with IR. This behaviour is also observed for thicker ‘smooth’ symmetrical  $L_{B1}=L_{B2}=4\text{nm}$  barriers in Fig. 3.9. The perturbation of the resonant peak bias  $V_r$  to higher bias appears to be caused by the effectively narrower QW brought about by IR along the QW. The slight reduction in QW charge density in Fig. 5.6(b) means that this perturbation in the resonant peak bias  $V_r$  to higher bias is not due to the space-charge density. The perturbation in the resonant peak bias  $V_r$  to higher bias can instead be explained by the increased ground QW energy eigenvalue brought about by an effectively narrower QW. The pronounced impact observed in Fig. 5.6 is caused by IR with an RMS asperity of only  $0.3\text{nm}$ , close to a monolayer. This notable change caused by IR highlights the importance of including IR in RTD simulations. And the observed changes in the effective barrier and QW thicknesses puts forward considerations for future design and optimisation of RTDs.

## 5.3 Interface Roughness in RTDs for PUFs

The purpose of this section is to first study the impact of IR with different asperity  $\Delta_{RMS}$  and correlation lengths  $L_C$  on ensembles of 25 RTDs in subsection 5.3.1, and to then explore the possibility of using the variation of the resonant peak of RTDs with IR to encode information as part of a PUF in subsection 5.3.2.

All simulations were in the ballistic regime for this section. A maximum of 120 NEGF-Poisson convergence loops were allowed for this section due to the comparatively quicker simulations in the ballistic regime and greater availability of computing resources at the time. Other simulation parameters are as described within section 2.5.

### 5.3.1 Variation in Asperity and Correlation Length

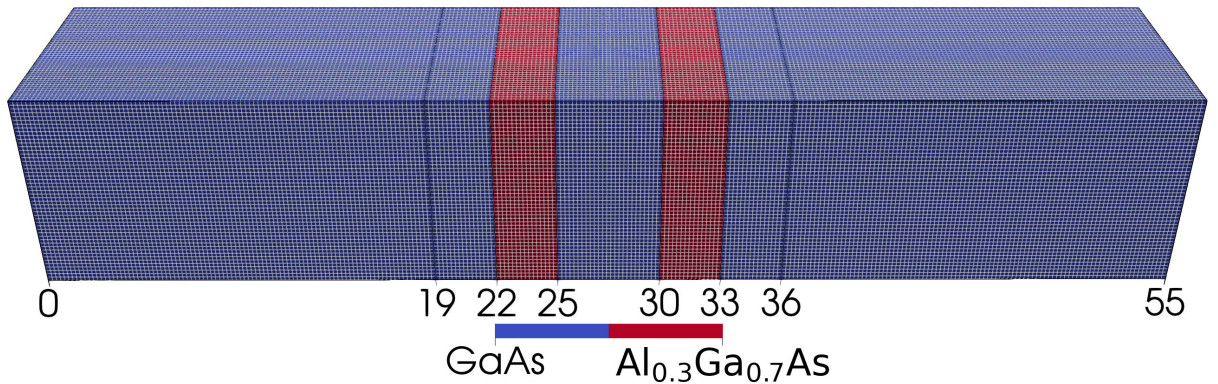


**Figure 5.7:** The GaAs-Al<sub>0.3</sub>Ga<sub>0.7</sub>As RTD under investigation [9]. This is a 55nm long GaAs nanowire with a 10nm×10nm cross-section, interrupted by two Al<sub>0.3</sub>Ga<sub>0.7</sub>As barriers. The device can be split into three regions, the 19nm source and drain which are  $2 \times 10^{18} \text{ cm}^{-3}$  n-doped, and the central 17nm device region which is  $1 \times 10^{15} \text{ cm}^{-3}$  n-doped. This central region has two 3nm buffer regions enclosing the 3nm Al<sub>0.3</sub>Ga<sub>0.7</sub>As, which themselves enclose a 5nm QW. This particular device is 'smooth' because IR has not been implemented. This figure [9] is licensed under CC BY 4.0.

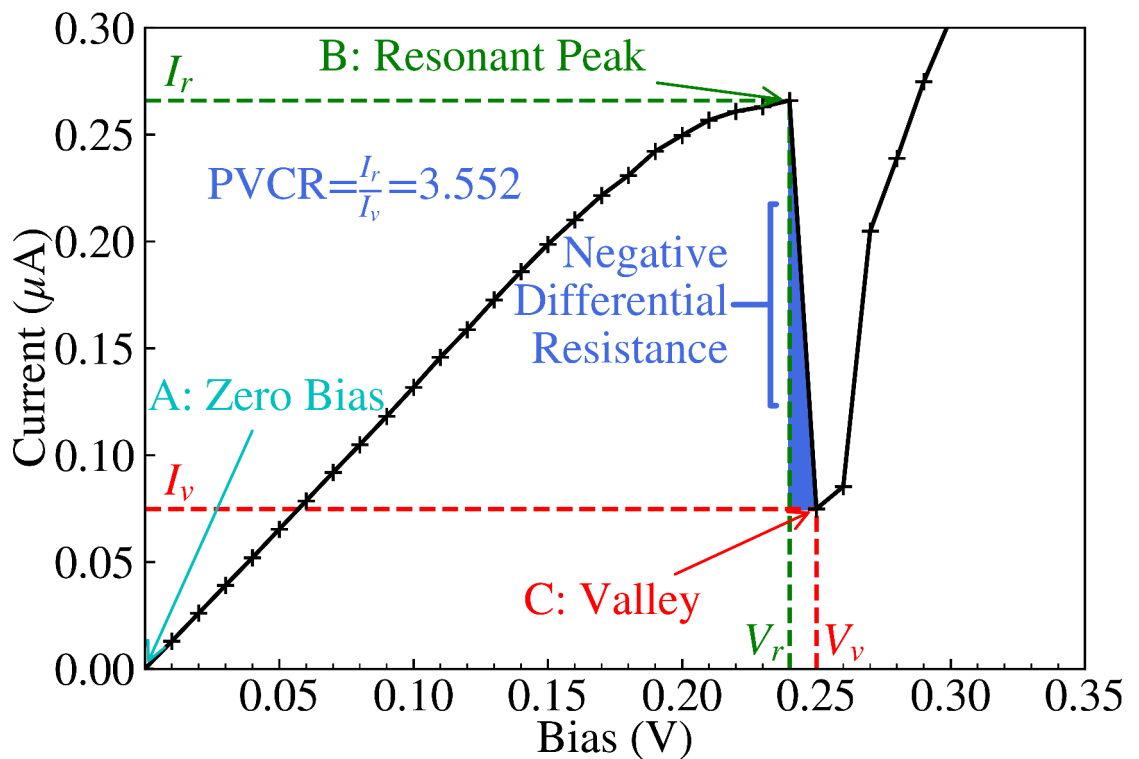


**Figure 5.8:** The annotated IV characteristic of the ‘smooth’ RTD [9] shown in Fig. 5.7, simulated in the ballistic regime. This figure [9] is licensed under CC BY 4.0.

A smooth RTD is depicted in 5.7, with the corresponding IV characteristic shown in Fig. 5.8 as an object of comparison.

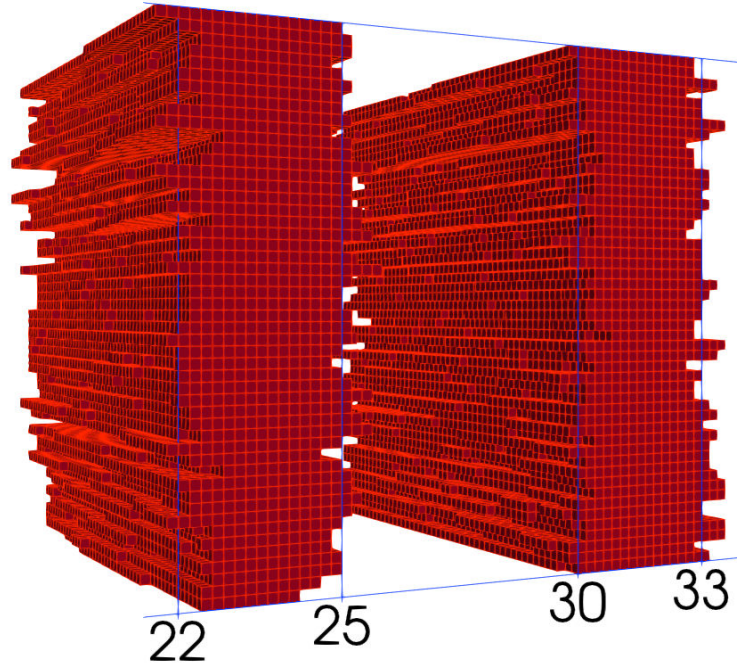


**Figure 5.9:** Al<sub>0.3</sub>Ga<sub>0.7</sub>As barriers for Device No. 1 with IR with an  $L_C$  of 7.5nm and  $\Delta_{RMS}$  of 0.3nm [9]. This figure [9] is licensed under CC BY 4.0.

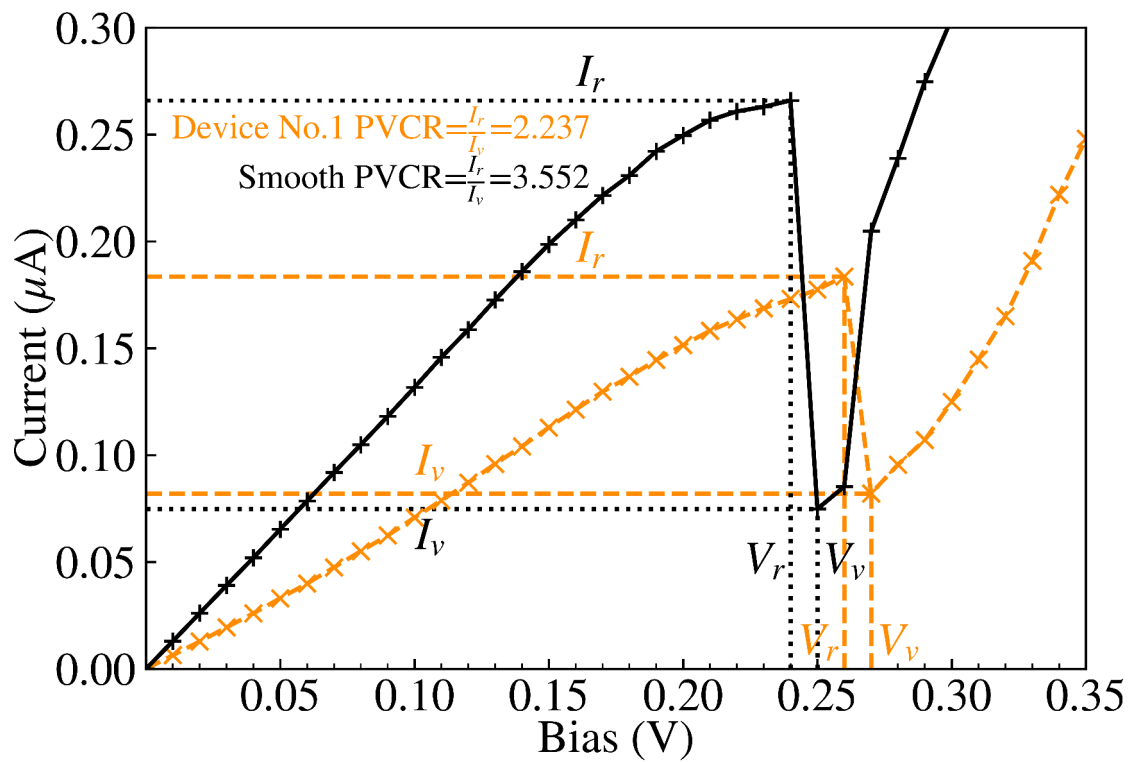


**Figure 5.10:** IV characteristics for Device No. 1 (orange dashed line) [9], corresponding to the rough Al<sub>0.3</sub>Ga<sub>0.7</sub>As barriers in Fig. 5.9, and a 'smooth' RTD IV characteristic (black solid line) as shown in Fig. 5.8. This figure [9] is licensed under CC BY 4.0.

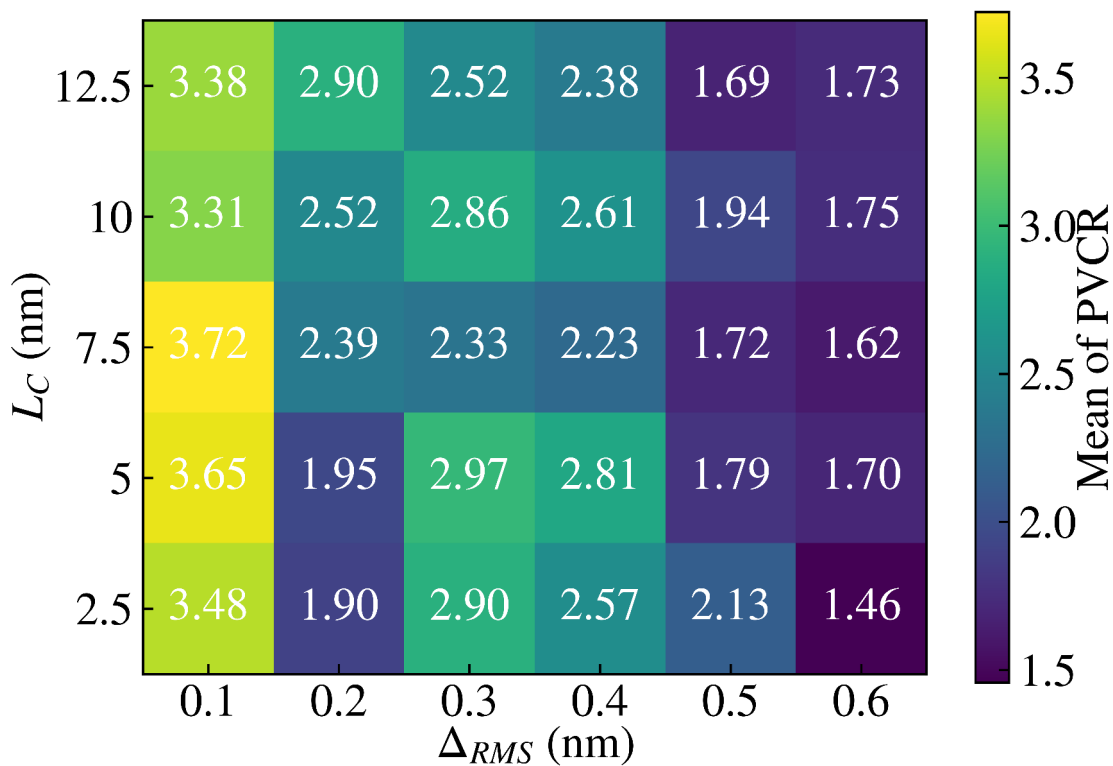


**Figure 5.11:** Colour-map of the mean of PVCR of 25 RTDs with randomly generated IR, for different  $L_C$  and  $\Delta_{RMS}$ . This figure is reproduced based on Figure 7 from [9], which is licensed under CC BY 4.0.

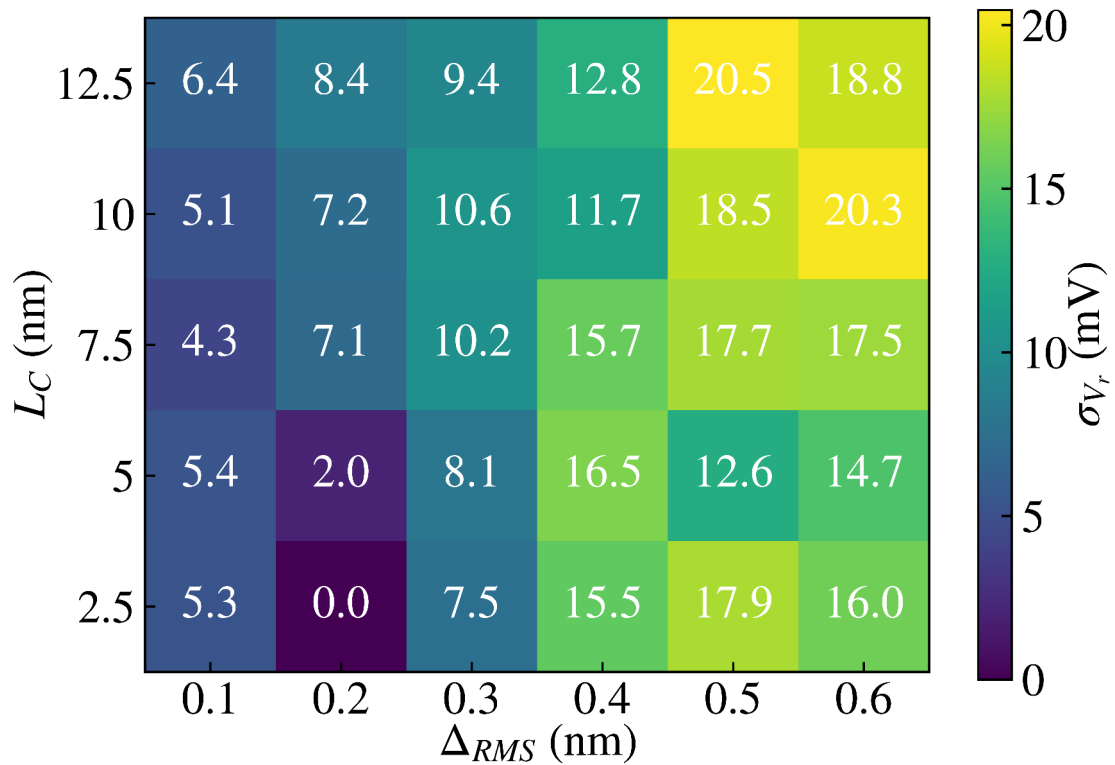


**Figure 5.12:** Colour-map of standard deviation of fitted normal curves to the distribution of the resonant peak voltage  $V_r$ , of 25 RTDs with randomly generated IR, for different  $L_C$  and  $\Delta_{RMS}$ . This figure is reproduced based on Figure 7 from [9], which is licensed under CC BY 4.0.

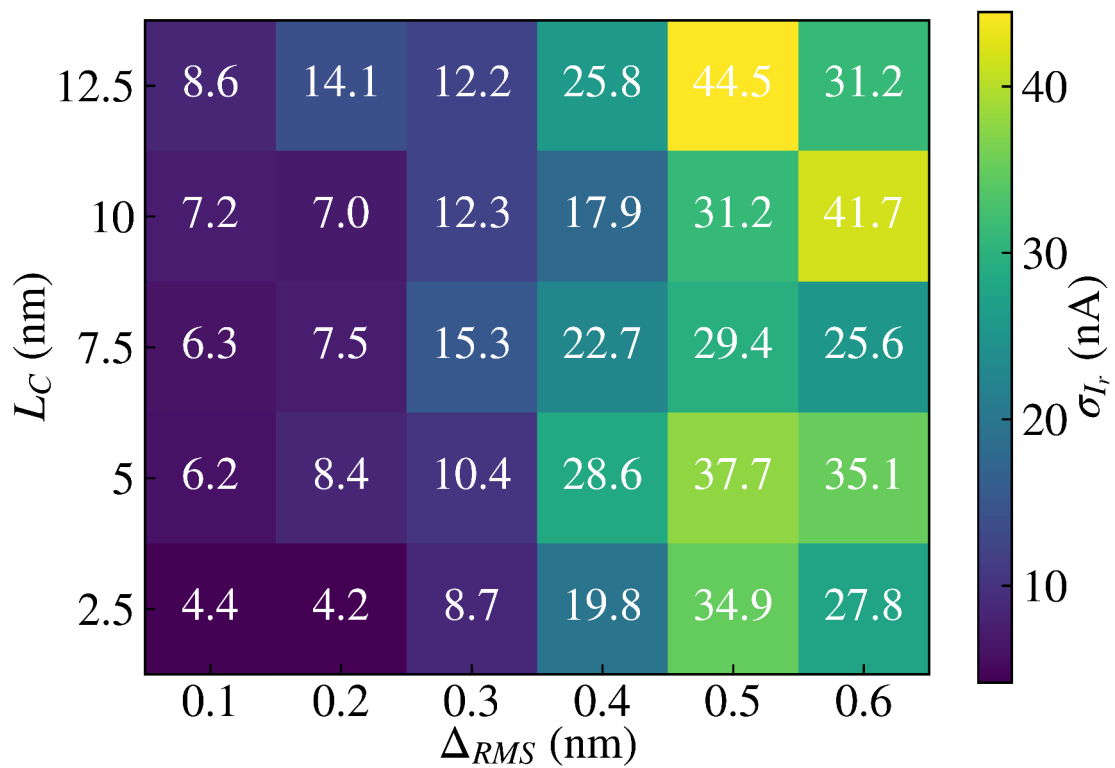


**Figure 5.13:** Colour-map of standard deviation of fitted normal curves to the distribution of the resonant peak current  $I_r$ , of 25 RTDs with randomly generated IR, for different  $L_C$  and  $\Delta_{RMS}$ . This figure is reproduced based on Figure 7 from [9], which is licensed under CC BY 4.0.

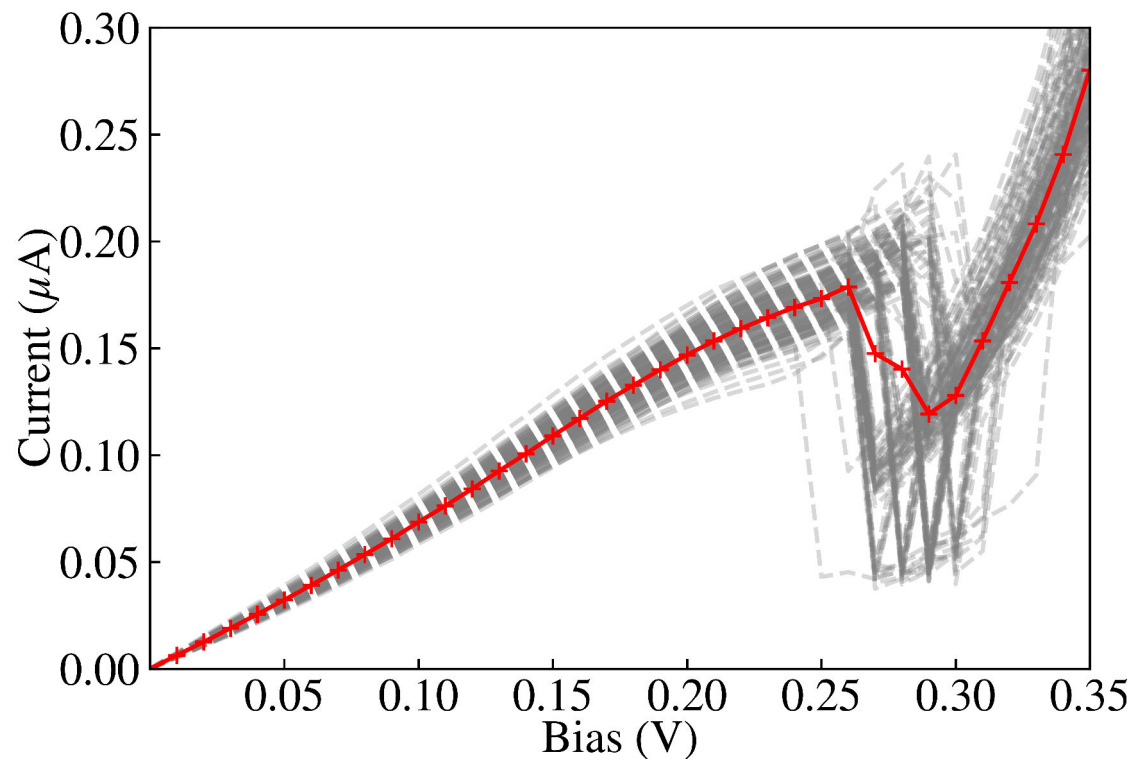


**Figure 5.14:** IV characteristics for 150 randomly generated RTDs with exponential IR of  $L_C=7.5\text{nm}$  and  $\Delta_{RMS}=0.3\text{nm}$  as grey dashed lines [9]. The mean current-voltage characteristic is a solid red line with plus markers. This figure [9] is licensed under CC BY 4.0.

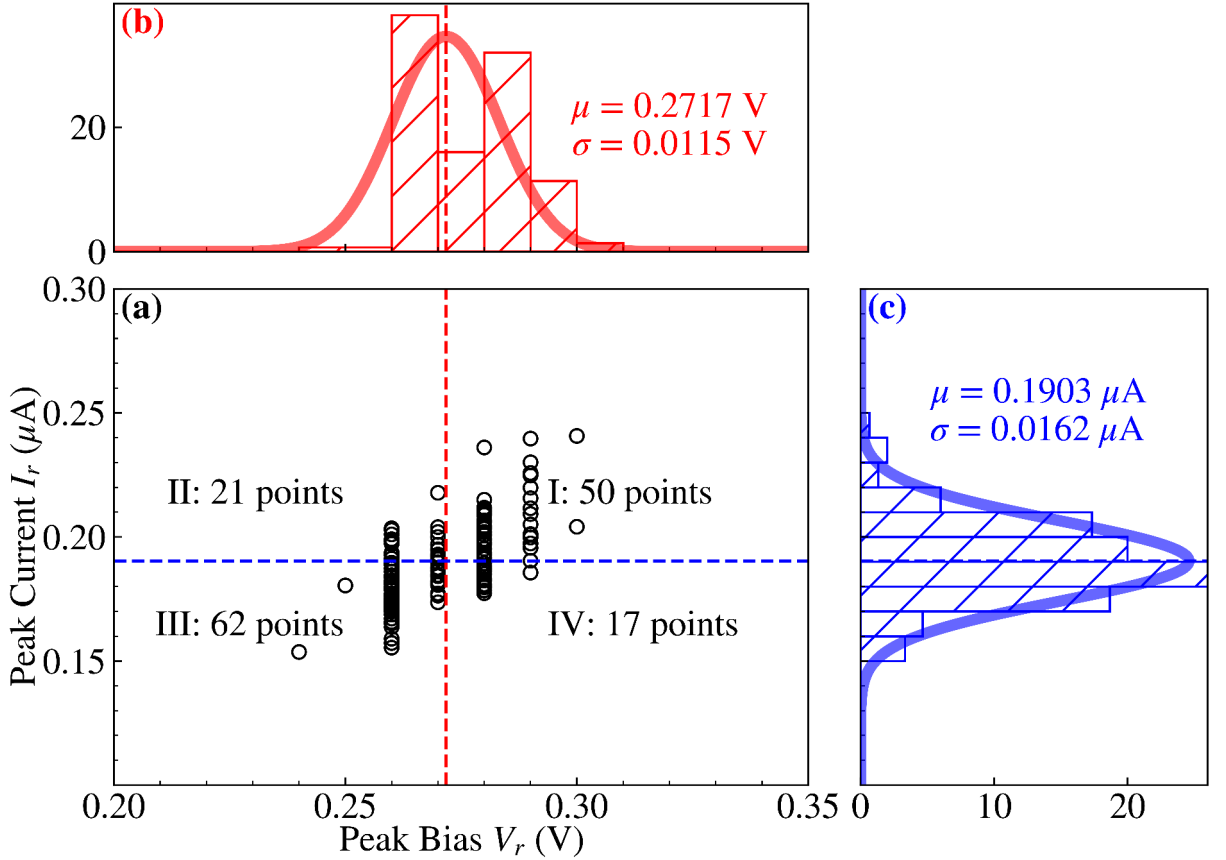


**Figure 5.15:** The resonant peak, or local maxima, of each current-voltage characteristic in Fig. 5.14 is shown in figure(a) and is split into 4 quadrants by the mean for the voltage (0.2717 V) and current (0.1903  $\mu\text{A}$ ) distributions as seen in figure(b) and figure(c) respectively. Figure(b) and figure(c) also show histograms and fitted normal distributions for occurrence of resonant peak values. This figure [9] is licensed under CC BY 4.0.

The  $\text{Al}_{0.3}\text{Ga}_{0.7}\text{As}$  barriers of Device No. 1 which has an IR with an  $L_C$  of 7.5nm and  $\Delta_{RMS}$  of 0.3nm are shown in Fig. 5.9, and the corresponding IV characteristic (orange dashed line) is compared against the ‘smooth’ RTD (black solid line) in Fig. 5.10. IR leads to a reduction in current and a drop in PVCR from  $\sim 3.6$  to  $\sim 2.2$ , and a perturbation in the NDR to higher bias by 0.02V.

To investigate the impact of varying correlation length  $L_C$  and roughness asperity  $\Delta_{RMS}$ , I randomly generated 25 RTD devices for each set of parameters. From these sets I extracted the mean of the PVCR and the standard deviation of voltage and current for the resonant peak, and plotted them respectively in Fig. 5.11, Fig. 5.12, and Fig. 5.13. In Fig. 5.11, Fig. 5.12, and Fig. 5.13 the main effect is due to  $\Delta_{RMS}$ , which as it increases leads

to a decrease in the PVCR and an increase in the standard deviations. Hence, for the purposes of designing RTDs with IR to encode information with the variation of resonant peak current and voltage,  $\Delta_{RMS}$  is an important factor to take into account for further research and manufacturing.

### 5.3.2 Min-entropy of RTDs with IR

In Fig. 5.11, Fig. 5.12 and Fig. 5.13  $\Delta_{RMS}=0.3\text{nm}$  and  $L_C=7.5\text{nm}$  balance a moderate PVCR with moderately large standard deviations, and is similar to the parameters studied in [160], so further investigation was carried out with this set of parameters. I simulated 150 RTDs, resulting in the IV curves (grey dashed lines) in Fig. 5.14 and the scatterplot of corresponding resonant peak values and attached histograms in Fig. 5.15. By splitting the scatterplot in Fig. 5.15(a) into quadrants with the mean of the current and voltage distributions, it is possible to encode information in which quadrant the resonant peak appears in. Using the most conservative measure of information min-entropy [22, 137],  $H_{min} = -\log_2(p_{max})$  where  $p_{max}$  is the probability of the most likely result, results in  $H_{min} = -\log_2(\frac{62}{150}) = 1.275$ . This means that a PUF composed of 100 RTDs can encode 127 bits. This described approach considers a PUF formed of RTDs as an array where each element corresponds to an RTD in one of 4 possible quadrant states. While this does not consider possible issues such as mismeasuring resonant current and voltage as being in the wrong quadrant, it nevertheless supports the case of RTDs with IR as PUF components.

## 5.4 Impact of IR Correlation on RTD Variation

Within this section, I introduce a new implementation of roughness that is described within subsection 2.2.3, which can be generated using two correlation lengths along a plane, allowing anisotropic IR and providing a more accurate model for practical devices. RTDs serve as an ideal test case for verifying this methodology used in simulation structure generation, due to their relatively simple structure.

Simulation parameters are set as listed within section 2.5, except with the ballistic regime used for efficient statistical simulation. A rather generous NEGF-Poisson convergence loop condition of 300 was used due to the great availability of computational resources with few other users at the time and the comparatively quicker simulations in the ballistic regime, compared to with electron-phonon scattering. In subsection 5.4.1 IR is compared with the previous implementation and the following subsection 5.4.2 briefly investigates anisotropic IR with two different correlation lengths.

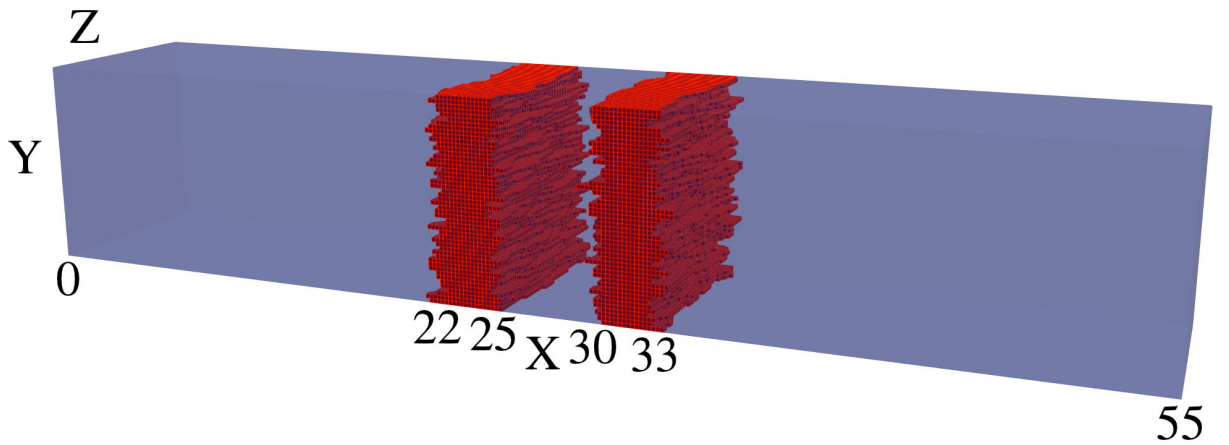


**Figure 5.16:** Visualisation of device 3 generated with an IR of correlation length  $L_C=2.5\text{nm}$  [10], one of 25 such RTD devices. The rough  $\text{Al}_{0.3}\text{Ga}_{0.7}\text{As}$  barriers (shown in red) are embedded within a GaAs (transparent blue) nanowire body. This figure [10] is licensed under CC BY 4.0.

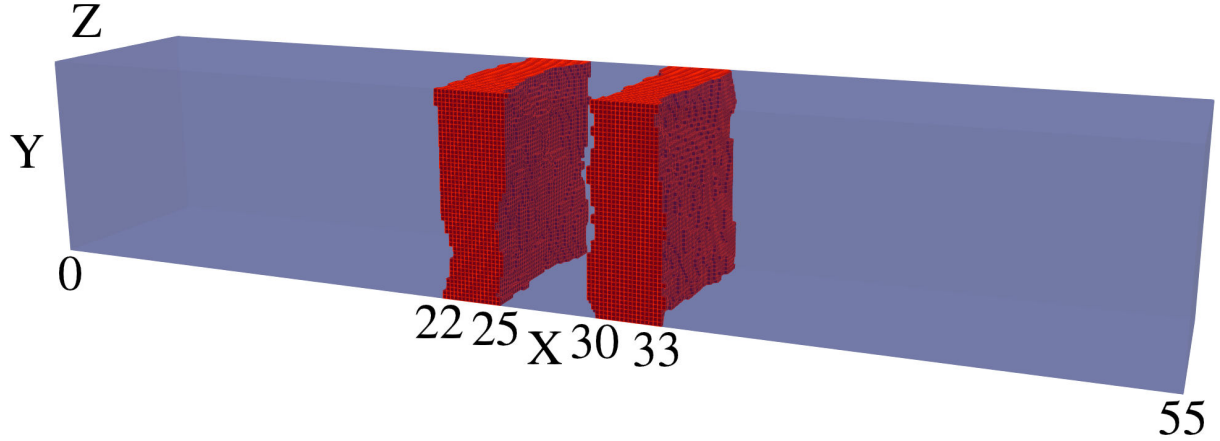


**Figure 5.17:** Visualisation of device 15 generated with ‘improved’ IR of isotropic correlation lengths  $L_C^Y=L_C^Z=2.5\text{nm}$  [10], one of 25 such RTD devices. The rough  $\text{Al}_{0.3}\text{Ga}_{0.7}\text{As}$  barriers (shown in red) are embedded within a GaAs (transparent blue) nanowire body. This figure [10] is licensed under CC BY 4.0.

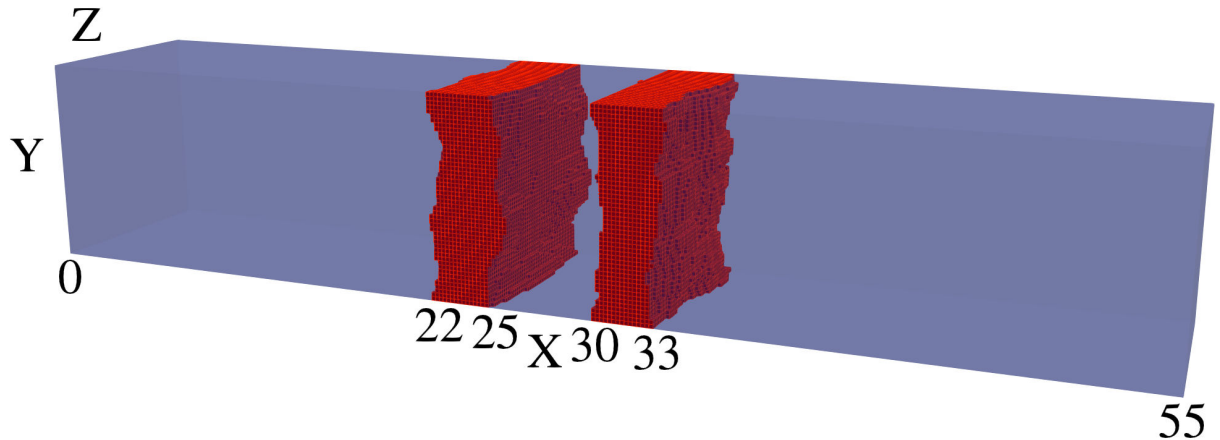


**Figure 5.18:** Visualisation of device 23 generated with ‘improved’ IR of anisotropic correlation lengths  $L_C^Y=2.5\text{nm}$  and  $L_C^Z=5\text{nm}$  [10], one of 25 such RTD devices. The rough  $\text{Al}_{0.3}\text{Ga}_{0.7}\text{As}$  barriers (shown in red) are embedded within a GaAs (transparent blue) nanowire body. This figure [10] is licensed under CC BY 4.0.

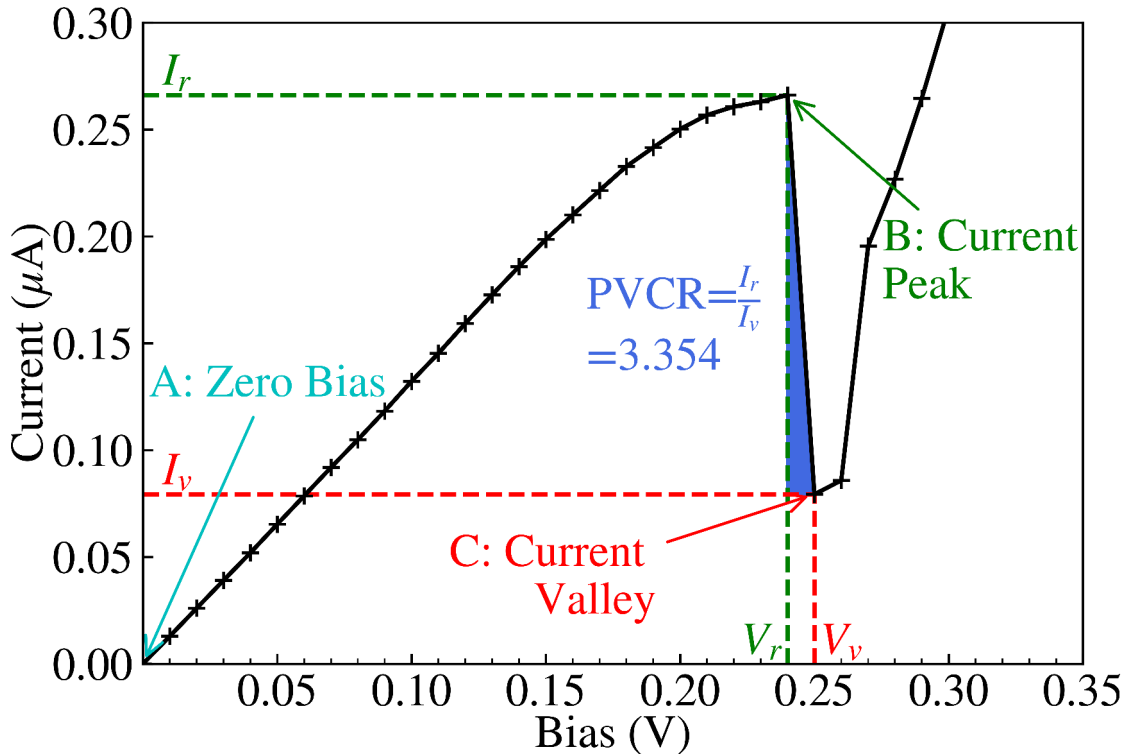


**Figure 5.19:** IV characteristic for the baseline RTD [10] shown in Fig. 5.7. The resonant peak, or local maxima in current  $I_r=0.2661\mu\text{A}$  at bias  $V_r=0.24\text{V}$ , and the valley, or local minima  $I_v=0.0793\mu\text{A}$  at  $V_v=0.25\text{V}$ , are two key points for this nonlinear IV characteristic. These bound the NDR, and define the figure of merit PVCR  $I_r/I_v$ . This figure [10] is licensed under CC BY 4.0.

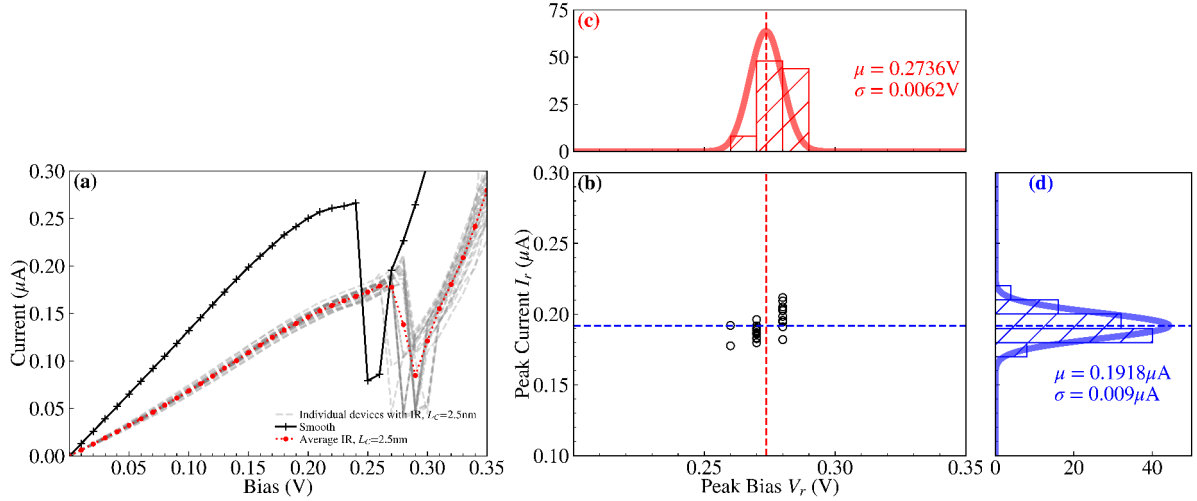


**Figure 5.20:** A composite figure [10] visualising the IV characteristics of 25 RTDs generated with an IR of correlation length  $L_C=2.5\text{nm}$ . Figure(a) depicts all the IV characteristics (grey dashed lines), with an average (red dotted line with dot markers) and a 'smooth' RTD (solid black line with plus markers) for comparison. Figure(b) is a scatterplot of the resonant peak IV values taken from figure(a), and is bifurcated with dashed lines at the mean values of the resonant peak values,  $V_r=0.2736\text{V}$  and  $I_r=0.1918\mu\text{A}$ . Figure(c) and figure(d) are accompanying histograms and fitted normal distributions for the resonant peak voltage  $V_r$  and current  $I_r$  distributions respectively. This figure [10] is licensed under CC BY 4.0.

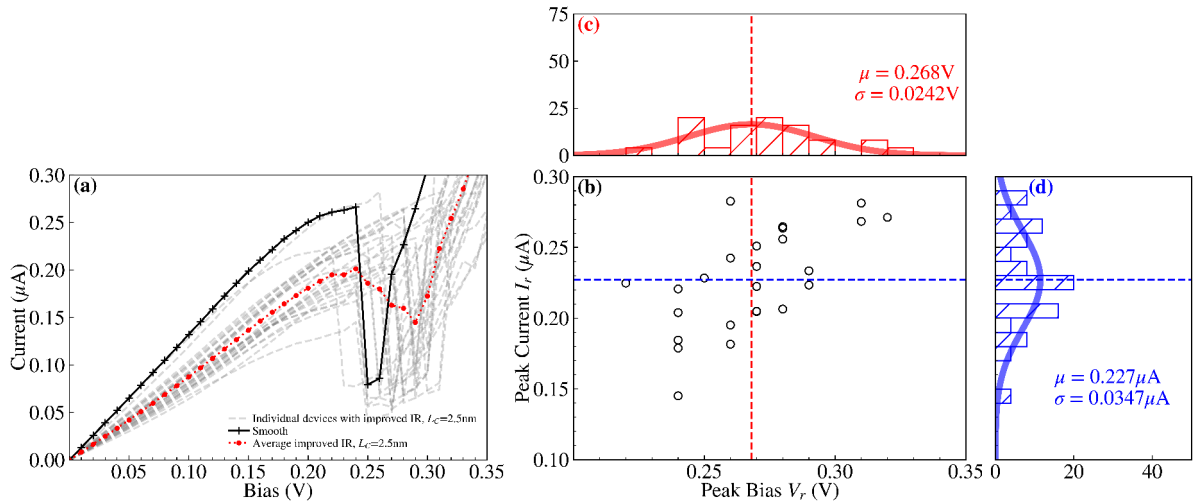


**Figure 5.21:** A composite figure [10] visualising the IV characteristics of 25 RTDs generated with an 'improved' isotropic IR of correlation lengths  $L_C^Y=L_C^Z=2.5\text{nm}$ . Figure(a) depicts all the IV characteristics (grey dashed lines), with an average (red dotted line with dot markers) and a 'smooth' RTD (solid black line with plus markers) for comparison. Figure(b) is a scatterplot of the resonant peak IV values taken from figure(a), and is bifurcated with dashed lines at the mean values of the resonant peak values,  $V_r=0.2680\text{V}$  and  $I_r=0.2270\mu\text{A}$ . Figure(c) and figure(d) are accompanying histograms and fitted normal distributions for the resonant peak voltage  $V_r$  and current  $I_r$  distributions respectively. This figure [10] is licensed under CC BY 4.0.

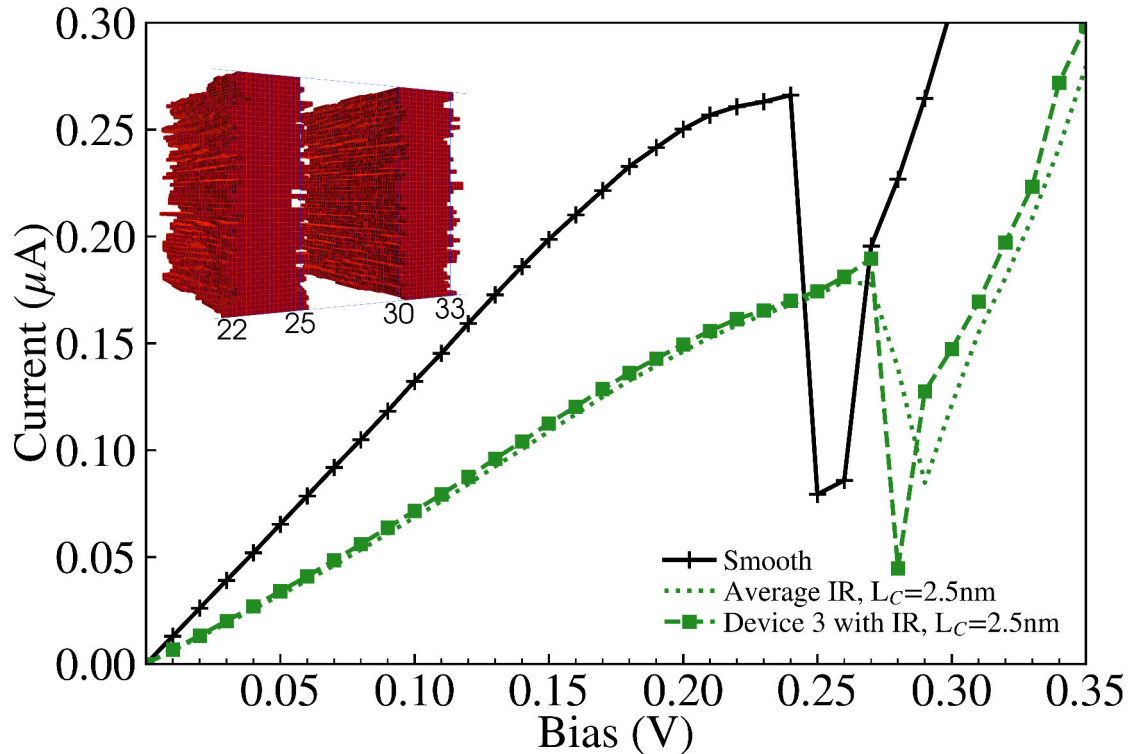


**Figure 5.22:** IV characteristics for device 3 (green dashed line with square markers) and the average (green dotted line) with IR of correlation length  $L_C=2.5\text{nm}$ , compared against the 'smooth' device IV characteristic (black solid line with plus markers) [10]. The inset contains the rough Al<sub>0.3</sub>Ga<sub>0.7</sub>As barriers for device 3, which is shown in Fig. 5.16. This figure [10] is licensed under CC BY 4.0.

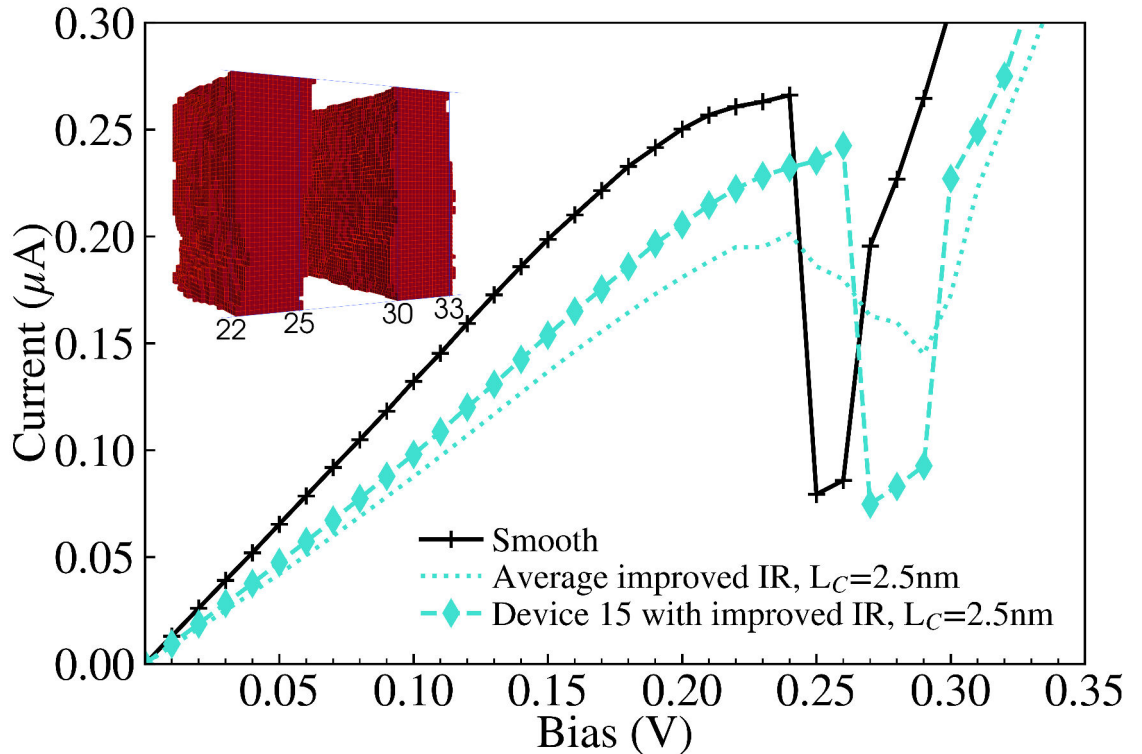


**Figure 5.23:** IV characteristics for device 15 (cyan dashed line with diamond markers) and the average (cyan dotted line) with ‘improved’ IR of correlation lengths  $L_C^Y=L_C^Z=2.5\text{nm}$ , compared against the ‘smooth’ device IV characteristic (black solid line with plus markers) [10]. The inset contains the rough  $\text{Al}_{0.3}\text{Ga}_{0.7}\text{As}$  barriers for device 15, which is shown in Fig. 5.17. This figure [10] is licensed under CC BY 4.0.

### 5.4.1 Improved Isotropic Interface Roughness

$L_C$ (nm)	IR		Improved IR	
	$V_r$ (V)	$I_r$ ( $\mu\text{A}$ )	$V_r$ (V)	$I_r$ ( $\mu\text{A}$ )
2.5	0.2736	0.1918	0.2680	0.2270
5.0	0.2764	0.1924	0.2716	0.2404
7.5	0.2788	0.1960	0.2640	0.2332
10.0	0.2748	0.1946	0.2536	0.2292

**Table 5.1:** Mean  $V_r$  and  $I_r$  for the previous and ‘improved’ IR for different correlation lengths [10].

$L_C$ (nm)	IR		Improved IR	
	$\sigma_{V_r}$ (mV)	$\sigma_{I_r}$ (nA)	$\sigma_{V_r}$ (mV)	$\sigma_{I_r}$ (nA)
2.5	6.2	9.0	24.2	34.7
5.0	6.9	10.2	28.7	47.6
7.5	11.4	17.2	35.9	68.8
10.0	11.7	18.8	38.8	80.9

**Table 5.2:** Standard deviations of  $V_r$  and  $I_r$  for the previous and ‘improved’ IR for different correlation lengths [10].

Within this subsection is a comparison of the previous implementation of IR with the ‘improved’ IR featuring isotropic correlation, while varying the correlation length from  $L_C=2.5\text{nm}$  to  $L_C=10\text{nm}$ . Fig. 5.20 and Fig. 5.21 each illustrate a distribution of 25 devices simulated with the previous and ‘improved’ IR models respectively, for  $L_C=2.5\text{nm}$ . Correspondingly, individual devices from these distributions are also presented in Fig. 5.22 and Fig. 5.23, and extracted values of the mean and standard deviation of resonant peak IV values are compared in Table 5.1 and Table 5.2 respectively.

A comparison of Fig. 5.20 and Fig. 5.21 shows that the use of the ‘improved’ IR generation method results in greater variation in the IV characteristics and the corresponding resonant peak current and voltage. The standard deviation of the resonant peak voltage and current are nearly four times greater with the ‘improved’ IR, increasing from 6.2mV and 9nA to 24.2mV and 34.7nA as shown in Table 5.2. For both distributions, the average resonant peak perturbs to a greater bias and lesser current than the ‘smooth’ case of  $I_r=0.2661\mu\text{A}$  at bias  $V_r=0.24\text{V}$ . As shown in Table 5.1, this perturbation in mean resonant peak values holds true for all the distributions simulated with IR. Additionally, for the ‘improved’ IR model, the mean  $I_r$  experiences a lesser reduction compared to the previous IR model, with greater mean  $I_r$  for all correlation lengths. Two specific device IV characteristics from these distributions of the previous and ‘improved’ IR are depicted respectively in Fig. 5.22 and Fig. 5.23, with the corresponding rough  $\text{Al}_{0.3}\text{Ga}_{0.7}\text{As}$  barriers shown in their inset and the average IV characteristics (dotted lines) also plotted. Stand-

ard deviations of resonant peak values for both IR models roughly double in magnitude as correlation length increases from  $L_C=2.5\text{nm}$  to  $L_C=10\text{nm}$  as shown in Table 5.2, with an increase from 6.2mV and 9nA to 11.7mV and 18.8nA for the previous IR model, and an increase from 24.2mV and 34.7nA to 38.8mV and 80.9nA for the ‘improved’ IR model.

#### 5.4.2 Improved Anisotropic Interface Roughness

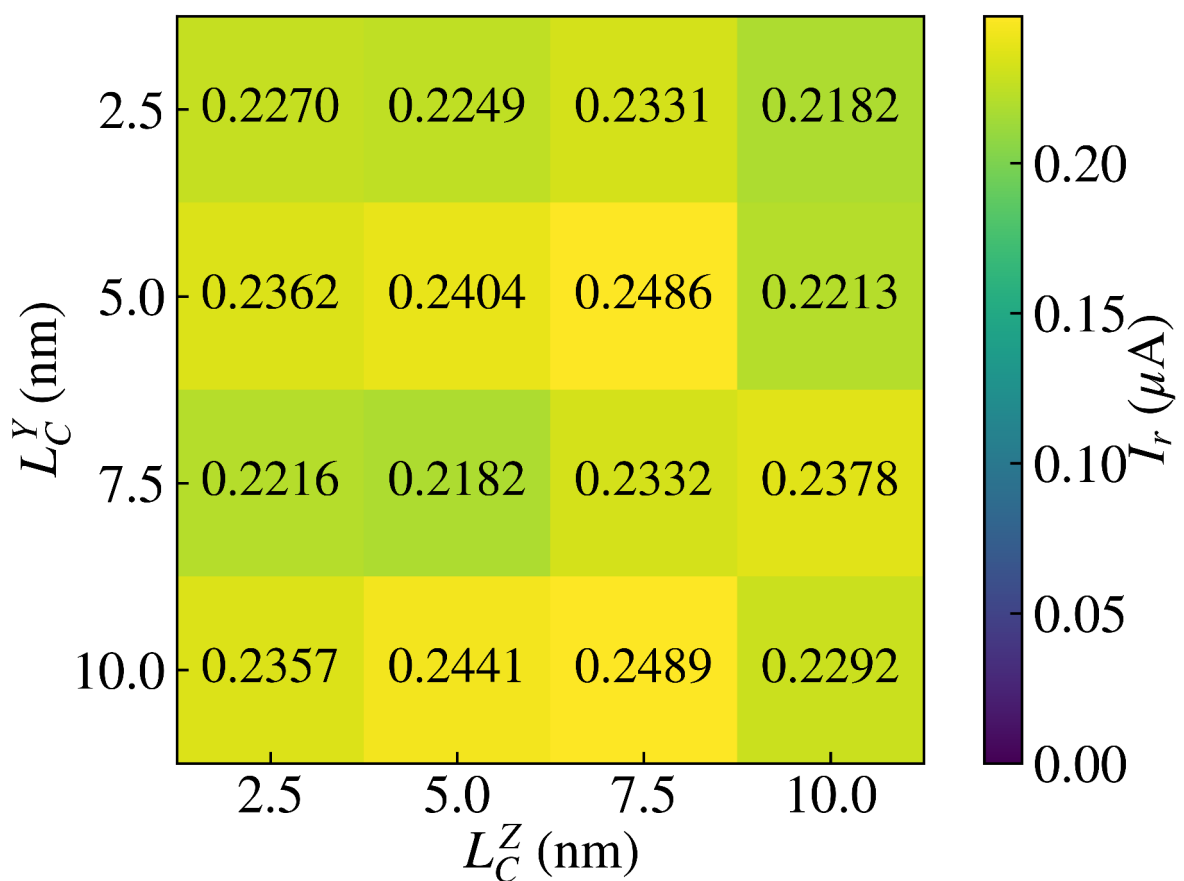


**Figure 5.24:** Mean of current peak  $I_r$  in microampere for different anisotropic correlation lengths  $L_C$  [10]. This figure [10] is licensed under CC BY 4.0.

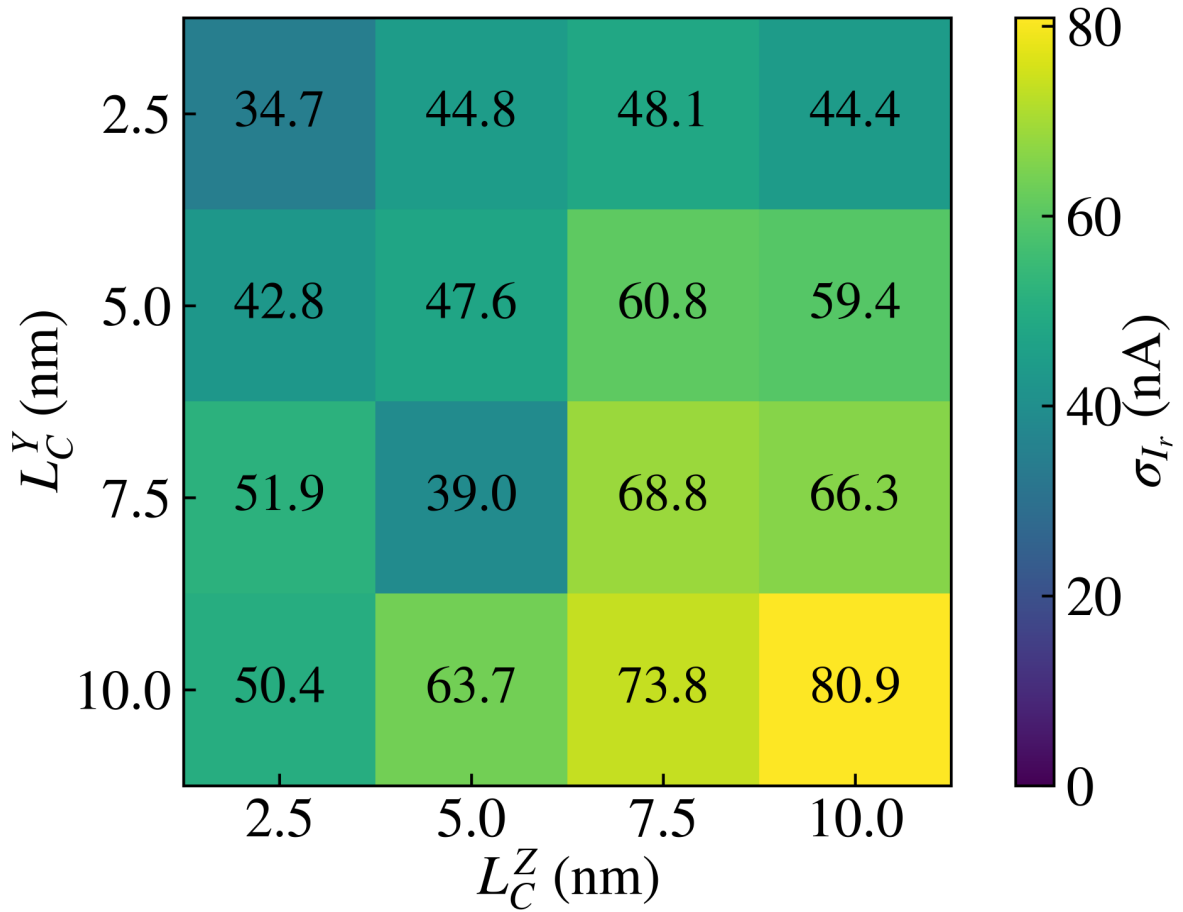


**Figure 5.25:** Standard deviation of current peak  $I_r$  in nanoampere for different anisotropic correlation lengths  $L_C$  [10]. This figure [10] is licensed under CC BY 4.0.

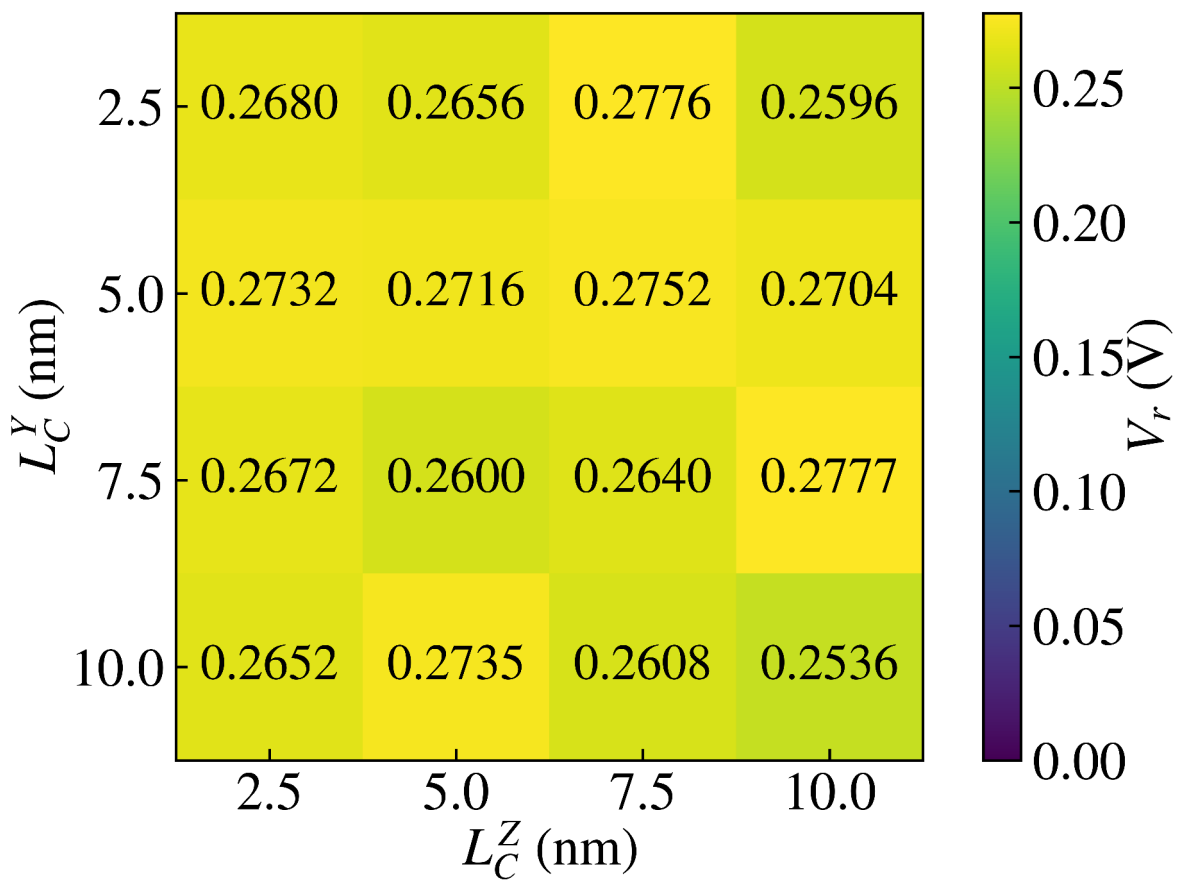


**Figure 5.26:** Mean of resonant voltage  $V_r$  in Volts for different anisotropic correlation lengths  $L_C$  [10]. This figure [10] is licensed under CC BY 4.0.

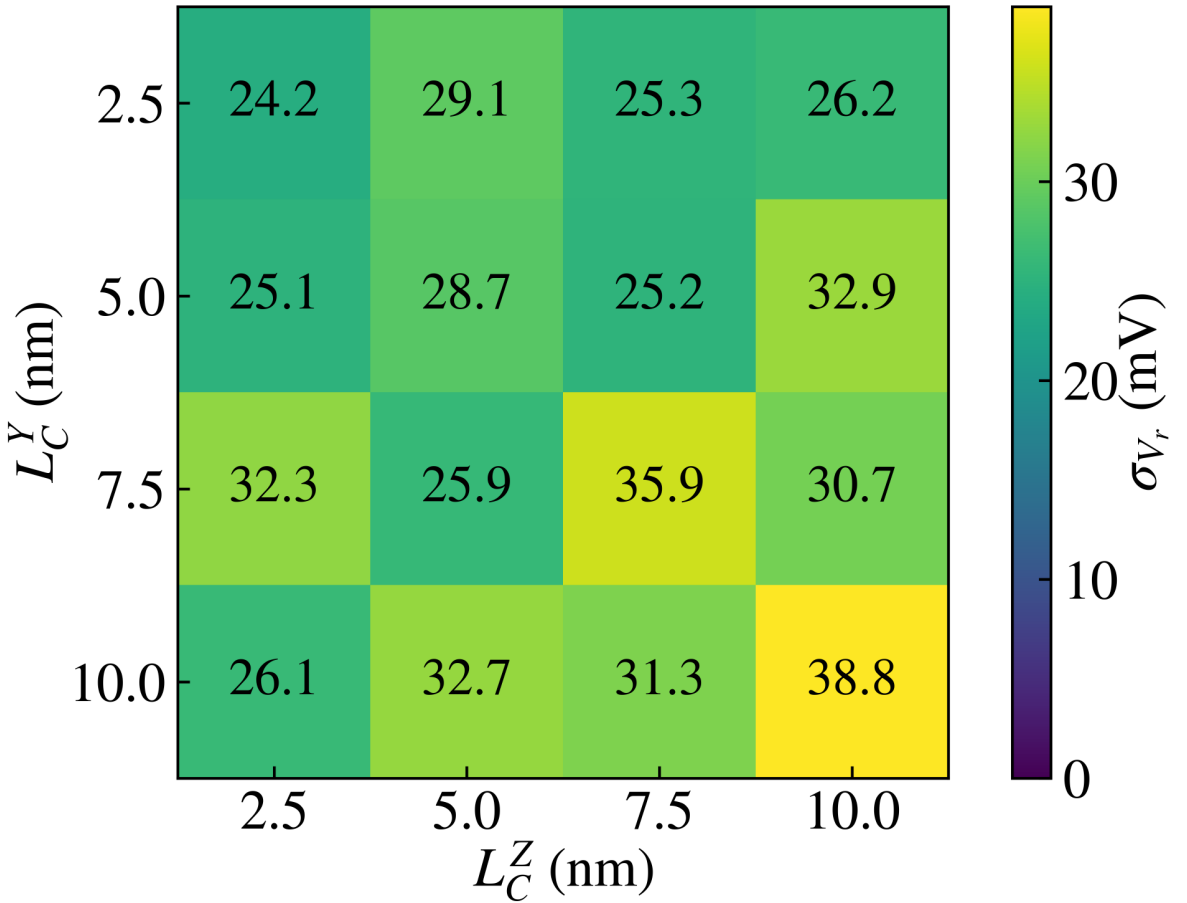


**Figure 5.27:** Standard deviation of resonant voltage  $V_r$  in millivolts for different anisotropic correlation lengths  $L_C$  [10]. This figure [10] is licensed under CC BY 4.0.

A new capacity of the ‘improved’ IR generation brought about by considering two correlation lengths is anisotropic IR, which is important because heterostructure interfaces often feature such anisotropic IR [238]. Fig. 5.24 and Fig. 5.25 represent the mean and standard deviation of  $I_r$  respectively for different anisotropic correlation lengths, and Fig. 5.26 and Fig. 5.27 similarly represent the mean and standard deviation of  $V_r$ . The diagonal grid values of these colour maps are for isotropic ‘improved’ isotropic roughness, as noted in Table 5.1 and Table 5.2. From Fig. 5.25 and Fig. 5.27, I found some variation in the standard deviations of resonant peak values, supporting the importance of including anisotropic IR for simulations of devices when studying device variation.

I have presented an improved simulation of roughness using NESS by including two correlation lengths to generate roughness along a plane, and used this to investigate Al<sub>0.3</sub>Ga<sub>0.7</sub>As/GaAs RTDs with IR along the Al<sub>0.3</sub>Ga<sub>0.7</sub>As barriers. The improved IR simulation approach has resulted in RTDs exhibiting greater variation in the IV characteristics across distributions of 25 RTDs with different correlation lengths. This variation has been quantified numerically as the standard deviation of resonant peak voltage  $V_r$  and current  $I_r$ . For a correlation length  $L_C=2.5\text{nm}$ , there is almost a four-fold increase in the standard deviations of resonant peak values, from 6.2mV and 9nA using the previous method to 24.2mV and 34.7nA with the improved IR method. Larger correlation lengths were found to increase the standard deviation of resonant peak values for both the previous and the new method, with the standard deviation roughly doubling as  $L_C$  increases from 2.5nm to 10nm. The improved IR generation method has also allowed me to measure standard deviations for anisotropic correlation, which exhibit variation with different correlation lengths. This increased variation and the ability to simulate anisotropic correlation lengths highlight the importance of this improvement to NESS, and suggests that future accurate simulations of device variation will require roughness with two correlation lengths.

## 5.5 Conclusion

In conclusion, IR was shown to have a significant effect on RTD behaviour, highlighting the importance of taking it into account for further research and development of RTDs.

IR along the first and second barriers leads to effectively thicker barriers regarding IV and charge density, except for increased emitter charge density for the case of a rough first barrier. IR along the inside of the QW results in an effectively thinner QW, except for slightly reduced current and QW charge density. The impact of IR along all four GaAs/Al<sub>0.3</sub>Ga<sub>0.7</sub>As interfaces can be explained by thicker effective barriers and a thinner

QW. Secondly, for a distribution of random devices  $\Delta_{RMS}$ , not  $L_C$ , was the main parameter to control IR. Increasing  $\Delta_{RMS}$  leads to a reduction of mean PVCR, and increased standard deviation of resonant peak IV values. For  $\Delta_{RMS}=0.3\text{nm}$  and  $L_C=7.5\text{nm}$ , I have found that RTDs with such IR could encode 1.275 bits in min-entropy, showing promise for RTDs with IR as a PUF component.

Lastly, an improved simulation of roughness using NESS, by including two correlation lengths to generate roughness along a plane, was achieved. This improved IR was used to investigate  $\text{Al}_{0.3}\text{Ga}_{0.7}\text{As}/\text{GaAs}$  RTDs with IR along the  $\text{Al}_{0.3}\text{Ga}_{0.7}\text{As}$  barriers. The improved IR simulation approach has resulted in RTDs exhibiting greater variation in IV characteristics across distributions of 25 RTDs with different correlation lengths. This variation has been quantified numerically as the standard deviation of resonant peak voltage  $V_r$  and current  $I_r$ . For a correlation length  $L_C=2.5\text{nm}$ , there is almost a four-fold increase in the standard deviation of resonant peak values, from 6.2mV and 9nA using the previous method to 24.2mV and 34.7nA with the improved IR method. Larger correlation lengths were found to increase the standard deviation for both the previous and the new method, with the standard deviation roughly doubling as  $L_C$  increases from 2.5nm to 10nm. The improved IR generation method has also allowed a measurement of standard deviations for anisotropic correlation lengths, which exhibit different correlation lengths. This increased variation and the ability to simulate anisotropic correlation lengths highlight the importance of this improvement to NESS. I would go as far as to suggest that future IR simulation research regarding RTDs and similar devices should model IR as being two-dimensional due this large impact on IV characteristics. Future accurate simulations of device variation with NESS will benefit from IR with two correlation lengths.

In summary, the key points from this chapter are that

1. IR leads to effectively thicker barriers and a thinner QW according to IV characteristics and charge lineplots. The mean resonant peak IV values for 25 RTDs with IR along all  $\text{Al}_{0.3}\text{Ga}_{0.7}\text{As}/\text{GaAs}$  interfaces demonstrate this, with a reduction of  $I_r$  from  $0.224\mu\text{A}$  to  $0.142\mu\text{A}$ , and an increase in  $V_r$  from  $0.22\text{V}$  to  $0.258\text{V}$ .
2.  $\Delta_{RMS}$  inversely affects mean PVCR, with a decrease of 3.72 for  $\Delta_{RMS}=0.1\text{nm}$  to 1.62 for  $\Delta_{RMS}=0.6\text{nm}$ , with  $L_C=7.5\text{nm}$ .
3. For 150 RTDs with an IR of  $\Delta_{RMS}=0.3\text{nm}$  and  $L_C=7.5\text{nm}$  a min-entropy of 1.275 bits was measured, showing promise for RTDs with IR as a PUF component.
4. Generating IR with two correlation lengths significantly increases device variation of produced RTDs, with an increase in standard deviation of resonant IV peaks from  $6.2\text{mV}$  and  $9\text{nA}$  to  $24.2\text{mV}$  and  $34.7\text{nA}$  for  $L_C=2.5\text{nm}$
5. Larger correlation lengths were found to increase the standard deviation of resonant IV peaks for both the previous and the new method with two correlation lengths, with the latter showing an increase from  $24.2\text{mV}$  and  $34.7\text{nA}$  at  $L_C=2.5\text{nm}$  to  $38.8\text{mV}$  and  $80.9\text{nA}$  at  $L_C=10\text{nm}$ .

Design considerations for RTDs can be drawn from each of the aforementioned points. Firstly, the effective thickening of barriers and narrowing of QW due to roughness is especially important due to these effects being noticeable even with a roughness of  $0.3\text{nm}$ . This means that when developing an RTD to have an expected IV characteristic, barriers will likely have to be made a bit narrower and the QW will have to be made slightly bigger, though the quantity of this shift has not been elucidated here and is a topic of further study. The second conclusion of the impact of RMS asperity shows that reducing RMS asperity is important for achieving higher PVCR values. The third conclusion shows that RTDs with IR are feasible for constructing PUFs, and with the variation in standard deviation of resonant peak values shown in fourth and fifth conclusions suggests that such RTDs should be developed with IR with long correlation lengths in both directions.

# Chapter 6

## Conclusion

### 6.1 Summary

RTDs (Resonant Tunnelling Diodes) were shown through NEGF (Non-equilibrium Green's Function) simulations with NESS (Nano-electronic Simulation Software) to be strongly influenced by device variation. This thesis has strengthened the case for RTDs with device variation to be used as PUF (Physical Unclonable Function) building blocks through NEGF simulations. After a literature review on RTDs in chapter 1 the theory and methods involved in this thesis were explored in chapter 2, forming a foundation for the research in chapters 3, 4 and 5.

First, a design of device study from first author paper [8] is explained in chapter 3, wherein three main observations were drawn

1. A narrower 4nm QW and thinner 2nm symmetric barriers, compared to a baseline RTD with a 5nm QW and 3nm symmetric barriers, both resulted in a perturbation of resonant peak bias  $V_r$  to greater values of 0.31V and 0.25V respectively from a baseline of 0.22V.

2. Asymmetric variation of the barriers controlled the perturbation of the resonant peak bias  $V_r$ , with a thinner 2nm first barrier resulting in a perturbation to a greater bias of  $V_r=0.32V$ , and a thinner 2nm second barrier resulting in the inverse effect of reduced bias of  $V_r=0.18V$ .
3. Both barrier thicknesses inversely impacted the current, with the first barrier having a greater impact. Specifically, a thicker 4nm first barrier reduced resonant peak current  $I_r$  from  $0.224\mu A$  to  $0.064\mu A$ , while a thicker 4nm second barrier only reduced  $I_r$  to  $0.153\mu A$ .

The conclusions drawn here can be used to assist design of RTDs. For example, if optimising for a lower resonant peak voltage, a thinner first barrier or thicker second barrier or wider QW can be considered.

In the following chapter 4 based on a published paper [7] a study of the effects of RDDs on RTDs was conducted with an ensemble of 75 NEGF simulations of RTDs with RDDs, 65 of which exhibited NDR behaviour. The following three points were concluded

1. RDDs strongly perturb the IV characteristics of RTDs, as well as the LDOS and CS for the resonant peak
2. The variation of resonant peak current  $I_r$  and resonant peak voltage  $V_r$  values due to RDDs form strongly correlated normal-like distributions which are not equivalent, with a Pearson coefficient of 0.663
3. When taking into account both  $I_r$  and  $V_r$  distributions and devices without an NDR, a min-entropy of 1.371 can be assigned to a given RTD with RDDs. This shows promise for composing a PUF (Physical Unclonable Function) out of multiple such RTDs with RDDs.

As seen within chapter 4 RDDs provide the potential to act as PUF components though also hold the potential to destroy the NDR, especially when within the QW. Hence, for the design of PUFs with RDDs, I would suggest either to avoid doping the QW region where there is a risk of destroying the NDR and/or take into account RTDs without an NDR to also encode information.

In the final results chapter 5, NESS was modified to simulate IR, and the effects of this on RTDs are explored in depth in three sections which are each based on a first author paper of mine [8–10]. The effects of IR were explored through investigating distributions of 25 RTDs with randomly generated IR for each configuration of IR, as well as individual devices characteristic of such a distribution. Additionally, within section 5.4, IR was improved to depend on two correlation lengths, which also allows anisotropic IR to be generated. In summary, the key points from this chapter are that

1. IR leads to effectively thicker barriers and a thinner QW according to IV characteristics and charge lineplots. The mean resonant peak IV values for 25 RTDs with IR along all  $\text{Al}_{0.3}\text{Ga}_{0.7}\text{As}/\text{GaAs}$  interfaces demonstrate this, with a reduction of  $I_r$  from  $0.224\mu\text{A}$  to  $0.142\mu\text{A}$ , and an increase in  $V_r$  from  $0.22\text{V}$  to  $0.258\text{V}$ .
2. RMS (root-mean-square) asperity  $\Delta_{RMS}$  inversely affects mean PVCR, with a decrease of 3.72 for  $\Delta_{RMS}=0.1\text{nm}$  to 1.62 for  $\Delta_{RMS}=0.6\text{nm}$ , with  $L_C=7.5\text{nm}$ .
3. For 150 RTDs with an IR of  $\Delta_{RMS}=0.3\text{nm}$  and  $L_C=7.5\text{nm}$  a min-entropy of 1.275 bits was measured, showing promise for RTDs with IR as a PUF component.
4. Generating IR with two correlation lengths increases device variation of produced RTDs, with an increase in standard deviation of resonant IV peaks from  $6.2\text{mV}$  and  $9\text{nA}$  to  $24.2\text{mV}$  and  $34.7\text{nA}$  for  $L_C=2.5\text{nm}$
5. Larger correlation lengths were found to increase the standard deviation of resonant IV peaks for both the previous and the new method with two correlation lengths, with the latter showing an increase from  $24.2\text{mV}$  and  $34.7\text{nA}$  at  $L_C=2.5\text{nm}$  to  $38.8\text{mV}$  and  $80.9\text{nA}$  at  $L_C=10\text{nm}$ .

Design considerations for RTDs can be drawn from each of the aforementioned points. Firstly, the effective thickening of barriers and narrowing of QW due to roughness is especially important due to these effects being noticeable even with a roughness of 0.3nm. This means that when developing an RTD to have an expected IV characteristic, barriers will likely have to be made a bit narrower and the QW will have to be made slightly bigger, though the quantity of this shift has not been elucidated here and is a topic of further study. The second conclusion of the impact of RMS asperity shows that reducing RMS asperity is important for achieving higher PVCR values. The third conclusion shows that RTDs with IR are feasible for constructing PUFs, and with the variation in standard deviation of resonant peak values shown in fourth and fifth conclusions suggests that such RTDs should be developed with IR with long correlation lengths in both directions.

## **6.2 Further Work**

I believe that there are three main research directions for further work based on research conducted within this thesis.

Firstly, a future research direction from this thesis includes demonstrating such RTD PUFs, through construction and testing of PUFs composed of RTDs with RDDs or IR. As can be preliminarily drawn from chapters 4 and 5, both RDDs and IR lead to noticeable variation allowing the encoding of information in the IV value of the resonant peak, but RDDs also risk destroying the NDR of RTDs. In light of this, I would suggest starting RTD PUF research with IR first, and if further variation is desired to add RDDs on top of this. If RDDs are added, then a way to deal with RTDs without an NDR also needs to be implemented, such as perhaps encoding information in the fact that the NDR has been destroyed as seen in chapter 4.

Secondly, as a simulation based thesis, experimental validation of the key points in this conclusion chapter, such as the relation between roughness and effective barrier thickness, will also be helpful for further development of RTDs and similar tunnelling based devices such as Josephson junctions.

Thirdly, another further research direction is studying how stochastic device variation such as IR and RDDs are reflected in the behaviour of THz RTD oscillators, which is directly applicable to the development of RTDs as THz devices.

# Appendices

## A Theory and Methods

### A1 Node-Centred Finite Volume Discretisation

This and the following appendix A2 is based on material from the manual for NESS (Nano-electronic Simulation Software), which is available upon request.

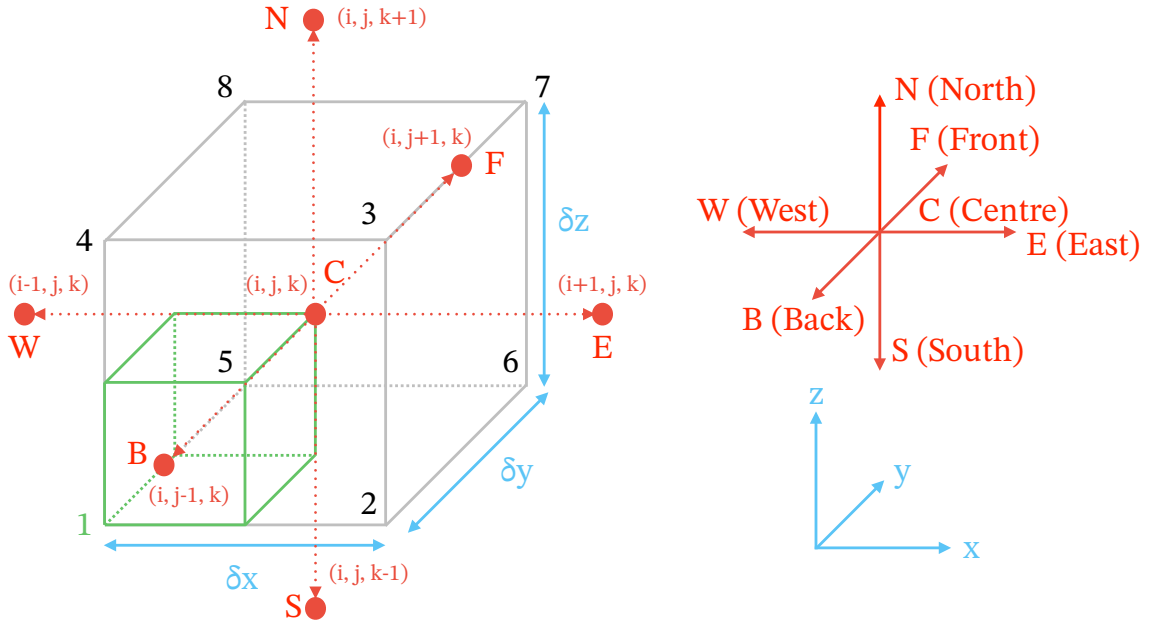


**Figure 6:** Diagram of node-centred control volume [205] (shown in grey) centred around a node 'C' at coordinate  $(i, j, k)$ , with a fractional control sub-volume associated with vertex 1 of this control volume (shown in green). Neighbouring real-space nodes are denoted by red circles and labelled according to the directions of the compass and 'F' for 'front' and 'B' for 'back'.

The Poisson equation for electrostatic potential is

$$\nabla \cdot (\epsilon \nabla V) = -q(p(\mathbf{r}) - n(\mathbf{r}) + N_D(\mathbf{r}) - N_A(\mathbf{r})) \quad (1)$$

Wherein  $N_D(\mathbf{r})$  and  $N_A(\mathbf{r})$  are respectively the donor and acceptor concentrations for location  $(\mathbf{r})$ , and  $q$  is the electron charge magnitude.

The Poisson equation for a given node  $i$  can be calculated as seen in below in equation 2, where  $V_i(D)$  is the electrostatic potential for the neighbouring node in one of the 6 directions ('F', 'B', 'N', 'E', 'S', 'W') as noted in Fig. 6.

$$\begin{aligned} \epsilon_i \frac{V_i(E) - V_i(C)}{dx} S_{yz} + \epsilon_i \frac{V_i(W) - V_i(C)}{\delta x} S_{yz} + \\ \epsilon_i \frac{V_i(N) - V_i(C)}{dz} S_{xy} + \epsilon_i \frac{V_i(S) - V_i(C)}{\delta z} S_{xz} + \\ \epsilon_i \frac{V_i(F) - V_i(C)}{dy} S_{xz} + \epsilon_i \frac{V_i(B) - V_i(C)}{\delta y} S_{xz} = -q(N_{D,i} - N_{A,i} + n_i - p_i) \Delta P_i \end{aligned} \quad (2)$$

$\Delta P_i$  is the control volume associated with node  $i$ . For a cuboid grid as shown here the surface area  $S_{ij}$  of each face along plane  $ij$ , with  $i, j = x, y, z$ , is  $S_{ij} = \delta i \delta j$  where  $\delta i$  is the length of the mesh cell in that direction.

Equation 2 can also be rearranged to depend on coefficients  $\alpha_D$  of  $V(D)$  as seen below

$$\begin{aligned} \alpha_{E,i} V_i(E) - \alpha_{W,i} V_i(W) + \\ \alpha_{N,i} V_i(N) - \alpha_{S,i} V_i(S) + \\ \alpha_{N,i} V_i(F) - \alpha_{S,i} V_i(B) + \\ \alpha_{C,i} = -q(N_{D,i} - N_{A,i} + n_i - p_i) \Delta P_i \end{aligned} \quad (3)$$

In NESS equation 3 has its coefficients calculated efficiently by summing contributions for the different fractional control volumes which are cycled through. For example for the fractional control volume ‘1’ in Fig. 6, the  $\alpha$  values are iterated as follows

$$\alpha_C = \alpha_C - \epsilon \left( \frac{S_{yz}}{4dx} + \frac{S_{xy}}{4dz} + \frac{S_{xz}}{4dy} \right) \quad (4)$$

$$\alpha_E = \alpha_E + \epsilon \left( \frac{S_{yz}}{4dx} \right) \quad (5)$$

$$\alpha_N = \alpha_N + \epsilon \left( \frac{S_{xy}}{4dz} \right) \quad (6)$$

$$\alpha_F = \alpha_F + \epsilon \left( \frac{S_{xz}}{4dy} \right) \quad (7)$$

This is then repeated for the other fractional control volumes ‘2’ to ‘8’,

## A2 Efficient solving of Poisson Potential

This and the preceding appendix A2 is based on material from the manual for NESS (Nano-electronic Simulation Software), which is available upon request.

The discretised Poisson potential equation for node  $i$  can be expressed as follows

$$F_i(\mathbf{V}, n, p) = \quad (8)$$

$$\begin{aligned} & \varepsilon_i \frac{V_i(E) - V_i(C)}{dx} S_{yz} + \epsilon_i \frac{V_i(W) - V_i(C)}{\delta x} S_{yz} + \\ & \epsilon_i \frac{V_i(N) - V_i(C)}{dz} S_{xy} + \epsilon_i \frac{V_i(S) - V_i(C)}{\delta z} S_{xy} + \\ & \epsilon_i \frac{V_i(F) - V_i(C)}{dy} S_{xz} + \epsilon_i \frac{V_i(B) - V_i(C)}{\delta y} S_{xz} + \end{aligned}$$

$$q(N_{D,i} - N_{A,i} + n_i - p_i) \Delta P_i = 0 \quad (9)$$

Equation 9 can be composed into the matrix form in equation 10 by taking into account all  $N$  nodes

$$F(\mathbf{V}, n, p) = A[V] - b = 0 \quad (10)$$

In equation 10,  $A$  is a matrix of coefficients,  $\mathbf{V}$  is a vector of electrostatic potentials, and  $b$  is a matrix of charge terms.

In NESS, the Newton-Raphson iterative method [206] is used to solve this nonlinear partial differential Poisson equation, where electron and hole densities depend non-linearly on the electrostatic potential.

$$J \Delta V^k = -F(V^{k-1}, n, p) \quad (11)$$

$$V^k = V^{k-1} + \Delta V^k \quad (12)$$

The Jacobian  $J$  of  $F(V^{k-1}, n, p)$  is equation 13 where there are  $N$  nodes in total

$$J = \begin{bmatrix} \frac{\partial F_0(V^{k-1}, n, p)}{\partial V_0} & \frac{\partial F_0(V^{k-1}, n, p)}{\partial V_1} & \dots & \frac{\partial F_0(V^{k-1}, n, p)}{\partial V_N} \\ \frac{\partial F_1(V^{k-1}, n, p)}{\partial V_0} & \frac{\partial F_1(V^{k-1}, n, p)}{\partial V_1} & \dots & \frac{\partial F_1(V^{k-1}, n, p)}{\partial V_N} \\ \vdots & \ddots & & \vdots \\ \frac{\partial F_N(V^{k-1}, n, p)}{\partial V_0} & \frac{\partial F_N(V^{k-1}, n, p)}{\partial V_1} & \dots & \frac{\partial F_N(V^{k-1}, n, p)}{\partial V_N} \end{bmatrix} \quad (13)$$

SOR (successive over-relaxation) [208, 209] can help speed iterations with a relaxation factor  $\omega$  by multiplying with the change  $\Delta x^k = x^k - x^{k-1}$  in iteration  $k$

$$x_i^{k'} = x_i^{k-1} + \omega \Delta x_i^k \quad (14)$$

$$x_i^{k'} = \omega x_i^k + (1 - \omega) x_i^{k-1} \quad (15)$$

Using SOR, the update to  $V_i^k$  for node  $i$  and iteration  $k$  within equation 12 is modified as follows

$$V_i^{k'} = \omega V_i^k + (1 - \omega) V_i^{k-1} \quad (16)$$

The Chebyshev acceleration scheme [210] is applied to modify this relaxation factor  $\omega$  for every iteration as noted below

$$\omega' = \frac{1}{1 - 0.25 \rho_{OPT}^2 \omega} \quad (17)$$

$$\rho_{OPT} = \sqrt{\frac{(\delta y \delta z)^2 \cos(\frac{\pi}{N_x}) + (\delta x \delta z)^2 \cos(\frac{\pi}{N_y}) + (\delta x \delta y)^2 \cos(\frac{\pi}{N_z})}{(\delta y \delta z)^2 + (\delta x \delta y)^2 + (\delta x \delta z)^2}} \quad (18)$$

Where  $\delta i$  for  $i = x, y, z$  is mesh spacing along direction  $i$  and  $N_i$  is the number of mesh nodes along that direction. Within NESS, the default initial value is  $\omega = 1.6$ .

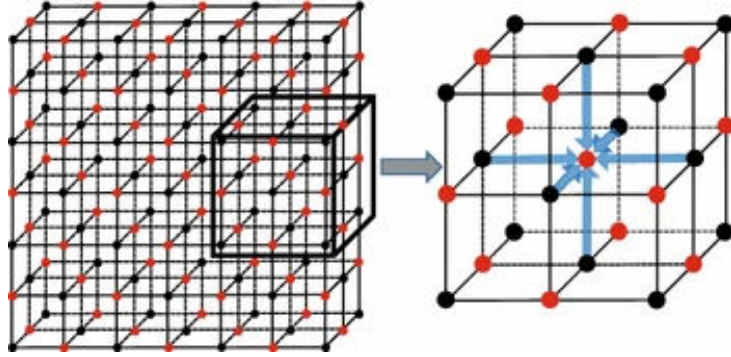


**Figure 7:** 3D grid visualising red-black ordering [211], with nearest neighbour nodes for any given node being of the opposite colour. Permission has been granted by Springer Nature to include this figure [211] within this thesis. © 2018, Springer Nature.

Red-black parallelism [211] is a method of parallelising the solution of the above equations. It splits the nodes into ‘red’ and ‘black’ nodes in a pattern similar to a chequerboard as seen in the 3D sketch in Fig. 7. For a 3D grid, with nodes of position  $\mathbf{r} = i\hat{x} + j\hat{y} + k\hat{z}$ , red-black ordering can be split as shown below in equation 19

$$\begin{cases} \text{black,} & \text{if } (i + j + k) \% 2 = 0 \\ \text{red,} & \text{if } (i + j + k) \% 2 = 1 \end{cases} \quad (19)$$

This means that for any ‘red’ node all its nearest neighbours are ‘black’, and vice-versa, which is advantageous in parallelising the solving of the Poisson solver.

### A3 Contacts

NEGF can be used to split two terminal nanoelectronic devices into an active region of  $N$  layers composed of the device itself and two semi-infinite contacts [212] as seen in Fig. 2.17 which only affect layers 1 and  $N$  of the device.

This means that the following matrix relation for the retarded Green's function  $G^R$  [212], where the matrix  $M$  describing the device and contacts is defined as  $[EI - H - \Sigma_S]$  and  $\Sigma_S$  is the scattering self-energy, can be split into 9 portions for each matrix involved as seen in equation 22 below.  $M_{LL}$ ,  $M_{DD}$ ,  $M_{RR}$  correspond respectively to the left contact, device, and right contact.

$$[EI - H - \Sigma_S]G^R = I \quad (20)$$

$$MG^R = I \quad (21)$$

Or in matrix representation

$$\begin{bmatrix} M_{LL} & M_{LD} & 0 \\ M_{DL} & M_{DD} & M_{DR} \\ 0 & M_{RD} & M_{RR} \end{bmatrix} \begin{bmatrix} G_{LL}^R & G_{LD}^R & G_{LR}^R \\ G_{DL}^R & G_{DD}^R & G_{DR}^R \\ G_{RL}^R & G_{RD}^R & G_{RR}^R \end{bmatrix} = \begin{bmatrix} I & 0 & 0 \\ 0 & I & 0 \\ 0 & 0 & I \end{bmatrix} \quad (22)$$

Where the left-hand side can be expanded as

$$\begin{bmatrix} M_{LL}G_{LL}^R + M_{LD}G_{DL}^R & M_{LL}G_{LD}^R + M_{LD}G_{DD}^R & M_{LL}G_{LR}^R + M_{LD}G_{DR}^R \\ M_{DL}G_{LL}^R + M_{DD}G_{DL}^R + M_{DR}G_{RL}^R & M_{DL}G_{LD}^R + M_{DD}G_{DD}^R + M_{DR}G_{RD}^R & M_{DL}G_{LR}^R + M_{DD}G_{DR}^R + M_{DR}G_{RR}^R \\ M_{RD}G_{DL}^R + M_{RR}G_{RR}^R & M_{RD}G_{DD}^R + M_{RR}G_{RD}^R & M_{RD}G_{DR}^R + M_{RR}G_{RR}^R \end{bmatrix} \quad (23)$$

This results in the following equations for the middle column in equation 23

$$M_{LL}G_{LD}^R + M_{LD}G_{DD}^R = 0 \quad (24)$$

$$M_{DL}G_{LD}^R + M_{DD}G_{DD}^R + M_{DR}G_{RD}^R = I \quad (25)$$

$$M_{RD}G_{DD}^R + M_{RR}G_{RD}^R = 0 \quad (26)$$

Where rearranging equations 24 and 26 respectively leads to  $G_{LD}^R = -M_{LL}^{-1}M_{LD}G_{DL}^R$  and  $G_{RD}^R = -M_{RR}^{-1}M_{RD}G_{DD}^R$ , which can then be substituted into equation 25 to result in equation 27

$$[-M_{DL}M_{LL}^{-1}M_{LD} + M_{DD} + M_{DR}M_{RR}^{-1}M_{RD}]G_{DD}^R = I \quad (27)$$

The 1st and 3rd terms on the left-hand side of equation 27 are the self energies  $\Sigma_C$  of coupling the device region with the left and right contacts respectively.

This lets us define [212] the retarded Green's function for both isolated semi-infinite contacts,  $g_L^R M_{LL}^1 = I$  and  $g_R^R M_{RR}^1 = I$ , or equivalently  $g_L^R = M_{LL}^{-1}$  and  $g_R^R = M_{RR}^{-1}$ .

The surface Green's functions are the values of the Green's function of these isolated contacts corresponding to the neighbouring contact layers 0 in Fig. 2.17. This means that the surface which would correspond to the top left values of  $M_{LL}^{-1}$  and  $M_{RR}^{-1}$ , hence [212] the retarded surface Green's functions for the left and right contacts are respectively  $g_{L,00}^R = M_{LL,00}^{-1}$  and  $g_{R,00}^R = M_{RR,00}^{-1}$ .

## A4 Sancho-Rubio Iterative Method

The Sancho-Rubio iterative method [215] is used to efficiently solve the surface Green's function noted in the preceding appendix A3, effectively by repeatedly halving the semi-infinite contact layers through  $i$  iterations until effectively  $2^i$  layers are included in layer 0 connected to the device itself.

The Hamiltonian of the contacts would be as seen in equations 2.3 and the Green's function representation for all the contact layers, omitting energy  $E$  and momentum dependence for brevity, is equation 28.

$$G_C(r) = \begin{pmatrix} g_{0,0} & g_{0,1} & g_{0,2} & g_{0,3} & \cdots \\ g_{1,0} & g_{1,1} & g_{1,2} & g_{1,3} & \cdots \\ g_{2,0} & g_{2,1} & g_{2,2} & g_{2,3} & \cdots \\ g_{3,0} & g_{3,1} & g_{3,2} & g_{3,3} & \cdots \\ \vdots & \vdots & \vdots & \vdots & \ddots \end{pmatrix} \quad (28)$$

Taking the simplifying assumptions [215] of constancy for the diagonals in  $h$ , or in other words  $h_{0,0} = h_{1,1} = h_{n,n}$  and  $h_{0,1} = h_{n,n+1}$ , a set of iterative equations 29 and 30 for iteration  $i$  and can be derived. Within this, the components are noted in equations (31) to (34) and initial conditions of such components are defined in equations (35) to (38). For further reading a derivation of the Sancho-Rubio algorithm equations is outlined in the following [212, 215].

$$(EI - \epsilon_i^s)g_{0,0} = I + a_i g_{2^i n, 0} \quad (29)$$

$$(EI - \epsilon_i)g_{2^i n, 0} = \beta_i g_{2^i(n-1), 0} + \alpha_i g_{2^i(n+1), 0} \quad (30)$$

Where the components iterate as

$$\epsilon_i^s = \epsilon_{i-1}^s + \alpha_{i-1}(EI - \epsilon_{i-1})^{-1}\beta_{i-1} \quad (31)$$

$$\epsilon_i = \epsilon_{i-1} + \beta_{i-1}(EI - \epsilon_{i-1})^{-1}\alpha_{i-1} + \alpha_{i-1}(EI - \epsilon_{i-1})^{-1}\beta_{i-1} \quad (32)$$

$$\alpha_i = \alpha_{i-1}(EI - \epsilon_{i-1})^{-1}\alpha_{i-1} \quad (33)$$

$$\beta_i = \beta_{i-1}(EI - \epsilon_{i-1})^{-1}\beta_{i-1} \quad (34)$$

With the initial values of  $\epsilon^s$ ,  $\epsilon$ ,  $\alpha$  and  $\beta$  being

$$\epsilon_0^s = h_{0,0} \quad (35)$$

$$\epsilon_0 = h_{0,0} \quad (36)$$

$$\alpha_0 = h_{0,1} \quad (37)$$

$$\beta_0 = h_{1,0} \quad (38)$$

This can be repeated  $i$  times to minimise coupling constants  $\alpha_i$  and  $\beta_i$  [212, 215].

The resulting surface Green's function  $g(C, C) = g_{0,0}$  for either contact, with contacts represented by  $C$ , can be used to calculate the self-energy of that contact, which can take into account interactions with the contact by assuming [196] that the contacts are transitionally invariant under unit cell transformation and in equilibrium.

$$\Sigma_C^R = H_{DC}g^R(C, C)H_{C,D} \quad (39)$$

This retarded contact self-energy  $\Sigma_C^R$  for a given contact can then be used to calculate [196, 216] the corresponding rate operator  $\Gamma$  with equation 40.

The lesser and greater contact self-energy for a contact  $C$  can then be calculated using the corresponding rate operator  $\Gamma_C$  and Fermi level  $\mu_C$ , in equations 41 and 42 respectively.

$$\Gamma_C(E) = i[\Sigma_C^R(E) - \Sigma_C^A(E)] \quad (40)$$

$$\Sigma_C^< = i\Gamma(E)f(E - \mu_C) \quad (41)$$

$$\Sigma_C^> = -i\Gamma(E)(1 - f(E - \mu_C)) \quad (42)$$

## A5 Electron-Phonon interactions

This appendix explains the implementation of electron-phonon scattering within the NEGF coupled mode space framework of NESS, and is based on an explanation of such given in a paper on NESS [196].

NESS has currently implemented acoustic and optical electron-phonons interactions [196], with their self-energies assumed [196, 212, 213, 220] to be local in time and space. This makes such self-energies block diagonal, allowing the use of the efficient recursive method [218] mentioned in appendix A6. A further explanation of this assumption is given in subsection 7.3 of the following textbook [212].

The lesser/greater self-energies for acoustic and optical phonons can be calculated by making use of the acoustic and optical coupling constants [196, 213, 221, 222] for electron-phonon interactions which are respectively  $P_{Ac}$  and  $P_{Op}$  which are obtained from deformation potential theory [222] and given as follows,

$$|P_{Ac}|^2 = \frac{\Xi^2 k_B T}{2\rho v_s^2} \quad (43)$$

$$|P_{Op,q}^{\gamma,\gamma'}|^2 = \frac{\hbar(D_t K_q)^2}{2\rho\omega_q} \quad (44)$$

Within equation 43 for a given material,  $\Xi$  is the acoustic deformation potential constant,  $\rho$  is the density, and  $v_s$  is the sound velocity. The optical deformation potential [196, 213, 221, 222]  $D_t K_q$  corresponds to the coupling to the phonons of the electronic valley  $\gamma'$  [196], and  $\omega_q$  is the corresponding angular frequency of the phonon.

These coupling constants are used in the following real-space self-energy equations for electronic valley  $\gamma$ , with a summation over phonon frequencies and electronic valleys performed for the optical self energies in equations 47 and 48.

$$\Sigma_{Ac}^<(\mathbf{r}; E; \gamma) = |P_{Ac}|^2 G^<(\mathbf{r}; E; \gamma) \quad (45)$$

$$\Sigma_{Ac}^>(\mathbf{r}; E; \gamma) = |P_{Ac}|^2 G^>(\mathbf{r}; E; \gamma) \quad (46)$$

$$\Sigma_{Op}^<(\mathbf{r}; E; \gamma) = \sum_{q, \gamma'} |P_{Op,q}^{\gamma, \gamma'}|^2 [n_{B,q} G^<(\mathbf{r}; E - \hbar\omega_q; \gamma') + (n_{B,q} + 1) G^<(\mathbf{r}; E + \hbar\omega_q; \gamma')] \quad (47)$$

$$\Sigma_{Op}^>(\mathbf{r}; E; \gamma) = \sum_{q, \gamma'} |P_{Op,q}^{\gamma, \gamma'}|^2 [n_{B,q} G^>(\mathbf{r}; E + \hbar\omega_q; \gamma') + (n_{B,q} + 1) G^>(\mathbf{r}; E - \hbar\omega_q; \gamma')] \quad (48)$$

In coupled mode space these self energy equations [196, 212, 239] can be rewritten as the following equations [196, 239] by making use of equation 2.23.

$$\tilde{\Sigma}_{Ac}^<(l, n; l, m; E; \gamma) = |P_{Ac}|^2 \sum_{u,v} F_{u,v}^{n,m}(l) \tilde{G}^<(l, u; l, v; E; \gamma) \quad (49)$$

$$\tilde{\Sigma}_{Ac}^>(l, n; l, m; E; \gamma) = |P_{Ac}|^2 \sum_{u,v} F_{u,v}^{n,m}(l) \tilde{G}^>(l, u; l, v; E; \gamma) \quad (50)$$

$$\tilde{\Sigma}_{Op}^<(l, n; l, m; E; \gamma) = \sum_{u,v} F_{u,v}^{n,m}(l) \sum_{q, \gamma'} |P_{Op,q}^{\gamma, \gamma'}|^2 [(n_{B,q} + \frac{1}{2} \pm \frac{1}{2}) \tilde{G}^<(l, u; l, v; (E \pm \hbar\omega_q); \gamma')] \quad (51)$$

$$\tilde{\Sigma}_{Op}^>(l, n; l, m; E; \gamma) = \sum_{u,v} F_{u,v}^{n,m}(l) \sum_{q, \gamma'} |P_{Op,q}^{\gamma, \gamma'}|^2 [(n_{B,q} + \frac{1}{2} \pm \frac{1}{2}) \tilde{G}^>(l, u; l, v; (E \mp \hbar\omega_q); \gamma')] \quad (52)$$

Where in the above equations the form factor  $F_{u,v}^{n,m}(l)$  is

$$F_{u,v}^{n,m}(l) = \int dy dz \phi_n^*(y, z; l) \phi_m(y, z; l) \phi_u(y, z; l) \phi_v^*(y, z; l) \quad (53)$$

Lesser/greater self-energies can easily be converted into the retarded self-energy with the following relation [196] in equation 54.

$$\Sigma^R = \frac{1}{2}[\Sigma^<(\mathbf{r}; E) - \Sigma^>(\mathbf{r}; E)] \quad (54)$$

The self energies corresponding to the contacts and scattering can then be summed as follows [196]

$$\Sigma^R = \Sigma_C^R + \Sigma_S^R \quad (55)$$

$$\Sigma^< = \Sigma_C^< + \Sigma_S^< \quad (56)$$

## A6 Recursive Solving of Green's Functions

Since we have been using block tridiagonal matrices under the assumption of local scattering [196] and calculating observables with these block diagonal terms, an efficient recursive method [218, 240, 241] can be used to solve only for these blocks for the Dyson equations [212, 218] of the Green's functions.

Similar to what is described in appendix A4, the Green's function gives rise to iterative equations, though this time with a partitioned Green's function describing the device. The partitioning in this case divides the device region seen in Fig. 2.17, and moves through the iterations from  $n = 1$  to  $n = N$  to calculate layer  $n + 1$  from  $n$  in a ‘right-ward’ direction before going in the reverse ‘left-ward’ direction to take into account coupling from the layers with greater  $n$  on those with lower  $n$ , and then finally uses this to calculate the lower and upper diagonal components.

### A6.1 Dyson Equations for Recursive Green's Function Solution

Using equations 20 and 21 and partitioning the device from layer 1 to  $n$  as  $Z$  and layer  $n + 1$  as  $Z'$  results in the equation 57 for the retarded Green's function  $G^R$ .

$$\begin{bmatrix} M_{Z,Z} & M_{Z,Z'} \\ M_{Z',Z} & M_{Z',Z'} \end{bmatrix} \begin{bmatrix} G_{Z,Z}^R & G_{Z,Z'}^R \\ G_{Z',Z}^R & G_{Z',Z'}^R \end{bmatrix} = \begin{bmatrix} I & 0 \\ 0 & I \end{bmatrix} \quad (57)$$

To simplify further calculations the following matrices  $M^0$ ,  $U$  and  $G^{R,0}$ , where  $M = M^0 - U$  and  $G^{R,0} = (M^0)^{-1}$ , can be defined.

$$M = \begin{bmatrix} M_{Z,Z} & M_{Z,Z'} \\ M_{Z',Z} & M_{Z',Z'} \end{bmatrix} \quad (58)$$

$$M^0 = \begin{bmatrix} M_{Z,Z} & 0 \\ 0 & M_{Z',Z'} \end{bmatrix} \quad (59)$$

$$U = \begin{bmatrix} 0 & -M_{Z,Z'} \\ -M_{Z',Z} & 0 \end{bmatrix} \quad (60)$$

$$G^R = \begin{bmatrix} G_{Z,Z}^R & G_{Z,Z'}^R \\ G_{Z',Z}^R & G_{Z',Z'}^R \end{bmatrix} \quad (61)$$

$$G^{R,0} = \begin{bmatrix} G_{Z,Z}^{R,0} & 0 \\ 0 & G_{Z',Z'}^{R,0} \end{bmatrix} = (M^0)^{-1} = \begin{bmatrix} M_{Z,Z}^{-1} & 0 \\ 0 & M_{Z',Z'}^{-1} \end{bmatrix} \quad (62)$$

$$(63)$$

The above relations allows equation 57 to be rewritten as

$$(M^0 - U)G^R = I \quad (64)$$

$$M^0 G^R = I + UG^R \quad (65)$$

$$G^R = (M^0)^{-1} + (M^0)^{-1}UG^R \quad (66)$$

$$G^R = G^{R,0} + G^R U G^{R,0} \quad (67)$$

An alternative formulation of  $G^R = G^{R,0} + G^{R,0} U G^R$  can also be achieved as described in appendix A7. Hence, the Dyson equation [218] for the retarded Green's function is

$$G^R = G^{R,0} + G^{R,0} U G^R = G^{R,0} + G^R U G^{R,0} \quad (68)$$

For the advanced Green's function  $G^A = (G^R)^\dagger$ , the Dyson equation is just the adjoint [218]

$$G^A = G^{A,0} + G^A U^\dagger G^{A,0} = G^{A,0} + G^{A,0} U^\dagger G^A \quad (69)$$

The lesser/greater Green's function  $G^{\lessgtr}$  can also be derived, which by making use of the relations in equation 2.6 and equation 21, results in equation 72 as seen below.

$$G^{\lessgtr} = G^R \Sigma^{\lessgtr} G^A \quad (70)$$

$$MG^{\lessgtr} = (MG^R) \Sigma^{\lessgtr} G^A \quad (71)$$

$$MG^{\lessgtr} = \Sigma^{\lessgtr} G^A \quad (72)$$

Equation 72 leads to the following matrix representation for lesser/greater Green's function  $G^{\lessgtr}$  in equation 73.

$$\begin{bmatrix} M_{Z,Z} & M_{Z,Z'} \\ M_{Z',Z} & M_{Z',Z'} \end{bmatrix} \begin{bmatrix} G_{Z,Z}^{\leq} & G_{Z,Z'}^{\leq} \\ G_{Z',Z}^{\leq} & G_{Z',Z'}^{\leq} \end{bmatrix} = \begin{bmatrix} \Sigma_{Z,Z}^{\leq} & \Sigma_{Z,Z'}^{\leq} \\ \Sigma_{Z',Z}^{\leq} & \Sigma_{Z',Z'}^{\leq} \end{bmatrix} \begin{bmatrix} G_{Z,Z}^A & G_{Z,Z'}^A \\ G_{Z',Z}^A & G_{Z',Z'}^A \end{bmatrix} \quad (73)$$

Equation 73 can be rewritten in the following Dyson equation in the following manner.

$$MG^{\leq} = \Sigma^{\leq}G^A \quad (74)$$

$$(M^0 - U)G^{\leq} = \Sigma^{\leq}G^A \quad (75)$$

$$M^0G^{\leq} = \Sigma^{\leq}G^A + U\Sigma^{\leq}G^A \quad (76)$$

$$G^{\leq} = (M^0)^{-1}\Sigma^{\leq}G^A + (M^0)^{-1}UG^{\leq} \quad (77)$$

$$G^{\leq} = G^{R,0}\Sigma^{\leq}G^A + G^{R,0}UG^{\leq} \quad (78)$$

## A6.2 Recursive Iterative Equations for Retarded Green's Function

Recursive iterative equations can be extracted for solving Green's equations [218], starting with the retarded Green's function  $G^R$ .

Corresponding to the first  $n$  layers of the device in Fig. 2.17 we can define a 'left-connected' retarded Green's function  $g_n^{R,l}$ , which exhibits the following behaviour.

$$M_{n,n}g_n^{R,l} = I \quad (79)$$

$$g_n^{R,l} = (M_{n,n})^{-1} \quad (80)$$

$$g_1^{R,l} = (M_{1,1})^{-1} \quad (81)$$

Equation 81 is the special case for  $n=1$  and is the starting point for the recursive equations.  $g_{n+1}^{R,l}$  is similar to  $g_n^{R,l}$ , but instead takes into the first  $n + 1$  layers, and can be calculated with the following equation 82 as noted in [218] and [212]

$$g_{n+1,n+1}^{R,l} = (M_{n+1,n+1} + M_{n+1,n}g_{n,n}^{R,l}M_{n,n+1})^{-1} \quad (82)$$

A derivation of equation 82 from the Dyson equation for left connected retarded Green's function as defined in explained in appendix A8. Equation 82 can be repeated up to  $n = N - 1$  until  $g_{N,N}^{R,l}$  is obtained, containing all the left connection effects leading which is equal to the retarded full Green's function  $G_{N,N}^R$  for  $n = N$  [218].

The following iterating equation 83 for the full retarded Green's function  $G_{n,n}^R$  from  $G_{n+1,n+1}^R$  and the left connected retarded Green's function  $g_{n,n}^{R,l}$  can then be iterated until  $n = 1$  to have a completed full retarded Green's function [218].

$$G_{n,n}^R = g_{n,n}^{R,l} + g_{n,n}^{R,l}M_{q,q+1}G_{n+1,n+1}^RM_{n,n+1}g_{n,n}^{R,l} \quad (83)$$

The derivation of equation 83 from the Dyson equation is described in appendix A8, along with how to calculate the off-diagonal components of the full retarded Green's function.

### A6.3 Recursive Iterative Equations for Lesser/Greater Green's Function

Using the Dyson equation 78 for lesser/greater Green's function  $G^{\lessgtr}$ , the following iterative equations 84 and 85 can similarly be derived as described in [218], which follow a similar format to those for the retarded Green's function  $G^R$ .

$$\begin{aligned} g_{n+1,n+1}^{\leqslant,l} &= g_{n+1,n+1}^{R,l} [\Sigma_{n+1,n+1}^{\leqslant} + M_{n+1,q} g_{n,n}^{\leqslant,l} M_{n,n+1}^{\dagger} \\ &\quad + \Sigma_{n+1,n}^{\leqslant} g_{n,n}^{A,l} M_{n,n+1}^{\dagger} + M_{n+1,n} g_{n,n}^{R,l} \Sigma_{n,n+1}^{\leqslant}] g_{n+1,n+1}^{A,l} \end{aligned} \quad (84)$$

$$\begin{aligned} G_{n,n}^{\leqslant} &= g_{n,n}^{\leqslant,l} + g_{n,n}^{R,l} M_{n,n+1} G_{n+1,n+1}^{\leqslant} M_{n+1,n}^{\dagger} g_{n,n}^{A,l} \\ &\quad + (g_{n,n}^{\leqslant,l} M_{n,n+1}^{\dagger} G_{n+1,n}^A + G_{n,n+1}^R M_{n+1,n} g_{n,n}^{\leqslant,l}) \\ &\quad + (g_{n,n}^{R,0} \Sigma_{n,n+1}^{\leqslant} g_{n+1,n+1}^{A,0} M_{n+1,n}^{\dagger} G_{n,n}^A + G_{n,n}^R M_{n,n+1} g_{n+1,n+1}^{R,0} \Sigma_{n+1,n}^{\leqslant} g_{n,n}^{A,0}) \end{aligned} \quad (85)$$

Note, the terms in the round brackets of equation 85 are Hermitian conjugates of each other [218].

The initial value [218] of the left connected lesser/greater Green's function is given by equation 86, which includes the left lead self energy  $\Sigma_L^{\leqslant}$

$$g_{1,1}^{\leqslant,l} = g_{1,1}^{R,0} \Sigma_L^{\leqslant} g_{1,1}^{A,0} \quad (86)$$

Equation 84 then iterates with incrementing  $n$  until  $G_{n,n}^{\leqslant} = g_{N,N}^{\leqslant,l}$ , which also similarly includes the right lead self-energy  $\Sigma_R^{\leqslant}$  [241]. Equation 85 then decrements  $n$  until  $n = 1$ , calculating the fully connected Greens function  $G_{n,n}^{\leqslant}$ .

For a further explanation and derivation of the equations, the following paper is recommended [218].

## A7 Matrix Inversion for Retard Greens Function Dyson Equation

An alternative formulation to  $G^R = G^{R,0} + G^{R,0}UG^R$  for the Dyson equation can be achieved by substituting in  $A = M^0$  and  $B = U$  into the following equation 87, before making use of  $M = M^0 - U$ ,  $G^{R,0} = (M^0)^{-1}$  and  $G^R = M^{-1}I$ , as shown below

$$(A - B)^{-1} = A^{-1} + A^{-1}B(A - B)^{-1} \quad (87)$$

$$(M^0 - U)^{-1} = (M^0)^{-1} + (M^0)^{-1}U(M^0 - U)^{-1} \quad (88)$$

$$G^R = G^{R,0} + G^{R,0}UG^R \quad (89)$$

The matrix inversion lemma in equation 87 can be constructed as follows

$$I = (A^{-1}A) \quad (90)$$

$$I = A^{-1}A + (-A^{-1}B + A^{-1}B) \quad (91)$$

$$I = A^{-1}(A - B) + A^{-1}B \quad (92)$$

$$I = A^{-1}(A - B) + A^{-1}B((A - B)^{-1}(A - B)) \quad (93)$$

$$I(A - B)^{-1} = A^{-1}((A - B)(A - B)^{-1}) + A^{-1}B(A - B)^{-1}((A - B)(A - B)^{-1}) \quad (94)$$

$$(A - B)^{-1} = A^{-1} + A^{-1}B(A - B)^{-1} \quad (95)$$

## A8 Derivation of Iterative Equation for Left-Connected Retarded Green's Function

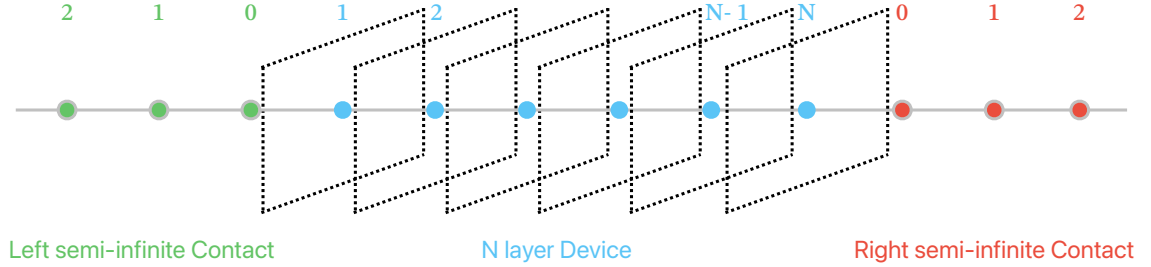


**Figure 8:** Layer representation of two-terminal device with  $N$  layers along the direction of current flow, and two semi-infinite contacts.

Corresponding to the first  $n$  layers of the device in Fig. 8 we can define a ‘left-connected’ retarded Green’s function  $g_n^{R,l}$  [218], which exhibits the following behaviour.

$$M_{n,n}g_n^{R,l} = I \quad (96)$$

$$g_n^{R,l} = (M_{n,n})^{-1} \quad (97)$$

$$g_1^{R,l} = (M_{1,1})^{-1} \quad (98)$$

Equation 98 is the special case for  $n=1$  and is the starting point for the recursive equations.  $g_{n+1}^{R,l}$  is similar to  $g_n^{R,l}$ , but instead takes into the first  $n+1$  layers. The Dyson equation for a retarded Green’s function is  $MG^R = I$ , hence with rearrangement the Dyson equation for the left connected Green’s function can be presented as shown below

$$\begin{bmatrix} g_{n,n}^{R,l} & g_{n,n+1}^{R,l} \\ g_{n+1,n}^{R,l} & g_{n+1,n+1}^{R,l} \end{bmatrix} = \begin{bmatrix} g_{n,n}^{R,l} - g_{n,n}^{R,l} M_{n,n+1} G_{n+1,n}^R & -g_{n,n}^{R,l} M_{n,n+1} G_{n+1,n+1}^R \\ -g_{n+1,n+1}^{R,l} M_{n+1,n} G_{n,n}^R & g_{n+1,n+1}^{R,l} - g_{n+1,n+1}^{R,l} M_{n+1,n} G_{n,n+1}^R \end{bmatrix} \quad (99)$$

The upper left partition of the full Green's function  $G^R$ ,  $G_{n,n}^R$  is then

$$G_{n,n}^R = g_{n,n}^{R,l} - g_{n,n}^{R,l} M_{n,n+1} G_{n+1,n}^R \quad (100)$$

Using an alternative arrangement of this Dyson equation 67, we can similarly extract the lower left partition  $G_{n+1,n}^R$  within equation 100

$$G^R = g^{R,l} + g^{R,l} U G^R \quad (101)$$

$$\begin{bmatrix} G_{n,n}^R & G_{n,n+1}^R \\ G_{n+1,n}^R & G_{n+1,n+1}^R \end{bmatrix} = \begin{bmatrix} g_{n,n}^{R,l} & 0 \\ 0 & g_{n+1,n+1}^{R,l} \end{bmatrix} + \begin{bmatrix} G_{n,n}^R & G_{n,n+1}^R \\ G_{n+1,n}^R & G_{n+1,n+1}^R \end{bmatrix} \begin{bmatrix} 0 & -M_{n,n+1} \\ -M_{n+1,n} & 0 \end{bmatrix} \begin{bmatrix} g_{n,n}^{R,l} & 0 \\ 0 & g_{n+1,n+1}^{R,l} \end{bmatrix} \quad (102)$$

$$\begin{bmatrix} G_{n,n}^R & G_{n,n+1}^R \\ G_{n+1,n}^R & G_{n+1,n+1}^R \end{bmatrix} = \begin{bmatrix} g_{n,n}^{R,l} - G_{n,n+1}^R M_{n+1,n} g_{n,n}^{R,l} & -G_{n,n}^R M_{n,n+1} g_{n+1,n+1}^{R,l} \\ -G_{n+1,n+1}^R M_{n+1,n} g_{n,n}^{R,l} & g_{n+1,n+1}^{R,l} - G_{n+1,n}^R M_{n,n+1} g_{n+1,n+1}^{R,l} \end{bmatrix} \quad (103)$$

The off-diagonal  $G_{n+1,n}^R$  within equation 100 can then be calculated as the lower left partition of  $G^R$  within equation 103

$$G_{n+1,n}^R = -G_{n+1,n+1}^R M_{n+1,n} g_{n,n}^{R,l} \quad (104)$$

Equation 104 can be substituted into equation 100 to create the following iterating equation 105 to acquire the full retarded Green's function [218]  $G_{n,n}^R$  from  $G_{n+1,n+1}^R$  and the left connected retarded Green's function  $g_{n,n}^{R,l}$

$$G_{n,n}^R = g_{n,n}^{R,l} + g_{n,n}^{R,l} M_{n,n+1} G_{n+1,n+1}^R M_{n+1,n} g_{n,n}^{R,l} \quad (105)$$

For completeness, the other diagonal component of the full retarded Green's function is

$$G_{n,n+1}^R = -G_{n,n}^R M_{n,n+1} g_{n+1,n+1}^{R,l} \quad (106)$$

# Bibliography

- [1] Y. Luo and D. C. Hall. ‘Nonselective wet oxidation of AlGaAs heterostructure waveguides through controlled addition of oxygen’. In: *Ieee Journal of Selected Topics in Quantum Electronics* 11.6 (2005), pp. 1284–1291. ISSN: 1077-260x. DOI: 10.1109/Jstqe.2005.859024. URL: <https://doi.org/10.1109/Jstqe.2005.859024>.
- [2] Chris Williamson et al. ‘Quantum Well-Based Physical Unclonable Functions for IoT Device Attestation’. In: *IEEE Access* 13 (2025), pp. 115079–115089. DOI: 10.1109/ACCESS.2025.3583881. URL: <https://ieeexplore.ieee.org/document/11053834>.
- [3] M. Asada and S. Suzuki. ‘Terahertz Emitter Using Resonant-Tunneling Diode and Applications’. In: *Sensors (Basel)* 21.4 (2021). ISSN: 1424-8220. DOI: 10.3390/s21041384. URL: <https://doi.org/10.3390/s21041384>.
- [4] D. T. Nguyen et al. ‘Impact of Slot Width on Performance of Symmetrical-Slot-Antenna Resonant-Tunneling-Diode Oscillators’. In: *IEEE Transactions on Terahertz Science and Technology* 14.1 (2024), pp. 29–38. ISSN: 2156-3446. DOI: 10.1109/TTHZ.2023.3329460. URL: <https://ieeexplore.ieee.org/abstract/document/10305408>.
- [5] Daniel Nagy et al. ‘Hierarchical simulation of nanosheet field effect transistor: NESS flow’. In: *Solid-State Electronics* 199 (2023), p. 108489. ISSN: 0038-1101. DOI: <https://doi.org/10.1016/j.sse.2022.108489>. URL: <https://www.sciencedirect.com/science/article/pii/S003811012200260X>.

- [6] T. Shiode et al. ‘Giga-bit wireless communication at 300 GHz using resonant tunnelling diode detector’. In: *Asia-Pacific Microwave Conference 2011*, pp. 1122–1125. URL: <https://ieeexplore.ieee.org/document/6173953/>.
- [7] Pranav Acharya et al. ‘Analysis of Random Discrete Dopants Embedded Nanowire Resonant Tunnelling Diodes for Generation of Physically Unclonable Functions’. In: *IEEE Transactions on Nanotechnology* 23 (2024), pp. 815–821. ISSN: 1941-0085. DOI: 10.1109/TNANO.2024.3504963. URL: <https://eprints.gla.ac.uk/342047>.
- [8] Pranav Acharya et al. ‘Sensitivity of resonant tunneling diodes to barrier variation and quantum well variation: A NEGF study’. In: *Micro and Nanostructures* 207 (2025), p. 208264. ISSN: 2773-0123. DOI: 10.1016/j.micrna.2025.208264. URL: <https://doi.org/10.1016/j.micrna.2025.208264>.
- [9] Pranav Acharya and Vihar Georgiev. ‘Interface roughness in resonant tunnelling diodes for physically unclonable functions’. In: *Solid-State Electronics* (2025), p. 109131. ISSN: 0038-1101. DOI: 10.1016/j.sse.2025.109131. URL: <https://www.sciencedirect.com/science/article/pii/S0038110125000760>.
- [10] Pranav Acharya et al. ‘Impact of interface roughness correlation on resonant tunnelling diode variation’. In: *Scientific Reports* 15.1 (2025), p. 26815. ISSN: 2045-2322. DOI: 10.1038/s41598-025-07720-0. URL: <https://doi.org/10.1038/s41598-025-07720-0>.
- [11] P. Aleksandrov, P. Acharya and V. Georgiev. ‘Diffusion-Based Machine Learning Method for Accelerating Quantum Transport Simulations in Nanowire Transistors’. In: *2024 International Conference on Simulation of Semiconductor Processes and Devices (SISPAD)*. 2024, pp. 1–4. DOI: 10.1109/SISPAD62626.2024.10733041. URL: <https://doi.org/10.1109/SISPAD62626.2024.10733041>.
- [12] Tongfei Liu et al. ‘The study of electron mobility on ultra-scaled silicon nanosheet FET’. In: *Physica Scripta* 99.7 (2024), p. 075410. ISSN: 1402-4896 0031-8949. DOI: 10.1088/1402-4896/ad56d9. URL: <https://dx.doi.org/10.1088/1402-4896/ad56d9>.

- [13] O. Badami et al. ‘Surface Roughness Scattering in NEGF using self-energy formulation’. In: *2019 International Conference on Simulation of Semiconductor Processes and Devices (SISPAD)*. 2019, pp. 1–4. ISBN: 978-1-7281-0940-4. DOI: 10.1109/SISPAD.2019.8870526. URL: <https://doi.org/10.1109/SISPAD.2019.8870526>.
- [14] Michael Feiginov. ‘Frequency Limitations of Resonant-Tunnelling Diodes in Sub-THz and THz Oscillators and Detectors’. In: *Journal of Infrared, Millimeter, and Terahertz Waves* 40.4 (2019), pp. 365–394. ISSN: 1866-6906. DOI: 10.1007/s10762-019-00573-5. URL: <https://doi.org/10.1007/s10762-019-00573-5>.
- [15] T. C. L. G. Sollner et al. ‘Resonant tunneling through quantum wells at frequencies up to 2.5 THz’. In: *Applied Physics Letters* 43.6 (1983), pp. 588–590. ISSN: 0003-6951. DOI: 10.1063/1.94434. URL: <https://doi.org/10.1063/1.94434>.
- [16] Frédéric Aniel et al. ‘Terahertz Electronic Devices’. In: *Springer Handbook of Semiconductor Devices*. Ed. by Massimo Rudan, Rossella Brunetti and Susanna Reggiani. Cham: Springer International Publishing, 2023, pp. 807–849. ISBN: 978-3-030-79827-7. DOI: 10.1007/978-3-030-79827-7\_22. URL: [https://doi.org/10.1007/978-3-030-79827-7\\_22](https://doi.org/10.1007/978-3-030-79827-7_22).
- [17] Sidney Perkowitz. ‘Navigating the terahertz gap’. In: *Physics World* 33.3 (2020), p. 37. ISSN: 2058-7058 0953-8585. DOI: 10.1088/2058-7058/33/3/31. URL: <https://dx.doi.org/10.1088/2058-7058/33/3/31>.
- [18] Reinhold Kleiner. ‘Filling the Terahertz Gap’. In: *Science* 318.5854 (2007), pp. 1254–1255. DOI: doi:10.1126/science.1151373. URL: <https://www.science.org/doi/abs/10.1126/science.1151373>.
- [19] Davide Cimbra et al. ‘Resonant Tunneling Diodes High-Speed Terahertz Wireless Communications - A Review’. In: *IEEE Transactions on Terahertz Science and Technology* 12.3 (2022), pp. 226–244. DOI: 10.1109/TTHZ.2022.3142965. URL: <https://ieeexplore.ieee.org/document/9681194>.
- [20] Jue Wang, Mira Naftaly and Edward Wasige. ‘An Overview of Terahertz Imaging with Resonant Tunneling Diodes’. In: *Applied Sciences* 12.8 (2022). ISSN: 2076-3417. DOI: 10.3390/app12083822. URL: <https://www.mdpi.com/2076-3417/12/8/3822>.

- [21] J Roberts et al. ‘Using Quantum Confinement to Uniquely Identify Devices’. In: *Sci Rep* 5 (2015), p. 16456. DOI: [doi.org/10.1038/srep16456](https://doi.org/10.1038/srep16456). URL: <https://doi.org/10.1038/srep16456>.
- [22] Ibrahim Ethem Bagci et al. ‘Resonant-Tunnelling Diodes as PUF Building Blocks’. In: *IEEE Transactions on Emerging Topics in Computing* 9.2 (2021), pp. 878–885. DOI: [10.1109/TETC.2019.2893040](https://doi.org/10.1109/TETC.2019.2893040). URL: <https://doi.org/10.1109/TETC.2019.2893040>.
- [23] Christoph Böhm and Maximilian Hofer. ‘Physical Unclonable Functions in Theory and Practice’. In: Springer, New York, NY, 2013, pp. 69–86. ISBN: 978-1-4614-5040-5. DOI: [10.1007/978-1-4614-5040-5](https://doi.org/10.1007/978-1-4614-5040-5). URL: <https://doi.org/10.1007/978-1-4614-5040-5>.
- [24] Jonathan Roberts and SpringerLink. *Using Imperfect Semiconductor Systems for Unique Identification*. Cham: Springer International Publishing, 2017. ISBN: 978-3-319-67891-7. DOI: [10.1007/978-3-319-67891-7](https://doi.org/10.1007/978-3-319-67891-7). URL: <https://doi.org/10.1007/978-3-319-67891-7>.
- [25] R. Tsu and L. Esaki. ‘Tunneling in a finite superlattice’. In: *Applied Physics Letters* 22.11 (1973), pp. 562–564. ISSN: 0003-6951. DOI: [10.1063/1.1654509](https://doi.org/10.1063/1.1654509). URL: <https://aip.scitation.org/doi/abs/10.1063/1.1654509>.
- [26] L. L. Chang, L. Esaki and R. Tsu. ‘Resonant tunneling in semiconductor double barriers’. In: *Applied Physics Letters* 24.12 (1974), pp. 593–595. ISSN: 0003-6951 1077-3118. DOI: [10.1063/1.1655067](https://doi.org/10.1063/1.1655067). URL: <https://aip.scitation.org/doi/abs/10.1063/1.1655067>.
- [27] LV Logansen. ‘Resonance tunneling of electrons in crystals’. In: *Soviet Phys. JETP* 20 (1965), pp. 180–185.
- [28] T. J. Shewchuk et al. ‘Resonant tunneling oscillations in a GaAs-Al<sub>x</sub>Ga<sub>1-x</sub>As heterostructure at room temperature’. In: *Applied Physics Letters* 46.5 (1985), pp. 508–510. ISSN: 0003-6951. DOI: [10.1063/1.95574](https://doi.org/10.1063/1.95574). URL: <https://doi.org/10.1063/1.95574>.

- [29] Masahiro Tsuchiya, Hiroyuki Sakaki and Junji Yoshino. ‘Room Temperature Observation of Differential Negative Resistance in an AlAs/GaAs/AlAs Resonant Tunneling Diode’. In: *Japanese Journal of Applied Physics* 24.6A (1985), p. L466. ISSN: 1347-4065 0021-4922. DOI: 10.1143/JJAP.24.L466. URL: <https://dx.doi.org/10.1143/JJAP.24.L466>.
- [30] TCL Sollner. ‘Resonant-tunneling oscillators and multipliers for submillimeter receivers’. In: *Report of the Asilomar 3 LDR Workshop*, pp. 88–89. URL: <https://ntrs.nasa.gov/citations/19900004151>.
- [31] E. R. Brown et al. ‘Oscillations up to 420 GHz in GaAs/AlAs resonant tunneling diodes’. In: *Applied Physics Letters* 55.17 (1989), pp. 1777–1779. ISSN: 0003-6951. DOI: 10.1063/1.102190. URL: <https://doi.org/10.1063/1.102190>.
- [32] R. E. Brown et al. ‘Oscillations up to 712 GHz in InAs/AlSb resonant-tunneling diodes’. In: *Applied Physics Letters* 58.20 (1991), pp. 2291–2293. ISSN: 0003-6951. DOI: <https://doi.org/10.1063/1.104902>.
- [33] N. Orihashi, S. Suzuki and M. Asada. ‘One THz harmonic oscillation of resonant tunneling diodes’. In: *Applied Physics Letters* 87.23 (2005). ISSN: 0003-6951. DOI: 10.1063/1.2139850. URL: <https://doi.org/10.1063/1.2139850>.
- [34] Safumi Suzuki et al. ‘Fundamental oscillation of resonant tunneling diodes above 1 THz at room temperature’. In: *Applied Physics Letters* 97.24 (2010). ISSN: 0003-6951. DOI: 10.1063/1.3525834. URL: <https://doi.org/10.1063/1.3525834>.
- [35] R. Izumi, S. Suzuki and M. Asada. ‘1.98 THz resonant-tunneling-diode oscillator with reduced conduction loss by thick antenna electrode’. In: *2017 42nd International Conference on Infrared, Millimeter, and Terahertz Waves (IRMMW-THz)*. 2017, pp. 1–2. DOI: 10.1109/IRMMW-THz.2017.8066877. URL: <https://ieeexplore.ieee.org/document/8066877>.
- [36] Z. Tang, Z. Zhao and S. Suzuki. ‘Coherent Oscillation in a Two-Dimensional Resonant-Tunneling-Diode Terahertz Oscillator Array’. In: *IEEE Transactions on Terahertz Science and Technology* (2025), pp. 1–9. ISSN: 2156-3446. DOI: 10.1109/TTHZ.2025.3541837. URL: <https://ieeexplore.ieee.org/document/10884831>.

- [37] S. Suzuki et al. ‘InP-Based Resonant-Tunneling-Diode Oscillators with Milliwatt Power Outputs in 600-700 GHz Range’. In: *2024 IEEE International Electron Devices Meeting (IEDM)*, pp. 1–4. DOI: 10.1109/IEDM50854.2024.10873497. URL: <https://ieeexplore.ieee.org/abstract/document/10873497>.
- [38] Fanqi Meng et al. ‘High-power in-phase and anti-phase mode emission from linear arrays of resonant-tunneling-diode oscillators in the 0.4-to-0.8-THz frequency range’. In: *APL Photonics* 9.8 (2024). ISSN: 2378-0967. DOI: 10.1063/5.0213695. URL: <https://doi.org/10.1063/5.0213695>.
- [39] Shoei Endo and Safumi Suzuki. ‘Terahertz resonant-tunneling-diode oscillator with two offset-fed slot-ring antennas’. In: *Applied Physics Express* 17.4 (2024), p. 044001. ISSN: 1882-0786 1882-0778. DOI: 10.35848/1882-0786/ad308b. URL: <https://dx.doi.org/10.35848/1882-0786/ad308b>.
- [40] P. Ourednik and M. Feiginov. ‘Double-resonant-tunneling-diode bridge-less patch-antenna oscillators operating up to 1.09 THz’. In: *Applied Physics Letters* 120.18 (2022). ISSN: 0003-6951. DOI: 10.1063/5.0090519. URL: <https://doi.org/10.1063/5.0090519>.
- [41] Y. Koyama et al. ‘A High-Power Terahertz Source Over 10 mW at 0.45 THz Using an Active Antenna Array With Integrated Patch Antennas and Resonant-Tunneling Diodes’. In: *IEEE Transactions on Terahertz Science and Technology* 12.5 (2022), pp. 510–519. ISSN: 2156-3446. DOI: 10.1109/TTHZ.2022.3180492. URL: <https://ieeexplore.ieee.org/abstract/document/9790085>.
- [42] Shuya Iwamatsu et al. ‘Terahertz coherent oscillator integrated with slot-ring antenna using two resonant tunneling diodes’. In: *Applied Physics Express* 14.3 (2021), p. 034001. ISSN: 1882-0786 1882-0778. DOI: 10.35848/1882-0786/abdb8f. URL: <https://dx.doi.org/10.35848/1882-0786/abdb8f>.
- [43] A. Al-Khalidi et al. ‘Resonant Tunneling Diode Terahertz Sources With up to 1 mW Output Power in the J-Band’. In: *IEEE Transactions on Terahertz Science and Technology* 10.2 (2020), pp. 150–157. ISSN: 2156-3446. DOI: 10.1109/TTHZ.2019.2959210. URL: <https://ieeexplore.ieee.org/document/8931638>.

- [44] M. Cahay et al. ‘Importance of space-charge effects in resonant tunneling devices’. In: *Applied Physics Letters* 50.10 (1987), pp. 612–614. ISSN: 0003-6951. DOI: 10.1063/1.98097. URL: <https://doi.org/10.1063/1.98097>.
- [45] M. Levinshtein, S. Rumyantsev and M. Shur. *Ternary And Quaternary III-V Compounds*. Vol. 2. Handbook Series on Semiconductor Parameters. World Scientific, 1996. ISBN: 978-981-283-208-5. DOI: 10.1142/2046-vol2. URL: <https://www.worldscientific.com/doi/abs/10.1142/2046-vol2>.
- [46] Serge Luryi. ‘Frequency limit of double-barrier resonant-tunneling oscillators’. In: *Applied Physics Letters* 47.5 (1985), pp. 490–492. ISSN: 0003-6951. DOI: 10.1063/1.96102. URL: <https://doi.org/10.1063/1.96102>.
- [47] Sun Jian Ping et al. ‘Resonant tunneling diodes: models and properties’. In: *Proceedings of the IEEE* 86.4 (1998), pp. 641–660. ISSN: 1558-2256. DOI: 10.1109/5.663541. URL: <https://ieeexplore.ieee.org/document/663541>.
- [48] Mira Naftaly, Nico Vieweg and Anselm Deninger. ‘Industrial Applications of Terahertz Sensing: State of Play’. In: *Sensors* 19.19 (2019), p. 4203. ISSN: 1424-8220. URL: <https://www.mdpi.com/1424-8220/19/19/4203>.
- [49] B. B. Hu and M. C. Nuss. ‘Imaging with terahertz waves’. In: *Optics Letters* 20.16 (1995), pp. 1716–1718. DOI: 10.1364/OL.20.001716. URL: <https://opg.optica.org/ol/abstract.cfm?URI=ol-20-16-1716>.
- [50] Yousuke Nishida et al. ‘Terahertz coherent receiver using a single resonant tunnelling diode’. In: *Scientific Reports* 9.1 (2019), p. 18125. ISSN: 2045-2322. DOI: 10.1038/s41598-019-54627-8. URL: <https://doi.org/10.1038/s41598-019-54627-8>.
- [51] Hiroki Konno et al. ‘Discrete Fourier Transform Radar in the Terahertz-Wave Range Based on a Resonant-Tunneling-Diode Oscillator’. In: *Sensors* 21.13 (2021), p. 4367. ISSN: 1424-8220. URL: <https://www.mdpi.com/1424-8220/21/13/4367>.
- [52] Seiichirou Kitagawa et al. ‘Frequency-tunable resonant-tunneling-diode terahertz oscillators applied to absorbance measurement’. In: *Japanese Journal of Applied Physics* 56.5 (2017), p. 058002. ISSN: 1347-4065 0021-4922. DOI: 10.7567/JJAP.56.058002. URL: <https://dx.doi.org/10.7567/JJAP.56.058002>.

- [53] U. Guin et al. ‘Counterfeit Integrated Circuits: A Rising Threat in the Global Semiconductor Supply Chain’. In: *Proceedings of the IEEE* 102.8 (2014), pp. 1207–1228. ISSN: 1558-2256. DOI: 10.1109/JPROC.2014.2332291. URL: <https://ieeexplore.ieee.org/document/6856206>.
- [54] *The Committee’s Investigation Into Counterfeit Electronic Parts In The Department Of Defense Supply Chain*. Hearing. 2011. URL: <https://www.armed-services.senate.gov/hearings/oversight-the-committees-investigation-into-counterfeit-electronic-parts-in-the-department-of-defense-supply-chain>.
- [55] Mark Tehranipoor, Ujjwal Guin and Domenic Forte. ‘Counterfeit Integrated Circuits’. In: *Counterfeit Integrated Circuits: Detection and Avoidance*. Cham: Springer International Publishing, 2015, pp. 15–36. ISBN: 978-3-319-11824-6. DOI: 10.1007/978-3-319-11824-6\_2. URL: [https://doi.org/10.1007/978-3-319-11824-6\\_2](https://doi.org/10.1007/978-3-319-11824-6_2).
- [56] Matěj Hejda et al. ‘Resonant Tunneling Diode Nano-Optoelectronic Excitable Nodes for Neuromorphic Spike-Based Information Processing’. In: *Physical Review Applied* 17.2 (2022), p. 024072. DOI: 10.1103/PhysRevApplied.17.024072. URL: <https://link.aps.org/doi/10.1103/PhysRevApplied.17.024072>.
- [57] Charlie Ironside, Bruno Romeira and José Figueiredo. *RTD photonics for neuromorphic computing*. Electronic Book Section. 2023. DOI: 10.1088/978-0-7503-5714-2ch9. URL: <https://dx.doi.org/10.1088/978-0-7503-5714-2ch9>.
- [58] Swagata Samanta. ‘GaAs-based resonant tunneling diode: Device aspects from design, manufacturing, characterization and applications’. In: *Journal of Semiconductors* 44.10 (2023), p. 103101. ISSN: 1674-4926. DOI: 10.1088/1674-4926/44/10/103101. URL: <https://dx.doi.org/10.1088/1674-4926/44/10/103101>.
- [59] ‘Semiconductor Heterojunctions’. In: *An Essential Guide to Electronic Material Surfaces and Interfaces*. 2016, pp. 223–248. DOI: <https://doi.org/10.1002/9781119027140.ch14>. URL: <https://onlinelibrary.wiley.com/doi/abs/10.1002/9781119027140.ch14>.

- [60] Rachid Bouregba et al. ‘Al<sub>0.3</sub>Ga<sub>0.7</sub>As-GaAs microwave resonant tunneling oscillator’. In: *Annales Des Télécommunications* 45.3 (1990), pp. 184–191. ISSN: 1958-9395. DOI: 10.1007/BF02995153. URL: <https://doi.org/10.1007/BF02995153>.
- [61] Shaffa Almansour and Hassen Dakhlaoui. ‘Electromodulation of the Negative Differential Resistance in an AlGaAs/GaAs Resonant Tunneling Diode’. In: *Journal of the Korean Physical Society* 74.1 (2019), pp. 36–40. ISSN: 1976-8524. DOI: 10.3938/jkps.74.36. URL: <https://doi.org/10.3938/jkps.74.36>.
- [62] I. Sanyal and M. Das Sarkar. ‘Parameter optimization of a single well nanoscale resonant tunneling diode for memory applications’. In: *2015 IEEE International Conference on Electron Devices and Solid-State Circuits (EDSSC)*. 2015, pp. 439–442. DOI: 10.1109/EDSSC.2015.7285145. URL: <https://ieeexplore.ieee.org/document/7285145>.
- [63] Wei Wang et al. ‘High peak-to-valley current ratio In0.53Ga0.47As/AlAs resonant tunneling diode with a high doping emitter’. In: *Journal of Semiconductors* 33.12 (2012), p. 124002. ISSN: 1674-4926. DOI: 10.1088/1674-4926/33/12/124002. URL: <https://dx.doi.org/10.1088/1674-4926/33/12/124002>.
- [64] R. Baba et al. ‘Epitaxial Designs for Maximizing Efficiency in Resonant Tunneling Diode Based Terahertz Emitters’. In: *IEEE Journal of Quantum Electronics* 54.2 (2018), pp. 1–11. ISSN: 1558-1713. DOI: 10.1109/JQE.2018.2797960. URL: <https://ieeexplore.ieee.org/document/8269246>.
- [65] Safumi Suzuki et al. ‘Fundamental Oscillation of up to 831 GHz in GaInAs/AlAs Resonant Tunneling Diode’. In: *Applied Physics Express* 2.5 (2009), p. 054501. ISSN: 1882-0786 1882-0778. DOI: 10.1143/APEX.2.054501. URL: <https://dx.doi.org/10.1143/APEX.2.054501>.
- [66] Michael Feiginov et al. ‘Resonant-tunnelling-diode oscillators operating at frequencies above 1.1 THz’. In: *Applied Physics Letters* 99.23 (2011). ISSN: 0003-6951. DOI: 10.1063/1.3667191. URL: <https://doi.org/10.1063/1.3667191>.

- [67] Hidetoshi Kanaya et al. ‘Structure dependence of oscillation characteristics of resonant-tunneling-diode terahertz oscillators associated with intrinsic and extrinsic delay times’. In: *Japanese Journal of Applied Physics* 54.9 (2015), p. 094103. ISSN: 1347-4065 0021-4922. DOI: 10.7567/JJAP.54.094103. URL: <https://dx.doi.org/10.7567/JJAP.54.094103>.
- [68] Patrick Roblin, Robert C. Potter and Ayub Fathimulla. ‘Interface roughness scattering in AlAs/InGaAs resonant tunneling diodes with an InAs subwell’. In: *Journal of Applied Physics* 79.5 (1996), pp. 2502–2508. ISSN: 0021-8979. DOI: 10.1063/1.361104. URL: <https://doi.org/10.1063/1.361104>.
- [69] J. Lee, M. Kim and J. Lee. ‘692 GHz High-Efficiency Compact-Size InP-Based Fundamental RTD Oscillator’. In: *IEEE Transactions on Terahertz Science and Technology* 11.6 (2021), pp. 716–719. ISSN: 2156-3446. DOI: 10.1109/TTHZ.2021.3108431. URL: <https://ieeexplore.ieee.org/document/9525169>.
- [70] X. Yu et al. ‘Highly Efficient Resonant Tunneling Diode Terahertz Oscillator With a Split Ring Resonator’. In: *IEEE Electron Device Letters* 42.7 (2021), pp. 982–985. ISSN: 1558-0563. DOI: 10.1109/LED.2021.3082577. URL: <https://ieeexplore.ieee.org/document/9438693>.
- [71] Daisuke Horikawa et al. ‘Resonant-tunneling-diode terahertz oscillator integrated with a radial line slot antenna for circularly polarized wave radiation’. In: *Semiconductor Science and Technology* 33.11 (2018), p. 114005. ISSN: 0268-1242. DOI: 10.1088/1361-6641/aae1ef. URL: <https://dx.doi.org/10.1088/1361-6641/aae1ef>.
- [72] Takeru Maekawa et al. ‘Oscillation up to 1.92 THz in resonant tunneling diode by reduced conduction loss’. In: *Applied Physics Express* 9.2 (2016). ISSN: 1882-0778 1882-0786. DOI: 10.7567/apex.9.024101. URL: <https://iopscience.iop.org/article/10.7567/APEX.9.024101>.
- [73] K. Okada et al. ‘Resonant-Tunneling-Diode Terahertz Oscillator Using Patch Antenna Integrated on Slot Resonator for Power Radiation’. In: *IEEE Transactions on Terahertz Science and Technology* 5.4 (2015), pp. 613–618. ISSN: 2156-3446. DOI: 10.1109/TTHZ.2015.2441740. URL: <https://ieeexplore.ieee.org/abstract/document/7124538>.

- [74] Shaojun Lin et al. ‘III-nitrides based resonant tunneling diodes’. In: *Journal of Physics D: Applied Physics* 53.25 (2020), p. 253002. ISSN: 0022-3727. DOI: 10.1088/1361-6463/ab7f71. URL: <https://dx.doi.org/10.1088/1361-6463/ab7f71>.
- [75] Masahiro Murayama et al. ‘Gallium nitride-based resonant tunneling diode oscillators’. In: *Applied Physics Letters* 125.11 (2024). ISSN: 0003-6951. DOI: 10.1063/5.0225312. URL: <https://doi.org/10.1063/5.0225312>.
- [76] Fang Liu et al. ‘Record peak current density of over 1500 kA/cm<sup>2</sup> in highly scaled AlN/GaN double-barrier resonant tunneling diodes on free-standing GaN substrates’. In: *Applied Physics Letters* 124.7 (2024). ISSN: 0003-6951. DOI: 10.1063/5.0180145. URL: <https://doi.org/10.1063/5.0180145>.
- [77] Fang Liu et al. ‘High-performance negative differential resistance characteristics in homoepitaxial AlN/GaN double-barrier resonant tunneling diodes’. In: *Japanese Journal of Applied Physics* 63.8 (2024), p. 080903. ISSN: 1347-4065 0021-4922. DOI: 10.35848/1347-4065/ad679b. URL: <https://dx.doi.org/10.35848/1347-4065/ad679b>.
- [78] ‘Metal Contacts to GaN and Processing’. In: *Handbook of Nitride Semiconductors and Devices*. 2008, pp. 1–119. DOI: <https://doi.org/10.1002/9783527628414.ch1>. URL: <https://onlinelibrary.wiley.com/doi/abs/10.1002/9783527628414.ch1>.
- [79] Qiuyao Pang et al. *Growth and fabrication of GaAs-based InAs/AlSb resonant tunneling diode*. Vol. 13287. Nineteenth National Conference on Laser Technology and Optoelectronics. SPIE, 2024. URL: <https://doi.org/10.1117/12.3038956>.
- [80] Brian R. Bennett et al. ‘Antimonide-based compound semiconductors for electronic devices: A review’. In: *Solid-State Electronics* 49.12 (2005), pp. 1875–1895. ISSN: 0038-1101. DOI: <https://doi.org/10.1016/j.sse.2005.09.008>. URL: <https://www.sciencedirect.com/science/article/pii/S0038110105002467>.
- [81] Mark Sweeny and Jingming Xu. ‘Resonant interband tunnel diodes’. In: *Applied Physics Letters* 54.6 (1989), pp. 546–548. ISSN: 0003-6951. DOI: 10.1063/1.100926. URL: <https://doi.org/10.1063/1.100926>.

- [82] J. R. Söderström, D. H. Chow and T. C. McGill. ‘New negative differential resistance device based on resonant interband tunneling’. In: *Applied Physics Letters* 55.11 (1989), pp. 1094–1096. ISSN: 0003-6951. DOI: 10.1063/1.101715. URL: <https://doi.org/10.1063/1.101715>.
- [83] Ulf Gennser et al. ‘Resonant tunneling of holes through silicon barriers’. In: *Journal of Vacuum Science & Technology B: Microelectronics Processing and Phenomena* 8.2 (1990), pp. 210–213. ISSN: 0734-211X. DOI: 10.1116/1.584811. URL: <https://doi.org/10.1116/1.584811>.
- [84] K. Ismail, B. S. Meyerson and P. J. Wang. ‘Electron resonant tunneling in Si/SiGe double barrier diodes’. In: *Applied Physics Letters* 59.8 (1991), pp. 973–975. ISSN: 0003-6951. DOI: 10.1063/1.106319. URL: <https://doi.org/10.1063/1.106319>.
- [85] Sean L. Rommel et al. ‘Room temperature operation of epitaxially grown Si/Si<sub>0.5</sub>Ge<sub>0.5</sub>/Si resonant interband tunneling diodes’. In: *Applied Physics Letters* 73.15 (1998), pp. 2191–2193. ISSN: 0003-6951. DOI: 10.1063/1.122419. URL: <https://doi.org/10.1063/1.122419>.
- [86] Yoshiyuki Suda et al. ‘Hole-tunneling Si<sub>0.82</sub>Ge<sub>0.18</sub>/Si triple-barrier resonant tunneling diodes with high peak current of 297 kA/cm<sup>2</sup> fabricated by sputter epitaxy’. In: *Applied Physics Letters* 124.9 (2024). ISSN: 0003-6951. DOI: 10.1063/5.0180934. URL: <https://doi.org/10.1063/5.0180934>.
- [87] Ayaka Shinkawa et al. ‘Hole-tunneling Si<sub>0.82</sub>Ge<sub>0.18</sub>/Si asymmetric-double-quantum-well resonant tunneling diode with high resonance current and suppressed thermionic emission’. In: *Japanese Journal of Applied Physics* 59.8 (2020), p. 080903. ISSN: 1347-4065 0021-4922. DOI: 10.35848/1347-4065/aba379. URL: <https://dx.doi.org/10.35848/1347-4065/aba379>.
- [88] Jagar Singh, Yong Tian Hou and Ming Fu Li. *Method of making resonant tunneling diodes and CMOS backend-process-compatible three dimensional (3-D) integration*. Generic. 2006. URL: <https://patents.google.com/patent/US7002175B1/en>.

- [89] Yang Lianfeng et al. ‘Si/SiGe heterostructure parameters for device simulations’. In: *Semiconductor Science and Technology* 19.10 (2004), p. 1174. ISSN: 0268-1242. DOI: 10.1088/0268-1242/19/10/002. URL: <https://dx.doi.org/10.1088/0268-1242/19/10/002>.
- [90] V. Hung Nguyen et al. ‘Resonant tunnelling diodes based on graphene/h-BN heterostructure’. In: *Journal of Physics D: Applied Physics* 45.32 (2012), p. 325104. ISSN: 0022-3727. DOI: 10.1088/0022-3727/45/32/325104. URL: <https://dx.doi.org/10.1088/0022-3727/45/32/325104>.
- [91] L. Britnell et al. ‘Resonant tunnelling and negative differential conductance in graphene transistors’. In: *Nature Communications* 4.1 (2013), p. 1794. ISSN: 2041-1723. DOI: 10.1038/ncomms2817. URL: <https://doi.org/10.1038/ncomms2817>.
- [92] Zihao Zhang et al. ‘Toward High-Peak-to-Valley-Ratio Graphene Resonant Tunneling Diodes’. In: *Nano Letters* 23.17 (2023), pp. 8132–8139. ISSN: 1530-6984. DOI: 10.1021/acs.nanolett.3c02281. URL: <https://doi.org/10.1021/acs.nanolett.3c02281>.
- [93] A. E. E. Sadi, M. R. Munna and M. Alam. ‘Performance Comparison of Different AGNR RTD’. In: *2022 12th International Conference on Electrical and Computer Engineering (ICECE)*, pp. 40–43. ISBN: 979-8-3503-9879-3. DOI: 10.1109/ICECE57408.2022.10088640. URL: <https://ieeexplore.ieee.org/document/10088640>.
- [94] S. Clochiatti et al. ‘Low-Noise Resonant Tunneling Diode Terahertz Detector’. In: *IEEE Transactions on Terahertz Science and Technology* 15.1 (2025), pp. 107–119. ISSN: 2156-3446. DOI: 10.1109/TTHZ.2024.3505599. URL: <https://ieeexplore.ieee.org/document/10766652>.
- [95] C. P. Allford and P. D. Buckle. ‘Strain Compensated InGaAs/AlAs Triple Barrier Resonant Tunneling Structures for THz Applications’. In: *IEEE Transactions on Terahertz Science and Technology* 7.6 (2017), pp. 772–779. ISSN: 2156-3446. DOI: 10.1109/TTHZ.2017.2758266. URL: <https://ieeexplore.ieee.org/document/8094268>.

- [96] S. Clochiatti et al. ‘InP RTD Detector for THz Applications’. In: *2023 18th European Microwave Integrated Circuits Conference (EuMIC)*, pp. 1–4. DOI: 10.23919/EuMIC58042.2023.10288943. URL: <https://ieeexplore.ieee.org/abstract/document/10288943>.
- [97] H. H. Tsai et al. ‘P-N double quantum well resonant interband tunneling diode with peak-to-valley current ratio of 144 at room temperature’. In: *IEEE Electron Device Letters* 15.9 (1994), pp. 357–359. ISSN: 1558-0563. DOI: 10.1109/55.311133. URL: <https://ieeexplore.ieee.org/document/311133>.
- [98] Charlie Ironside, Bruno Romeira and José Figueiredo. *Resonant Tunnelling Diode Photonics Devices and Applications (Second Edition)*. Electronic Book. 2023. DOI: 10.1088/978-0-7503-5714-2. URL: <https://dx.doi.org/10.1088/978-0-7503-5714-2>.
- [99] Hiroki Sugiyama et al. ‘High-uniformity InP-based resonant tunneling diode wafers with peak current density of over  $6 \times 10^5 \text{ A/cm}^2$  grown by metal-organic vapor-phase epitaxy’. In: *Journal of Crystal Growth* 336.1 (2011), pp. 24–28. ISSN: 0022-0248. DOI: <https://doi.org/10.1016/j.jcrysGro.2011.09.010>. URL: <https://www.sciencedirect.com/science/article/pii/S0022024811007524>.
- [100] T. S. Moise et al. ‘Experimental sensitivity analysis of pseudomorphic InGaAs/AlAs resonant-tunneling diodes’. In: *Journal of Applied Physics* 78.10 (1995), pp. 6305–6317. DOI: 10.1063/1.360511. URL: <https://doi.org/10.1063/1.360511>.
- [101] M. Missous, M. J. Kelly and J. Sexton. ‘Extremely Uniform Tunnel Barriers for Low-Cost Device Manufacture’. In: *IEEE Electron Device Letters* 36.6 (2015), pp. 543–545. ISSN: 1558-0563. DOI: 10.1109/LED.2015.2427335. URL: <https://doi.org/10.1109/LED.2015.2427335>.
- [102] M. Cito et al. ‘Micro-PL analysis of high current density resonant tunneling diodes for THz applications’. In: *Applied Physics Letters* 119.7 (2021). DOI: 10.1063/5.0059339. URL: <https://doi.org/10.1063/5.0059339>.
- [103] W. Pötz and Z. Q. Li. ‘Imperfections and resonant tunneling in quantum-well heterostructures’. In: *Solid-State Electronics* 32.12 (1989), pp. 1353–1357. ISSN: 0038-1101. DOI: 10.1016/0038-1101(89)90239-6. URL: [https://doi.org/10.1016/0038-1101\(89\)90239-6](https://doi.org/10.1016/0038-1101(89)90239-6).

- [104] Jiang Li et al. ‘Effect of interface roughness on performance of AlGaAs/InGaAs/GaAs resonant tunneling diodes’. In: *Journal of Crystal Growth* 195.1 (1998), pp. 617–623. ISSN: 0022-0248. DOI: 10.1016/S0022-0248(98)00581-8. URL: [https://doi.org/10.1016/S0022-0248\(98\)00581-8](https://doi.org/10.1016/S0022-0248(98)00581-8).
- [105] A. Grier et al. ‘Coherent vertical electron transport and interface roughness effects in AlGaN/GaN intersubband devices’. In: *Journal of Applied Physics* 118.22 (Dec. 2015), p. 224308. ISSN: 0021-8979. DOI: 10.1063/1.4936962. eprint: [https://pubs.aip.org/aip/jap/article-pdf/doi/10.1063/1.4936962/14830449/224308\\\_1\\\_online.pdf](https://pubs.aip.org/aip/jap/article-pdf/doi/10.1063/1.4936962/14830449/224308\_1\_online.pdf). URL: <https://doi.org/10.1063/1.4936962>.
- [106] David J. Griffiths and Darrell F. Schroeter. *Introduction to Quantum Mechanics*. 3rd ed. Cambridge: Cambridge University Press, 2018. ISBN: 9781107189638. DOI: DOI:10.1017/9781316995433. URL: <https://www.cambridge.org/core/product/990799CA07A83FC5312402AF6860311E>.
- [107] Changhwan Shin. ‘Line Edge Roughness (LER)’. In: *Variation-Aware Advanced CMOS Devices and SRAM*. Dordrecht: Springer Netherlands, 2016, pp. 19–35. ISBN: 978-94-017-7597-7. DOI: 10.1007/978-94-017-7597-7\_2. URL: [https://doi.org/10.1007/978-94-017-7597-7\\_2](https://doi.org/10.1007/978-94-017-7597-7_2).
- [108] Ravi Bonam et al. *Comprehensive analysis of line-edge and line-width roughness for EUV lithography*. Vol. 10143. SPIE Advanced Lithography. SPIE, 2017. URL: <https://doi.org/10.1117/12.2258194>.
- [109] Wei Xiang et al. ‘InAs homoepitaxy and InAs/AlSb/GaSb resonant interband tunneling diodes on InAs substrate’. In: *Journal of Crystal Growth* 443 (2016), pp. 85–89. ISSN: 0022-0248. DOI: <https://doi.org/10.1016/j.jcrysgro.2016.03.021>. URL: <https://www.sciencedirect.com/science/article/pii/S0022024816301002>.
- [110] Michihiko Suhara et al. ‘Atomically flat OMVPE growth of GaInAs and InP observed by AFM for level narrowing in resonant tunneling diodes’. In: *Journal of Crystal Growth* 179.1 (1997), pp. 18–25. ISSN: 0022-0248. DOI: [https://doi.org/10.1016/S0022-0248\(97\)00103-6](https://doi.org/10.1016/S0022-0248(97)00103-6). URL: <https://www.sciencedirect.com/science/article/pii/S0022024897001036>.

- [111] Yang Zhang et al. ‘Dependence of the electrical and optical properties on growth interruption in AlAs/In0.53Ga0.47As/InAs resonant tunneling diodes’. In: *Nanoscale Research Letters* 6.1 (2011), p. 603. ISSN: 1556-276X. DOI: 10.1186/1556-276X-6-603. URL: <https://doi.org/10.1186/1556-276X-6-603>.
- [112] C. R. Wang et al. ‘Fabrication of resonant-tunneling diodes by Sb surfactant modified growth of Si films on CaF<sub>2</sub>/Si’. In: *IEEE Transactions on Nanotechnology* 2.4 (2003), pp. 236–240. ISSN: 1941-0085. DOI: 10.1109/TNANO.2003.820795. URL: <https://doi.org/10.1109/TNANO.2003.820795>.
- [113] L. Gottwaldt et al. ‘Correlation of the physical properties and the interface morphology of AlGaAs/GaAs heterostructures’. In: *Journal of Applied Physics* 94.4 (2003), pp. 2464–2472. ISSN: 0021-8979. DOI: 10.1063/1.1588360. URL: <https://doi.org/10.1063/1.1588360>.
- [114] Masanori Shinohara, Haruki Yokoyama and Naohisa Inoue. ‘Effects of interface flatness and abruptness on optical and electrical characteristics of GaAs/AlGaAs quantum structures grown by metalorganic vapor phase epitaxy’. In: *Journal of Vacuum Science & Technology B: Microelectronics and Nanometer Structures Processing, Measurement, and Phenomena* 13.4 (1995), pp. 1773–1779. ISSN: 1071-1023. DOI: 10.1116/1.587811. URL: <https://doi.org/10.1116/1.587811>.
- [115] J. E. Oh et al. ‘The effect of molecular-beam-epitaxial growth conditions on the electrical characteristics of In0.52Al0.48As/In0.53Ga0.47As resonant tunneling diodes’. In: *Journal of Applied Physics* 65.2 (1989), pp. 842–845. ISSN: 0021-8979. DOI: 10.1063/1.343075. URL: <https://doi.org/10.1063/1.343075>.
- [116] W. D. Zhang et al. ‘Investigation of Peak-to-Valley Current Ratio of GaN/AlN Resonant Tunneling Diodes’. In: *IEEE Transactions on Electron Devices* 70.7 (2023), pp. 3483–3488. ISSN: 1557-9646. DOI: 10.1109/TED.2023.3279806. URL: <https://ieeexplore.ieee.org/document/10144376>.
- [117] Răzvan Baba et al. ‘Non-destructive characterization of thin layer resonant tunneling diodes’. In: *Journal of Applied Physics* 126.12 (2019). ISSN: 0021-8979. DOI: 10.1063/1.5113585. URL: <https://doi.org/10.1063/1.5113585>.

- [118] Ali Rezaei et al. ‘Statistical device simulations of III-V nanowire resonant tunneling diodes as physical unclonable functions source’. In: *Solid-State Electronics* 194 (2022). ISSN: 00381101. DOI: 10.1016/j.sse.2022.108339. URL: <https://doi.org/10.1016/j.sse.2022.108339>.
- [119] N. Zagni et al. ‘Random dopant fluctuation variability in scaled InGaAs dual-gate ultra-thin body MOSFETs: Source and drain doping effect’. In: *2017 IEEE International Integrated Reliability Workshop (IIRW)*, pp. 1–4. ISBN: 978-1-5386-2332-9. DOI: 10.1109/IIRW.2017.8361227. URL: <https://ieeexplore.ieee.org/document/8361227>.
- [120] N. Seoane et al. ‘Random Dopant, Line-Edge Roughness, and Gate Workfunction Variability in a Nano InGaAs FinFET’. In: *IEEE Transactions on Electron Devices* 61.2 (2014), pp. 466–472. ISSN: 1557-9646. DOI: 10.1109/TED.2013.2294213. URL: <https://ieeexplore.ieee.org/document/6691941>.
- [121] A. Asenov. ‘Random dopant induced threshold voltage lowering and fluctuations in sub-0.1  $\mu\text{m}$  MOSFET’s: A 3-D ”atomistic” simulation study’. In: *IEEE Transactions on Electron Devices* 45.12 (1998), pp. 2505–2513. DOI: 10.1109/16.735728. URL: <https://ieeexplore.ieee.org/document/735728>.
- [122] Nurul Ezaila Alias et al. ‘Threshold voltage shifts and their variability behaviors in p-channel FETs by high voltage on-state and off-state stress’. In: *Japanese Journal of Applied Physics* 53.8S1 (2014), p. 08LC01. ISSN: 1347-4065 0021-4922. DOI: 10.7567/JJAP.53.08LC01. URL: <https://dx.doi.org/10.7567/JJAP.53.08LC01>.
- [123] Hon-Sum Philip Wong, Yuan Taur and David J. Frank. ‘Discrete random dopant distribution effects in nanometer-scale MOSFETs’. In: *Microelectronics Reliability* 38.9 (1998), pp. 1447–1456. ISSN: 0026-2714. DOI: [https://doi.org/10.1016/S0026-2714\(98\)00053-5](https://doi.org/10.1016/S0026-2714(98)00053-5). URL: <https://www.sciencedirect.com/science/article/pii/S0026271498000535>.
- [124] Fikru Adamu-Lema. ‘Scaling and intrinsic parameter fluctuations in nano-CMOS devices’. Thesis. University of Glasgow, 2005. Chap. 5. URL: <https://theses.gla.ac.uk/7086/>.

- [125] Somaia Sarwat Sylvia et al. ‘Effect of Random, Discrete Source Dopant Distributions on Nanowire Tunnel FETs’. In: *IEEE Transactions on Electron Devices* 61.6 (2014), pp. 2208–2214. DOI: 10.1109/TED.2014.2318521. URL: <https://ieeexplore.ieee.org/document/6812119>.
- [126] Yiming Li and Chih-Hong Hwang. ‘Discrete-dopant-induced characteristic fluctuations in 16nm multiple-gate silicon-on-insulator devices’. In: *Journal of Applied Physics* 102.8 (Oct. 2007), p. 084509. ISSN: 0021-8979. DOI: 10.1063/1.2801013. eprint: [https://pubs.aip.org/aip/jap/article-pdf/doi/10.1063/1.2801013/15003051/084509\\_1\\_online.pdf](https://pubs.aip.org/aip/jap/article-pdf/doi/10.1063/1.2801013/15003051/084509_1_online.pdf). URL: <https://doi.org/10.1063/1.2801013>.
- [127] K. J. P. Jacobs et al. ‘Valley current characterization of high current density resonant tunnelling diodes for terahertz-wave applications’. In: *AIP Advances* 7.10 (2017). ISSN: 2158-3226. DOI: 10.1063/1.4997664. URL: <https://doi.org/10.1063/1.4997664>.
- [128] Abhranil Maiti, Vikash Gunreddy and Patrick Schaumont. ‘A Systematic Method to Evaluate and Compare the Performance of Physical Unclonable Functions’. In: *Embedded Systems Design with FPGAs*. Ed. by Peter Athanas, Dionisios Pnevmatikatos and Nicolas Sklavos. New York, NY: Springer New York, 2013, pp. 245–267. ISBN: 978-1-4614-1362-2. DOI: 10.1007/978-1-4614-1362-2\_11. URL: [https://doi.org/10.1007/978-1-4614-1362-2\\_11](https://doi.org/10.1007/978-1-4614-1362-2_11).
- [129] Mohd Syafiq Mispan and Basel Halak. ‘Physical Unclonable Function: A Hardware Fingerprinting Solution’. In: *Authentication of Embedded Devices: Technologies, Protocols and Emerging Applications*. Ed. by Basel Halak. Cham: Springer International Publishing, 2021, pp. 29–51. ISBN: 978-3-030-60769-2. DOI: 10.1007/978-3-030-60769-2\_2. URL: [https://doi.org/10.1007/978-3-030-60769-2\\_2](https://doi.org/10.1007/978-3-030-60769-2_2).
- [130] Yansong Gao, Said F. Al-Sarawi and Derek Abbott. ‘Physical unclonable functions’. In: *Nature Electronics* 3.2 (2020), pp. 81–91. ISSN: 2520-1131. DOI: 10.1038/s41928-020-0372-5. URL: <https://doi.org/10.1038/s41928-020-0372-5>.
- [131] Bryan T Horvath. *Not all parts are created equal: The impact of counterfeit parts in the air force supply chain*. Report. Air War College, Air University Maxwell AFB United States, 2017. URL: <https://apps.dtic.mil/sti/citations/AD1037985>.

- [132] Thomas McGrath. ‘Statistical evaluation of PUF implementation techniques as applied to quantum confinement semiconductors’. Thesis. 2021. DOI: 10.17635/lancaster/thesis/1407. URL: <https://doi.org/10.17635/lancaster/thesis/1407>.
- [133] M. Asada, S. Suzuki and T. Fukuma. ‘Measurements of temperature characteristics and estimation of terahertz negative differential conductance in resonant-tunneling-diode oscillators’. In: *AIP Advances* 7.11 (2017). ISSN: 2158-3226. DOI: 10.1063/1.5007093. URL: <https://doi.org/10.1063/1.5007093>.
- [134] Thomas McGrath et al. ‘A PUF taxonomy’. In: *Applied Physics Reviews* 6.1 (2019). ISSN: 1931-9401. DOI: 10.1063/1.5079407. URL: <https://doi.org/10.1063/1.5079407>.
- [135] Paul Horowitz and Winfield Hill. *The art of electronics*. English. Third. Cambridge;New York, NY, USA; Cambridge University Press, 2015. ISBN: 9780521809269;052180
- [136] Onur Günlü and Rafael F. Schaefer. ‘An Optimality Summary: Secret Key Agreement with Physical Unclonable Functions’. In: *Entropy* 23.1 (2021), p. 16. ISSN: 1099-4300. URL: <https://www.mdpi.com/1099-4300/23/1/16>.
- [137] Jonathan Katz and Yehuda Lindell. ‘Hash Functions and Applications’. In: *Introduction to Modern Cryptography*. 2nd. 2014. ISBN: 9780429101489. DOI: <https://doi.org/10.1201/b17668>.
- [138] Ramón Bernardo-Gavito et al. ‘Extracting random numbers from quantum tunnelling through a single diode’. In: *Scientific Reports* 7.1 (2017), p. 17879. ISSN: 2045-2322. DOI: 10.1038/s41598-017-18161-9. URL: <https://doi.org/10.1038/s41598-017-18161-9>.
- [139] D. Banasree, P. Manas and M. Saikat. ‘Effects on I-V characteristics of RTD due to different parametric variations’. In: *2017 Devices for Integrated Circuit (DevIC)*, pp. 257–261. DOI: 10.1109/DEVIC.2017.8073947. URL: <https://ieeexplore.ieee.org/document/8073947>.
- [140] Michele Cito. ‘Resonant tunnelling diode epitaxial wafer design manufacture and characterisation’. Thesis. 2022. DOI: 10.5525/gla.thesis.83238. URL: <https://theses.gla.ac.uk/id/eprint/83238>.

- [141] S. G. Muttlak et al. ‘InGaAs/AlAs Resonant Tunneling Diodes for THz Applications: An Experimental Investigation’. In: *IEEE Journal of the Electron Devices Society* 6 (2018), pp. 254–262. ISSN: 2168-6734. DOI: 10.1109/JEDS.2018.2797951. URL: <https://ieeexplore.ieee.org/document/8279410>.
- [142] E. R. Brown, W. D. Goodhue and T. C. L. G. Sollner. ‘Fundamental oscillations up to 200 GHz in resonant tunneling diodes and new estimates of their maximum oscillation frequency from stationary-state tunneling theory’. In: *Journal of Applied Physics* 64.3 (1988), pp. 1519–1529. ISSN: 0021-8979. DOI: 10.1063/1.341827. URL: <https://doi.org/10.1063/1.341827>.
- [143] L. E. Dickens. ‘Spreading Resistance as a Function of Frequency’. In: *IEEE Transactions on Microwave Theory and Techniques* 15.2 (1967), pp. 101–109. ISSN: 1557-9670. DOI: 10.1109/TMTT.1967.1126383. URL: <https://ieeexplore.ieee.org/document/1126383>.
- [144] Dinh Tuan Nguyen. ‘Optimization of sub-THz and THz resonant-tunneling-diode oscillators with symmetrical slot antennas’. Thesis. 2023. DOI: 10.34726/hss.2023.92043. URL: <https://doi.org/10.34726/hss.2023.92043>.
- [145] Naoyuki Orihashi et al. ‘Experimental and Theoretical Characteristics of Sub-Terahertz and Terahertz Oscillations of Resonant Tunneling Diodes Integrated with Slot Antennas’. In: *Japanese Journal of Applied Physics* 44.11R (2005), p. 7809. ISSN: 1347-4065 0021-4922. DOI: 10.1143/JJAP.44.7809. URL: <https://dx.doi.org/10.1143/JJAP.44.7809>.
- [146] ‘Basic Device Physics’. In: *Fundamentals of Modern VLSI Devices*. Ed. by Yuan Taur and Tak H. Ning. 3rd ed. Cambridge: Cambridge University Press, 2021, pp. 9–42. ISBN: 9781108480024. DOI: DOI:10.1017/9781108847087.005. URL: <https://www.cambridge.org/core/product/9B69376CA6C548C5AA4F107FAC06EE03>.
- [147] Tyler A. Growden et al. ‘431 kA/cm<sup>2</sup> peak tunneling current density in GaN/AlN resonant tunneling diodes’. In: *Applied Physics Letters* 112.3 (2018). ISSN: 0003-6951. DOI: 10.1063/1.5010794. URL: <https://doi.org/10.1063/1.5010794>.

- [148] Tom P. E. Broekaert and Clifton G. Fonstad. ‘In<sub>0.53</sub>Ga<sub>0.47</sub>As/AlAs resonant tunneling diodes with peak current densities in excess of 450 kA/cm<sup>2</sup>’. In: *Journal of Applied Physics* 68.8 (1990), pp. 4310–4312. ISSN: 0021-8979. DOI: 10.1063/1.346226. URL: <https://doi.org/10.1063/1.346226>.
- [149] Safumi Suzuki and Masahiro Asada. ‘Resonant Tunneling Diode (RTD) THz Sources’. In: *Advances in Terahertz Source Technologies*. Jenny Stanford Publishing, 2024, pp. 250–272. ISBN: 9781003459675. URL: <https://www.taylorfrancis.com/chapters/edit/10.1201/9781003459675-11/resonant-tunneling-diode-rtd-thz-sources-safumi-suzuki-masahiro-asada>.
- [150] M. O. Makeev, S. A. Meshkov and V. Yu Sinyakin. ‘Degradation study of AlAs/GaAs resonant tunneling diode IV curves under influence of high temperatures’. In: *Journal of Physics: Conference Series* 917.9 (2017), p. 092004. ISSN: 1742-6596 1742-6588. DOI: 10.1088/1742-6596/917/9/092004. URL: <https://dx.doi.org/10.1088/1742-6596/917/9/092004>.
- [151] Hiroki Tanaka et al. ‘Investigation of heat-dissipation structures in resonant tunneling diodes and their characteristics on terahertz oscillators’. In: *Japanese Journal of Applied Physics* 63.1 (2024), p. 011004. ISSN: 1347-4065 0021-4922. DOI: 10.35848/1347-4065/ad169a. URL: <https://dx.doi.org/10.35848/1347-4065/ad169a>.
- [152] Adam M. Crook et al. ‘Low resistance, nonalloyed Ohmic contacts to InGaAs’. In: *Applied Physics Letters* 91.19 (2007). ISSN: 0003-6951. DOI: 10.1063/1.2806235. URL: <https://doi.org/10.1063/1.2806235>.
- [153] C. Spudat et al. ‘Limitations of Output Power and Efficiency of Simple Resonant-Tunneling-Diode Oscillators’. In: *IEEE Transactions on Terahertz Science and Technology* 13.1 (2023), pp. 82–92. ISSN: 2156-3446. DOI: 10.1109/TTHZ.2022.3228069.
- [154] Fan Zhao et al. ‘Analysis of the eight parameter variation of the resonant tunneling diode (RTD) in the rapid thermal annealing process with resistance compensation effect’. In: *AIP Advances* 10.3 (2020). ISSN: 2158-3226. DOI: 10.1063/1.5133899. URL: <https://doi.org/10.1063/1.5133899>.

- [155] Michael N. Feiginov and Dibakar Roy Chowdhury. ‘Operation of resonant-tunneling diodes beyond resonant-state-lifetime limit’. In: *Applied Physics Letters* 91.20 (2007). ISSN: 0003-6951. DOI: 10.1063/1.2806922. URL: <https://doi.org/10.1063/1.2806922>.
- [156] Hiroki Sugiyama et al. ‘Extremely High Peak Current Densities of over  $1 \times 10^6$  A/cm<sup>2</sup> in InP-Based InGaAs/AlAs Resonant Tunneling Diodes Grown by Metal-Organic Vapor-Phase Epitaxy’. In: *Japanese Journal of Applied Physics* 49.5R (2010), p. 051201. ISSN: 1347-4065 0021-4922. DOI: 10.1143/JJAP.49.051201. URL: <https://dx.doi.org/10.1143/JJAP.49.051201>.
- [157] B. Ściana et al. ‘LP-MOVPE growth and properties of high Si-doped InGaAs contact layer for quantum cascade laser applications’. In: *Opto-Electronics Review* 24.2 (2016), pp. 95–102. DOI: doi:10.1515/oere-2016-0013. URL: <https://doi.org/10.1515/oere-2016-0013>.
- [158] F. F. Ouali and L. J. Challis. ‘Phonon-assisted tunnelling’. In: *Electron-Phonon Interactions in Low-Dimensional Structures*. Ed. by Lawrence Challis. Oxford University Press, 2003, pp. 185–238. ISBN: 9780191709319. DOI: 10.1093/acprof:oso/9780198507321.003.0006. URL: <https://doi.org/10.1093/acprof:oso/9780198507321.003.0006>.
- [159] ‘Scattering-assisted resonant tunnelling’. In: *The Physics and Applications of Resonant Tunnelling Diodes*. Ed. by Hiroshi Mizuta and Tomonori Tanoue. Cambridge Studies in Semiconductor Physics and Microelectronic Engineering. Cambridge: Cambridge University Press, 1995, pp. 52–87. ISBN: 9780521432184. DOI: DOI: 10.1017/CBO9780511629013.004. URL: <https://www.cambridge.org/core/product/139753117F31D3302E2ACFECFOACD2EC>.
- [160] Patrick Roblin and Wan-Rone Liou. ‘Three-dimensional scattering-assisted tunneling in resonant-tunneling diodes’. In: *Physical Review B* 47.4 (1993), pp. 2146–2161. ISSN: 0163-1829 (Print) 0163-1829 (Linking). DOI: 10.1103/PhysRevB.47.2146. URL: <https://link.aps.org/doi/10.1103/PhysRevB.47.2146>.

- [161] R. Lake et al. ‘Interface roughness, polar optical phonons, and the valley current of a resonant tunneling diode’. In: *Superlattices and Microstructures* 20.3 (1996), pp. 279–285. ISSN: 0749-6036. DOI: <https://doi.org/10.1006/spmi.1996.0079>. URL: <https://www.sciencedirect.com/science/article/pii/S0749603696900798>.
- [162] John A. Gil-Corrales et al. ‘Study of Electronic and Transport Properties in Double-Barrier Resonant Tunneling Systems’. In: *Nanomaterials* 12.10 (2022), p. 1714. ISSN: 2079-4991. DOI: 10.3390/nano12101714. URL: <https://www.mdpi.com/2079-4991/12/10/1714>.
- [163] V. J. Goldman, D. C. Tsui and J. E. Cunningham. ‘Evidence for LO-phonon-emission-assisted tunneling in double-barrier heterostructures’. In: *Physical Review B* 36.14 (1987), pp. 7635–7637. DOI: 10.1103/PhysRevB.36.7635. URL: <https://link.aps.org/doi/10.1103/PhysRevB.36.7635>.
- [164] T. Mori et al. ‘Experimental analysis of resonant-tunneling hot-electron transistors operated at room temperature’. In: *IEEE Transactions on Electron Devices* 35.12 (1988), p. 2453. ISSN: 1557-9646. DOI: 10.1109/16.8888. URL: <https://ieeexplore.ieee.org/document/8888>.
- [165] D. Rakoczy et al. ‘L-valley electron transport in GaAs-AlAs double-barrier resonant tunneling structures studied by ballistic electron emission microscopy’. In: *Physical Review B* 66.3 (2002), p. 033309. DOI: 10.1103/PhysRevB.66.033309. URL: <https://link.aps.org/doi/10.1103/PhysRevB.66.033309>.
- [166] S. A. Vitusevich et al. ‘Tunneling through X-valley-related impurity states in GaAs/AlAs resonant-tunneling diodes’. In: *Physical Review B* 61.16 (2000), pp. 10898–10904. DOI: 10.1103/PhysRevB.61.10898. URL: <https://link.aps.org/doi/10.1103/PhysRevB.61.10898>.
- [167] Hidetoshi Kanaya et al. ‘Fundamental Oscillation up to 1.31 THz in Resonant Tunneling Diodes with Thin Well and Barriers’. In: *Applied Physics Express* 5.12 (2012), p. 124101. ISSN: 1882-0786 1882-0778. DOI: 10.1143/APEX.5.124101. URL: <https://dx.doi.org/10.1143/APEX.5.124101>.

- [168] *TeraHertz technology (THz); Identification of frequency bands of interest for THz communication systems.* Report. European Telecommunications Standards Institute, 2024. URL: [http://webapp.etsi.org/workprogram/Report\\_WorkItem.asp?WKI\\_ID=67656](http://webapp.etsi.org/workprogram/Report_WorkItem.asp?WKI_ID=67656).
- [169] Enrique Castro-Camus, Martin Koch and Daniel M. Mittleman. ‘Recent advances in terahertz imaging: 1999 to 2021’. In: *Applied Physics B* 128.1 (2021), p. 12. ISSN: 1432-0649. DOI: 10.1007/s00340-021-07732-4. URL: <https://doi.org/10.1007/s00340-021-07732-4>.
- [170] Hidetoshi Kanaya et al. ‘Fundamental Oscillation up to 1.42 THz in Resonant Tunneling Diodes by Optimized Collector Spacer Thickness’. In: *Journal of Infrared, Millimeter, and Terahertz Waves* 35.5 (2014), pp. 425–431. ISSN: 1866-6906. DOI: 10.1007/s10762-014-0058-z. URL: <https://doi.org/10.1007/s10762-014-0058-z>.
- [171] K. Ishigaki et al. *Direct intensity modulation and wireless data transmission characteristics of terahertz-oscillating resonant tunnelling diodes*. Electronic Article. 2012. URL: <https://digital-library.theiet.org/content/journals/10.1049/el.2012.0849>.
- [172] Masato Shiraishi et al. ‘High Output Power ( 400  $\mu$ W) Oscillators at around 550 GHz Using Resonant Tunneling Diodes with Graded Emitter and Thin Barriers’. In: *Applied Physics Express* 4.6 (2011), p. 064101. ISSN: 1882-0786 1882-0778. DOI: 10.1143/APEX.4.064101. URL: <https://dx.doi.org/10.1143/APEX.4.064101>.
- [173] Kenta Urayama et al. ‘Sub-Terahertz Resonant Tunneling Diode Oscillators Integrated with Tapered Slot Antennas for Horizontal Radiation’. In: *Applied Physics Express* 2.4 (2009), p. 044501. ISSN: 1882-0786 1882-0778. DOI: 10.1143/APEX.2.044501. URL: <https://dx.doi.org/10.1143/APEX.2.044501>.
- [174] S. Suzuki et al. ‘High-Power Operation of Terahertz Oscillators With Resonant Tunneling Diodes Using Impedance-Matched Antennas and Array Configuration’. In: *IEEE Journal of Selected Topics in Quantum Electronics* 19.1 (2013), pp. 8500108–8500108. ISSN: 1558-4542. DOI: 10.1109/JSTQE.2012.2215017.

- [175] Alan Bensky. ‘Chapter 3 - Antennas and transmission lines’. In: *Short-range Wireless Communication (Third Edition)*. Ed. by Alan Bensky. Newnes, 2019, pp. 43–83. ISBN: 978-0-12-815405-2. DOI: <https://doi.org/10.1016/B978-0-12-815405-2.00003-8>. URL: <https://www.sciencedirect.com/science/article/pii/B9780128154052000038>.
- [176] G. Picco et al. ‘Generalized Analysis of Output-Power Limitations of Resonant-Tunnelling-Diode Oscillators With Symmetrical Slot Antennas’. In: *IEEE Transactions on Terahertz Science and Technology* 14.5 (2024), pp. 621–631. ISSN: 2156-3446. DOI: 10.1109/TTHZ.2024.3435464. URL: <https://doi.org/10.1109/TTHZ.2024.3435464>.
- [177] Teruo Matsushita. ‘Theorems for Electric Circuits’. In: *Electricity : Electromagnetism and Electric Circuits*. Cham: Springer Nature Switzerland, 2023, pp. 213–238. ISBN: 978-3-031-44002-1. DOI: 10.1007/978-3-031-44002-1\_11. URL: [https://doi.org/10.1007/978-3-031-44002-1\\_11](https://doi.org/10.1007/978-3-031-44002-1_11).
- [178] Ta Van Mai et al. ‘Structure-Simplified Resonant-Tunneling-Diode Terahertz Oscillator Without Metal-Insulator-Metal Capacitors’. In: *Journal of Infrared, Millimeter, and Terahertz Waves* 41.12 (2020), pp. 1498–1507. ISSN: 1866-6906. DOI: 10.1007/s10762-020-00738-7. URL: <https://doi.org/10.1007/s10762-020-00738-7>.
- [179] Hou-Tong Chen et al. ‘Active terahertz metamaterial devices’. In: *Nature* 444.7119 (2006), pp. 597–600. ISSN: 1476-4687. DOI: 10.1038/nature05343. URL: <https://doi.org/10.1038/nature05343>.
- [180] D. Schurig, J. J. Mock and D. R. Smith. ‘Electric-field-coupled resonators for negative permittivity metamaterials’. In: *Applied Physics Letters* 88.4 (2006). ISSN: 0003-6951. DOI: 10.1063/1.2166681. URL: <https://doi.org/10.1063/1.2166681>.
- [181] Y. Yoshida et al. ‘Resonant-tunneling-diode oscillator with offset slot-ring antenna for efficient radiation of second harmonic signal exceeding 2 THz’. In: *2024 49th International Conference on Infrared, Millimeter, and Terahertz Waves (IRMMW-THz)*, pp. 1–2. DOI: 10.1109/IRMMW-THz60956.2024.10697537. URL: <https://ieeexplore.ieee.org/document/10697537>.

- [182] T. Sato, T. Van Mai and S. Suzuki. ‘Limit of oscillation frequency in two-element slot-ring type RTD oscillator array’. In: *2023 48th International Conference on Infrared, Millimeter, and Terahertz Waves (IRMMW-THz)*, pp. 1–2. DOI: 10.1109/IRMMW-THz57677. 2023. 10299277. URL: <https://ieeexplore.ieee.org/document/10299277>.
- [183] P. Ourednik et al. ‘Double-resonant-tunneling-diode patch-antenna oscillators’. In: *Applied Physics Letters* 119.26 (2021). ISSN: 0003-6951. DOI: 10.1063/5.0068114. URL: <https://doi.org/10.1063/5.0068114>.
- [184] Kouhei Kasagi, Safumi Suzuki and Masahiro Asada. ‘Large-scale array of resonant-tunneling-diode terahertz oscillators for high output power at 1 THz’. In: *Journal of Applied Physics* 125.15 (2019). ISSN: 0021-8979. DOI: 10.1063/1.5051007. URL: <https://doi.org/10.1063/1.5051007>.
- [185] Masahiro Asada and Safumi Suzuki. ‘THz Resonant Tunneling Devices’. In: *Fundamentals of Terahertz Devices and Applications*. 2021, pp. 447–477. DOI: <https://doi.org/10.1002/9781119460749.ch11>. URL: <https://onlinelibrary.wiley.com/doi/abs/10.1002/9781119460749.ch11>.
- [186] Masahiro Asada and Safumi Suzuki. ‘Theoretical analysis of external feedback effect on oscillation characteristics of resonant-tunneling-diode terahertz oscillators’. In: *Japanese Journal of Applied Physics* 54.7 (2015), p. 070309. ISSN: 1347-4065 0021-4922. DOI: 10.7567/JJAP.54.070309. URL: <https://dx.doi.org/10.7567/JJAP.54.070309>.
- [187] Masahiro Asada and Safumi Suzuki. ‘Room-Temperature Oscillation of Resonant Tunneling Diodes close to 2 THz and Their Functions for Various Applications’. In: *Journal of Infrared, Millimeter, and Terahertz Waves* 37.12 (2016), pp. 1185–1198. ISSN: 1866-6906. DOI: 10.1007/s10762-016-0321-6. URL: <https://doi.org/10.1007/s10762-016-0321-6>.
- [188] B. Hong and A. Hajimiri. ‘A General Theory of Injection Locking and Pulling in Electrical Oscillators-Part I: Time-Synchronous Modeling and Injection Waveform Design’. In: *IEEE Journal of Solid-State Circuits* 54.8 (2019), pp. 2109–2121. ISSN: 1558-173X. DOI: 10.1109/JSSC.2019.2908753. URL: <https://ieeexplore.ieee.org/document/8753733>.

- [189] Kota Ogino, Safumi Suzuki and Masahiro Asada. ‘Spectral Narrowing of a Varactor-Integrated Resonant-Tunneling-Diode Terahertz Oscillator by Phase-Locked Loop’. In: *Journal of Infrared, Millimeter, and Terahertz Waves* 38.12 (2017), pp. 1477–1486. ISSN: 1866-6906. DOI: 10.1007/s10762-017-0439-1. URL: <https://doi.org/10.1007/s10762-017-0439-1>.
- [190] N. Nishigami et al. ‘Resonant Tunneling Diode Receiver for Coherent Terahertz Wireless Communication’. In: *2018 Asia-Pacific Microwave Conference (APMC)*, pp. 726–728. DOI: 10.23919/APMC.2018.8617565. URL: <https://ieeexplore.ieee.org/document/8617565>.
- [191] Masahiro Asada, Safumi Suzuki and Naomichi Kishimoto. ‘Resonant Tunneling Diodes for Sub-Terahertz and Terahertz Oscillators’. In: *Japanese Journal of Applied Physics* 47.6 (2008), pp. 4375–4384. ISSN: 0021-4922 1347-4065. DOI: 10.1143/jjap.47.4375. URL: <https://iopscience.iop.org/article/10.1143/JJAP.47.4375>.
- [192] Robert Lacoste. ‘Chapter 1 - Impedance Matching Basics’. In: *Robert Lacoste’s The Darker Side*. Ed. by Robert Lacoste. Boston: Newnes, 2010, pp. 3–16. ISBN: 978-1-85617-762-7. DOI: <https://doi.org/10.1016/B978-1-85617-762-7.00001-0>. URL: <https://www.sciencedirect.com/science/article/pii/B9781856177627000010>.
- [193] Ryunosuke Izumi et al. ‘Resonant-tunneling-diode terahertz oscillator with a cylindrical cavity for high-frequency oscillation’. In: *AIP Advances* 9.8 (2019). ISSN: 2158-3226. DOI: 10.1063/1.5114963. URL: <https://doi.org/10.1063/1.5114963>.
- [194] Mikhail Bezhko, Safumi Suzuki and Masahiro Asada. ‘Frequency increase in resonant-tunneling diode cavity-type terahertz oscillator by simulation-based structure optimization’. In: *Japanese Journal of Applied Physics* 59.3 (2020), p. 032004. ISSN: 1347-4065 0021-4922. DOI: 10.35848/1347-4065/ab7355. URL: <https://dx.doi.org/10.35848/1347-4065/ab7355>.

- [195] D. Cimbri et al. ‘Accurate Quantum Transport Modeling of High-Speed In<sub>0.53</sub>Ga<sub>0.47</sub>As/Al<sub>x</sub>Ga<sub>1-x</sub>As Double-Barrier Resonant Tunneling Diodes’. In: *IEEE Transactions on Electron Devices* 69.8 (2022), pp. 4638–4645. ISSN: 1557-9646. DOI: 10.1109/TED.2022.3178360. URL: <https://ieeexplore.ieee.org/document/9791098>.
- [196] Salim Berrada et al. ‘Nano-electronic Simulation Software (NESS): a flexible nano-device simulation platform’. In: *Journal of Computational Electronics* 19.3 (2020), pp. 1031–1046. ISSN: 1569-8025 1572-8137. DOI: 10.1007/s10825-020-01519-0. URL: <https://doi.org/10.1007/s10825-020-01519-0>.
- [197] Hamilton Carrillo-Nunez et al. ‘Simulation of Si nanowire quantum-dot devices for authentication’. In: *2019 Joint International EUROSOI Workshop and International Conference on Ultimate Integration on Silicon (EUROSOI-ULIS)*. 2019, pp. 1–4. DOI: 10.1109/EUROSOI-ULIS45800.2019.9041864. URL: <https://doi.org/10.1109/EUROSOI-ULIS45800.2019.9041864>.
- [198] M. Hori et al. ‘Performance enhancement of semiconductor devices by control of discrete dopant distribution’. In: *Nanotechnology* 20.36 (2009), p. 365205. ISSN: 0957-4484. DOI: 10.1088/0957-4484/20/36/365205. URL: <https://dx.doi.org/10.1088/0957-4484/20/36/365205>.
- [199] B. R. Nag. ‘Interface roughness scattering limited mobility in AlAs/GaAs, Al-GaAs/GaAs and GaInP/GaAs quantum wells’. In: *Semiconductor Science and Technology* 19.2 (2004), pp. 162–166. ISSN: 0268-1242. DOI: PiS0268-1242(04)64937-6Doi10.1088/0268-1242/19/2/006. URL: <https://iopscience.iop.org/article/10.1088/0268-1242/19/2/006>.
- [200] J. M. Li et al. ‘A model for scattering due to interface roughness in finite quantum wells’. In: *Semiconductor Science and Technology* 20.12 (2005), pp. 1207–1212. ISSN: 0268-1242. DOI: 10.1088/0268-1242/20/12/011. URL: <https://iopscience.iop.org/article/10.1088/0268-1242/20/12/011/pdf>.
- [201] Naresh Chand and S. N. G. Chu. ‘Origin and improvement of interface roughness in AlGaAs/GaAs heterostructures grown by molecular beam epitaxy’. In: *Applied Physics Letters* 57.17 (1990), pp. 1796–1798. ISSN: 0003-6951. DOI: 10.1063/1.104025. URL: <https://doi.org/10.1063/1.104025>.

- [202] J. A. Ogilvy and J. R. Foster. ‘Rough Surfaces: Gaussian or Exponential Statistics?’ In: *Journal of Physics D: Applied Physics* 22.9 (1989), p. 1243. ISSN: 0022-3727. DOI: 10.1088/0022-3727/22/9/001. URL: <https://dx.doi.org/10.1088/0022-3727/22/9/001>.
- [203] Yiping Zhao, Gwo-Ching Wang and Toh-Ming Lu. ‘Examples of Random Rough Surfaces’. In: *Characterization of Amorphous and Crystalline Rough Surface: Principles and Applications*. Vol. 37. Experimental Methods in the Physical Sciences. Academic Press, 2001, pp. 33–61. ISBN: 9780124759848. DOI: 10.1016/S1079-4042(01)80058-8. URL: [https://doi.org/10.1016/S1079-4042\(01\)80058-8](https://doi.org/10.1016/S1079-4042(01)80058-8).
- [204] Y. Z. Hu and K. Tonder. ‘Simulation of 3-D random rough surface by 2-D digital filter and fourier analysis’. In: *International Journal of Machine Tools and Manufacture* 32.1 (1992), pp. 83–90. ISSN: 0890-6955. DOI: [https://doi.org/10.1016/0890-6955\(92\)90064-N](https://doi.org/10.1016/0890-6955(92)90064-N). URL: <https://www.sciencedirect.com/science/article/pii/089069559290064N>.
- [205] Clovis R. Maliska. ‘The Finite Volume Method’. In: *Fundamentals of Computational Fluid Dynamics: The Finite Volume Method*. Cham: Springer International Publishing, 2023, pp. 41–83. ISBN: 978-3-031-18235-8. DOI: 10.1007/978-3-031-18235-8\_3. URL: [https://doi.org/10.1007/978-3-031-18235-8\\_3](https://doi.org/10.1007/978-3-031-18235-8_3).
- [206] Johan Verbeke and Ronald Cools. ‘The Newton-Raphson method’. In: *International Journal of Mathematical Education in Science and Technology* 26.2 (1995), pp. 177–193. ISSN: 0020-739X. DOI: 10.1080/0020739950260202. URL: <https://doi.org/10.1080/0020739950260202>.
- [207] T. Dutta et al. ‘Density Gradient Based Quantum-Corrected 3D Drift-Diffusion Simulator for Nanoscale MOSFETs’. In: *2021 IEEE 16th Nanotechnology Materials and Devices Conference (NMDC)*, pp. 1–4. DOI: 10.1109/NMDC50713.2021.9677480. URL: <https://ieeexplore.ieee.org/document/9677480>.
- [208] A. Hadjidimos. ‘Successive overrelaxation (SOR) and related methods’. In: *Journal of Computational and Applied Mathematics* 123.1 (2000), pp. 177–199. ISSN: 0377-0427. DOI: [https://doi.org/10.1016/S0377-0427\(00\)00403-9](https://doi.org/10.1016/S0377-0427(00)00403-9). URL: <https://www.sciencedirect.com/science/article/pii/S0377042700004039>.

- [209] Clovis R. Maliska. ‘Solution of the Linear System’. In: *Fundamentals of Computational Fluid Dynamics: The Finite Volume Method*. Cham: Springer International Publishing, 2023, pp. 85–111. ISBN: 978-3-031-18235-8. DOI: 10.1007/978-3-031-18235-8\_4. URL: [https://doi.org/10.1007/978-3-031-18235-8\\_4](https://doi.org/10.1007/978-3-031-18235-8_4).
- [210] Roger W. Hockney. *Computer simulation using particles*. Place of publication not identified: CRC Press, 1988. ISBN: 9780367806934. DOI: 10.1201/9780367806934. URL: <https://doi.org/10.1201/9780367806934>.
- [211] Feifei Wan, Yong Yin and Suiyu Zhang. ‘3D Parallel Multigrid Methods for Real-Time Fluid Simulation’. In: *3D Research* 9.1 (2018), p. 8. ISSN: 2092-6731. DOI: 10.1007/s13319-018-0157-z. URL: <https://doi.org/10.1007/s13319-018-0157-z>.
- [212] Mahdi Pourfath. *The non-equilibrium Green’s function method for nanoscale device simulation*. Wien: Springer, 2014. ISBN: 978-3-7091-1800-9. URL: <https://link.springer.com/book/10.1007/978-3-7091-1800-9>.
- [213] Seonghoon Jin, Young June Park and Hong Shick Min. ‘A three-dimensional simulation of quantum transport in silicon nanowire transistor in the presence of electron-phonon interactions’. In: *Journal of Applied Physics* 99.12 (2006). ISSN: 0021-8979. DOI: 10.1063/1.2206885. URL: <https://doi.org/10.1063/1.2206885>.
- [214] Mathieu Luisier and Gerhard Klimeck. ‘Atomistic full-band simulations of silicon nanowire transistors: Effects of electron-phonon scattering’. In: *Phys. Rev. B* 80 (15 2009), p. 155430. DOI: 10.1103/PhysRevB.80.155430. URL: <https://link.aps.org/doi/10.1103/PhysRevB.80.155430>.
- [215] M. P. Lopez Sancho et al. ‘Highly convergent schemes for the calculation of bulk and surface Green functions’. In: *Journal of Physics F: Metal Physics* 15.4 (1985), p. 851. ISSN: 0305-4608. DOI: 10.1088/0305-4608/15/4/009. URL: <https://dx.doi.org/10.1088/0305-4608/15/4/009>.
- [216] Gianluca Stefanucci and Robert van Leeuwen. *Nonequilibrium Many-Body Theory of Quantum Systems: A Modern Introduction*. Cambridge: Cambridge University Press, 2013. DOI: 10.1017/CBO9781139023979. URL: <https://doi.org/10.1017/CBO9781139023979>.

- [217] Mathieu Luisier, Andreas Schenk and Wolfgang Fichtner. ‘Quantum transport in two- and three-dimensional nanoscale transistors: Coupled mode effects in the nonequilibrium Green’s function formalism’. In: *Journal of Applied Physics* 100.4 (2006). ISSN: 0021-8979. DOI: 10.1063/1.2244522. URL: <https://doi.org/10.1063/1.2244522>.
- [218] A. Svizhenko et al. ‘Two-dimensional quantum mechanical modeling of nanotransistors’. In: *Journal of Applied Physics* 91.4 (2002), pp. 2343–2354. ISSN: 0021-8979. DOI: 10.1063/1.1432117. URL: <https://doi.org/10.1063/1.1432117>.
- [219] Daniel A. Lemus, James Charles and Tillmann Kubis. ‘Mode-space-compatible inelastic scattering in atomistic nonequilibrium Green’s function implementations’. In: *Journal of Computational Electronics* 19.4 (2020), pp. 1389–1398. ISSN: 1572-8137. DOI: 10.1007/s10825-020-01549-8. URL: <https://doi.org/10.1007/s10825-020-01549-8>.
- [220] Aryan Afzalian. ‘Computationally efficient self-consistent born approximation treatments of phonon scattering for coupled-mode space non-equilibrium Green’s function’. In: *Journal of Applied Physics* 110.9 (2011). ISSN: 0021-8979. DOI: 10.1063/1.3658809. URL: <https://doi.org/10.1063/1.3658809>.
- [221] Aniello Esposito, Martin Frey and Andreas Schenk. ‘Quantum transport including nonparabolicity and phonon scattering: application to silicon nanowires’. In: *Journal of Computational Electronics* 8.3 (2009), pp. 336–348. ISSN: 1572-8137. DOI: 10.1007/s10825-009-0276-0. URL: <https://doi.org/10.1007/s10825-009-0276-0>.
- [222] Carlo Jacoboni and Lino Reggiani. ‘The Monte Carlo method for the solution of charge transport in semiconductors with applications to covalent materials’. In: *Reviews of Modern Physics* 55.3 (1983), pp. 645–705. DOI: 10.1103/RevModPhys.55.645. URL: <https://link.aps.org/doi/10.1103/RevModPhys.55.645>.
- [223] C. H. Grein, S. Zollner and M. Cardona. ‘Calculation of intervalley scattering rates in  $\text{Al}_x\text{Ga}_{1-x}\text{As}$ : Effects of alloy and phonon scattering’. In: *Physical Review B* 44.23 (1991), pp. 12761–12768. DOI: 10.1103/PhysRevB.44.12761. URL: <https://link.aps.org/doi/10.1103/PhysRevB.44.12761>.

- [224] M.V. Fischetti. ‘Monte Carlo simulation of transport in technologically significant semiconductors of the diamond and zinc-blende structures. I. Homogeneous transport’. In: *IEEE Transactions on Electron Devices* 38.3 (1991), pp. 634–649. DOI: 10.1109/16.75176. URL: <https://doi.org/10.1109/16.75176>.
- [225] Hong-Hyun Park et al. *Resonant Tunneling Diode Simulation with NEGF*. Generic. 2018. DOI: 10.4231/D3125QC2M. URL: <https://nanohub.org/resources/rtdnegf>.
- [226] S. Steiger et al. ‘NEMO5: A Parallel Multiscale Nanoelectronics Modeling Tool’. In: *IEEE Transactions on Nanotechnology* 10.6 (2011), pp. 1464–1474. ISSN: 1941-0085. DOI: 10.1109/TNANO.2011.2166164. URL: <https://ieeexplore.ieee.org/document/6069914>.
- [227] P. Blaise et al. ‘Nanoscale FET: How To Make Atomistic Simulation Versatile, Predictive, and Fast at 5nm Node and Below’. In: *2020 International Conference on Simulation of Semiconductor Processes and Devices (SISPAD)*. World Scientific, pp. 249–252. ISBN: 978-4-86348-763-5. DOI: 10.23919/SISPAD49475.2020.9241651. URL: <https://ieeexplore.ieee.org/document/9241651>.
- [228] Gerhard Klimeck et al. ‘Quantum device simulation with a generalized tunneling formula’. In: *Applied Physics Letters* 67.17 (1995), pp. 2539–2541. DOI: 10.1063/1.114451. URL: <https://aip.scitation.org/doi/abs/10.1063/1.114451>.
- [229] Y. Guan et al. ‘Impact of the Figures of Merit (FoMs) Definitions on the Variability in Nanowire TFET: NEGF Simulation Study’. In: *IEEE Transactions on Electron Devices* 69.11 (2022), pp. 6394–6399. ISSN: 1557-9646. DOI: 10.1109/TED.2022.3204596. URL: <https://ieeexplore.ieee.org/document/9894379>.
- [230] T. Schmidt et al. ‘Peak-to-valley ratio of small resonant-tunneling diodes with various barrier-thickness asymmetries’. In: *Applied Physics Letters* 68.6 (1996), pp. 838–840. ISSN: 0003-6951. DOI: 10.1063/1.116550. URL: <https://doi.org/10.1063/1.116550>.

- [231] J. J. Shi, B. C. Sanders and S. H. Pan. ‘Asymmetric double barrier resonant tunnelling structures with improved characteristics’. In: *Solid State Communications* 110.7 (1999), pp. 393–396. ISSN: 0038-1098. DOI: [https://doi.org/10.1016/S0038-1098\(99\)00072-1](https://doi.org/10.1016/S0038-1098(99)00072-1). URL: [https://doi.org/10.1016/S0038-1098\(99\)00072-1](https://doi.org/10.1016/S0038-1098(99)00072-1).
- [232] Sushree Ipsita, P. K. Mahapatra and P. Panchadhyayee. ‘Optimum device parameters to attain the highest peak to valley current ratio (PVCR) in resonant tunneling diodes (RTD)’. In: *Physica B: Condensed Matter* 611 (2021), p. 412788. ISSN: 0921-4526. DOI: <https://doi.org/10.1016/j.physb.2020.412788>. URL: <https://www.sciencedirect.com/science/article/pii/S0921452620307614>.
- [233] N. Rueangnetr and K. Sivalertporn. ‘Effect of quantum well width on the electron and hole states in different single quantum well structures’. In: *Journal of Physics: Conference Series* 1380.1 (2019), p. 012082. ISSN: 1742-6596 1742-6588. DOI: 10.1088/1742-6596/1380/1/012082. URL: <https://dx.doi.org/10.1088/1742-6596/1380/1/012082>.
- [234] W.J. Conover. *Practical Nonparametric Statistics*. John Wiley Sons, 1971. ISBN: 9780471168515.
- [235] JL Hodges Jr. ‘The significance probability of the Smirnov two-sample test’. In: *Arkiv för matematik* 3.5 (1958), pp. 469–486.
- [236] Andreas Löffler. ‘Über eine Partition der nat. Zahlen und ihre Anwendung beim U-Test’. In: *Wissenschaftliche Zeitschrift der Martin-Luther-Universität Halle-Wittenberg. Mathematisch-Naturwissenschaftliche Reihe* (Jan. 1983).
- [237] Yashuang Mu, Xiaodong Liu and Lidong Wang. ‘A Pearson’s correlation coefficient based decision tree and its parallel implementation’. In: *Information Sciences* 435 (2018), pp. 40–58. ISSN: 0020-0255. DOI: <https://doi.org/10.1016/j.ins.2017.12.059>. URL: <https://www.sciencedirect.com/science/article/pii/S0020025517311763>.
- [238] Y. Tokura et al. ‘Anisotropic roughness scattering at a heterostructure interface’. In: *Physical Review B* 46.23 (1992), pp. 15558–15561. DOI: 10.1103/PhysRevB.46.15558. URL: <https://link.aps.org/doi/10.1103/PhysRevB.46.15558>.

- [239] M. Aldegunde, A. Martinez and A. Asenov. ‘Non-equilibrium Green’s function analysis of cross section and channel length dependence of phonon scattering and its impact on the performance of Si nanowire field effect transistors’. In: *Journal of Applied Physics* 110.9 (2011). ISSN: 0021-8979. DOI: 10.1063/1.3658856. URL: <https://doi.org/10.1063/1.3658856>.
- [240] G. Thorgilsson, G. Viktorsson and S. I. Erlingsson. ‘Recursive Green’s function method for multi-terminal nanostructures’. In: *Journal of Computational Physics* 261 (2014), pp. 256–266. ISSN: 0021-9991. DOI: <https://doi.org/10.1016/j.jcp.2013.12.054>. URL: <https://www.sciencedirect.com/science/article/pii/S0021999114000096>.
- [241] X. W. Zhang and Y. L. Liu. ‘Electronic transport and spatial current patterns of 2D electronic system: A recursive Green’s function method study’. In: *AIP Advances* 9.11 (2019). ISSN: 2158-3226. DOI: 10.1063/1.5130534. URL: <https://doi.org/10.1063/1.5130534>.